Measurement and modelling of heat fluxes received by a RF electrode in a magnetized plasma

Anil Cherukulappurath Mana

Measurement and modelling of heat fluxes received by a RF electrode in a magnetized plasma

THÈSE

présentée et soutenue publiquement le 27 Novembre 2023

pour l'obtention du

Doctorat de l'Université de Lorraine

Mention : Physique. Spécialité: Physique des plasmas

par

Anil Cherukulappurath Mana

Composition du jury

Rapporteurs :	M. James Gunn	Chercheur CEA - HDR, IRFM, CEA Cadarache
	Mme. Kristel Crombé	Professeur des universités UniGhent
Examinateurs :	M. Stephane Heuraux (Président du jury)	Professeur des universités, IJL, Université de Lorraine
	M. Volodymyr Bobkov	Chercheur Max-Planck-IPP, Garching
Directeur :	M. Fréderic Brochard	Professeur des Universités, IJL, Université de Lorraine
Co-directeur :	M. Eric Faudot	maître de conférences, IJL, Université de Lorraine

Institut Jean Lamour | UMR CNRS 7198, Nancy, France, Université de Lorraine

Contents

Résumé **3**

1 Introduction **9**

1.1 Plasma, Nuclear Fusion and Applications . . . 10
1.2 Plasma inside a Tokamak . . . 11
1.3 Ion Cyclotron Resonance Heating (ICRH) . . . 12
1.4 RF Plasma in Material Processing . . . 13
1.5 Debye Sheath . . . 14
1.6 RF power coupling . . . 16
1.7 RF Sheath . . . 17
1.7.1 Sheath rectification in RF discharge . . . 17
1.7.2 Estimation of the self bias . . . 19
1.7.3 DC self-bias in asymmetric CCP RF discharge . . . 19
1.7.4 Double sheath model in asymmetric RF discharge . . . 20
1.7.5 Double Saturated Probe (DSP) model . . . 22
1.7.6 Magnetized oblique sheaths . . . 22
1.7.7 Stochastic heating . . . 23
1.7.8 Stochastic heating in presence of a magnetic field . . . 25
1.8 The heat flux and motivation of the thesis . . . 26

2 Experimental Setup and Diagnostics **29**

2.1 ALINE Plasma Device . . . 30
2.1.1 RF electrode types . . . 31
2.2 Diagnostic tools in ALINE . . . 33

2.2.1 RF compensated Langmuir probe . . . 33
2.2.2 Analysis of probe data . . . 35
2.2.3 Floating Probe . . . 40
2.2.4 IR Camera . . . 40
2.2.5 Fast Camera Imaging . . . 43

3 Measurement and Modelling of Highly Negative Floating Potential Measurements around One-faced RF Electrode in an RF Discharge 47

3.1 Langmuir Probe Measurements in a Magnetized Capacitive Discharge Around a Tilted RF Electrode . . . 48
3.1.1 Introduction . . . 48
3.1.2 Setup and Experiment . . . 49
3.1.3 Langmuir Probe Measurements in ALINE . . . 49
3.1.4 Theoretical floating potential for supra-thermal electrons . . . 57
3.2 PIC Simulation of the Electron Energy Distribution Function in a RF Magnetized Plasma Column Connected to a Tilted Electrode . . . 60
3.2.1 PIC Simulations . . . 61
3.3 Conclusion . . . 70

4 Positive Self-bias and Sheath Reversal in Magnetized Asymmetric RF CCP Helium Discharge 73

4.1 Positive Self-Bias in a magnetized RF plasma discharge . . . 74
4.1.1 Introduction . . . 74
4.1.2 Experiment . . . 75
4.1.3 Model . . . 75
4.1.4 Observations and results . . . 78
4.2 Experimental observation of sheath reversal in magnetized asymmetric RF CCP Helium Discharge . . . 83
4.2.1 Introduction . . . 83
4.2.2 Setup and Experimental Parameters . . . 84
4.2.3 Model : IV analysis in case of hot and cold electron population 84
4.2.4 Results and Discussions . . . 86

4.3 Conclusion . . . 97

5 Experimental investigation on Effect of Drifts in ALINE Device 99

5.1 Introduction . . . 100

5.2 Drift structures in the vicinity of an Electrode With Grounded Copper Shield . . . 101

5.2.1 Setup and Experiment . . . 101

5.2.2 Results and Discussions . . . 102

5.3 Experiments with Tungsten Electrode with Ceramic Covering . . . 114

5.3.1 Angle Dependence . . . 114

5.3.2 Magnetic field dependence . . . 119

5.3.3 Fast Camera results . . . 123

5.4 Experiments with Tungsten Electrode . . . 125

5.4.1 Capacitively Coupled Discharge Results . . . 126

5.5 Conclusion . . . 137

6 Experimental Investigation of Heat Flux to the RF antenna at grazing angles in Magnetized RF Discharge 141

6.1 Introduction . . . 142

6.2 Experiment and Analysis . . . 143

6.3 Script of the Heat flux Analytical Model . . . 143

6.4 Results : One faced Electrode . . . 147

6.4.1 Langmuir probe results . . . 147

6.4.2 IR Camera Measurements . . . 149

6.4.3 IR Camera Results using TEDDY . . . 151

6.4.4 Results : $\alpha = 0^{\circ}$ . . . 152

6.4.5 α=5° Measurements . . . 157

6.4.6 $\alpha = 20^{\circ}$ Results . . . 160

6.5 Experiments with Tungsten Electrode . . . 161

6.5.1 DC self-bias . . . 161

6.5.2 Heat flux Measurement results . . . 162

6.5.3 Comparison to the Analytical Model . . . 164

6.6 COMSOL Results 165
6.7 Conclusions 169

7 Conclusions, limitations and future perspectives **171**

Bibliography **175**

Acknowledgement

At first, I wasn't sure about doing a PhD during my master's, but the three years of my PhD turned out to be an amazing journey. It had its ups and downs, but I got to explore various academic and non-academic areas. I'm grateful to everyone who supported and guided me throughout my PhD journey.

I express my gratitude to Dr. Eric Faudot for the opportunity to work with him during my PhD. His consistent support and guidance were crucial to my journey. Beyond learning about plasma physics and experimental techniques, I appreciate his encouragement and patience, making this collaboration a valuable and enriching experience. All the memories from the ALINE room, TCRFPP, and our conversations over coffee and pain au chocolat will always stay with me.

I am grateful to Dr. Frederic Brochard, my advisor, for his unwavering support throughout my research journey and beyond. His consistently positive attitude and steadfast encouragement were invaluable during my PhD. He not only encouraged me to take on new challenges but also served as a role model whom I deeply admire.

I would like to thank Dr Stephane Heuraux and Debraj Mandal for the late-evening scientific discussions and your kind support. I would like to extend my gratitude to Dr Nicolas Lemoine, Dr Maxime Lesur and Dr Jerome Moritz for their kind support and encouragement.

I am incredibly proud and overjoyed to be a part of Team 107 at IJL, and I consider myself fortunate to have such exceptional colleagues. I want to express my heartfelt gratitude to Guillaume Lo-cascio, Alejandro Guillevic, Luigui Salazar, Sarah Chouchene, Louis Fevre, and Kyungtak Lim. Your love and support mean the world to me. I want to acknowledge the profound influence each of you has had on my life. You've collectively become role models for me inspiring me in various aspects. I am genuinely grateful for the positive impact you've had on my personal and professional journey. Thank you for being such invaluable sources of support and inspiration.

Deep appreciation to our esteemed collaborators from the SHEAR project at the University of Basel and EPFL, with special thanks to Dr Laurent Marot and Paul Hiret. I want to extend my heartfelt gratitude to Dr Jan Horacek and Dr Jordan Cavalier. Working with you on our paper and engaging in scientific discussions has been an invaluable experience. I am genuinely thankful for the opportunity to collaborate, as it allowed me to gain profound insights into fusion physics and research.

Throughout my PhD journey, I have been fortunate to have support from my mother, Jayasree T N, my father, Krishnan C M and my sister, Athira.

I extend my sincere gratitude to Dr V K Deshpande, Sudhir Cherukulappurath, Dr Shishir Deshpande, Dr Mainak Bandyopadhyay, and Kaushal Pandya for their unwavering support. My research journey commenced under their guidance, and I am truly thankful for the opportunity to intern at the University of Goa and the Institute for

Plasma Research. Dr. Mainak's motivation and inspiration played a pivotal role in steering my career toward plasma physics. I am grateful to Dr Prashant and the team ROBIN for their insightful scientific discussions.

I embarked on my research journey, drawing inspiration from my friend Jithin, and for that, I am immensely grateful. A special thanks to Dr Arun Pandey for his continuous mentorship, guidance, and motivation. Your unwavering support has been a constant source of inspiration. My heartfelt gratitude extends to my dear friends Aleena, Nitha, Vishnu O, Priya, and Harpreet.

To Aswin, Vishnu, Krupali, Kaushalya, Sreelakshmi, Chithra, Camille, Abha, and Akilan—words fall short of expressing my thanks and love. Your support means the world to me. Thanks to everyone who taught me to dream and those who held my hands to the dreams.

Résumé

La connaissance de la science derrière la production d'énergie dans les étoiles a ouvert la voie à une source d'énergie potentiellement abondante, inspirant divers concepts de réacteurs de fusion nucléaire. Le gaz peut être chauffé à plusieurs millions de degrés Celsius pour former un plasma chaud, où deux noyaux fusionnent pour former un noyau plus lourd, libérant de l'énergie à extraire des réacteurs de fusion. Les combustibles de fusion les plus courants sont le deutérium (D) et le tritium (T), qui sont des isotopes de l'hydrogène pouvant fusionner pour former des noyaux d'hélium et des neutrons, produisant une grande quantité d'énergie équivalente à la différence de masse perdue lors de la réaction (17,6 MeV). Cette réaction a une section efficace plus élevée pour la fusion à des températures plus basses que d'autres réactions telles que la réaction D-D et la réaction D-$He3$ (Hélium-3). 80 % de l'énergie totale produite se présente sous forme d'énergie cinétique des neutrons. La réaction peut être exprimée comme suit :

$$ {}^{2}_{1}\mathrm{H} + {}^{3}_{1}\mathrm{H} \rightarrow {}^{4}_{2}\mathrm{He} + {}^{1}_{0}\mathrm{n}(14,1MeV) \tag{1} $$

L'une des approches de production d'énergie par fusion nucléaire repose sur le confinement magnétique. Il existe principalement deux approches d'ingénierie basées sur le confinement magnétique : (1) le Tokamak 1 et (2) le Stellarator. Plusieurs défis subsistent pour atteindre la fusion nucléaire sur Terre. L'un des défis est le chauffage du plasma. Il existe plusieurs méthodes pour chauffer le plasma, notamment le chauffage par résonance cyclotron électronique (ECRH), le chauffage par onde hybride inférieure (LH), et le chauffage par résonance cyclotron ionique (ICRH) 2. Une autre méthode est l'injection de faisceau neutre (NBI), qui consiste à envoyer des particules neutres à grande vitesse depuis l'extérieur du plasma pour transférer de l'énergie cinétique. Le chauffage ohmique est également possible en faisant passer un courant à travers le plasma, mais seulement dans les tokamaks (car il n'y a pas de courant central dans les stellarators) et à des températures de plasma relativement basses (jusqu'à 10^6K, au-delà desquelles la résistivité du plasma devient trop faible).

L'un des principaux défis non résolus qui doivent être abordés dans les dispositifs de confinement magnétique est l'interaction du plasma avec les composants en contact avec le plasma (PFCs), y compris les antennes RF nécessaires pour lancer l'onde RF dans

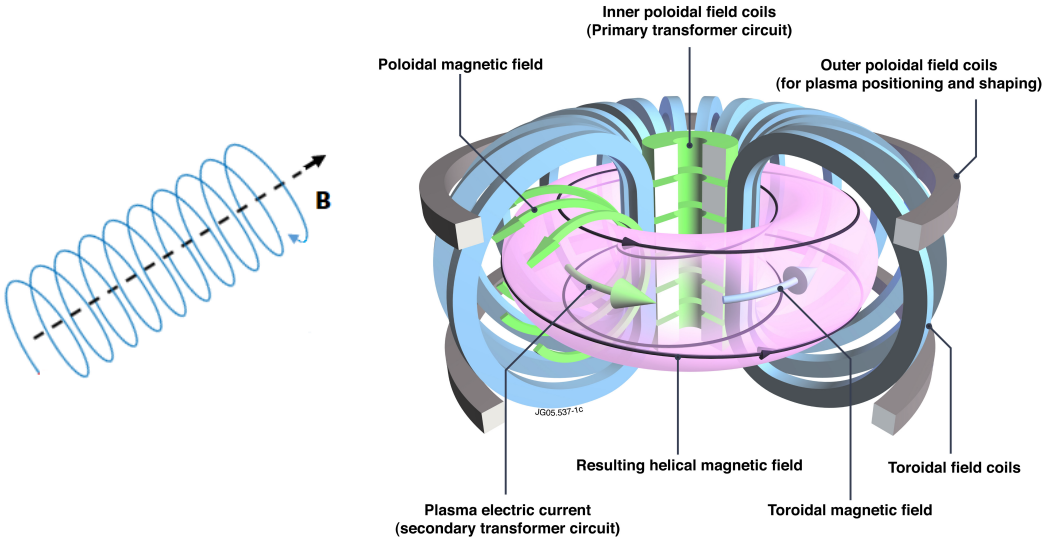

Figure 1: a) Gyration of particles in an axial magnetic field (left) and b) schematic representation of tokamak (right) [1]

le plasma.

La surchauffe excessive de l'électrode/antenne RF en raison d'un flux de chaleur élevé a des impacts néfastes sur les perspectives de fusion ou de traitement des matériaux en plasma. Le chauffage dû aux électrons peut augmenter la température de surface et faire fondre le matériau, réduisant ainsi finalement l'efficacité du couplage de puissance de l'antenne. Étant donné que le chauffage par résonance cyclotronique des ions (ICRH) est l'un des mécanismes de chauffage auxiliaires dans les réacteurs à fusion modernes et que les décharges à couplage capacitif sont utilisées pour nettoyer les premiers miroirs dans les tokamaks, les investigations sur le flux de particules/flux de chaleur à la surface de l'antenne/électrode dans un environnement RF magnétisé revêtent une importance suprême. La thèse présentée tente de comprendre les facteurs affectant le flux de chaleur en réalisant une expérience et en la comparant avec des modèles analytiques/théoriques simples.

Les expériences sont réalisées dans le dispositif expérimental ALINE (A LInear) avec trois électrodes dans deux mécanismes de couplage RF (couplage direct et capacitif) 3. Les expériences sont effectuées à l'aide d'une électrode RF avec des parois mises à la terre et revêtues de molybdène de 200 nm pour étudier le processus de pulvérisation dans le cadre de notre collaboration avec UniBasel pour des applications de nettoyage de miroirs. Les paramètres du plasma sont mesurés à l'aide d'une sonde de Langmuir compensée en RF pour comprendre le schéma de pulvérisation non uniforme évolué. Les valeurs de potentiel flottant bas observées lors des mesures de la sonde révèlent l'existence d'une population d'électrons chauds près de l'électrode RF due au chauffage

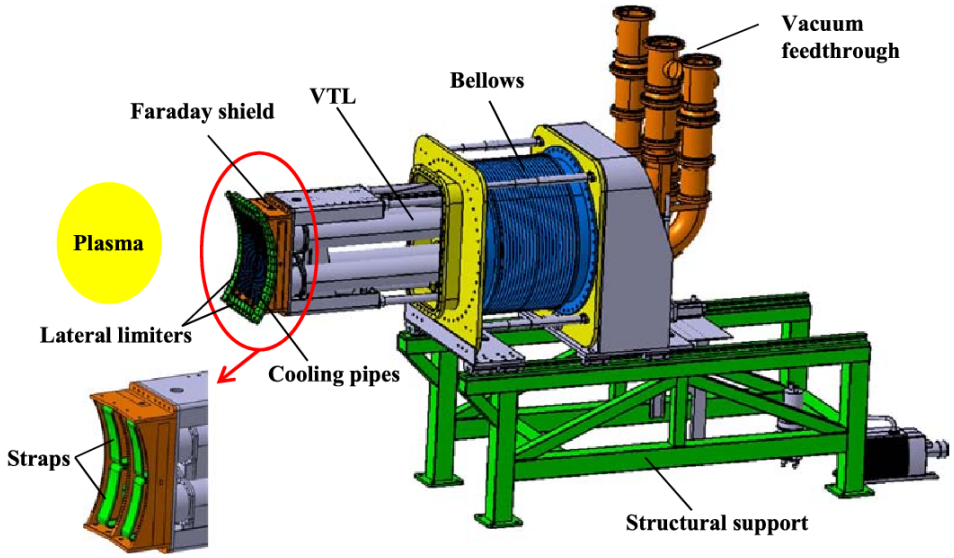

Figure 2: Schematic of EAST ICRH antenna [2].

stochastique, étudiée expérimentalement et vérifiée à l'aide de simulations théoriques et PIC.

Le schéma de pulvérisation observé est compris comme étant dû à l'inhomogénéité induite par le dérive, vérifiée à l'aide de cartes de dérive diamagnétique E×B dérivées des cartes de densité et de potentiel 2D. En effectuant les expériences à des angles d'inclinaison plus élevés, la localisation de la population d'électrons chauds et l'inhomogénéité de la distribution de densité peuvent être réduites, ce qui peut entraîner des schémas de pulvérisation uniformes. Les expériences avec une électrode RF facettée avec une paroi céramique flottante montrent des distributions fortement inhomogènes, comme observé précédemment, et confirment le flux de chaleur/particules non uniforme vers la surface de l'électrode, en particulier aux angles de raccordement.

Dans le couplage capacitif, l'auto-polarisation de la surface de l'électrode RF détermine les ions qui y parviennent. Dans les décharges à basse pression, à bas champ magnétique ou en présence d'un flux parallèle d'électrons, la polarisation de la surface de l'électrode RF est négative, et le flux de chaleur vers l'électrode RF peut être estimé à l'aide de l'équation de Bohm. Les expériences avec l'électrode RF monoface montrent une polarisation positive à basse pression et à fort champ magnétique (0,1 T). Les mesures de la sonde à proximité de l'électrode RF montrent un potentiel de plasma plus bas et l'inversion du champ électrique devant l'électrode RF. L'inversion du champ électrique localement devant une surface conductrice et l'accélération des électrons ont déjà été signalées.

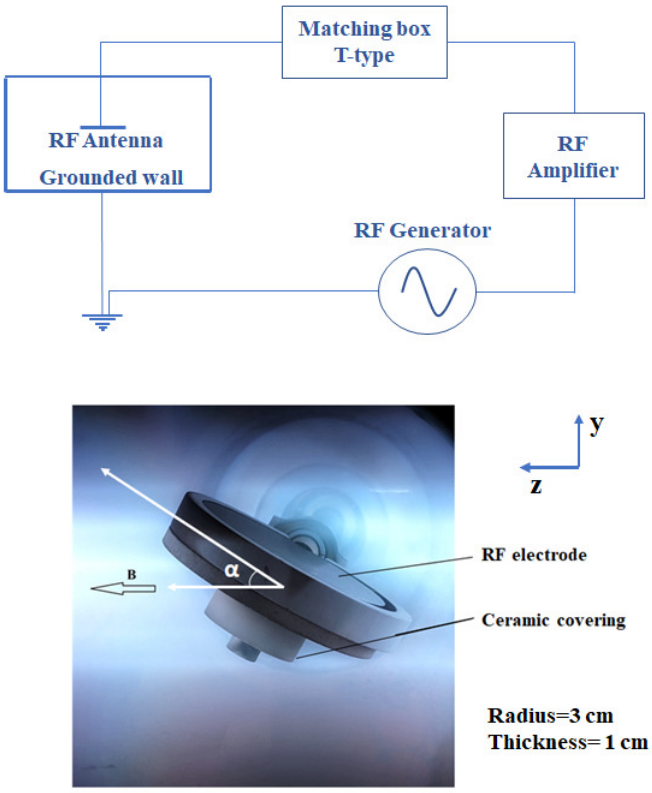

Figure 3: Schematic of the RF circuit and picture of the RF electrode in ALINE.

Le chauffage de l'électrode RF est mesuré à l'aide d'une caméra infrarouge, et le flux de chaleur est calculé à l'aide du code TEDDY pour l'électrode en tungstène monoface et l'électrode en tungstène. En mode CCP, un chauffage plus élevé de l'électrode RF est observé lorsque la polarisation est positive et proche de zéro en raison de la contribution des électrons. Les résultats expérimentaux sont comparés à un modèle analytique. La polarisation positive sur la surface de l'électrode RF réduit la pulvérisation de l'électrode RF en repoussant les ions positifs dans le plasma mais pas le chauffage.

Un modèle simple COMSOL a été développé pour étalonner le profil temps-température observé expérimentalement de l'électrode RF, donnant des résultats proches des tracés expérimentaux. Même si le flux de chaleur vers l'électrode RF est plus élevé pour l'électrode en céramique dans les mêmes conditions de décharge, la température finale de l'électrode est trouvée être plus basse qu'avec l'électrode en tungstène pur dans le cas de couplage direct en raison de la plus faible surface de collecte du flux de chaleur. Pour cette raison, l'électrode "céramique" constitue une alternative intéressante pour les opérations de décharge prolongées.

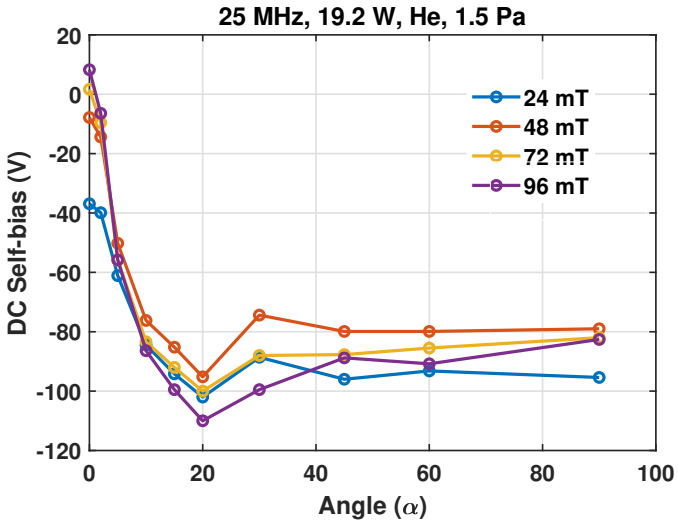

Figure 4: Variation of DC self-bias voltage with angle of electrode (He gas, 1.5 Pa, 25 MHz, 19.2 W coupled RF power) when the RF electrode is parallel to the magnetic field.

Chapter 1

Introduction

Contents

1.1 Plasma, Nuclear Fusion and Applications 10
1.2 Plasma inside a Tokamak 11
1.3 Ion Cyclotron Resonance Heating (ICRH) 12
1.4 RF Plasma in Material Processing 13
1.5 Debye Sheath 14
1.6 RF power coupling 16
1.7 RF Sheath 17
1.7.1 Sheath rectification in RF discharge 17
1.7.2 Estimation of the self bias 19
1.7.3 DC self-bias in asymmetric CCP RF discharge 19
1.7.4 Double sheath model in asymmetric RF discharge 20
1.7.5 Double Saturated Probe (DSP) model 22
1.7.6 Magnetized oblique sheaths 22
1.7.7 Stochastic heating 23
1.7.8 Stochastic heating in presence of a magnetic field 25
1.8 The heat flux and motivation of the thesis 26

1.1 Plasma, Nuclear Fusion and Applications

"Plasma is a quasineutral gas of charged and neutral particles, which exhibits collective properties" says the definition, but plasma can also be in the liquid and solid forms [3]. Plasma is the fourth state of matter. Under low pressure, at low collision frequency (long mean free path), when sufficient energy is given to the gas, the free electrons are accelerated and they ionize the surrounding gas, creating the plasma. The term plasma is used to represent many forms of matter, from cold laboratory discharges to interstellar matter and even hot matter found in the core of a star or a fusion reactor. Stellar plasma can be given as an example of naturally occurring plasma. In the core of stars, gravity compresses the gas, creating hot plasma in which the ions are fused to form heavier ions. This reaction, the process of "Nuclear Fusion" releases energy that counterbalances the gravitational pressure, creating a delicate balance that can support the star's structure and brightness for billions of years.

The Townsend discharge is an example of a laboratory plasma, which occurs when free electrons in a gas are accelerated by an electric field, causing them to collide with neutral atoms or molecules. This results in the release of additional electrons, the creation of ions, and the initiation of an electron avalanche, ultimately leading to the formation of a plasma discharge. As the power fed to the plasma is zero, the ions and electrons recombine to the neutral gas state. To maintain the plasma, constant power input is provided to offset the recombination and losses to the walls of the discharge chamber. The knowledge of the science behind the energy production in stars opened up a way to a potential abundant energy source, inspiring various concepts of nuclear fusion reactors. The gas can be heated to several millions of Celsius degrees to form hot plasma, where two nuclei fuse to form a heavier nucleus, releasing energy to be extracted from the fusion reactors. The most common fusion fuels are deuterium (D) and tritium (T), which are hydrogen isotopes that can fuse together to form helium nuclei and neutrons and produce a large amount of energy equivalent to the mass difference lost during the reaction (17.6 MeV). This reaction has a higher cross section for fusion at lower temperatures than other reactions such as the D-D reaction and the D-$He3$ (Helium-3) reaction. 80% of the total energy produced is in the form of kinetic energy of neutrons. The reaction can be expressed as follows:

$$ {}^{2}_{1}\mathrm{H} + {}^{3}_{1}\mathrm{H} \rightarrow {}^{4}_{2}\mathrm{He} + {}^{1}_{0}\mathrm{n}(14.1MeV) \tag{1.1} $$

One of the approaches towards energy production through nuclear fusion is based on magnetic confinement. There are predominantly two engineering approaches based on the magnetic confinement, (1) Tokamak and (2) Stellarator. There are several challenges in achieving nuclear fusion on Earth. One of the challenges is the heating of the plasma. There are several ways to heat plasma, including Electron Cyclotron Resonance Heating (ECRH), Lower Hybrid Heating (LH), and Ion Cyclotron Resonance

Heating (ICRH). Another method is Neutral Beam Injection (NBI), which involves sending fast-moving neutral particles from outside the plasma to transfer kinetic energy. Ohmic heating is also possible by driving a current through the plasma, but only in tokamaks (since there is no central current in stellarators) and at relatively low plasma temperature (up to 10^6 K, beyond which the plasma resistivity becomes too low).

One of the main challenges that remain unsolved and need to be addressed in magnetic confinement devices is the interaction of the plasma with the plasma-facing components (PFCs), including the RF antennas required to launch the RF wave into the plasma. Higher energetic particles in the plasma can interact with the PFCs and create impurities in the system, which is not in favour of the fusion reactions. While the interaction of plasma with PFCs creates significant challenges for fusion research, it is worth noting that plasma, with its unique properties, finds extensive applications in material processing. The potential structures which accelerates the charged species is utilised widely in material processing applications. Due to the distinctive properties of plasma and its capacity to interact with various materials, plasma has a broad range of applications in the processing of materials. Some of the essential uses of plasma in material processing include surface cleaning and activation, etching, sputtering, deposition, surface modification by plasma nitriding, etc. Hence, the understanding of the physics of the plasma-surface interactions arouses a lot of interest due to its vast potential and applications [4; 5].

1.2 Plasma inside a Tokamak

The understanding of the motion of the charged particle in combined electric and magnetic fields introduced a new way of confining the particles. When an external magnetic field is applied, the charged particle follows the magnetic field direction by gyrating about the magnetic field lines as shown in figure 1.1. If a species (ions or electrons) with mass m_s and electric charge q has a velocity perpendicular to magnetic field B, its Larmour radius (gyro radius) is $r = m_s/qB$. The basic design of a tokamak involves using magnetic fields to confine a hot plasma inside a doughnut-shaped vacuum chamber to minimize the axial losses of particles. The effective magnetic field is brought by the poloidal and toroidal magnetic field coils and plasma current resulting in a helical magnetic field as shown in figure 1.1b. This configuration allows limiting the losses of the particles into the walls of the tokamak. The plasma is heated to several tens of millions of Celsius degrees in its core, and is almost cold at the edge where the plasma interacts with the metallic wall and other plasma-facing components.

The region extending between the core plasma where fusion reactions occur and the Last Closed Flux Surface (LCFS) is called the edge plasma, and the region in between the LCFS and the cold walls in contact with the plasma is called the Scrape-Off-

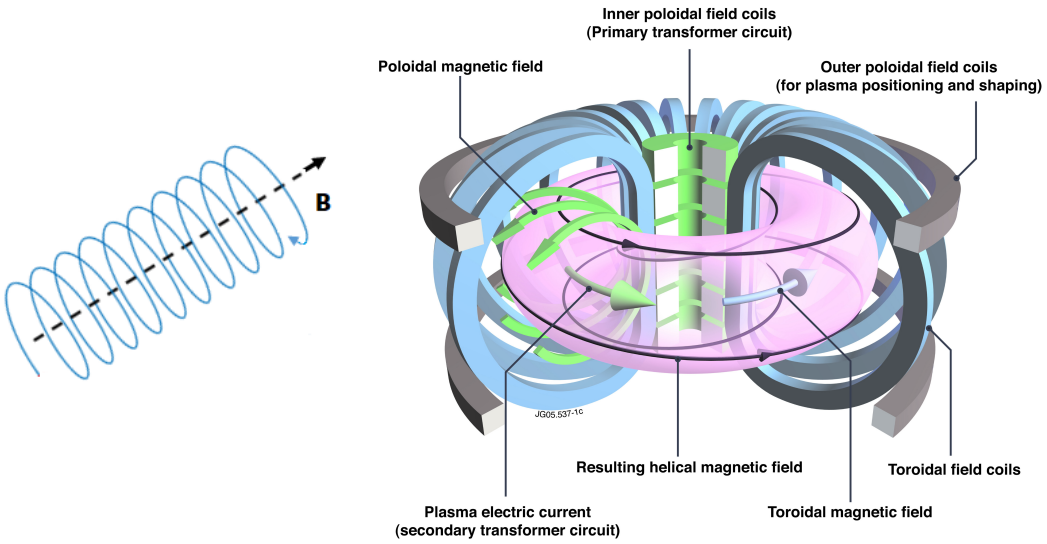

Figure 1.1: a) Gyration of particles around an axial magnetic field (left) and schematic representation of tokamak (right) [1]

Layer (SOL). The physics in the plasma edge and SOL is very important and different from the core plasma. Moving from the core to the edge, one can see a strong gradient in the density, potential and pressure. These gradients feed various instabilities and the resulting turbulence can drive the hot plasma out of the confined region towards the plasma-facing components. As mentioned earlier, ICRH heating is one of the heating mechanisms that is used to heat the plasma to the required temperature for fusion. For effective coupling of the power and the propagation of the electromagnetic waves into the plasma, the antenna should be in close contact with the plasma. The electric potential developed on the surface of the RF antenna favours the acceleration of ions, and fast ions impinging on the surface of the antenna cause sputtering and inject impurities into the plasma, which is not favourable for the fusion process [6; 7].

1.3 Ion Cyclotron Resonance Heating (ICRH)

Charged particles can change direction, speed up, or slow down under the influence of electromagnetic fields. This acceleration is equivalent to gaining energy and thus heats plasma particles. It has already been mentioned that the ions gyrate around the magnetic field lines with a specific Larmor radius depending on its energy. The frequency of rotation along the direction of the magnetic field lines is called the cyclotron frequency Ω_{ci}. When an external RF antenna emits electromagnetic waves with a frequency ω, matching the cyclotron frequency of ions, called the resonance condition, net energy is transferred from the wave to the ions. This process is called Ion Cyclotron

Resonance Heating (ICRH).

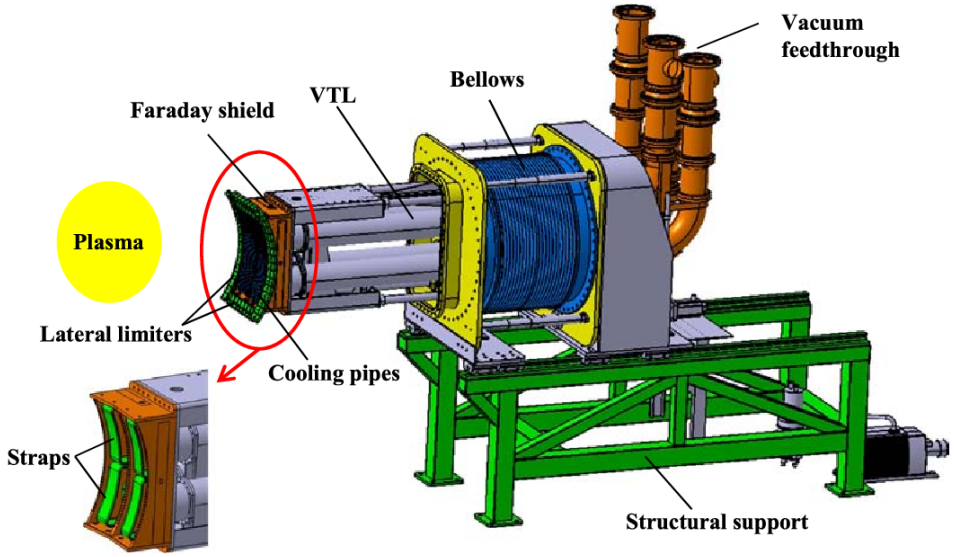

Figure 1.2: Schematic of EAST ICRH antenna [2].

The schematic of an ICRH system is shown in figure 1.2. The RF power from the RF generator-amplifier system is fed through RF transmission co-axial cables to the RF antenna grid. The frequency of the RF radiation is in the range of 30 to 80 MHz. The antennas are made of straps that are short-circuited at one end to produce the magnetic field exciting the fast magnetosonic waves. Recent antennas consist of poloidal and toroidal straps. The currents in each strap must be controlled to generate the necessary wave spectrum for the given physics scenario for maximum power coupling. The maximum power transfer occurs at the resonant frequency ω=Ω_{ci}. ICRH heating is one of the most common heating techniques employed for heating the plasma in magnetic fusion devices (tokamaks and stellarators). A detailed study of the ICRH power coupling in fusion devices has been addressed by several authors. The basic underlying physics of ICRH power coupling via RF antenna has been discussed in the doctoral thesis of Mariia Usoltceva [8].

1.4 RF Plasma in Material Processing

RF plasma is used in material processing to modify surfaces, deposit thin films, and treat surfaces. It is vital in industries like electronics, aerospace, and automotive due to its ability to create controlled and reactive environments. There are different modes

of coupling of the RF power to the plasma per say, capacitive, inductive and helicon modes of power coupling. The physics of each mode of power coupling is different and is discussed in [9; 3; 10]. When the plasma interacts with a material surface, potential structures develop at the plasma-substrate interface which can accelerate the ions exploited for the treatment of the surface. The developed interface strongly depends on the power coupling mechanism.

1.5 Debye Sheath

Plasma, in general, is quasi-neutral. Under the influence of an external charge, the plasma is perturbed, but it tends to shield the perturbation within a small scale length called the Debye length and denoted λ_D. When the plasma interacts with the material due to the difference in the energies (velocities) of the electrons and ions and other factors such as the collection area or magnetic field, the particles leaving the plasma reach and bias the substrate surface. This creates a charge separation between the plasma and the substrate, creating an electric field in between. If the substrate/surface is not biased, the potential or the electric field acts to equalize the collection of the ion and electron fluxes. This space-charge region in which the quasi-neutrality of the plasma is not valid is the Debye sheath [9].

When plasma first comes in contact with a surface, since the thermal velocity of electrons $v_e = \sqrt{k_b T_e / m_e}$ is greater than that of ions $v_i = \sqrt{k_b T_i / m_i}$ (mass of electrons is smaller than that of ions by orders of magnitude $m_i >> m_e$), electrons are rushed to the surface biasing the surface negatively, leaving the plasma positively charged. Here, k_b is the Boltzmann constant, T_i and T_e are the ion and electron temperatures respectively. The potential between the plasma and surface then tends to bring an equilibrium between the ion and electron fluxes on the substrate surface. This potential is called the floating potential (V_f), whereas the plasma stays at a higher potential compared to the surface and the potential of the plasma is known as the plasma potential (V_P). A diagram representing the potential and the density variation at the plasma wall interface is depicted in figure 1.3. The floating potential can be expressed by the formula:

$$V_f = \frac{kT_e}{2e} \ln \frac{2\pi m_e}{m_i} \tag{1.2}$$

The value of the plasma potential can simply be evaluated by adding the sheath drop potential to the floating potential which is around $4.03 \times T_e$ in the case of a helium plasma [11]. While moving from the bulk plasma to the electrode surface, there is a minimum critical velocity that ions should have reached for the formation of the RF sheath. Below this value, the solution for Poisson's equation while solving the potential profile becomes oscillatory and a sheath is not formed. This critical velocity is called

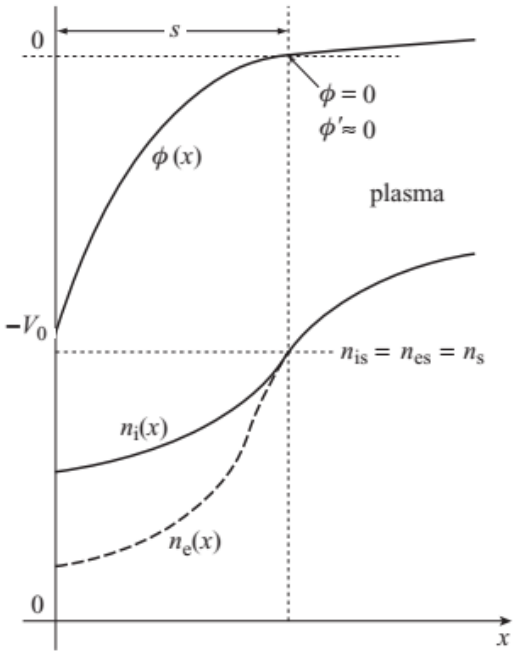

Figure 1.3: Densities and potential variation near the plasma/sheath transition region [9].

the "Bohm velocity" (u_B), and the condition for sheath formation is called the "Bohm criterion", which can be mathematically expressed as [3]:

$$u_B \geq \sqrt{k_b T_e / m_i} = C_s \tag{1.3}$$

The Bohm velocity is also known as the ion acoustic velocity and expressed by the term C_s. In the region of space between the bulk plasma and the Debye sheath, there exists a region where the ions are reaching u_B, where the quasi-neutrality of the plasma prevails, but the density of the plasma is slightly reduced, called the pre-sheath region. Considering static electrons in the bulk plasma at potential V_P, they are accelerated to the ion acoustic velocity in the pre-sheath region and one can write:

$$eV_P = \frac{1}{2} M {C_s}^2 \tag{1.4a}$$

$$V_P = \frac{1}{2} \frac{k_B T_e}{e} \tag{1.4b}$$

Assuming that the quasineutrality of the plasma is still valid at the interface of the Debye sheath and presheath, the density of the plasma at the entrance of the Debye sheath can be determined by:

$$n_{es} = n_i(0) = n_e(0) = n_0 \exp\left(-\frac{eV_P}{k_B T_e}\right) = n_0 e^{-1/2} \approx 0.61 \times n_0 \tag{1.5}$$

If the potential drop (V_0) inside the sheath is known, the size of the sheath s can be determined based on the Child-Langmuir law as [9], see figure 1.3:

$$s = \frac{\sqrt{2}}{3}\lambda_{De}\left(2\frac{e|V_0|}{k_B T_e}\right)^{3/4} \tag{1.6}$$

where $\lambda_{De} = \sqrt{\frac{\varepsilon_0 k_B T_e}{n_{es} e^2}}$ is the Debye length.

1.6 RF power coupling

RF power from the generator-amplifier array can be delivered to the plasma in different modes namely (a) using an RF antenna (or RF electrode) either in direct coupling or capacitive coupling (CCP), (b) inductive coupling, or (c) helicon discharge. The inductive and helicon methods of power coupling are non-contact methods, where the antenna is not in direct contact with the plasma, and the power is coupled via the waves produced by the variations in the RF current/voltage through the RF antenna. This thesis solely focuses on the experiments that utilized a RF electrode in direct or capacitive power coupling and thus, the other two methods are not included in the discussion.

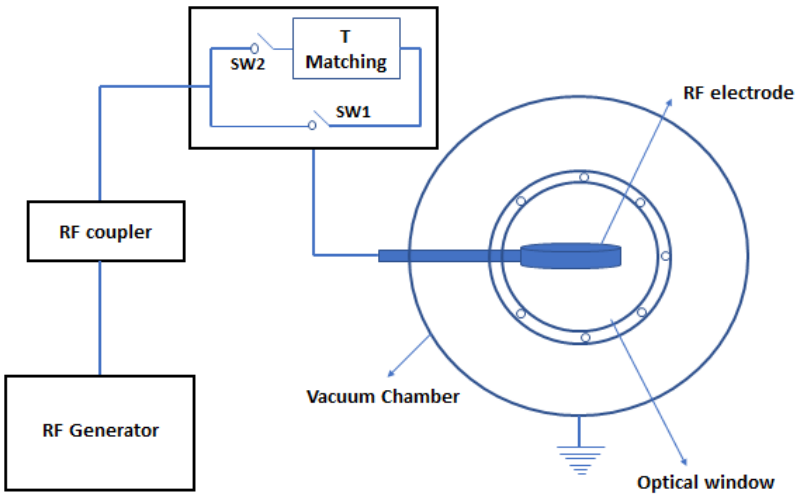

Figure 1.4: Diagram representing the asymmetric discharge in ALINE

In a simple RF discharge using an electrode, the active electrode receives the RF power while the counter electrode remains grounded. If the area ratio between the

grounded to the active electrode is high, such discharges are called asymmetric discharge. Generally, in asymmetric RF discharges, the wall of the reactor or the vacuum chamber is grounded. A diagram representing an asymmetric RF discharge is presented in the figure 1.4. In direct coupling, the RF power from the RF generator is coupled directly to the RF electrode via an RF coupler (case SW1). In direct coupling, the DC current is allowed to flow through the electrode, the average potential over one RF period is zero, and the RF voltage is modulated with respect to the zero voltage on the surface of the RF electrode. SW2 represents the capacitive mode of power coupling in which the power from the RF coupler is fed to the electrode via a matching box. The matching circuit aims at ensuring maximum power coupling to the plasma with minimum reflected power. The matching network is an array of capacitors and inductors, which do not allow the flow of the DC current through the circuit, resulting in a "DC self-bias" on the surface of the RF electrode depending on the type and the flux of the species reaching the electrode surface. But the capacitor allows the flow of a displacement current through the electrode, where the displacement current is current to the electrode due to the time varying electric field (E) and is given by $I_d = \varepsilon_0 \frac{dE}{dt}$ [9].

1.7 RF Sheath

Instead of a constant DC voltage, an oscillating potential of the form $V_0 = V_{DC} + V_{rf} sin\omega t$ is applied on the RF electrode. Here V_{DC} is the mean DC voltage, ω is the RF frequency, V_{rf} is the peak RF voltage. The frequency can vary in the range from 1 to 100 MHz and the nature of the discharge varies significantly with the applied RF frequency. The major difference in the plasma properties are introduced by the response of the particles with the oscillating RF potential. The RF oscillations are in the range between the ion plasma frequency and electron plasma frequency, i.e. $\omega_{pi} << \omega << \omega_{pe}$, where $\omega_{pi} = \sqrt{ne^2/M\varepsilon_0}$ and $\omega_{pe} = \sqrt{ne^2/m\varepsilon_0}$, M and m are the mass of ions and electrons respectively. The ions cannot respond to the instantaneous changes in the RF potential due to their inertia, whereas electrons are more mobile and can follow the RF oscillations.

Detailed discussion on the RF discharge, RF sheath and its dynamics are discussed in [9; 10; 12]. The electron and ion dynamics with the oscillating voltage brings a lot of complex physical processes. In this part, some of the important processes are discussed in order to explain the physics and the context of the research presented here.

1.7.1 Sheath rectification in RF discharge

In a setup represented by the figure 1.4, the electric field changes direction periodically at the RF frequency. The electrons can follow the instantaneous variations in the RF electric field, but ions being heavier cannot and respond to the time-averaged poten-

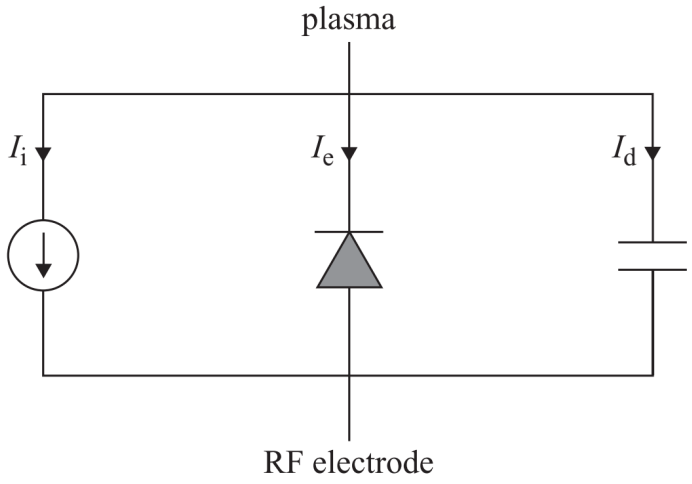

Figure 1.5: A schematic circuit model of RF sheath, with constant current source representing the ion current, the electron current is represented by a reverse-biased diode and a non linear capacitor to represent the displacement current.

tial. The RF sheath is formed at the plasma electrode interface and also oscillates as a response to the RF potential variations. Due to the differences in the electron and ion mobility and the asymmetrical behaviour of the plasma around the RF electrode, the sheath does not follow the RF potential linearly and leads to the development of a net DC component in the plasma sheath voltage waveform. This means that during the positive phase of the RF cycle, the voltage drop across the sheath may differ from that during the negative phase over a certain period. This phenomenon is known as sheath rectification. This DC component decides the energy of ions reaching the electrode surface and affects the material sputtering rate and this phenomenon is exploited in the sputtering, etching and surface modification applications using the plasma discharge [9].

The total current through the RF sheath has ion, electron and displacement currents (I_d) components. It can be expressed as:

$$I_{RF} = -n_0 e u_B A + \frac{n_0 e \overline{v_e}}{4} A \exp\left(\frac{-eV_{sh}}{kT_e}\right) + I_d \tag{1.7}$$

Here, A is the electrode area, $\overline{v_e}$ is the average velocity of electrons and V_{sh} is the potential drop inside the sheath. When the RF frequency is high enough so that the ions do not respond to the instantaneous variations, the ion current can be represented as a constant ion source. The electron current across the sheath is controlled by a Boltzmann exponential function of the voltage, resulting in a current-voltage characteristic of a reverse-biased diode. Since a capacitor allows a displacement current to flow, it becomes the third parallel element of the circuit shown in Figure 1.5. The displacement

current varies as a function of the amplitude of RF modulation.

1.7.2 Estimation of the self bias

Suppose V1 and ω be the RF potential and the RF frequency, the self bias on the surface of the RF electrode can be calculated using the time averaged flux balance. As mentioned earlier, since the ions are not responding to the instantaneous RF potential variations, their motion is dependent on the potential drop inside the sheath, and it can be represented by the Bohm flux. Balancing the electron and ion flux yields:

$$\frac{1}{4} n_s \overline{v_e} \exp\left(\frac{e(V_{f_{RF}})}{kT_e}\right) (\omega/2\pi) \int_0^{2\pi/\omega} \exp\left(\frac{eV_1 sin(\omega t)}{kT_e}\right) dt = nu_B \tag{1.8}$$

The integral term can be expressed in terms of modified Bessel function

$$\frac{1}{4} n_s \overline{v_e} \exp\left(\frac{e(V_{f_{RF}})}{kT_e}\right) I_0\left(\frac{eV_1}{kT_e}\right) = nu_B \tag{1.9}$$

Putting the expression for $\overline{v_e}$ and u_B and rearranging the terms gives the floating potential under RF-biased conditions:

$$V_{f_{RF}} = \frac{kT_e}{e}\left[\frac{1}{2}\left(\frac{2\pi m}{M}\right) - \ln I_0\left(\frac{eV_1}{kT_e}\right)\right] \tag{1.10}$$

A reference electrode without RF bias would adopt a potential given by equation 1.2, so in front of the RF biased surface the potential developed has an additional term (second term in the RHS of equation 3.1), called the self-bias voltage (these formula are valid for a single sheath)[9].

1.7.3 DC self-bias in asymmetric CCP RF discharge

As mentioned earlier, the average speed of electrons is larger than that of ions, leading to the higher flux of electrons reaching the electrode surface. In the blocking capacitor scheme, the net current through the electrode biases the electrode negatively (in general). This bias ensures the net current collected by the electrode for a complete RF cycle is zero. The DC self-bias developed on the surface of the RF electrode depends on several factors such as the RF power/voltage on the surface of the RF electrode, gas pressure and the collisions in the system, ratio of the grounded to active RF electrode area and in a magnetized discharge, the strength of the magnetic field.

Considering an asymmetric discharge, with a small active electrode with area A_1 and a larger grounded electrode with area A_2>A_1, the average voltage falls $\overline{V1}$ (i.e. the DC component of the potential across the sheath at electrode 1) [9] is much greater than $\overline{V2}$ in the grounded electrode sheath. The magnitude of $\overline{V2}$ coincides with the

plasma potential $\overline{V_P}$ relative to the ground. Let $A_1/A_2 << 1$, due to the higher capacitance of the blocking capacitor, the DC self-bias developed on the RF electrode can be expressed as:

$$V_{dc} = -\overline{V1} + \overline{V2} \tag{1.11}$$

which is close in value to the RF voltage amplitude V_a. It is also dependent on the area ratio $\eta = A_1/A_2$

$$\frac{\overline{V1}}{\overline{V2}} = \left(\frac{A_2}{A_1}\right)^q \tag{1.12}$$

where q is the power index, which is also dependent on η but varying in a narrow range q≈1-1.4. This relation is derived from the interpolation based on an experimental data which is explained in the Raizer et al. book [12].

Chabert et al. [9], based on the RF current continuity considering the constant ion density model, linked the relation between the DC component of the voltages and the area of the electrodes as:

$$\frac{\overline{V1}}{\overline{V2}} = \left(\frac{A_2}{A_1}\right)^2 \tag{1.13}$$

indicating larger DC voltage adjacent to the smaller electrode. The different sheath voltages creates a DC bias between the electrodes unlike in the symmetric discharge and it can be expressed as:

$$\overline{V2} - \overline{V1} = \overline{V2}\left(1 - \left(\frac{A_2}{A_1}\right)^2\right) \tag{1.14}$$

This means that at higher asymmetry, almost all the RF potential is rectified by the larger sheath. The asymmetry of the electrodes' sizes plays an important role in the sheath dynamics, the energy of ions reaching the electrode and nature of the boundary wall sheaths at the RF electrode. This point has been elaborated for both direct and capacitive discharge cases by Kohler in [13]. The time averaged plasma potential for an asymmetric RF discharge has been discussed on the basis of a capacitive model RF sheath in [14]. The study on rectified potential, the DC bias and energy of ions reaching the RF electrode is reported in [15; 16; 17].

1.7.4 Double sheath model in asymmetric RF discharge

For the direct coupling case, when the RF electrode is connected directly to the RF generator via the generator resistance instead of the usual blocking capacitor, the sheath can be modelled using a double sheath model [18]. Since there is no blocking capacitor,

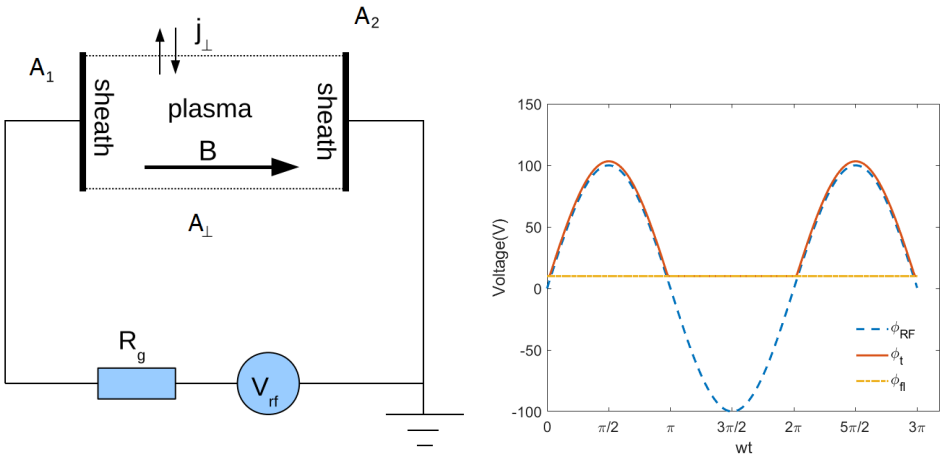

Figure 1.6: Diagram showing magnetic flux tube exchanging RF currents [18] (left) and sheath rectification plot in asymmetric discharge based on equation 1.15(right).

it allows DC currents to follow. The model explains the effect of sheath capacitance, electrode surface ratio, plasma and generator resistances, and the applied RF potential on the DC current to the RF electrode. According to the model, when the the displacement currents in the sheath are neglected: $C1$ and $C2 \rightarrow 0$, the rectified RF potential can be represented as:

$$\phi(t) = \phi_{fl} + \ln\left(\frac{A_2}{A_1 + A_2}\right) + \ln\left[1 + \frac{A_1}{A_2}\exp\{\phi_{RF}(t)\}\right] \tag{1.15}$$

Here, $\phi = \frac{eV}{K_B T_e}$ is the plasma potential, $\phi_{fl} = \frac{eV_{fl}}{K_B T_e}$ is the floating potential, A_1 and A_2 are the area of the active and grounded electrodes and $\phi_{RF} = \frac{eV_{RF}}{K_B T_e}$ is the RF potential. In the special case of a symmetric discharge, the time averaged potential in the plasma has the following well-known expression [12]:

$$< \phi >= \phi_{fl} + \frac{\overline{\phi_{RF}}}{\pi} \tag{1.16}$$

For the infinite sheath capacitance case, meaning RF displacement currents are higher than non linear conduction currents, the new expression is :

$$\phi(t) = \phi_{fl} + \gamma_1 \phi_{RF}(t) + \ln\left(\frac{\exp(\phi_b) A_1 I_0(\gamma_2 \overline{\phi_{RF}}) + A_2 I_0(-\gamma_1 \overline{\phi_{RF}})}{A_1 + A_2}\right) \tag{1.17}$$

with $\gamma_1 = \frac{C_1}{C_1 + C_2}$ and $\gamma_2 = \frac{C_2}{C_1 + C_2}$. The model is applicable for the asymmetric RF discharge or to a symmetric magnetized RF discharge where the asymmetry is introduced by the external magnetic field.

1.7.5 Double Saturated Probe (DSP) model

The double probe model can be modified to take into account the saturation of the electron current [19]. In that case the current is like an asymmetric double probe model with 2 saturations (ionic and electronic). To simplify the derivation of this model, a "tanh" function has been used. This model allows to compute the real time plasma potential during an RF oscillatins. The DSP model explains a drastic fall in plasma potential values when the area ratio is higher than the electron over ion saturation current ratio. This model has been compared to Aanesland's model [20] and to PIC simulations with a good accordance as shown in figure 1.7.

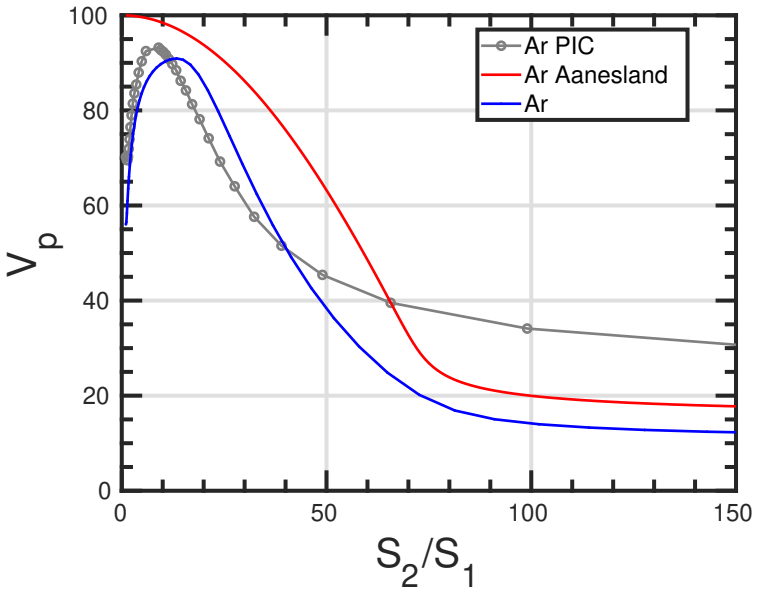

Figure 1.7: Plasma potential with respect to the Wall/Electrode ratio S_2/S_1. Comparison of the DSP model (blue curve) to PIC simulations (gray curve) and Aanesland's model (red curve).

1.7.6 Magnetized oblique sheaths

An external magnetic field can change the character of the plasma discharge drastically. The extent of magnetization cannot only be described by the strength of the magnetic field, it also depends on the collisions in the system. However, the presence of an external magnetic field limits the motion of charged particles perpendicular to the magnetic fields by confining them among the magnetic field lines. This favours higher collisions in certain regions inside the plasma and higher ionization. The magnetic

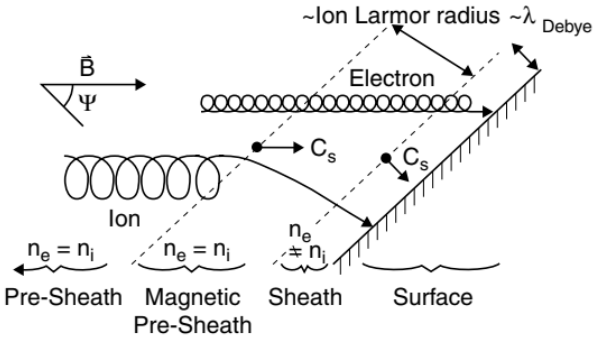

Figure 1.8: Diagram of Chodura sheath [21]

field increases the motion of charged particles along the field lines and modifies the potential and density distributions of the plasma, which can create drifts. The drifts and the effect of magnetic fields in the diagnostics of the plasma are discussed in the experimental perspective in the next chapter. Here, the discussion is limited to the sheath structure in a magnetic environment.

In the presence of an external magnetic field, the motion of the ion from the bulk plasma to the surface of the RF electrode is presented in figure 1.8. According to Chodura, the velocity of ions at the presheath- magnetic presheath edge (MPSE) is constrained such that:

$$v \parallel B, MPSE \geq u_B \tag{1.18}$$

This is known as the Chodura criterion [22; 23]. The typical length scale of the magnetic presheath is a few ion Larmor radii, and at the entrance of the debye sheath, the ion velocity perpendicular to the solid surface should be at least equal or larger than C_s [24]. Chodura predicts that the Debye sheath vanishes beyond a critical angle called the "Chodura angle" at which the total potential drop beween the plasma and the surface will take place inside the magnetic presheath itself. The detailed discussion on this topic has been done by Riemann and Stangeby in [25; 21]. The discussion of plasma-surface interaction has been extended to the parallel case by Stangeby in [21; 26; 27; 28] and the possibility of positive self-bias has been explored below the critical angle in [29].

1.7.7 Stochastic heating

The rectification process of RF electric fields occurring in the electrode sheaths causes the rise in the potential barrier in which positive ions are accelerated towards the surface, and the electrons are pushed back into the plasma, creating a plasma sheath boundary. With oscillating RF potential, the plasma sheath boundary will also oscillate

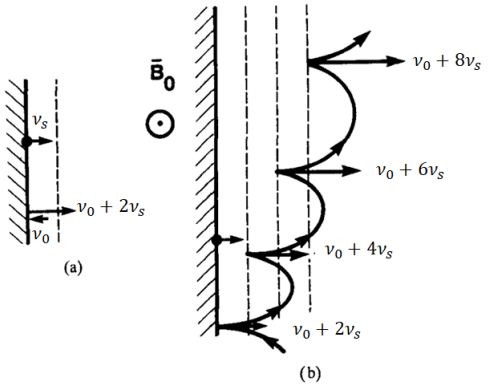

Figure 1.9: Non-collisional heating of electrons (a) without magnetic field (b) with magnetic field.

about a mean position S_0 called the time-averaged sheath thickness, which is evaluated using the Child-Langmuir law. When an electron interacts with an oscillating boundary that moves opposite to the direction of the electron, the electron is reflected to the plasma, like a ball on a moving wall, with an increased velocity, $v_0 + 2v_s$, where v_0 is the initial velocity and v_s is the velocity of the oscillating sheath edge 1.9. This non-collisional process in which electron gain a net energy from an oscillating sheath is called the stochastic heating. An analytical model explaining the process and the energy transfer is available in [10]. The simplest expression for the stochastic heating, considering a Maxwellian electron distribution $f_{es}(u,t)$ at the entrance of the sheath is given as follows :

$$S_{stoc} = -2m \int_{v_s}^{\infty} v_s (u - v_s)^2 f_{es}(u,t) du \tag{1.19}$$

The mean stochastic heating $\overline{P_{stoc}}$, considering $v_s = u_0 \cos(\omega t)$, with u_0 the peak sheath velocity and ω the RF frequency, is given by:

$$\overline{S_{stoc}} = \frac{1}{2} m u_0^2 n \overline{v_e} \tag{1.20}$$

It appears that the average power density transferred to electrons by the oscillating sheath is proportional to the square sheath edge velocity. And the sheath velocity is $\frac{ds}{dt}$ with s the sheath thickness from the Child Langmuir law. Here this is an oscillating sheath so that $s(t) = s_0 \sin(\omega t)$ and then $u_0 = \omega s_0$ is proportionnal to $\omega V_{RF}^{3/4}$, meaning that the stochastic heating is much higher at high RF frequencies and high RF voltages. Stochastic heating is a dominant heating mechanism in low pressure RF discharges [30; 31; 12; 9; 32; 33; 34] where the ohmic heating can be neglected as it will be the case in most of our experiments in the ALINE plasma device. Some more elaborated models

have been built, considering non Maxwellian varying distribution [35] but a true self consistent model is almost impossible to solve, considering that the stochastic heating strongly disturbs the distribution function [36]. At low pressure, high RF voltages can generate bi-Maxwellian electron distribution, with most of the population at low temperature and a high energetic tail, responsible for higher ionisation rate. This effect can also be increased by secondary electron emission. PIC simulations [37] have reproduced this mechanism already observed by Godyak experimentally [31], showing the transition from a two-temperature distribution at 70 mTorr to a single-temperature distribution at 500 mTorr. Another simulation of discharge behavior [38] was performed at a pressure of 3 mTorr (argon) with again a two temperature distribution. This effect is even enhanced by the presence of a grazing magnetic field above the surface of the electrode as it will be explained in next section and chapter 3.

1.7.8 Stochastic heating in presence of a magnetic field

In the presence of a magnetic field, when electrons interact with oscillating plasma sheath boundary, they are not directly recoiled back into the plasma. Instead, because of the cyclotron gyration, they undergo multiple correlated collisions with the RF sheath as seen in figure 1.9 and gain energy during each interaction resulting in higher net energy gain. This mechanism occurs in the magnetically enhanced reactive ion etcher (MERIE) or RF magnetrons in which magnetic field ranges from 50 to 200 G. The total power deposited in the plasma due to the stochastic heating is given by Lieberman [39]:

$$\langle P_{stoch} \rangle = \frac{1}{2} m v_s^2 n \bar{v}_e \frac{\omega_{ce} \left(\nu_{col} + \omega_{ce}/\pi \right)}{2\pi(\nu_{col}^2 + \omega^2)} \tag{1.21}$$

Where v_s is the velocity with which the sheath boundary moves, ν_{col} is the electron collision frequency. $\omega_{ce} = qB_0/m$ is the electron cyclotron frequency, in which m is the mass of electrons, $\overline{v_e}$ is the average electron energy, q is the electronic charge and B_0 is the strength of the magnetic field and ν_{col} is the collision frequency. Stochastic heating is proportional to B_0^2 and dominates the ohmic heating at low pressures and high magnetic fields. In low pressure discharges, due to lower collisions, the classical stochastic heating is enhanced by a factor ω_{ce}^2/ω^2, which can lead to the generation of hot electrons near the surface of the RF electrode, and the deviation of the electron distribution from Maxwellian locally inside the plasma [40]. This energy gain at each bounce increases mainly the perpendicular electron velocity. Now considering a grazing magnetic field above the electrode surface, the perpendicular velocity is given by v_s, but the parallel sheath velocity is sensitively enhanced and, in the upper limit and for an infinitely long electrode, can be written as $v_{s\parallel} = v_s/sin(\alpha)$. Of course, this is a purely theoretical velocity assuming no inertia for electrons, and it is not valid at $\alpha = 0$. In the ideal case of a magnetic field perfectly aligned with the surface of an

electrode with a radius R, the longitudinal sheath velocity can be deduced from the perpendicular velocity as follows:

$$v_{s\parallel} = v_s \frac{R}{s} \tag{1.22}$$

Thus the enhancement factor is simply the ratio of the sheath thickness (perpendicular to the surface of the electrode) over the electrode radius, again considering that electrons can accelerate with almost no inertia.

To conclude, at 0° or grazing angles (like in MERIE systems and our device ALINE), this results in a quite higher acceleration of the electrons in the magnetic field direction, in a small layer equal to the sheath thickness above the electrode. This phenomenon has been simulated and experimentally observed in chapter 3 for different magnetic field strength and angles.

1.8 The heat flux and motivation of the thesis

In direct coupling, due to the sheath rectification, the plasma stays at a higher potential compared to the RF electrode, which favours the acceleration of the ions from the plasma to the RF electrode. When the instantaneous RF voltage on the surface of the electrode is higher than the plasma potential, the electrons from the plasma will accelerate to the RF electrode in the electric field developed, and each species will transfer its energy to the RF electrode, leading to the heating of the RF electrode. Inside a tokamak, the potential developed in front of the RF antenna can be very high, in which the ions can be accelerated eventually causing the sputtering of the antenna [41; 42; 43; 44]. In capacitive coupling, the ions are also accelerated to the active electrode, which is exploited for instance in sputtering applications. But in both these cases, the potential developed favours the heating of the RF electrode, which will eventually reduce the efficacy of the power coupling to the plasma.

In the perspective of surface treatments, the bias developed on the RF electrode or the sheath rectification is the key to having adequate flux to the RF electrode and deciding the energy of ions. In the presence of an external magnetic field, the sheath in front of the RF electrode is modified, which also changes the distribution of the density and potential around the RF electrode. In the fusion research perspective, since the surfaces of the fusion devices makes grazing angles with magnetic field lines, it is important to study the dynamics of the RF sheath at grazing angles to the magnetic field. Even though many authors have worked on the magnetized sheath, the area of the magnetized RF sheath and its influence on the heating and heat flux to the RF electrode, especially at grazing angles needs to be further explored to improve the power coupling without impurity generation, and to have control over the processing of surfaces with RF plasma. Different aspects affecting heat flux to the RF electrode are

presented in figure 1.10.

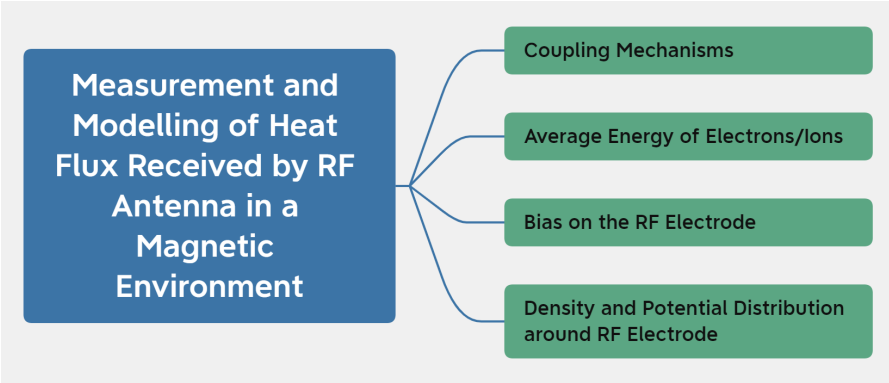

Figure 1.10: Factors affecting heat flux to the RF electrode.

This thesis aims to understand the heat flux to the RF electrode for different discharge conditions. The experiments are performed in the linear plasma device ALINE by varying the coupling mechanism, gas pressure, RF power, strength of the magnetic field and tilt angle of the RF electrode. Chapter 2 is dedicated to introducing the experimental setup, diagnostics and theories that are used for analysing the experimental data. The background of this research topic, which is relevant for pursuing the investigation and important studies that have already been conducted in magnetized RF plasma are briefly presented in this chapter. The experimental and PIC simulation results based on highly negative floating potential observed around the RF electrode are presented in Chapter 3. In Chapter 4, the observation of positive self-bias and reversal of the sheath in front of the RF electrode observed during the experiment with a faced RF electrode at the low-pressure and high magnetic field is discussed. Chapter 5 is dedicated to studying the density and potential distribution around the RF electrode for different electrode configurations. The heating and heat flux results based on the experimental measurements and the corresponding analytical model are presented in Chapter 6. The conclusion and perspectives of the presented work are discussed in the final chapter.

Chapter 2

Experimental Setup and Diagnostics

Contents

2.1 ALINE Plasma Device 30

2.1.1 RF electrode types 31

2.2 Diagnostic tools in ALINE 33

2.2.1 RF compensated Langmuir probe 33

2.2.2 Analysis of probe data 35

2.2.3 Floating Probe 40

2.2.4 IR Camera 40

2.2.5 Fast Camera Imaging 43

2.1 ALINE Plasma Device

All the experiments discussed in this thesis are performed in ALINE (A LINEar) plasma device. An image of the experimental set up is presented in figure 2.1. The cylindrical vacuum chamber of ALINE is 1 m long and 30 cm in diameter [8; 45; 46; 11]. One of the circular ends of the vacuum chamber is connected to the 3D manipulator array which is identified as (b) in the image. An RF compensated Langmuir probe is used to measure the plasma parameters. The power delivered by the RF amplifier (Prana DP600) is coupled to the plasma via a RF electrode either directly or capacitively connected through a matching box. The RF power generator, amplifier and matching network array are represented by (c) in figure 2.1. An IR camera is placed above the RF electrode to study the heating of the RF electrode through an IR window. When it is not operated the vacuum vessel is maintained at 5×10^{-7} mbar, thanks to the turbo molecular pump.

A uniform axial magnetic field up to 0.1 T is produced by six 75 turn water-cooled copper coils insulated with 1 mm PVC layer. These coils are powered by three Elektro-Automatik PS 8000 3U devices, capable to deliver 15 kW each with a DC current ranging from 0 to 510 A between 0 and 80V. Each unit is connected to a pair of coils mounted in series to vary the magnetic field longitudinally. Temperature controllers are attached to each coil, enabling them to be deactivated if overheating occurs, to prevent the PVC layer on the copper tubes from melting [45].

A 3D manipulator connected to a Langmuir probe allows measurements of plasma parameters around the RF electrode and inside the plasma column in the volume connected to the RF electrode in all 3 axes. It can move 50 cm along the axis of the cylinder (z axis) and 10 cm along both x and y axes. It is used to realize profiles and 2D (or even 3D) maps of the plasma parameters automatically with a 1 millimeter resolution [45].

The Prana DP 600 broadband amplifier can couple RF power in the frequency bandwidth from 10 kHz to 250 MHz. Its nominal power is close to 600 W but it can deliver a maximum power of 1100 W at 1 MHz range. The amplifier is linked to a coupler that measures forward and reflected powers on the coaxial cable feeding the antenna in the plasma chamber. MFJ-989D antenna tuner matching box is used for improving the power coupling efficiency corresponding to different experimental conditions in capacitively coupled plasma discharge (CCP). It consists of two series capacitors (500 pF air variable capacitors) and a shunt inductors (AirCore Roller Inductor). The set-up can couple a maximum power of 1500 W in the frequency range 1.8 to 30 MHz. The discharge in capacitive coupling is performed at 25 MHz and in direct coupling performed at 34 MHz for better coupling efficiency.

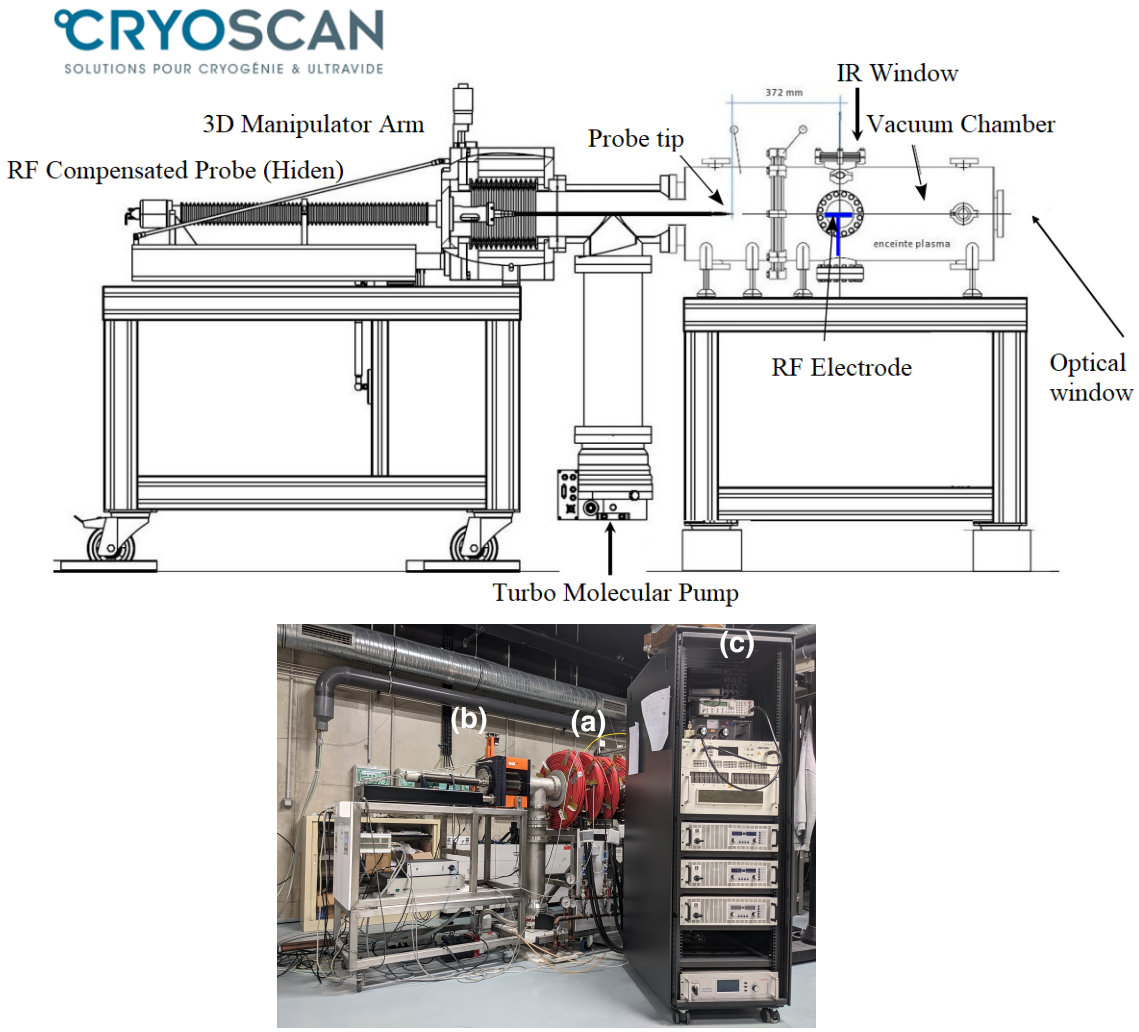

Figure 2.1: Sketch (top) and picture (bottom) of the ALINE plasma device (a), 3D probe manipulator (b) and rack holding the RF power generator, amplifier and coils power supplies (c)

2.1.1 RF electrode types

3 different electrode configurations are used in the framework of this thesis to perform experiments. The images of the electrodes are presented in figure 2.3. One can see the RF electrode is held by a stainless steel rod at the center of the cylindrical chamber, which is connected to a rotor, and allows to make a tilt angle α with the axial magnetic field ranging from 0-90°.

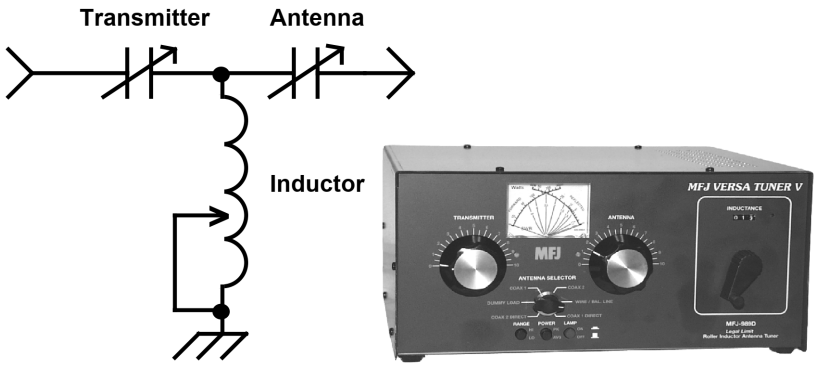

Figure 2.2: T-type Matching network in ALINE

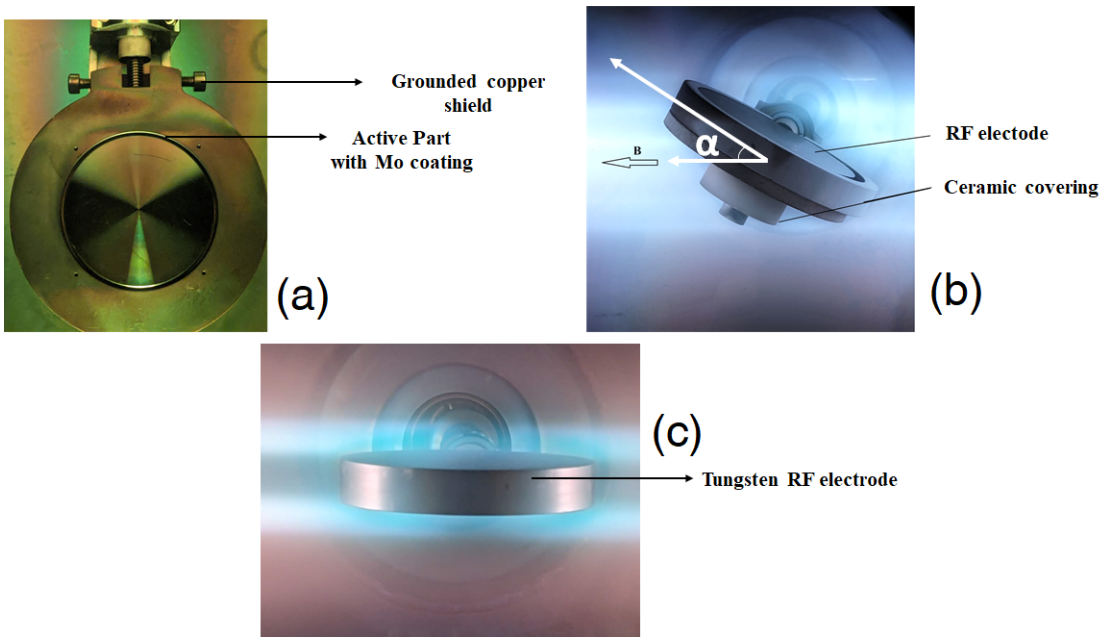

Figure 2.3: Three different electrode configurations used for experiments in ALINE (a) copper electrode with grounded shield (b) tungsten electrode with ceramic covering (c) simple tungsten electrode.

Copper RF electrode with grounded copper shield

RF capacitive coupling based set-up for in-situ cleaning of the first mirrors to recover the optical efficiency in tokamaks are currently in development in Univeristy of Basel. As a part of our collaboration with Laurent Marot and Paul Hiret through the SHEAR project experiments were performed in ALINE plasma device to study the sputter-

ing at 0.1 T magnetic field. Results from the probe measurements are used to explain the in-homogeneous sputtering pattern evolved by understanding the drifts in plasma. Experiments performed at different tilt angles to study the potential and density distribution of the plasma around the electrode with a perspective of understanding and improving the sputtering pattern. The results of this measurements are published in [47].

The RF electrode has 2 parts, The active electrode made of copper has a diameter of 4.8 cm and 0.6 cm thick, coated with a thin layer of Molybdenum (200 nm). There is a grounded shield made of copper (1.6 cm wide) as shown in figure 2.3a, covering all the sides of the RF electrode allowing the plasma electrode interaction only at the coated surface of the active RF electrode. The experiments, results and discussions based on this electrode is presented in chapter 3 and 5.

Tungsten RF electrode with Ceramic covering

The active part of the electrode is made of tungsten and it has a dimension of 6 cm by diameter and 1 cm in thickness 2.3b. The lateral side of the disc shaped electrode is covered with a ceramic ring (made of Mullite C610) at the lateral side with inner radius 3.2 cm and outer radius 3.7 cm. The bottom side of the RF electrode is covered with a ceramic disc of diameter 6.5 cm and during the discharge the ceramic part of the RF electrode is floating with respect to the plasma. Hence the ceramic covering ensure the collection of particle by the RF electrode through the lateral side and one of the circular sides to be zero.

Tungsten RF electrode

The ceramic covering of the tungsten RF electrode presented in the last case is removed and the whole surface of the RF electrode is exposed to the plasma during the discharge (R= 3 cm, t= 1 cm). The typical discharge using the RF electrode is shown in figure 2.3c. The probe characteristics around the RF electrode and the heating of the RF electrode is studied for different discharge parameters at different tilt angle and the results are discussed in chapter 5 and 6.

2.2 Diagnostic tools in ALINE

2.2.1 RF compensated Langmuir probe

Langmuir probes are the most common technique used to characterize plasma. From the IV curve obtained, one can estimate the density, temperature and potential of the plasma. Despite of the practical challenges in the measurements in the magnetic environment, probes are still the leading candidate for plasma characterization

[48; 49; 50; 51]. The probe measurements are influenced by a number of variables, including collisionality, magnetization, the type of probe tip, the surroundings, and the probe's orientation in relation to the magnetic field. According to each instance, the probe analysis can change. One difficulty is the lack of technical solutions and theories for measurement and analysis in exceedingly difficult environments like measurements near the RF antenna in a magnetic environment [52; 50; 53].

Probe setup in ALINE

ALINE is equipped with an RF compensated Langmuir probe with cylindrical probe tip. The probe tip is aligned parallel to the magnetic field lines, combined with the 3D manipulator array, precise localised measurements of plasma in each millimeter is possible. This ESPION probe is built by Hiden [54]. The probe provides a passive compensation to the RF noises based on [55] by AC decoupling the probe from the DC measurement circuit and allowing the tip to follow RF variations.

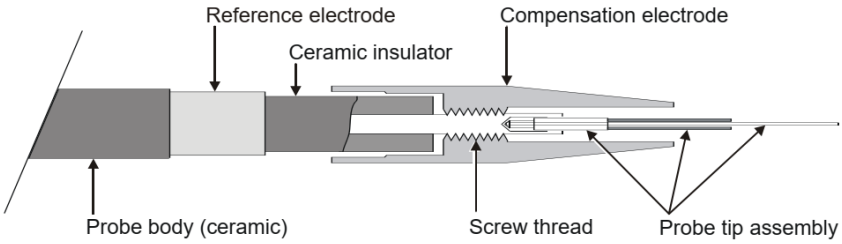

Figure 2.4: RF compensation in Langmuir probe in ALINE [54].

The probe can be biased from -200 to 100 V and the measurements were taken at a swept frequency of 65 kHz. For a cleaner profile, 20 measurements were averaged. Note that at this frequency, the measurement can be considered to be stationary, since the measurement frequency of measurement is much smaller than the characteristic plasma frequencies.

Probe tips

Two different probe tips are used for Langmuir probe analysis in ALINE plasma.

Cylindrical probe tip : The cylindrical probe tip is made of tungsten. It is 10 mm long and 75μm in diameter, see figure 2.5.

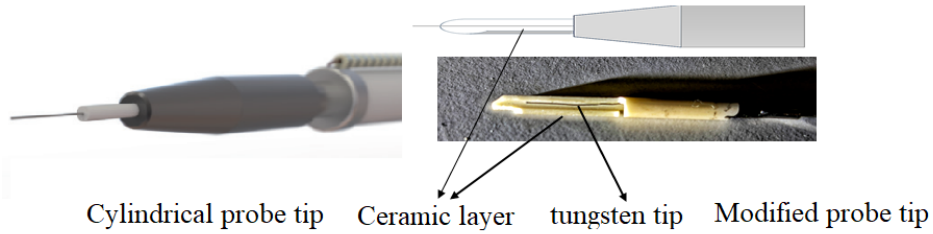

Figure 2.5: Different probe tips used for measurements in ALINE .

Modified probe tip : To study the effect of drift the cylindrical probe tip is modified by covering half of the collection area of the tungsten probe tip with a ceramic. The ceramic layer has half hollow cylinder shape of outer radius 2.5 mm and thickness 0.5 mm. The results using the modified probe tip is presented in chapter 3.

2.2.2 Analysis of probe data

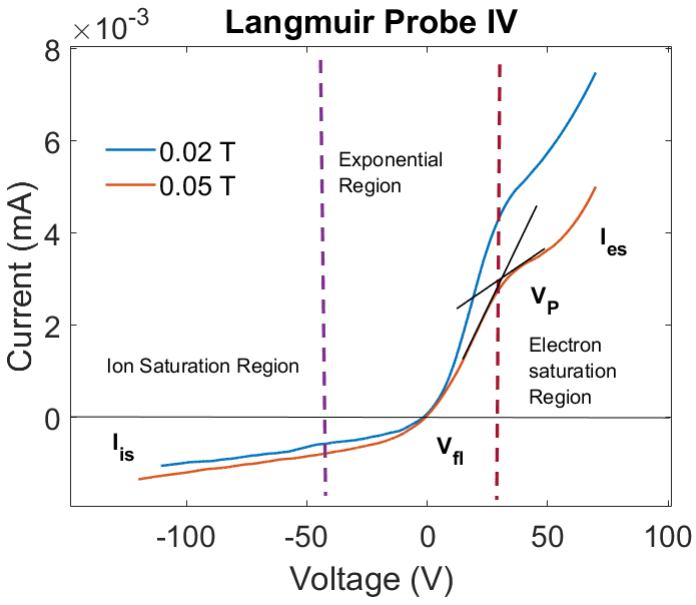

Figure 2.6: IV curve from RF compensated Langmuir probe measurements in ALINE.

IV analysis

2 Sample curves corresponding to a 0.02 and 0.05 T magnetic fields are presented in the figure 2.7. One can divide the IV curves in to thee region, ion saturation region, ex-

ponential region and the electron saturation region. When the probe is biased at lower voltage, it collects only the ion current, with increasing bias voltage, it starts to collect the Maxwellian electrons, which gives the exponential region and at highly positive voltages, the probe only collects the electrons. Ion saturation current and the electron saturation currents are represented by the I_{is} and I_{es} respectively. In the transition region, the ion current is negligible and the electron current I_e can be represented as:

$$I_e = I_{es} \exp\left(\frac{e(V_B - V_P)}{KT_e}\right) \tag{2.1a}$$

$$I_{es} = en_e A\bar{v}/4 = en_e A\left(\frac{KT_e}{2\pi m}\right) \tag{2.1b}$$

A is the area of the probe tip exposed to the plasma. V_B is the voltage on the probe, V_P is the plasma potential or the space potential and $\bar{v}$ is the average electron velocity. The potential at which the probe drives a net zero current from the plasma (equal ion and electron current) is called the floating potential and represented by V_{fl}. Floating potential can be determined from the zero crossing point of the IV curve. The point at which the electron current begins to saturates represents the end of the repelling sheath and corresponds to the plasma potential.

There are 3 methods employed in this thesis to find out the plasma potential :

The first method is the intersection method, which is shown in the figure 2.7 by finding the intersection point of the lines extrapolated from the exponential and the electron saturation part of the IV curve [8; 11] In the second method (the most used), the peak of the first derivative of the IV curve can also be taken as the position of the plasma potential.
With increasing magnetic field there is a significant reduction in the electron saturation, which is visible in the figure 2.7. At higher magnetic fields, near the RF electrode, especially at low pressure, the first derivative method is not reliable since there can be multiple peaks in the first derivative, representing different populations of electrons with different energies. Under this condition, the second derivative is taken and different peaks identified to find out the plasma potential. This third method is explained in detail in section 4.2.3.

OML Theory

OML theory is the simplest theory used for analysis of Langmuir probe IVs [56]. Considering ions are coming from infinity to an attracting probe tip with velocity v_0 with an impact parameter p. The plasma potential V is 0 at infinity and negative everywhere, varying gently towards the negative probe potential Vp. The conservation of

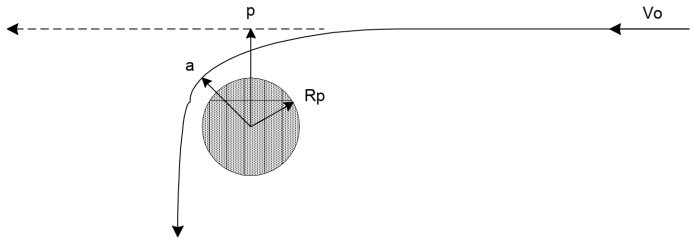

Figure 2.7: IV curve from RF compensated Langmuir probe measurements in ALINE.

energy and angular momentum results in

$$\frac{1}{2}mv_0^2 = \frac{1}{2}mv_a^2 + eV_a = -eV_0 \tag{2.2a}$$

$$pv_0 = av_a \tag{2.2b}$$

conservation of energy and angular momentum results in

$$\frac{1}{2}mv_a^2 = \frac{1}{2}mv_0^2\left(1+\frac{V_a}{V_0}\right) \tag{2.3a}$$

$$p = av_a/v_0 = a\left(1+\frac{V_a}{V_0}\right)^{1/2} \tag{2.3b}$$

If a $\leq R_p$,the ion is collected and the effective probe radius is taken to be $P(R_p)$. For mono-energetic particles the flux to the probe of length L can be written as:

$$dI = \frac{qv_0}{\pi}dn2\pi r_p L_p\sqrt{1+\frac{V}{V_0}} \quad where \quad dn = 2\pi n_0 v_0\left(\frac{m}{2\pi KT}\right)\exp\left(\frac{mv_0^2}{2KT}\right)dv_0 \tag{2.4}$$

Here (v_0/π)dn represents the flux crossing a unit area. The total current to the probe tip can be found by integrating over the speed from 0 to ∞:

$$I(V) = I_0\int_0^\infty x\sqrt{x^2+\beta^2}\exp(-x^2) \quad where \quad I_0 = 4qn_0 r_p L_p\sqrt{\frac{2KT}{m}} \tag{2.5}$$

Note that for $x^2 = mv^2/2KT$ and $\beta^2 = eV_p/KT$, The integral can be simplified to:

$$I(V) = \frac{1}{4}an_0A_p\sqrt{\frac{8KT}{\pi m}}\left[2\sqrt{\frac{\varphi}{\pi}}+\exp(\varphi)erfc\sqrt{\varphi}\right] \qquad where \qquad \varphi = \frac{eV}{KT} \tag{2.6}$$

Here, A_p is the area of the probe. This formula is true for ions and for electrons when the size of the sheath s is significantly larger than the probe radius, ie, $r_p <<$

s. Since the average sheath size is a few debye length λ_D, with increasing r_p/λ_D ratio, the validity of the OML theory becomes questionable.

The peculiarity of this theory is that when the ion temperature $T_i \to 0$ the current becomes independent of the ion temperature and the equation becomes.

$$I_i(V) \to \frac{\sqrt{2}}{\pi} e n_0 A_p \sqrt{\frac{eV}{M}} \tag{2.7}$$

Note that here, V is the probe potential relative to the plasma potential. In practice, V should be replaced by V_p-V.

OML method is used to find out the plasma density in ALINE plasma device. The density is evaluated from the ion saturation part where the I_p^2(V) profile is linear. An experimental and theoretical work was performed by Pelling et al. [57] to study the collisional effects on the analysis of probe data using OML method. All the experiments were performed at lower pressures (0.6 and 1 Pa where the collision effects are negligible. When the magnetic field is 0.1 T the ions are weakly magnetized because the collision frequency is still higher than the cyclotron frequency, especially in Argon gas. At lower collision rates, the ions are magnetized, they move in helical orbits along the magnetic field lines, but the Bohm condition for the ion collection to the electrode is still valid, if the area of collection is considered to be the projection area of the probe along the magnetic field lines [58]. The algorithm used for the determination of the plasma parameters around the RF electrode for different areas of projection in ALINE are explained in [59; 60; 11]

Bi-Maxwellian EEDF

In a CCP discharge, due to the stochastic heating resulting from electron-RF sheath interaction, a hot electron population can get generated near the vicinity of the RF electrode. In the presence of a magnetic field, the electrons can have multiple encounters with the oscillating sheath before returning to the bulk plasma and gaining higher energy compared to the case of no magnetic field. But probe measurements near the RF electrode in a magnetic environment can leave the IV curves noisy, and this results in bad electron temperature evaluation. But the presence of supra-thermal electrons can shift the floating potential to negative values, and this has been observed in the ALINE device when the probe takes measurements at the flux tubes connected to the RF electrode. A detailed investigation of a shift of floating potential and its dependence on various input conditions is studied in [61]. These are studied using PIC simulations and analytically in [62]. Here, an attempt has been made to evaluate the electron temperature from the IV profile measured using the probe employing the Druyvesteyn method. The probe measurements were smoothed over 100 points, and the Druyvesteyn method was applied.

The electron energy probability function (EEPF) can be expressed as:

$$g_p(\varepsilon) = \frac{\sqrt{8m_e}}{e^3 A_p} \frac{d^2 I_e}{dV^2} \tag{2.8}$$

if the distribution of electrons are Maxwellian, equation 2.8 can be represented as:

$$g_p(\varepsilon) = \frac{2}{\sqrt{\pi}} n_e k T_e{}^{-3/2} e^{-\varepsilon/kT_e} \tag{2.9}$$

Here T_e is the electron temperature and $\varepsilon = e(V_P - V_B) = eV$ is the electron energy. If the natural logarithm of Eq. 2.8 and Eq. 2.9 are taken then natural logarithm of EEPF is directly proportional to the inverse of the temperature as shown in Eq. 10:

$$\ln(g_p(\varepsilon)) = \ln\left(\frac{d^2 I_e}{dV^2}\right) + constant = -\frac{\varepsilon}{kT_e} + constant \tag{2.10}$$

Where the electron current $I_e = I_p - I_i$, I_p the total probe current and I_i is the ion saturation current. Using this slope of the curve, the average electron energy of the electrons has been evaluated.

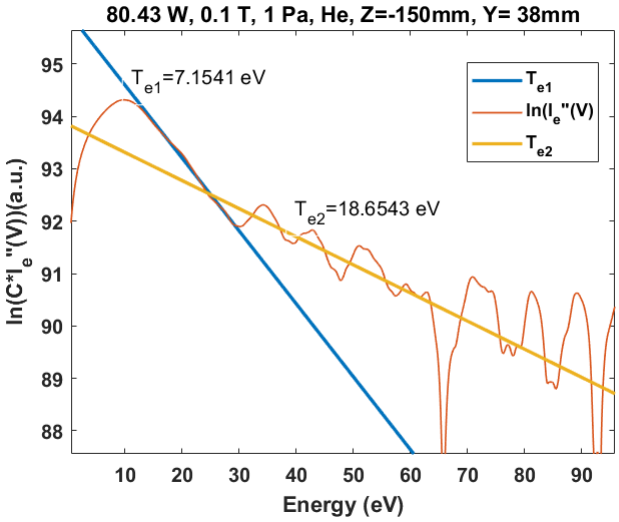

Figure 2.8: Electron temperature evaluation using Druyvesteyn method.

We found two slopes for the curve in which the tail part represents the temperature of the hot electron population. The confidence on this measured values are not so high because of the noisy IV curves and different smoothing methods (mainly Savitzky-Golay method).

2.2.3 Floating Probe

A floating probe is a simple setup in which a tungsten probe tip floats on the plasma and is connected to an oscilloscope. Measured the voltage on the probe tip gives the floating potential of the plasma. If the oscilloscope allows the measurement of voltage variation with higher time resolution (Higher frequencies), one can measure the RF oscillations (noise) in the plasma.

To study the influence of the RF perturbations, floating probe measurements were taken for 1.2 Pa argon discharge, 0.1 T magnetic field and in capacitive coupling, see figure 2.9. Here RF represents the reference signal and the noise corresponding to different Y position in the plasma are measured and compared. Floating probe study revealed that the RF noise is small and negligible and the probe measurements with RF compensations are not very much affected due to the same, because the RF floating potential component had a very low magnitude (less than 1 V), especially in capacitive coupling where the plasma potential is low (10-20 V) according to the thermal electron temperature (3-5 eV).

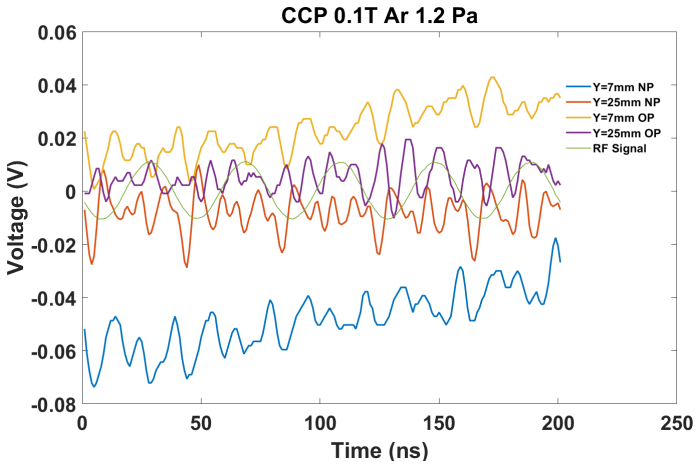

Figure 2.9: Floating probe measurements inside ALINE using simple tungsten probe tip (OP) and modified probe tip (NP). The green curve represents the Reference signal.

2.2.4 IR Camera

In fusion research, IR thermography is widely used across various fusion devices to assess the heat loads on the first wall and ensure equipment safety [63; 64]. Studies by Balboa et al.[65] , Sieglin et al.[66] , Gauthier et al.[67], and Takeuchi et al.[68] have demonstrated its effectiveness. With the progress made in IR camera technology in the past two decades, it is now possible to investigate rapid events in the tokamak

plasma [69]. This section aims to explain the basic principles of IR thermography and IR camera setup used in ALINE.

Basic principle

Any material with temperature greater than absolute zero, emit thermal radiations. Maximum radiant power emitted per unit projected area of an object in a given wavelength range to a unit solid angle can be expressed by Plancks law:

$$L_{\lambda}^{BB}(\lambda,T)d\lambda = \frac{2hc^2}{\lambda^5}\left[\frac{1}{\exp\{\frac{hc}{\lambda kT}\}-1}\right]d\lambda \tag{2.11}$$

here $L_{\lambda}^{BB}(\lambda,T)$ is the spectral radiance in Wm^{-3} sr^{-1}, h, the Planck's constant =6.626$\times 10^{-34}$ Js k is the Boltzmann constant, c is the speed of light in vacuum and T is the absolute temperature of the object in K. The wavelength λ_{max} at which the spectral radiance peaks for a given temperature T can be found using Wien's displacement law.

$$\lambda_{max} = \frac{b}{T} \tag{2.12}$$

where Wien's displacement constant b$\approx$2.898 $\times 10^{-3}$ mK. Total radian power emitted in a given wavelength range $(\lambda, \lambda + d\lambda)$ per unit area by a blackbody is given by spectral excitance $M_{\lambda}(\lambda,T)$ $[Wm^{-3}]$.

$$\begin{aligned} M_{\lambda}(\lambda,T)d\lambda &= \int_{hemisphere} L_{\lambda} cos\delta d\Omega d\lambda \\ &= \int_0^{\pi/2}\int_0^{2\pi} L_{\lambda} cos\delta sin\delta d\delta d\varphi d\lambda = \frac{2\pi hc^2}{\lambda^5}\left[\frac{1}{\exp\{\frac{hc}{\lambda kT}\}-1}\right]d\lambda \end{aligned} \tag{2.13}$$

δ and φ are the zenith and the azimuthal angle. The total excitance M(T) (with units $[Wm^{-2}]$) of the unit area of the black body is given by the Stefan-Boltzmann law:

$$M(T) = \int_0^{\infty} M_{\lambda}(\lambda,T)d\lambda = \sigma T^4 \tag{2.14}$$

$\sigma = \frac{2\pi^5 k^4}{15ch^3}$=5.67 $\times 10^{-8}$ $Wm^{-2}K^{-4}$ is the Stefan-Boltzmann constant.

A perfect black body absorbs all incoming radiations and reflects and only a black body can have the radiance value given by the Planck's law. A real body doesn't emit all the radiation which it absorbs like a black body in the same temperature and the radiance of a real object is dependent on several factors such as the angle of observation, surface properties and environmental conditions etc. The ratio of the radiance of

an object and of a black body is given by emissivity (ε), which will be in the range of $0 \leq \varepsilon \leq 1$.

$$\varepsilon(\lambda, \delta, \varphi, T) = \frac{L_\lambda(\lambda, \delta, \varphi, T)}{L_\lambda^{BB}(\lambda, T)} \tag{2.15}$$

Incoming radiation to an object is either reflected, transmitted or absorbed. Hence one can write $\rho + \tau + \alpha = 1$. Where ρ, τ, α are the reflectance, transmittance and absorptance. For an opaque object, emissivity can be expressed as $\varepsilon = 1 - \rho$.

IR camera in ALINE

ALINE is equipped with Optris PI400i IR camera. The IR camera is looking through an IR window and placed right above the RF electrode. There are two different sensors that are used in IR camera the (a) thermal detectors and (b) photon detectors. Thermal detectors rely on changes in physical properties of detector material (metal or semi-conductor) caused by absorption of incident radiation, such as temperature-dependent electrical resistance in a bolometer. Optris PI400i IR camera has a Focal plane array (17 μm) uncooled sensor, which is a thermal sensor. Thermal detectors may experience signal leakage among individual detector elements due to their principle, which also makes them slower than photon detectors. However, their lower cost is an advantage. Technical details of the IR camera are given in the table 2.1.

Table 2.1: Technical details of Optris PI 400i IR camera.

Detector	FPA, uncooled (17μm)
Optical resolution	382 × 288
Spectral range	8-14 μm
Temperature range	-20-1500° C
Accuracy	+/-2°C or +/-2%

TEDDY

TEDDY stands for (Thermography Estimate of Deposited Heat DYnamics) and is a 2D linear thermographic inversion algorithm [70] developed for heat flux studies of divertor in WEST tokamak. TEDDY has been used in this thesis to estimate the heat flux from the surface temperature of the RF electrode. Though the heat diffusion is a 3D problem, assuming here that the heat flux will diffuse only in 2 directions, (i) along the profile of deposited heat flux (denoted by x) and (ii) along y direction through the depth of the tile. The heat equation can be written as:

$$\rho C_p(T) \partial_t T = -\vec{\nabla}.\vec{q} \tag{2.16}$$

Where ρ is the volumetric mass (kg/m^{-3}) of the RF electrode material, C_p is the specific heat capacity in J/Kg.K T denotes the local temperature in K and he is the heat flux W/m^{-2}. The emissivity of the tungsten is around 0.125, and TEDDY neglects the radiation losses since it is negligible, as well as the heat loss to the electrode holder. The details of the code are explained in detail in [70]. The temperature measurements from the IR camera corresponding to 11 measurement points are given as input to the TEDDY, and the heat flux to the RF electrode is measured using the reverse model.

Since the electrode is receiving heat flux from both the circular faces and also through the lateral side, heat flux is assumed to be constant all along the surface. Also the electrode is considered as 2 separate tile of 0.5 mm thick receiving constant flux.

2.2.5 Fast Camera Imaging

Fast cameras are widely used in nuclear fusion research for providing valuable insights into plasma behaviour, implosion dynamics, impurity tracking and diagnostics. The visible imaging technique for plasma diagnostics has been used since 1985. Recent technological advances in high-speed cameras capable of recording movies at very high frame rates and higher resolutions have opened up the possibility of using high-speed camera imaging as a reliable tool for plasma diagnostics. Visible imaging techniques are used with the gas puffing technique by Nishino et al [71]. for studying the plasma rotation due to the electron drift waves in the GAMMA 10 tandem mirror. Fast camera imaging is used in TORPEX plasma device to study the low-frequency electrostatic fluctuations due to the drift waves to complement the Langmuir probe measurements [72].

While diagnosing the plasma with fast camera the light intensity recorded by the camera I_{cam} is often compared with measurements of the ion saturation current (I_{isat}) with a cross-correlation of up to 0.75 as given in [73; 74].This is because the intensity of the light can be used as a proxy for (I_{isat}) or the density of the plasma (n) [73; 74; 75]. The relationship between I_{cam} and the physical parameters of the plasma is explored based on a simple model explained in doctoral thesis of Simon Vincent [76]. The discussion is limited to the normalization and 2D-FT techniques used in our experiments, as we do not use these methods to find plasma parameters from the intensity of the lights.

Optical set-up

FASTCAM SA-Z by Photron camera is used for the fast camera imaging of ALINE plasma [77]. ALINE has an optical port at one of the circular ends of the cylindrical vacuum chamber and the camera is placed at Z position Z= +80 cm. Fast camera measurements were taken at the frame rate in range 67.2-100 k frames per second over a square region of size =8 cm of the plasma with a resolution of 384×328 .

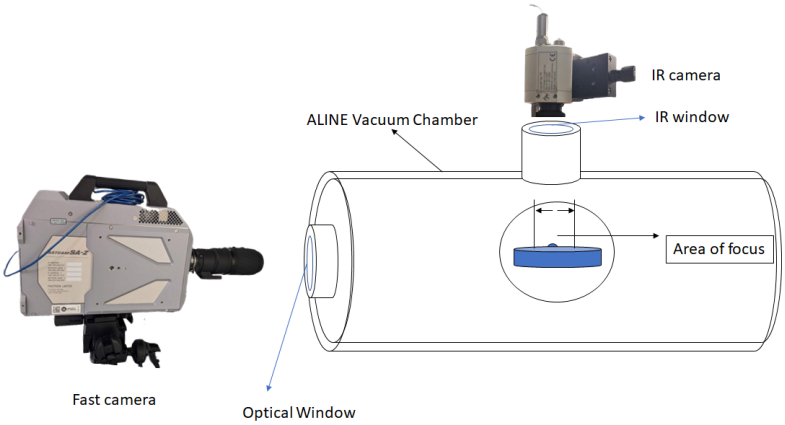

Figure 2.10: Diagram representing fast camera and IR camera imaging in ALINE

Image analysis tools

The tools that are used to analyse the images from the fast camera are presented here. This is preceded by a normalizing process of the form:

$$\tilde{I}_{nmd} = \frac{\tilde{I}(\vec{x},t)}{\tilde{I}_{avg}(\vec{x})} \tag{2.17}$$

$\tilde{I}_{avg}$ is the normalised light intensity obtained from the time averaged value of I_{cam}

$$\tilde{I}_{avg}(\vec{x}) = \langle \tilde{I}_{cam}(\vec{x},t) \rangle_t \tag{2.18}$$

2D Fourier Transform (2D-FT)

The camera images are analyzed by mode decomposition technique. 2-D Fourier decomposition technique is used to study the flow of rotating structures. Hence, a spatial decomposition of the fluctuations along θ and their corresponding time frequencies are being derived. 2D-FT of 2 variables, function reads $\hat{f} = \int\int f(x,t)\exp\{-i(kx+\omega t)\}dxdt$. the time series $\tilde{I}_{nmd}(,t)$ is extracted from the images at a given radius r and the 2D-FT is computed as : $\hat{I}(k_\theta,\omega) = \int\int \tilde{I}_{nmd}(r*,\theta,t)\exp\{-i(k_\theta r*\theta+\omega t)\}d\theta dt$ to transform it in to the θ spatial direction. Since the variations in θ are periodic, the wavelengths can be calculated by : $\lambda = 2\pi r*/m$, where m is an integer. Different modes are identified by the mode number m, with

$$k_\theta = \frac{m}{r*} \tag{2.19}$$

In addition, the frequencies are expressed systematically in Hertz to simplify the physical interpretation. More concise representation of 2D-FT is in the form :

$$\hat{I}_{r*}(m,f) = \int\int \tilde{I}_{nmd}(r*,\theta,t)\exp\{-i(m\theta + 2\pi ft)\}d\theta dt \tag{2.20}$$

Experiments are performed using a 50 mm lens with f/1.2 mounted on the camera. The camera is aligned parallel to the RF electrode to reduce the paralax error and the videos recorded by focusing on a narrow region over the RF electrode as shown in figure, thanks to shallow depth of field of the lens. the The camera Results based on the 2D FT of the fast camera analysis is presented in chapter 5, in the case of one-faced RF electrode.

Chapter 3

Measurement and Modelling of Highly Negative Floating Potential Measurements around One-faced RF Electrode in an RF Discharge

Contents

3.1 Langmuir Probe Measurements in a Magnetized Capacitive Discharge Around a Tilted RF Electrode 48

3.1.1 Introduction 48

3.1.2 Setup and Experiment 49

3.1.3 Langmuir Probe Measurements in ALINE 49

3.1.4 Theoretical floating potential for supra-thermal electrons . 57

3.2 PIC Simulation of the Electron Energy Distribution Function in a RF Magnetized Plasma Column Connected to a Tilted Electrode 60

3.2.1 PIC Simulations 61

3.3 Conclusion 70

3.1 Langmuir Probe Measurements in a Magnetized Capacitive Discharge Around a Tilted RF Electrode

3.1.1 Introduction

Since the end goal of this work is to measure the heat flux received by an RF electrode, the characteristics of the plasma around the RF electrode are important to know the factors that affect the heat flux and must first be studied. One of the most widely used diagnostics is the Langmuir probe, which allows to get the plasma density, potential and temperature of electrons [31; 52; 78; 40; 79]. This characterization work of the plasma all around the RF electrode has been started in a previous thesis [11]. It has been shown that in such magnetized plasma in the ALINE device where the magnetic field never exceeds 0.1 T, ions can be considered as almost unmagnetized and then follow the classical OML theory [80; 81]. Chen already demonstrated "the surprising validity of the OML theory in Helicon plasmas" [51]. Nevertheless, if 2D or even 3D maps of the plasma density can be drawn thanks to the 3D manipulator, the surprisingly very negative floating potentials measured by the probe when magnetically connected to the RF electrode sheath have not been explained properly, especially when the electrode is tilted at grazing angles (see figure 3.1). As it has been explained in the introduction chapter (section 1.7.7), stochastic heating may be the best candidate to explain these very negative floating potentials due to high energetic electrons accelerated in the moving RF sheath. This effect has already been observed in MERIE devices at lower magnetic fields [82; 39], but deeper investigations have been necessary for the ALINE device. In the first experimental part, this effect is studied by scanning many parameters such as the magnetic field strength, tilt angle or gas pressure. These floating potential measurements are compared to PIC simulations in the 2nd part, allowing us to conclude their origin and the existence of the bi-Maxwellian distribution

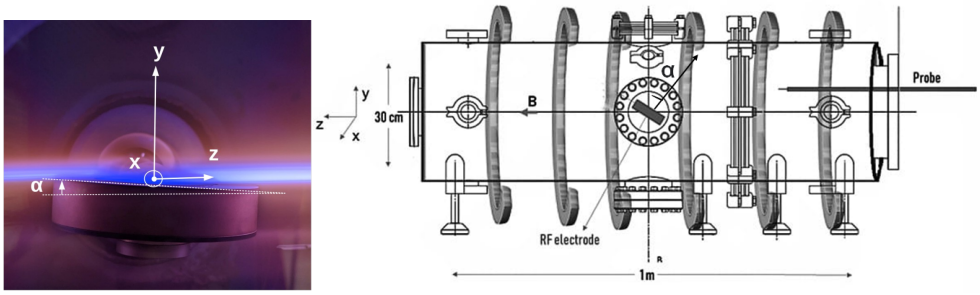

Figure 3.1: Argon plasma discharge in ALINE for 5° tilt angle (left), and schematic view of ALINE reactor (right).

of electrons with temperatures as high as 20 eV.

3.1.2 Setup and Experiment

ALINE (A LINEar machine) is a 1 m long, 30 cm diameter cylindrical device designed to study the RF sheath and sheath dynamics [45; 59]. At the maximum axial magnetic field of 0.1T, the electrons in the system are magnetized and ions are weakly or not magnetized (depending on the pressure). ALINE is equipped with an RF-compensated Langmuir probe coupled to a 3D manipulator, facilitating the measurement of the plasma parameters in all three directions. A sketch of the reactor and a photo of the antenna and plasma are depicted in figure3.1 [60]. The electrode is placed at the geometrical centre of the chamber. RF electrode is a specially designed one consisting of an active part, a disk placed at the centre through which the RF power is coupled to plasma via a matching network (capacitive) or directly. The active part of the electrode is surrounded by a grounded copper shield 3.2. The inner copper disk is 48 mm in diameter, and 11 mm thick grounded outer cover. The density of the plasma is significantly low below the electrode because the excitation of the plasma is formed only above the active part (figure 3.1). The electrode is connected to a rotor (piloted manually) which enables the rotation of the electrode, making an angle α with the axial magnetic field. The RF power (35 W for the current study) to the plasma is coupled either directly (Direct coupling) or through a matching box (Capacitive coupling). The angle between the electrode and the axial magnetic field has been varied to study the effect of the tilt angle on the floating potential, plasma potential and density.

3.1.3 Langmuir Probe Measurements in ALINE

To interpret the results, we assume that the plasma can be seen as a set of adjacent flux tubes since the electrons are magnetized, and the electron mobility perpendicular to the magnetic field is much lower than that along the parallel direction. On the contrary, the electrons in the flux tube connected to the grounded part of the electrode move along the axis of the cylinder 3.2, and are collected on the lateral side of the electrode or the wall cutting the magnetic field lines (the circular end of the ALINE chamber). On the other hand, the electrons connected to the active side/Edge of the electrode oscillate back and forth in the RF electric field of the sheath, creating a bright region inside the plasma, see figure 3.2. Plasma parameters have been measured using the moving probe along the y direction, from 2 cm above the centre of the RF electrode to 2 cm below the RF electrode for three z-positions (60, 80, and 100 mm). The effect of gas pressure, tilt of the electrode and magnetic field strength on plasma parameters are studied separately.

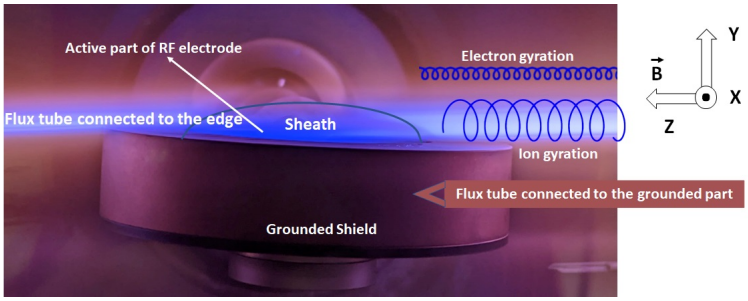

Figure 3.2: The diagram explaining design of the RF electrode and the flux tubes/ plasma columns connected to different regions of the RF electrode.

IV Curves inside the plasma column connected to the RF electrode

The IV curves measured from the bright plasma column connected to the RF electrode and one that from two centimeters are quite different from each other. In figure 3.3a, IV curves inside and outside of the flux tube are compared from both direct and capacitive coupling cases for 0°, 35 W, 0.8 Pa argon discharge. The IV curve inside the bright column have the specific characteristics representing higher density by higher ion saturation current, lower floating potential values and two slopes in the exponential region compared to the ones from outside the flux tube. The double derivative and the EEPFs (IV curves smoothed using sgolay function in matlab by preserving the original shape of the curve) are compared for the capacitive discharge case in figure 3.3b. The curves corresponding to the ones from inside the bright plasma column (Y=0 mm) represents higher energetic thermal electrons and followed by a long tail due to the hot electrons, whereas outside the flux tube (Y=-19 mm) there are no hot electrons and the thermal electrons are cooler which can be interpreted from the second derivative and EEPF profiles. In the following parts the focus is given to the parameters inside the plasma column connected to the RF electrode.

Effect of Gas Pressure

In this study, experiments were performed in ALINE at three gas pressures 0.8 Pa, 1.5 Pa and 3 Pa to study the variation of the plasma parameters at low, intermediate and high pressures, and the results from the probe measurements are shown in figure 3.4.

At 0.1 T magnetic field, the electrons are highly magnetized (ω_c/ν_c =1280, 684, 342 for 0.8, 1.5, 3 Pa respectively) and they are confined inside the flux tube above the RF electrode. These energetic electrons increase the density due to the increase in effective and ionization collision cross section [83], inside the flux tube significantly compared to the surrounding plasma 3.4(a). In addition, collisions favour the cross-field motion of electrons, which causes a widening of the flux tube inside the plasma along Y direction. For higher Z positions, since the length of the plasma column increases

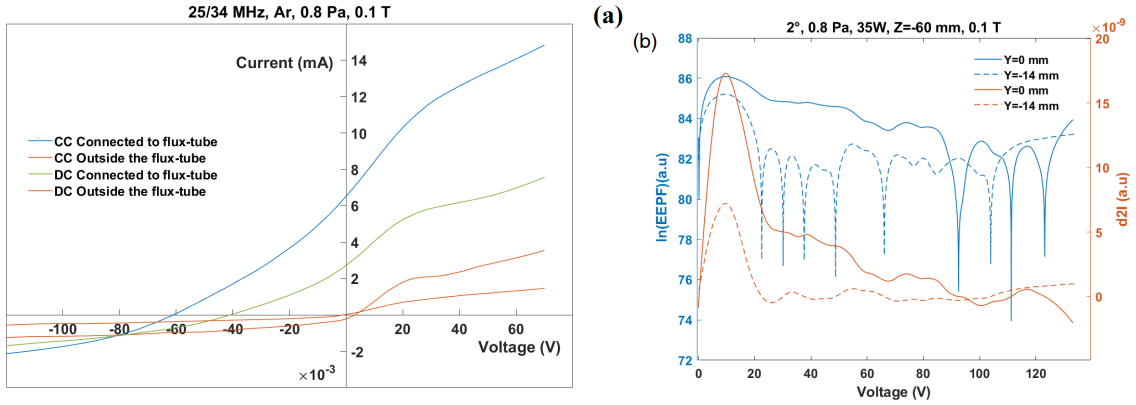

Figure 3.3: I-V characteristics (a) and I''_p (d2I) and EEDF plot (b) taken at different radial positions at a 0.8 Pa discharge.

to a few mean free paths (λ^e_{mfp} =68.4, 36.5, 18.2 mm for 0.8, 1.5, 3 Pa, respectively for electrons), due to higher collisions the density is slightly improved (15-20% for 0.8 and 1.5 Pa). Higher collision frequency reduces the average electron temperature, which results in a reduction in the magnitude of the floating potential profile (up to -60 V). This can be seen in the floating potential values inside the magnetic flux tube in figure 3.4b. The stochastic processes in RF discharges have been known and widely studied for the last few decades [34; 84; 85; 86]. It is the dominant heating mechanism at low-pressure RF discharges. The electrons are accelerated in the oscillating RF sheath and gain energy from the electric fields at low pressure. At higher pressures, the collision rate inside the plasma increases, and the stochastic heating process becomes lower than the Ohmic heating.

At low gas pressure discharge, the electrons are not thermalised close to the RF electrode. The second derivative of the IV curve and EEPF corresponding to Y=3 mm in the flux tube is plotted as a function of the energy in figure 3.4c. At Y=3 mm, even the thermal electrons have high energy (15 eV) corresponding to 0.8 Pa measurement, and as the pressure doubles, at 1.5 Pa, the average energy of the electrons drops to 8.8 eV. At 3 Pa, where the collisions are high, all the electrons are thermalised, and the energy of the electrons inside the flux tube has almost the same energy as the electrons outside (2.1-2.5 eV), figure 3.4c [87; 40](measured from the inverse of the slope of ln(EEPF)). At lower pressures there is a deviation of the electron distribution from Maxwellian to non-Maxwellian with two or more electron populations inside the magnetic flux tube connected to the RF electrode.

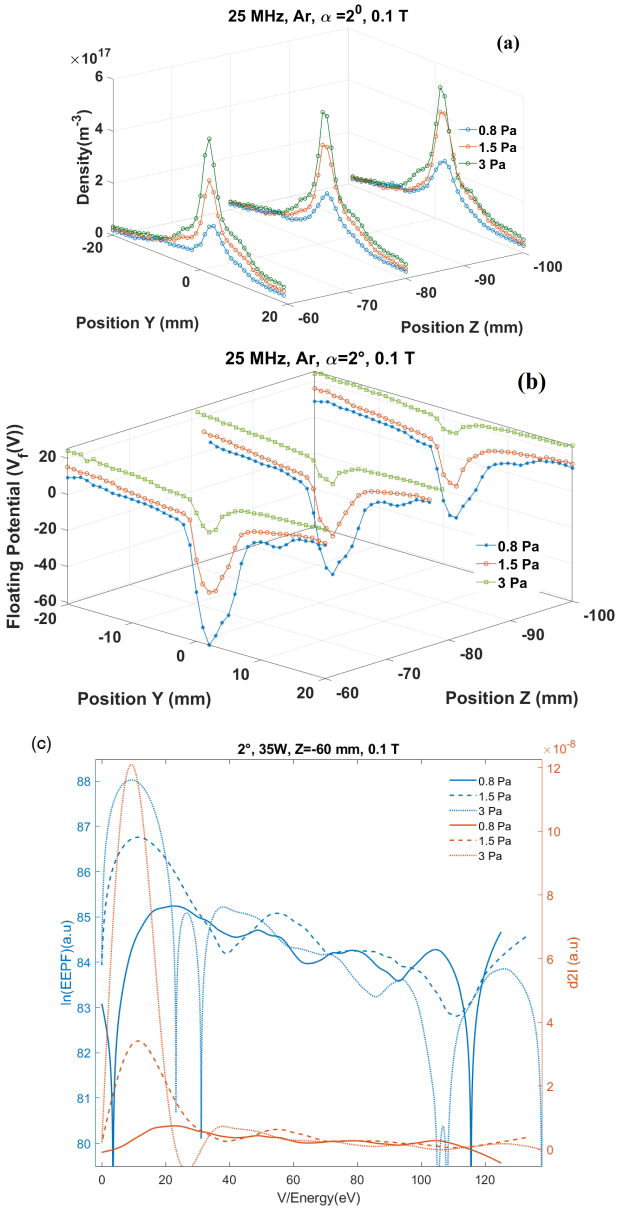

Figure 3.4: Dependencies of density (a) floating potential (b) and natural logarithm of EEDF and the second derivative (d2I) inside the flux tube connected to the RF electrode (c) on gas pressure for capacitive discharge in ALINE device.

Effect of tilt of the Electrode

The dependence of the tilt angle between the RF electrode and the magnetic field on the plasma parameters inside the flux tube connected to the RF electrode is discussed here.

The experiments were performed at 0.1 T magnetic field for 0.8 Pa argon gas pressure at 35 W coupled RF power for both capacitive and direct coupling cases. RF power is coupled through capacitive and direct coupling at 25 MHz and 34 MHz frequencies respectively for better power coupling. The results are depicted in the figures 3.5 for capacitive coupling and 3.6 for direct coupling.

The density and the floating potential profiles are shown in figure 3.5. The density profiles have much narrower and higher peaks at lower angles 3.5(a). At 0°, the peak density value measured by the probe is around $1.5\times10^{17}m^{-3}$ at $Z = -60mm$ and it increases for lower Z values. As the tilt angles increases the peak values reduces and the density profile is widened. The density peaks are corresponding to the positive Y values due to the edge effect as explained before. Similarly the floating potential values are highly negative for lower angles 3.5(b). Absolute values of floating potential are decreasing with the increasing distance from the RF electrode due to collisions with neutrals. While the position of the measurements is far from the electrode by a few times the mean free path of the electrons, the electrons encounter multiple collisions, and they are thermalised. As for the gas pressure scans, the possible explanation of the negative floating potential can be associated with stochastic heating generating a population of supra-thermal electrons inside the magnetic flux tube, as reported before [88; 89; 90; 91]. As the tilt angle increases, the width of the plasma column increases because the projection of the electrode surface along the magnetic field is increased. When the electrode is rotated from 0° to 2° as we can see from the profile, even if the width of the flux tube increased, there is no reduction in the density profiles or the magnitude of the floating potential inside the flux tube. The stochastic heating process is more efficient at grazing angles with the magnetic field since electrons are pushed out of the sheath along the magnetic field and gain a net acceleration. Also, the electrons gyrating along the magnetic field lines can have multiple interactions with the oscillating sheath and gain more energy [39]. At higher angles, the acceleration of electrons is less efficient, leading to flatter profiles for the floating potentials (figure 3.5(b)). This dependence is observed for both direct and capacitive modes of power coupling.

An attempt has been made to see the effect of the tilt angles in the EEPFs inside the flux tube connected to the RF electrode. For this study, the IVs corresponding to the position of the most negative floating potential are taken and compared with the EEPF for different angles (figure 3.5c). The error margins in the tail of the curve can be high due to the noises in the probe and severe smoothing of the IV curves. So in this case, we stick our discussions by comparing the slope corresponding to the thermalised electron part (or the cold electrons). The inverse of the slope of the dashed line indicates the average electron temperature. The slope is almost the same for 0° and 2°, indicating higher electron temperatures, and higher efficiency of stochastic heating. The average slope increases and then the electron energy is decreased at higher angles (5° and 20°)

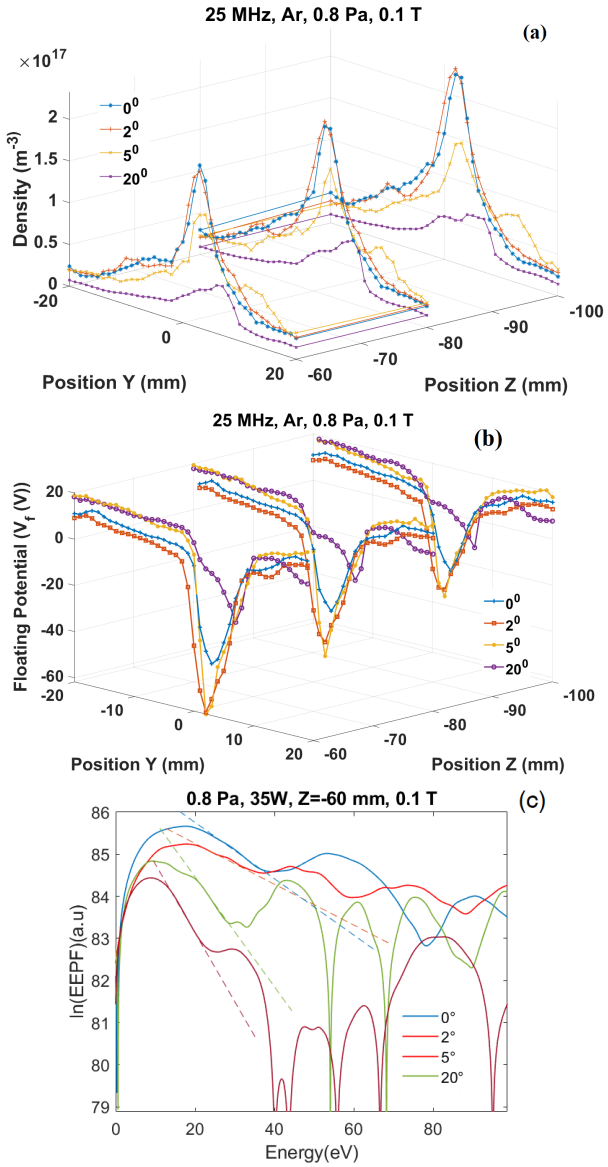

Figure 3.5: (a) Density measurement, (b) floating potential and (c) natural logarithm of EEPF for different tilt angles inside the magnetic flux tube in capacitive coupling. The inverse of the slope of the dashed line represents the average energy of thermal electrons in each case.

as one can see from the figure 3.5c. Similar trends for the density and floating potential variations are observed in direct coupling as well, see figure 3.6.

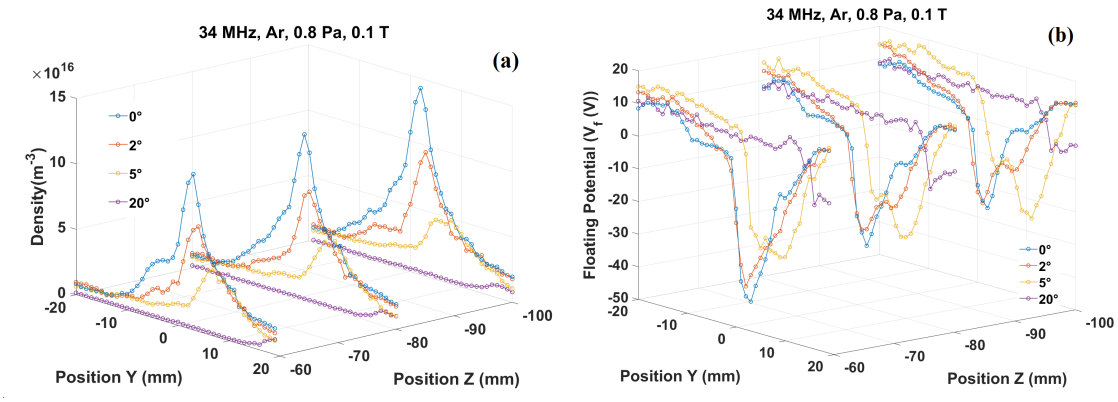

Figure 3.6: Density measurement (a) and floating potential profiles (b) in ALINE for 4 different angles (α) in direct coupling.

Effect of the magnetic field strength

Here the discussions are based on the measurements corresponding to a 0.8 Pa argon discharge at 35 W coupled RF power for 4 different magnetic field values (25, 50, 75 and 100 mT) in capacitive coupling.

Variations of the floating potential along the Y direction, corresponding to both direct coupling and capacitive coupling for two magnetic fields and two distances of the measurements, are shown in figure 3.7a. These measurements were taken using the floating probe (section 2.2.3) and observed highly negative floating potential values inside the flux tube connected to the RF electrode. The value of the floating potential measured by the floating probe is more negative at higher B field and its magnitude decreases with increasing distance from the RF electrode, which is in agreement with the RF compensated Langmuir probe. This observation is revisited in the next section, comparing the PIC simulation results. The variation of the floating potential corresponding to four magnetic fields along the Y direction is displayed in the figure 3.7b. The lowest of the floating potential is observed for the measurement corresponding to highest magnetic field. The region of space along Y direction where the floating potential is negative is widened with decrease in the magnetic field.

From the scans taken along the Y axis, the density of the plasma is plotted in figure 3.8(a).

The density of the plasma grows significantly when the magnetic field is increased from 0.025 to 0.05 T. The width of the plasma column connected to the RF electrode becomes narrower and the peak of the density profiles is shifted closer to the RF electrode. The reduction of the self-bias on the surface of the RF electrode can explain this observed behavior. With the increasing magnetic field, the magnitude of the RF voltage is reduced, and the density above the RF electrode is increased. This reduces the size of the sheath above the RF electrode. As mentioned earlier, at grazing angles

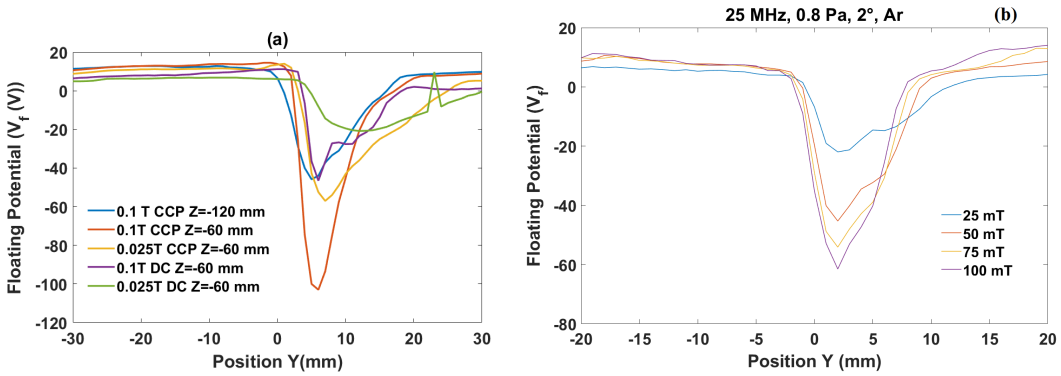

Figure 3.7: Floating probe measurement results for 0° in direct coupling (DC) and capacitive coupling (CCP) (a) and dependence of floating potential (b) on the applied magnetic field measured using conventional RF compensated probe .

(2° here), the magnetic field enhances the efficiency of the stochastic heating, along with that, better confinement improves the density significantly. The first derivatives corresponding to the IVs from inside the flux tube are presented in figure 3.8(b). At lower pressure, since the collisions inside the plasma are low, the energetic electrons generated due to the interaction with the sheath are not thermalised. In figure 3.8(c) it is seen that the plasma has a hot electron population inside the flux tube connected to the RF electrode. For the 0.025, 0.05 and 0.075 T cases, this can be seen from the elongated tail as shown in figure 3.8(c). When the magnetic field is 0.1 T, there is a change of shape in the first derivative of the IV curves inside the flux tube corresponding to Y=3 mm position figure 3.8(b). The first derivative of the 0.1 T IV curves is different from the lower magnetic field ones with a bump after the maximum of the curve corresponding to the thermal electron population. This kind of profiles makes the analysis complicated [92]. The potential of the plasma can't be determined from the peak of the first derivative. At this point, the population of the hot electrons are higher than the thermal ones which is determined using the Druyvesteyn method and the actual plasma potential can be shifted to the small bump of the first derivative corresponding to the thermal electrons on the right.

An attempt has been made to determine the electron temperature from each IVs using the Druyvesteyn method and the results are portrayed in the figure 3.8(c). The temperature values obtained from the curves are tabulated in the figure. The values of the hot electrons can have huge error bars but the thermal electrons in the flux tube have almost the same temperatures in the range 6-7 eV for the lower B cases. The higher magnetic field measurements have lower slopes, implying higher temperature values.

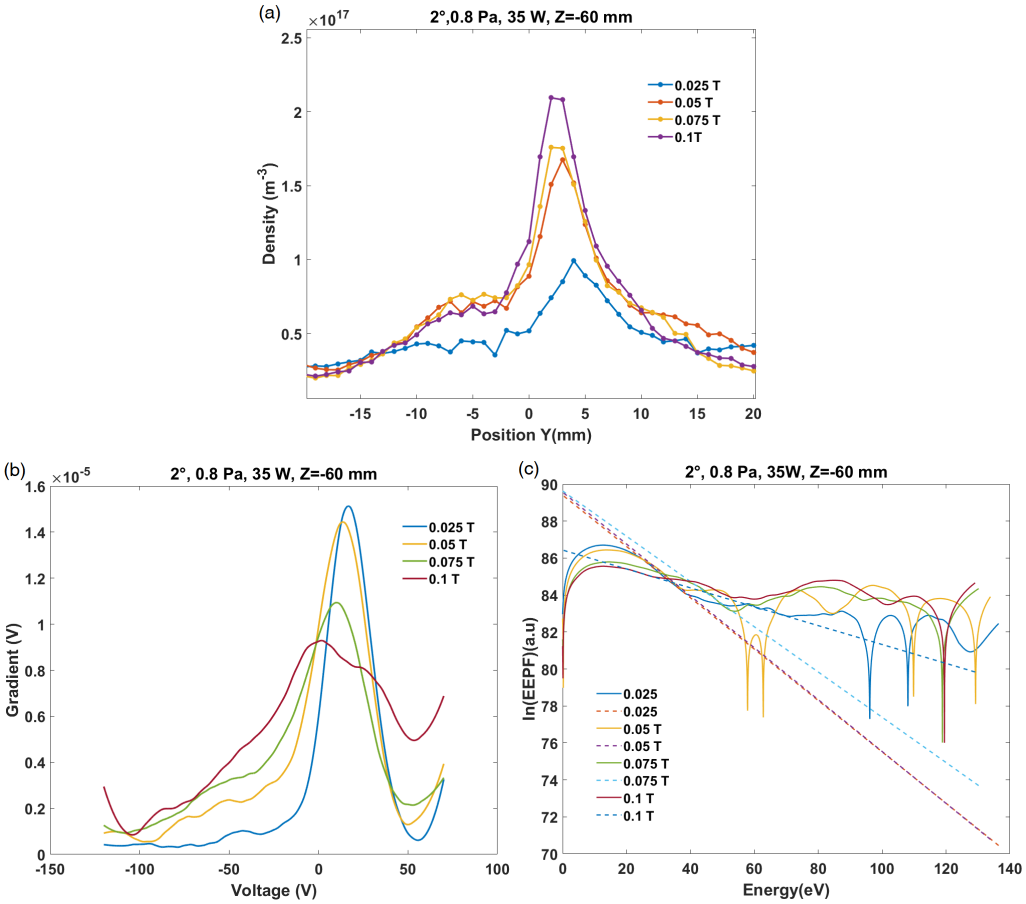

Figure 3.8: Dependencies of density profile (a) and Variations in the gradient of IV profiles inside the magnetic flux tube (b) and log of the (C*D2I) on gas magnetic field for CCP discharge in ALINE device at 0.8 Pa argon discharge for 35 W coupled RF power.

3.1.4 Theoretical floating potential for supra-thermal electrons

Considering Maxwell-Boltzmann velocity distribution for electrons, the electron flux contribution from the thermal electrons to a wall biased at a potential ϕ can be determined by:

$$\Gamma_x = \int_{v_0}^{\infty}\int_{-\infty}^{\infty}\int_{-\infty}^{\infty} v_x f(v) dv_x dv_y dv_z = n_0\sqrt{\frac{kT}{2\pi m_e}} exp(-\chi) \tag{3.1}$$

where n_0, T, m, v are the density, temperature of thermal electrons, mass of electrons and thermal velocity respectively, and $\chi = \frac{mv_0{}^2}{2kT} = \frac{eV}{kT}$. Equating the ion flux

equal to the Bohm flux $\Gamma_i = n_0 C_s$ with the thermal electron flux yields the famous formula of the floating potential for a plasma given by equation 3.2, which should not be confused with the floating potential of a probe plunged into the plasma. As a matter of fact, the floating potential of the plasma is the gap between the plasma potential V_p and the probe V_{probe} as follows : $V_p - V_{probe} = V_{fl}$. Here this floating potential is defined as positive because the minus sign is already in equation 3.1.

$$V_{fl} = -\frac{kT_e}{2e} ln\left[\left(2\pi\frac{m_e}{m_i}\right)\left(1+\frac{T_i}{T_e}\right)\right] \tag{3.2}$$

The magnitude of the floating potential measured by the probe is then proportional to the electron temperature T_e, assuming a simple Maxwellian velocity distribution, with m_e and m_i the electron and ion mass respectively and T_i the ion temperature.

Now considering a population of supra-thermal electrons with density n_s and temperature T_s with a shifted distribution function with a drift v_d along the x direction, the contribution of the flux to the electrode can be determined as follows.

$$f_d(v_x, v_y, v_z) = n_s\left(\frac{m}{2\pi kT_s}\right)^{3/2} \exp\left(-\frac{m((v_x - v_d)^2 + v_y^2 + v_z^2)}{2kT_s}\right) \tag{3.3}$$

The general solution for the supra-thermal flux is :

$$\Gamma_x^s = \int_{v_0}^{\infty}\int_{-\infty}^{\infty}\int_{-\infty}^{\infty} v_x f_d(v) \exp(-\chi_s)\, dv_x dv_y dv_z \tag{3.4}$$

$$\Gamma_x^s = n_s\left[\frac{v_d}{2}\left(1 - erf\left(\sqrt{\frac{m}{2kT_s}}(v_0 - v_d)\right)\right) + \sqrt{\frac{kT_s}{2\pi m}}\exp\left(-\frac{m(v_0 - v_d)^2}{2kT_s}\right)\right] \tag{3.5}$$

with $\chi_s = \frac{mv_0^2}{2kT_s} = \frac{eV}{kT_s}$

For $v_d = 0$, we find

$$\Gamma_x^s = n_s\sqrt{\frac{kT_s}{2\pi m}}\exp(-\chi_s) \tag{3.6}$$

The total electron flux is then $\Gamma_e = \Gamma_x + \Gamma_x^s$. The ion flux is still the Bohm flux, and equating now the total electron flux to the ion flux allows to determine the new floating potential of the plasma. The equation is solved numerically to yield the floating potential gap V_{fl} between the plasma potential V_p and the probe floating potential V_{probe}. The floating potential magnitudes deduced for different density ratio n_s/n_0 of the supra thermal to thermal electrons are plotted in figure 3.9. For the non-zero drift

condition, the floating potential values from the model replicates the experimental results seen in figure 3.7 for density ratios between $5-20\%$. The floating potential values at 0.8 Pa range from 35 to 55 V with 20 eV supra-thermal electrons. For the condition $v_d = 0$, floating potentials show lower magnitudes but are comparable with the negative floating potential of the probe from figure 3.7 because $V_{probe} = V_p - V_{fl}$, and the plasma potential is between 10 and 20 V as measured by the probe

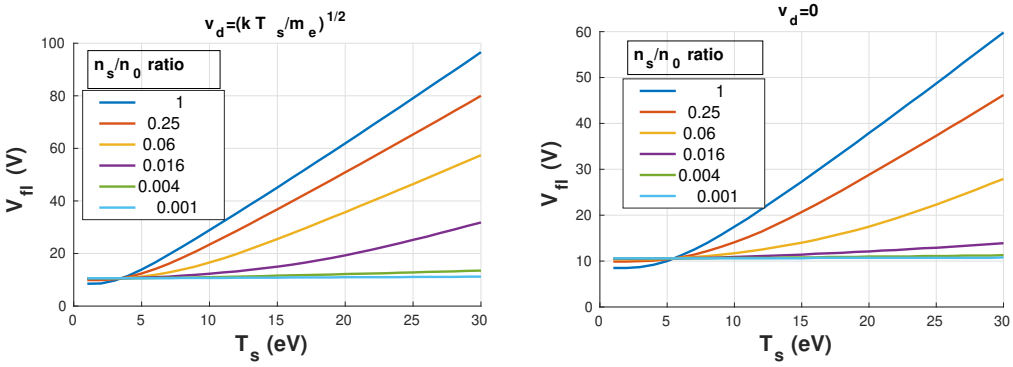

Figure 3.9: Floating potential from the model for different supra thermal to thermal electron population ratios (n_s/n_0) for (a) $v_d = \sqrt{kT_s/m_e}$, (b) $v_d = 0$.

3.2 PIC Simulation of the Electron Energy Distribution Function in a RF Magnetized Plasma Column Connected to a Tilted Electrode

As seen in the last section of this chapter, a tilting electrode allows to change the angle of the active RF surface with respect to the magnetic field. At grazing angles some very negative floating potentials (figure 3.7a) have been measured [61] with a RF compensated Langmuir probe [55].

The first hypothesis for this observed behaviour was that it might be due to the bad RF compensation due to the probe. The floating probe measurements showed that the effect of RF noise is smaller as explained in the last chapter. Another possible reason was due to the drifting of electrons in the plasma. To check the effect of the drifted electrons on the observed behavior, the IVs taken at different Y positions using the normal probe tip and the modified probe tip is compared for a 1.2 Pa argon discharge, 35W couple RF power and at 0.1 T magnetic field, see figure 3.10. The details of the modified probe tip is provided in Chapter 2. Since the direction of the drift should be in different direction due to the change in direction of electric fields inside the plasma, there should be a significant difference in the probe measurements made using normal probe tip and the modified probe tip. Since the collection area of the probe tip is reduced by half, the ion and electron current is reduced, and no effect of drift is observed while comparing the IVs.

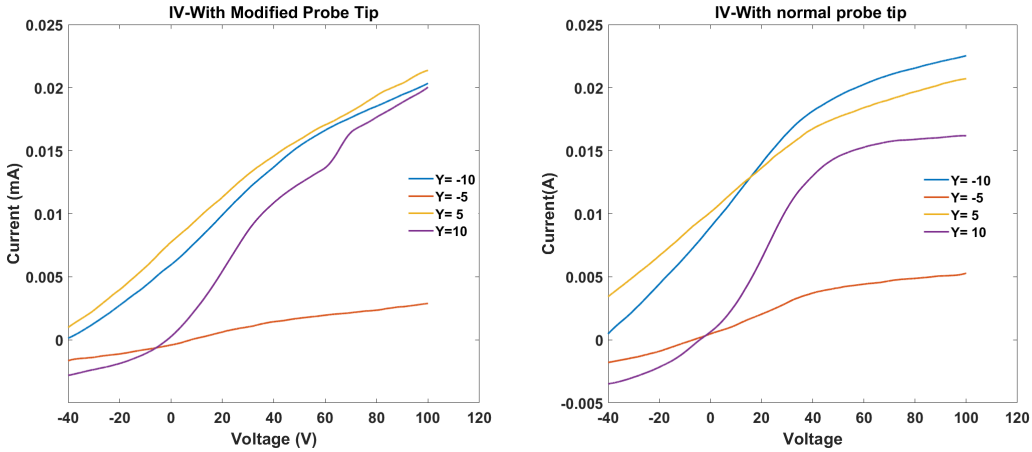

Figure 3.10: IV curves corresponding to near or inside the magnetic flux tube using modified probe tip and tungsten probe tip (normal probe tip).

The third hypothesis is a bi-Maxwellian distribution with supra-thermal electrons [50] as explained in the previous theoretical model. This implies that electrons have

been highly accelerated by the grazing electrode due to stochastic heating [39].

3.2.1 PIC Simulations

To test the last assumptions, some PIC simulations have been run, scanning the RF voltage, the bias DC voltage on the electrode, the plasma density and the tilt angle of the magnetic field with respect to the active RF surface as sketched in figure 3.11a.

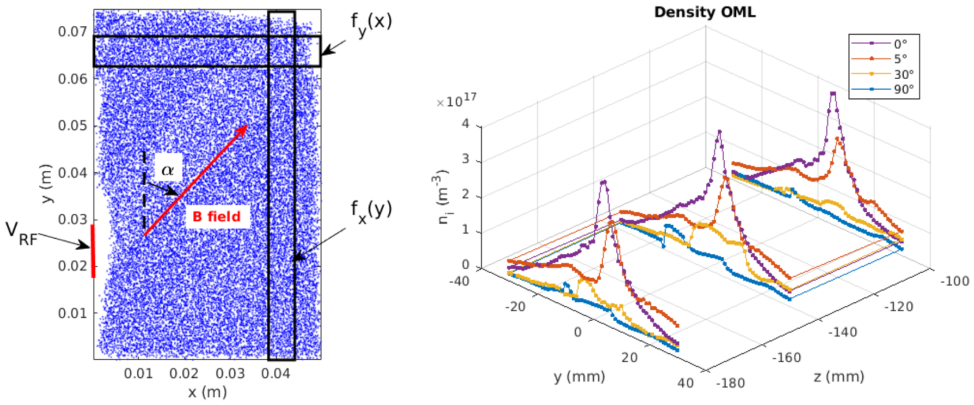

Figure 3.11: (a) PIC simulation box (b) Density profiles at different probe positions (z is the distance between the probe and the electrode center)

The GPUPIC code is based on a Matlab script with specific CUDA functions running on a RTX6000 GPU with 24 GB of memory. It is able to run up to 67 millions super-particles. The code is quite simple, no collision, no ionization, FFT electrostatic solver, Lorentz integrator is a Tajima implicit method, ion or electron number can be chosen as constant in the box to allow negative biasing of the plasma. The PIC code has been compared to Xoopic [93] simulations with exactly the same conditions to be validated. In both cases (Xoopic and GPUPIC), a 100x50 cells rectangular box has been simulated in a Helium plasma at B=0.1 T. Many diagnostics have been compared (velocity distribution, potential map and profiles, potential as a function of time...), but only density profiles are shown here in figures 3.12. It can be seen that electron and ion densities are very close for each code (Xoopic and GPUPIC).

The GPUPIC code is able to simulate rather large area of magnetized plasma : here 7.5 cm height by 5 cm width. The plasma density is either 10^{15} or $10^{16} m^{-3}$, which is lower than the experimental density, measured by a Langmuir probe using Orbital Motion Limit (OML) method [94], in the core plasma (few 10^{17} m^{-3}, see figure 3.11b). But at such higher densities in the simulations, electrostatic waves grow inside the box and the whole plasma is heated so that it does not represent the thin plasma layer we observed experimentally. To do so the PIC code should include ionization and

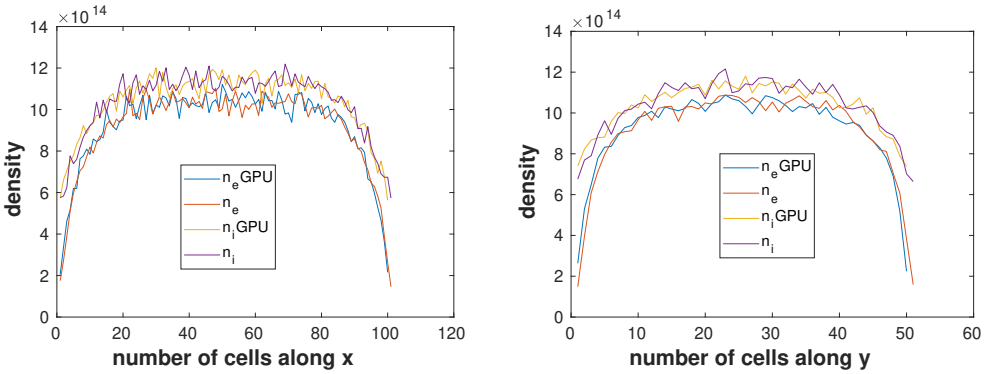

Figure 3.12: (a) Density profiles along the magnetic field (x direction) (b) Density profiles perpendicular to the magnetic field (y direction).

collisions, as it can be done in Xoopic but at a much lower speed because the code is not natively multicore. At the end, the choice has been done to keep the plasma density constant all over the box to isolate the effect of the RF electrode on the particle energy only, to prove the existence of stochastic heating only (no collisions, no ionization in the code, no electromagnetic waves).

Capacitive Coupling Results

The simulated potential maps appear in figure 3.13 for a 100 V RF voltage at 25 MHz (same as experiment) and a DC bias voltage of -100 V to simulate the self biasing of the cathode in capacitive coupling. The plasma flux tube magnetically connected to the RF electrode segment can be clearly seen as green or yellow with respect to angle in the potential map. 6 tilt angles are tested (5.7, 11.3, 26.5, 45, 63.4 and 90°). The electrode position is given by the -100 V DC bias appearing on the left side of the maps.

Other simulations have been performed for V(t)=-200+200.sin(ωt), and in direct coupling : V(t)=100.sin(ωt) and V(t)=200.sin(ωt). Only the case V(t)=-100+100.sin(ωt) is discussed here at a density of $10^{16}\ m^{-3}$ and the direct coupling scenario is presented in the next subsection. The density maps are shown in figure 3.14 for the 6 tilt angles cited before. The RF flux tube connected to the RF electrode, and following the magnetic field direction is barely visible at higher angles (above 26.5 °). As for the grazing angles (5.7 and 11.3°), there is a small density depletion in the connected RF flux tube as it can be typically seen in direct coupling discharges (see next section and [60; 19; 95]). The oscillation of the sheaths at both sides of the flux tube results in a net pumping of electrons (considering no secondary emission of the wall or electrode). While electrons move back and forth along magnetic lines, ions oscillates mainly in the perpendicular direction to conserve the total current. To compensate the lack of electrons and the neutrality, more ions are expelled from the biased flux tube, that's why this region is

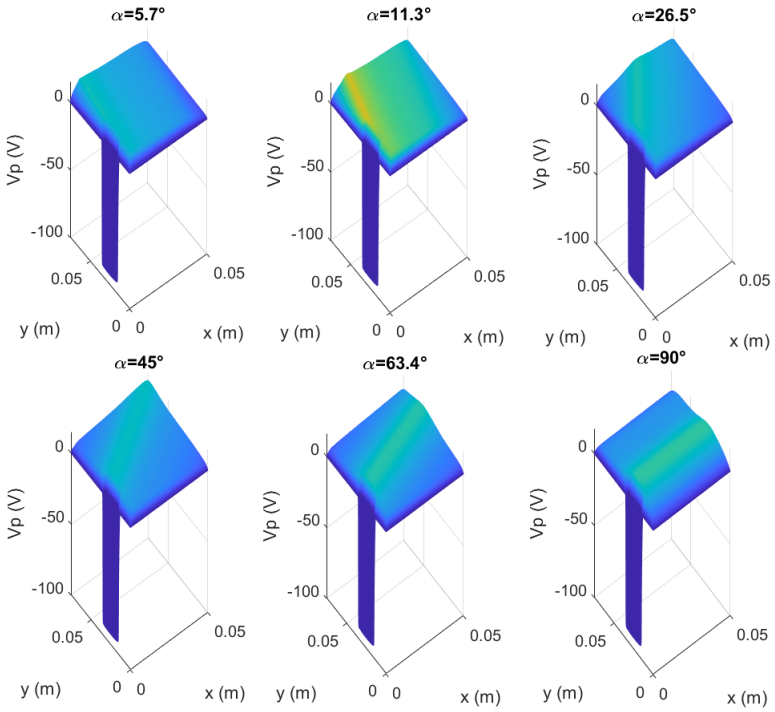

Figure 3.13: 2D maps of the plasma potential at 6 different angles between magnetic field and y direction.

depleted. However at higher angles, the plasma potential of the connected flux tube does not oscillate so much, reducing the ion outer flux and then, the depletion. The RF plasma potential of the flux tube can be seen as almost constant, reducing in the same way the perturbation on the probe measurements due to a bad RF compensation.

The Electron Velocity Distribution is shown in figure 3.15 , which is representative of what happens for the different angles under RF excitation. The reader must pay attention to the "y" labels in figure 3.15. As a matter of fact, the velocity distribution is diagnosed along y axis (v_y) or along x axis (v_x) in rectangular areas shown in figure 3.11(a). So v_y distribution is given for low angles (5.7, 11.3, 26.5 and 45) because the flux tube connected to the RF electrode only hit the upper wall for these angle values (as seen in the potential maps figure 3.13) . Beyond 45°, the RF flux tube starts to hit the right wall and then the v_x distribution is shown.

It can be seen that the initial Maxwellian distribution of v_y is only disturbed at low angles (5.7 and 11.3°) while, at 26.5 and 45°, it remains mainly Maxwellian at the same temperature. The 3 last sub-figures are plots of v_x as a function of y and are diagnosed in the vertical rectangular box in figure 3.11a. A small perturbation appears at 90° angle but is much lower than at 5.7°, meaning the acceleration process through

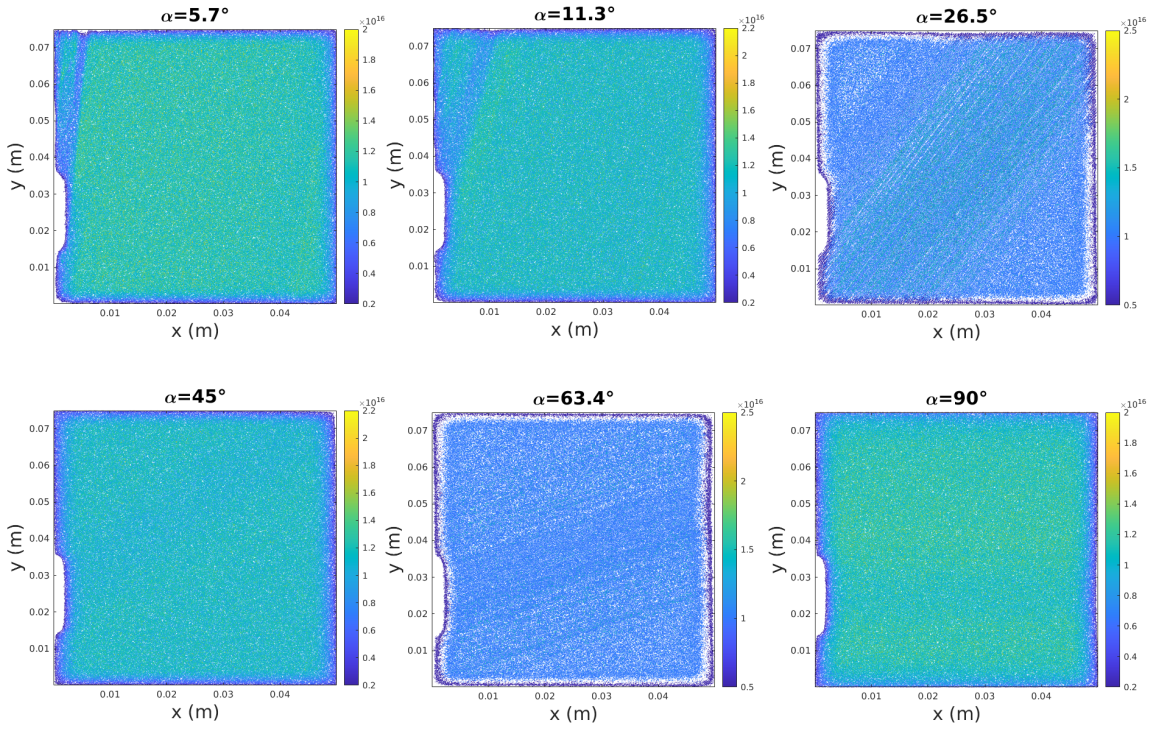

Figure 3.14: 2D maps of the electron density at 6 different angles between magnetic field and y direction in direct coupling.

stochastic heating is much more efficient at low angles. The 0° angle has not been tested in the PIC code to avoid the effect of the grounded wall because the RF electrode is aligned with the wall. The consequence of this electron acceleration is an increase of the electron flux and then an increase of the floating potential magnitude measured by the probe placed on the beam trajectory imposed by the magnetic field angle.

Both plasma potential and floating potential of a probe, V_p and V_f respectively, are plotted in figure 3.16. The floating potential as it is measured by a virtual probe, can be calculated from $\Gamma_e = \Gamma_i$ with Γ_e the electron flux and Γ_i the ion flux. The last one is given by $\Gamma_i = n.C_s$ with C_s the ion acoustic speed and n the plasma density at the entrance of the sheath, as provided by the Bohm criterion. A limit velocity v_0 can next be deduced from the electron velocity distribution calculated by the PIC code as follows :

$$\Gamma_i = n_0 C_s = \int_{v_0}^{\infty} v_e f_e(v) dv \tag{3.7}$$

The floating potential can be calculated from $V_{fl} = m_e.v_0^2/(2e)$ in the same way as

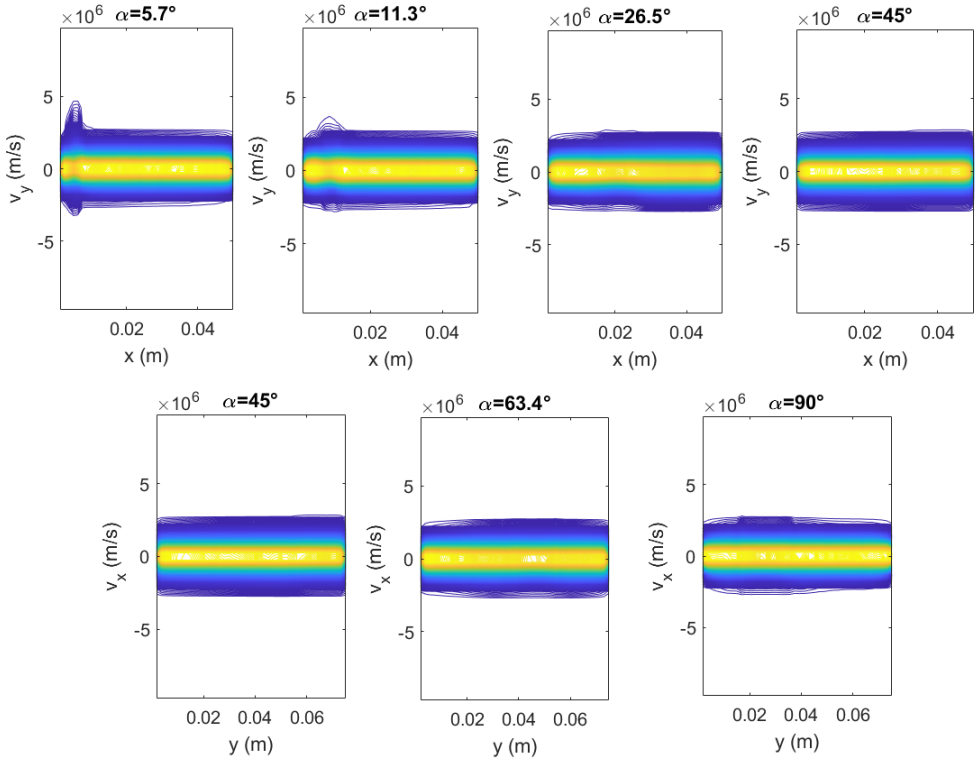

Figure 3.15: Electron velocity distribution at 6 different angles for capacitive coupling

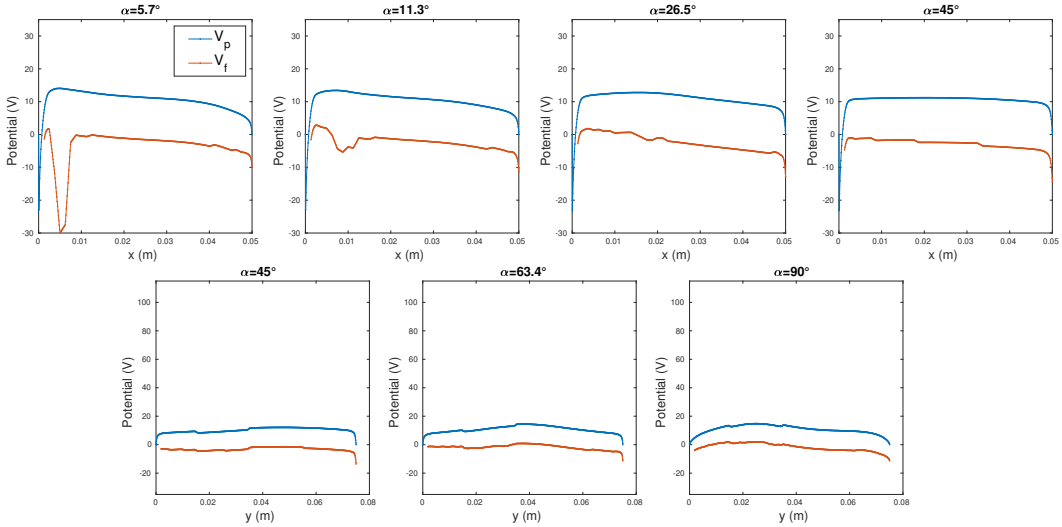

Figure 3.16: Plasma (blue) and floating (red) potential profiles at 6 different angles

in section 3.1.4. The floating potential of a probe V_f is deduced from $V_f = V_p - V_{fl}$.

At 5.7°, one can see the floating potential of the probe V_f is strongly negative (-30 V) due to high electron flux in the region connected to the RF electrode. This floating potential can be as negative as -180 V for the case $V(t) = -200 + 200.sin(\omega t)$ at low density (10^{15} m^{-3}) as shown in figure 3.17 where all RF biasings are gathered for the 5.7° angle only. The first number in the legend is the plasma density and the second is the RF potential in direct coupling when it's positive, and the DC bias potential when it's negative (knowing that the RF potential magnitude is the same as the DC potential). To be clear, 10^{15} 200 means a plasma density equal to 10^{15} m^{-3} and $V(t) = 200.sin(\omega t)$ direct coupling and 10^{16} -100 means a plasma density equal to 10^{16} m^{-3} and $V(t) = -100 + 100.sin(\omega t)$ capacitive coupling.

The velocity distribution also reveals that at 90° angle, significant perturbations can be seen at the edge of the biased flux tube. The heating, in that case, occurs in the strong perpendicular potential gradient region.

But the most spurious consequence of the electron acceleration at grazing angle is the possible generation of a hot spot on surfaces connected the active RF surfaces. Such hot spots are observed on the structure of ICRH antenna, either due to their own power or to ECRH antenna output magnetically connected to them in fusion devices. If this high energy flux hit a surface the local negative biasing can again accelerate the ions to balance the current and finally induce hot spot, sputtering and impurity generation.

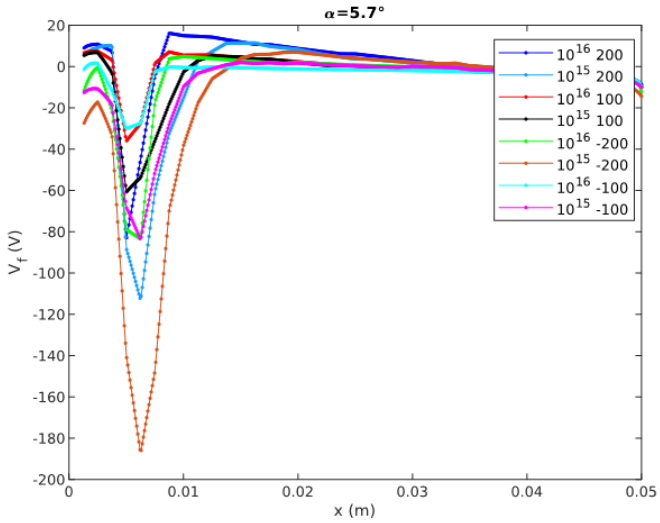

Figure 3.17: Floating potential of a probe obtained from EEDF measured in GPUPIC for direct and capacitive couplings at 2 different density values.

Direct Coupling Results

Here the discussion is on V(t)=100.sin(ωt), 10^{15} m^{-3} case. The plasma potential profile corresponding to 6 angles in the case of direct coupling obtained from the PIC model are presented in the figure 3.18. Unlike the capacitive coupling case, the time averaged RF electrode potential stays at zero because it is directly connected to the RF amplifier. As seen in the figure, the magnitude of the plasma potential in the magnetic flux tube connected to the RF electrode is higher with respect to other regions of the plasma. The averaged plasma potential values are higher compared to the capacitive coupling values.

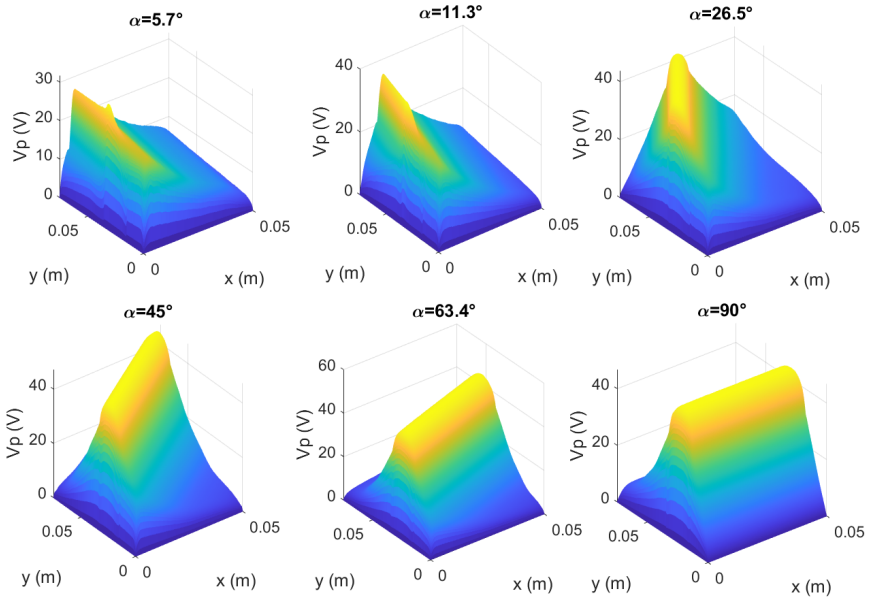

Figure 3.18: 2D maps of the plasma potential at 6 different angles between magnetic field and y direction in direct coupling.

The density maps (figure 3.19) exhibit a strong depletion of the electron density, and thus the ion density as well outside of the sheath. The RF sheath clearly appears in front of the RF electrode where no electrons are present (white area). At the other end of the flux tube, the sheath size is also larger because of the oscillation of the plasma potential in the RF connected flux tubes. This oscillation is also responsible for depleting the flux tube due to strong RF ion currents perpendicular to the magnetic field. These currents allow the parallel electron currents to be high (by current conservation) and then increase the electron pumping by the RF electrode, resulting in a net density depletion. This phenomenon is quite strong at 11.3° where the RF flux tube is totally blank, all electrons have been expelled. This effect can be observed also for all over

angles, but at 63.4 and 90°, the density depletion is a little bit higher in the region magnetically connected to the edges of the electrode, where the transverse potential gradients are quite strong. This corresponds to the highest transverse ion currents, proportional to the transverse electric field [19].

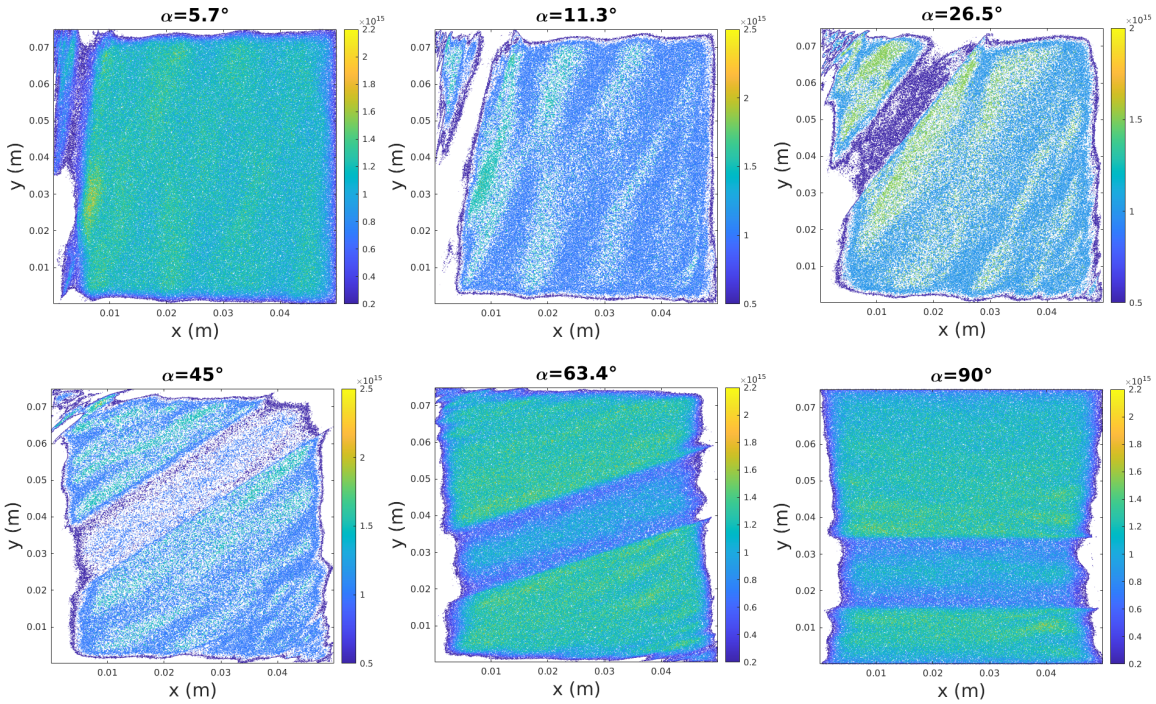

Figure 3.19: 2D maps of the electron density at 6 different angles between magnetic field and y direction in direct coupling.

As seen in the previous capacitive coupling case, the velocity distribution is highly perturbed from the classical Maxwellian to a long tail distribution function at lower angles (5.7 and 11.3°), see figure 3.20. Unlike the capacitive coupling case, the velocity distribution is affected by the influence of the electrode at higher angles as well (up to 26.5°) but the disturbance stays much lower than for the grazing angles. This difference from the capacitive coupling case, comes from the lower plasma density (10^{15} instead of 10^{16} m^{-3}). The electron acceleration is then higher because the larger sheath thickness allows to accelerate a bigger volume of electrons along the magnetic field lines.

The plasma potential and the floating potential of a probe are presented in figure 3.21. When $\alpha = 5.7$ and 11.3° the floating potential is highly negative (<-100 V) inside the flux tube connected to the RF electrode. This is due to the long tail electron distribution at 5.7 and 11.3°. The floating potential is directly proportional to the energy of

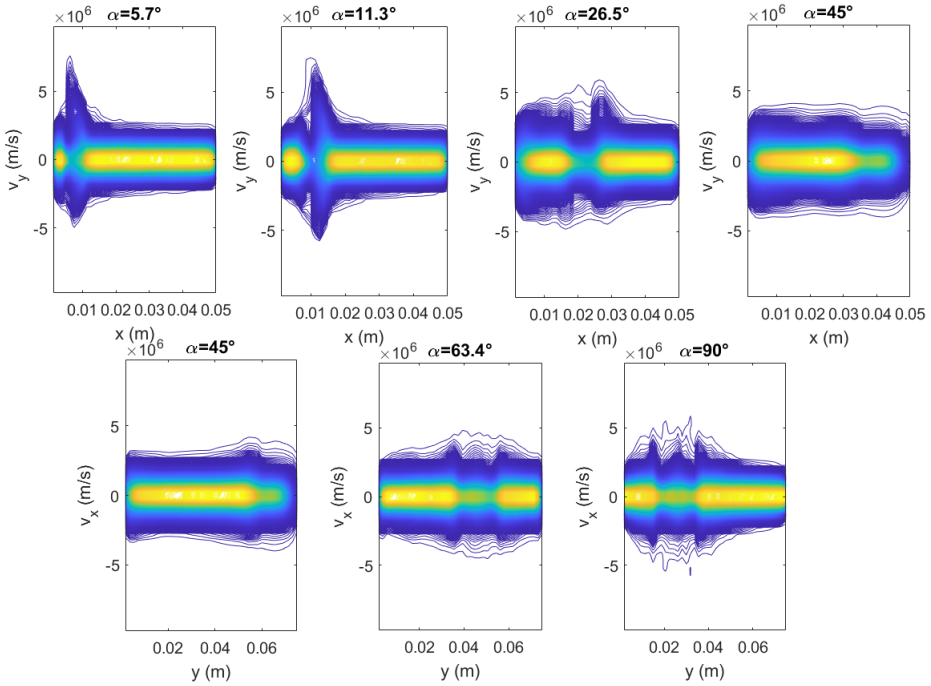

Figure 3.20: Electron velocity distribution at 6 different angles in direct coupling.

the hot electrons. At higher angles (63.4 and 90°), the plasma potential rises up to 60 V and the floating potential is here slightly disturbed by the hotter electrons, so that both profiles look the same.

To summarize, the PIC simulations of potential profiles and velocity distributions corresponding to both capacitive coupling and direct coupling showed the presence of hot electrons inside the flux tube connected to the RF electrode at grazing angles.

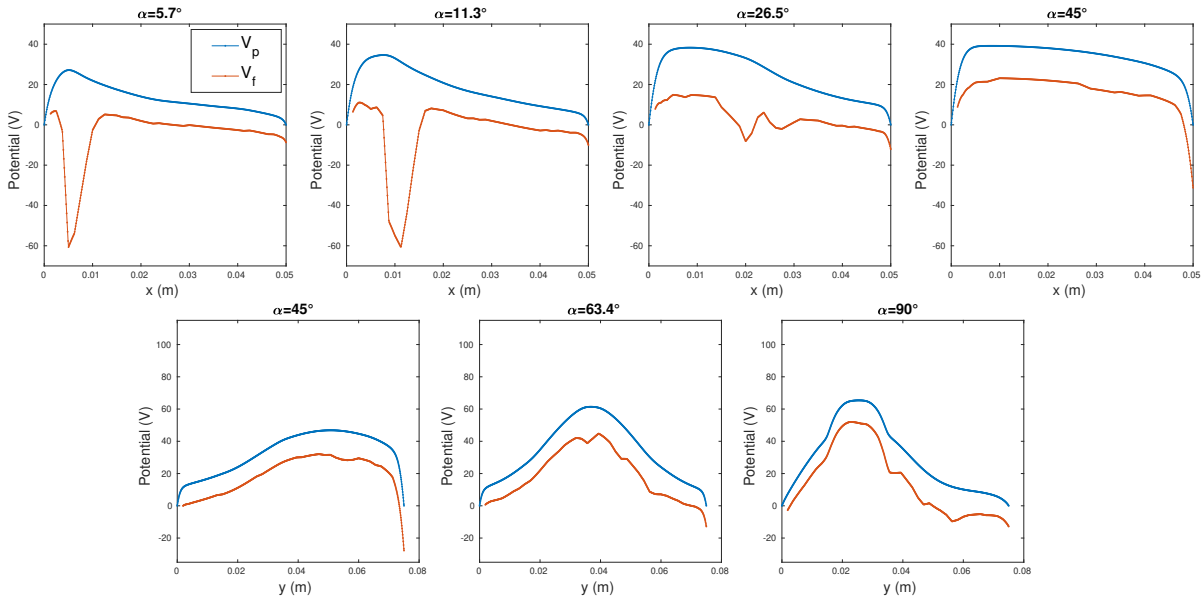

Figure 3.21: Plasma (blue) and floating (red) potential profiles at 6 different angles in direct coupling.

3.3 Conclusion

The dependence of gas pressure, magnetic field and tilt angle on the floating potential has been studied in the ALINE experiment in direct and capacitive coupling. The minimum floating potential value, -100 V, has been measured in capacitive discharge at a tilt angle (0°), highest permitted magnetic field (0.1 T) and low pressure (<1Pa) at 35 W of coupled RF power. This shift in the floating potential to more negative values is a result from accelerated electrons in the RF sheath of the electrode at a grazing angle due to stochastic heating. The combined effect of improved stochastic heating at grazing angles at lower pressures, higher confinement and higher density of hot electrons leads to highly negative floating potential values. Based on simple theoretical considerations equation the floating potential values were deduced for different fractions of hot electron population. A simple analytical model based on a 2 population distribution of electrons showed that only a tiny fraction (0.1) of fast electrons (at 20 eV) is needed to get a -50 V floating potential on a probe.

The final steps to measure the effect of stochastic heating only was the use of PIC simulations for ALINE-like conditions. The PIC code has been implemented without collision and ionization processes, avoiding ohmic heating. In the same way the solver being only electrostatic, no electromagnetic waves could be responsible for heating the plasma. It appears that the same negative floating potential values were observed at grazing angles, as seen in the experiments. In the case of a RF electrode, it appears that

the electrons are much highly accelerated at grazing angle (0-10°), which can result in high energy electron beams able to bias the connected wall or a probe at strong negative potentials. This negative biasing can next result in the acceleration of ions in the local electric field, leading to high energy ion fluxes and local hot spots as it can be seen on the structure of the ICRH antenna in Tokamaks. The study of these EEDF in front of a RF biased electrode shows that only grazing angles induce such localized energetic electrons (up to the RF magnitude in eV) which are accelerated within the RF sheath mainly in the magnetic field directions. The energy gain and the floating potential are higher at lower density (larger sheath), higher RF potential and larger negative DC self-biasing of the electrode.

Experiments and simulations are consistent with each other. In the future, the EEDF inside the flux tube can be measured using an RFEA (Retarding Field Energy Analyzer) probe.

Chapter 4

Positive Self-bias and Sheath Reversal in Magnetized Asymmetric RF CCP Helium Discharge

Contents

4.1 Positive Self-Bias in a magnetized RF plasma discharge 74

4.1.1 Introduction 74

4.1.2 Experiment 75

4.1.3 Model 75

4.1.4 Observations and results 78

4.2 Experimental observation of sheath reversal in magnetized asymmetric RF CCP Helium Discharge 83

4.2.1 Introduction 83

4.2.2 Setup and Experimental Parameters 84

4.2.3 Model : IV analysis in case of hot and cold electron population 84

4.2.4 Results and Discussions 86

4.3 Conclusion 97

4.1 Positive Self-Bias in a magnetized RF plasma discharge

4.1.1 Introduction

Capacitive coupled plasma discharges are one of the widely used techniques in plasma physics for processing of materials and have been thoroughly studied mainly without magnetic field [12; 9]. The addition of magnetic field to the system makes physics more complex, especially for the RF (Radio-frequency) sheath structure in front of the electrode depending on the electrode tilt angle. In unmagnetized plasma, the asymmetry between the area of the capacitive electrode and that of the grounded wall of the vacuum vessel results in a net self-bias voltage on the electrode connected to RF power supply [12], or a net direct current (DC) bias of the plasma in direct coupling discharges [20; 19]. In the case of a small active electrode and large grounded wall discharge, the self-bias is strongly negative due to the higher electron mobility. On the contrary, it can be positive when the RF electrode is much larger than the wall [3]. In most plasma devices, the DC self-bias potential is negative and accelerate ions towards the electrode, also known as cathode. This behavior is exploited in etching and sputtering applications. In high-power magnetized plasmas like in magnetically confined fusion reactors, the main goal is to mitigate the heat flux to the wall or active RF surfaces on which hot spots can dramatically damage the material [96]. At the same time, the heavier ions accelerated in the potential difference between the plasma and the wall, can sputter the wall surface and inject impurities inside the bulk plasma. Impurities generated via sputtering process can eventually induce disruptions inside Tokamaks. The magnetic field reduces the particle flux perpendicular to its direction so that the potential drop inside the sheath decreases with the magnetic field strength [39] and the tilting angle of the electrode [97; 98; 99].

The particular case when the magnetic field is perfectly parallel [28; 26] to the surface rarely happens in complex reactors such as tokamaks or stellarators, where magnetic field lines are slightly tilted with respect to the wall [100]. Nevertheless, some parts of the wall, like active antenna (or electrode in magnetrons, for instance [39]) can be quasi-parallel to the magnetic field, hence changing the boundary condition of the plasma locally.

As a result, the electric field inside the sheath at grazing angles [27; 101] can reverse at low enough electron perpendicular mobility (at high magnetic field and low collisionality). This has been observed in PIC simulations for well magnetized ions, i.e. $\varepsilon = \rho_i/\lambda \ll 1$ where ε is the gyroradius to mean free path ratio for ions [102; 103] . It occurs as soon as the ion flux is larger than the electron flux, leading to a positive bias of the wall with respect to the plasma.

In the same way, the self-bias of an RF capacitively coupled electrode parallel to

the magnetic field could be positive despite of the perturbations due to the oscillating sheath which enhances microinstabilities and stochastic heating [39]. The possibility of a positive self-bias on the active RF electrode has been already reported in magnetron systems using the magnetic asymmetry effect [104]. In the present work, a general case study in a system with a uniform magnetic field has been explored, a situation of practical interest in various configurations. Here, the positive biasing has been observed with a one-face RF electrode and investigated as a function of gas pressure, magnetic field, RF power and tilt angle of the electrode for well-magnetized electrons and almost unmagnetized ions (Table 1).

4.1.2 Experiment

The experiments have been held in ALINE for a wide range of plasma parameters. For the present study, the pressure varied from 0.25 Pa to 3 Pa, the strength of the magnetic field from 0.01T to 0.1 T, and the input RF power from 10 to 180 W for angles ranging from 0-90°. Power from the RF generator is coupled to the plasma using the RF electrode via a matching box at the frequency of 25 MHz. The coupled RF power, RF voltage and current are measured using an Octiv Mono IV probe from Impedans. DC self-bias developed on the RF electrode was measured using a probe connected to the electrode through an inductor of high inductance to reduce the RF perturbations in the system. The rotor to which the RF electrode is attached enables its rotation along its diameter, defining (α) an angle with the axial magnetic field (Figure 4.1). The experiments have been performed by covering the lateral side and one of the circular faces of the tungsten electrode with ceramic to limit the particle flux to the electrode. In this configuration, at $\alpha = 0$, the flux of particles perpendicular perpendicular to the magnetic field can only reach the powered surface of the RF electrode.

4.1.3 Model

The ion and electron fluxes to the RF electrode can be modelled to deduce the angle at which the averaged sheath collapses, meaning the DC potential drop in the sheath is zero, and the collected ion and electron fluxes are naturally equal. Due to the presence of the magnetic field, the parallel and perpendicular fluxes to the electrode have to be calculated separately as a function of the tilt angle of the electrode. Considering a homogeneous plasma density and magnetic field, with some poorly magnetized ions ($\omega_{ci} \leq \nu_{iN}$) and well magnetized electrons ($\nu_{eN} \ll \omega_{ce}$), with $\omega_{ci,e}$ and $\nu_{i,eN}$ the ion and electron cyclotron frequencies and ion and electron-neutral collision frequencies, the ion flux is merely Bohm flux but electron flux has parallel and perpendicular components. The last component is mainly driven by electron-neutral collisions through the perpendicular mobility $\mu_\perp$ [3] and the perpendicular electric field $E_\perp$ in the RF sheath : $E_\perp = \bar{E} + \tilde{E}\sin(\omega t)$, with the driving RF amplitude $\tilde{E}$ and the DC component

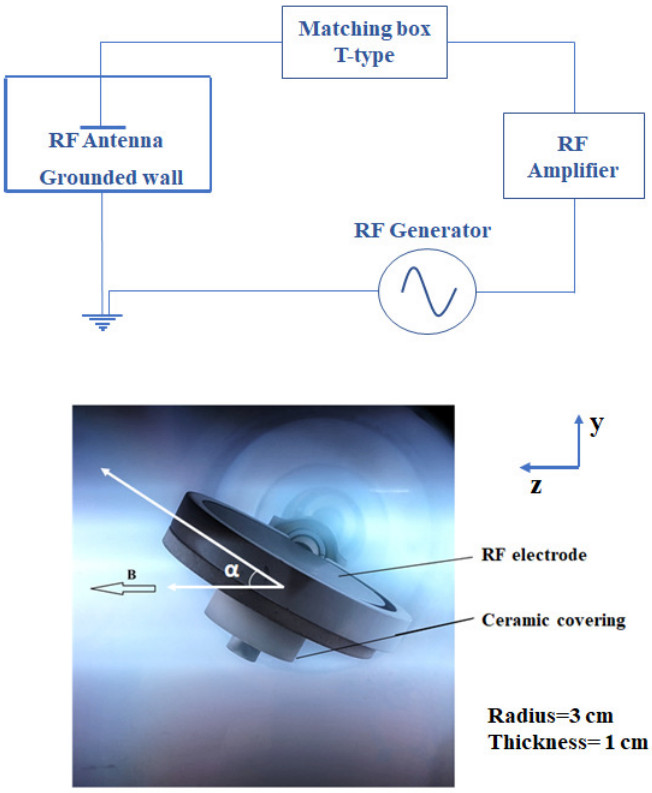

Figure 4.1: Schematic of the RF circuit and picture of the RF electrode in ALINE.

$\bar{E}$ due to the self-bias of the capacitive electrode. The diffusion due to density gradients and the drift velocities (E×B and diamagnetic drift) are neglected here. In the whole modelling, the plasma potential is assumed to be close to zero (actually of the order of the plasma floating potential), which usually occurs in unequal capacitive discharges [12]. Finally, the parallel electron flux connected to the electrode can be estimated directly (Chodura model [99]) for an angle α, but another component has to be taken into account for zero angles. All electrons closer than two electron gyro radii $2r_L$ will intersect the electrode surface so that the electrons in the layer of thickness $2r_L$ above the surface will be collected [105]. In the end, equating ion flux (Γ^i) and electron flux, it follows :

$$\Gamma^i = n\mu_\perp E_\perp + \Gamma^e_\parallel \left(\frac{4r_L}{\pi R} + \sin\alpha \right) \tag{4.1}$$

with n the plasma density, $\mu_\perp = \mu/(1+\frac{\omega_{ce}^2}{\nu_{eN}^2})$ with ω_{ce} and ν_{eN} the electron cyclotron and electron-neutral frequencies, $\Gamma^e_\parallel = nc_e$ [100] with $c_e = \sqrt{\frac{k_B T_e}{2\pi m_e}}$, k_B the Boltz-

man constant, T_e the electron temperature, m_e the electron mass. R is the electrode radius.

From this equation, the angle at which the ion and electron fluxes are equal can be deduced. According to the literature, [27; 101] this angle is usually less than 5°, so that $\sin(\alpha)$ can be approximated as α. Assuming that $\Gamma^i = nC_s$ with C_s the Bohm velocity :

$$\alpha = \frac{C_s - \mu_\perp < \tilde{E} >}{c_e} - \frac{4r_L}{\pi R} \tag{4.2}$$

In this equation, the DC component of $E_\perp$, i.e. $\bar{E}$ is null because the DC self-bias of the electrode is supposed equal to the DC plasma potential, which means there is no DC sheath potential drop. Electrons can be accelerated towards the electrode surface by the RF electric field during half a period (when the electric field is directed towards the electrode surface). Then the time average effective electric field over 1 period is $< \tilde{E} >= \frac{1}{2}\int_0^{T/2} \tilde{E} sin(\omega t) dt = \tilde{E}/\pi$. The electric field can be simply deduced from $\tilde{V}/s$ with s the sheath thickness defined by the Child-Langmuir law as follows :

$$s = \gamma \lambda_{De} \left(\frac{V_{rf}}{T_e} \right)^{3/4} \tag{4.3}$$

The Debye length λ_{De} depends on the plasma density at the entrance of the sheath, V_{rf} is the amplitude of the rf potential and γ is a coefficient which has been chosen at 0.4 to match the experimental measurements. Due to their higher mass, ions do not respond to the high frequency RF oscillations, and therefore they are not accelerated in the RF electric field of the sheath, while the DC part is supposed to be 0, so that they are neither accelerated nor repelled. Hence the ion flux can be simply expressed as the classical Bohm flux. The results have been compared to the experiments in the next sections. Similar observations on the angles have been reported already in the case of tokamak plasmas with a cross-field anomalous diffusion [101] and in the case of pure ambipolar diffusion in higher collisionality plasmas [27]. These angles apply in steady-state plasmas, not in the case of an RF-driven sheath. Another crucial parameter is the B (magnetic field in Tesla) and p (the pressure in Pa) pair, in the case of a straight electrode ($\alpha = 0$) for which the DC self-bias is zero. To obtain these parameters, the following polynomial needs to be solved.

$$\nu_{eN}^2 - \nu_{eN} \frac{e\tilde{E}}{m_e \left(C_s - c_e \left(\frac{4r_L}{\pi R} + \alpha \right) \right)} + \omega_{ce}^2 = 0 \tag{4.4}$$

There are two solutions for this equation, but the acceptable one is the one which satisfies $\nu_{eN} \ll \omega_{ce}$, in which the electrons remain well magnetized, which is one of the main assumptions of the model. The corresponding pressure $p = n_g k_B T_g$ is the neutral gas pressure and $\nu_{eN} = \sigma n_g v_{T_e}$, where σ is the electron-neutral cross-section, n_g the

neutral gas density, T_g the gas temperature and v_{Te} is the thermal electron velocity; and the magnetic field B is deduced from $\omega_{ce} = eB/m_e$. The main unknown in this equation is the amplitude of the RF electric field inside the sheath. It can be measured experimentally [106] or calculated from the RF electrode potential and the sheath size. The sheath structure can be complex in the presence of a magnetic field. At oblique angles higher than the Chodura angle, the sheath is composed of a magnetic presheath, where the potential drop is still negative (which means the wall is negative with respect to the plasma potential). At grazing angles, the sheath can collapse [101; 27], hence its thickness depends on either the Debye length for $\omega_{pi} > \omega_{ci}$ or the ion Larmor radius for $\omega_{pi} < \omega_{ci}$; always assuming well-magnetized electrons [26; 28]. The electric field inside the sheath can be as high as several thousands V/m in a non-RF sheath [106; 27], and it can be much higher in a driven RF sheath in front of a capacitively coupled electrode (up to 10^5 V/m depending on the RF power and the plasma density).

4.1.4 Observations and results

The main parameters of the He plasma column in ALINE are displayed in table 1. The plasma is highly non-uniform along the y-direction due to 1) the active RF electrode being at the centre of the chamber, and 2) one of the circular faces and the lateral side of the electrode covered with the ceramic shield. The magnetic field confines the electrons along a thin layer above the active surface of the electrode in which the density can be 10 times higher than the surrounding plasma.

Table 4.1: ALINE plasma parameter.

Quantity	Ions (He^+)	Electrons
Density(n)(m^{-3})	$1-60\times10^{16}$	$1-60\times10^{16}$
T (eV)	0.026	3-6
$\lambda_{mfp}(cm)$	1.50	1.4-5.2
$\nu_c\ (s^{-1})$	380×10^3	3×10^9
$\nu_p\ (s^{-1})$	$7-23\times10^6$	$635-2000\times10^6$
$\omega_c/\nu_{(e/i)N}$	0.1-5.6	17-967

Effect of pressure and magnetic field

The pressure values and the magnetic field varied from 0.3 to 3 Pa and from 0 to 96 mT, respectively. Considering a cross-section of $5\times10^{-19}\ m^2$ for electron-neutral collisions, the magnetization parameter ω_{ce}/ν_{eN} for electrons varies from 17 to 967 and for

ions from 0.1 to 5.6 showing the poor magnetization of ions except at “high" magnetic field and low pressure. The RF power coupled to the plasma is around 35 W. Figure 4.2 shows a ‘Makuma’ interpolation of 6 by 4 points formed by pressure and magnetic field scans. In 3/4 of the domain (low magnetic field and high pressure), the self-bias is negative like usually measured in most experiments. But at a high magnetic field and low pressure (0.3 Pa and 96 mT), the self-bias becomes positive up to values of 55 V. The points where the electrons and ion currents to the electrode are equal (i.e. self-bias null), estimated from the model, are represented by the black curve in the figure. The inputs to the analytical model are the cyclotron frequency, the electron-neutral collision frequency, and the electric field inside the RF sheath, which depends on the electrode RF voltage and also the plasma density (from which the sheath thickness can be measured using Child-Langmuir law). The experimentally measured plasma density using the Langmuir probe via OML theory is between 5×10^{16} and 5×10^{17} m^{-3}. Hence the corresponding sheath size is less than 1 mm for an RMS RF potential of 100 V, yielding an electric field of the order of 10^5 V/m inside the sheath. The RF voltage at the electrode or the output of the matching box between the RF amplifier and the electrode is measured using the Octiv RF power meter, and it is in the range of 45 to 283 V. In the model, the electric field input is equal to 1.1×10^5 V/m to match the 0 V isopotential in figure 4.2, which is consistent with the experimental values. Of course, this is a constant value taken for all the domains, but varying the pressure results in density variation as well, hence changing the current collected by the electrode and, in the same way, the RF potential since we operate at constant power. (P,B) pairs at which self-bias values are zero (denoted by * in figure 4.2) have been added to check the experimental electric field operating along the isopotential = 0. These 3 measurements show an electric field of 1.5×10^5, 4.3×10^5 and 4.8×10^5 V/m at pressures of 0.44, 1.2 and 1.5 Pa and magnetic field of 0.05, 0.075 and 0.08 T respectively. The densities deduced from OML (which usually overestimates the density) are between 4×10^{16} and 4×10^{17} m^{-3}. The electric field value taken in the model (1.1×10^5 V/m) is thus at least 1.5 times lower than those deduced from measurements, but according to the wide uncertainties in the density and RF potential across the sheath, the trend of the model is quite good. Finally, along with this isopotential, the magnetization parameter ω_{ce}/ν_{eN} does not vary much, from 60 to 90 for electrons, which makes this parameter a consistent one to characterize the 0 V biasing.

Effect of the RF power

Several studies have already reported a linear increase in the magnitude of the self-bias voltage with input RF power/voltage [104; 107]. Here, the variation of the self-bias with the coupled RF power has been studied for four different gas pressures at 0.096 T (Figure 4.3). A linear decrease in the self-bias values was observed with increasing the coupled power from 3 to 120 W (corresponding to RF voltage from 40 to 300 V),

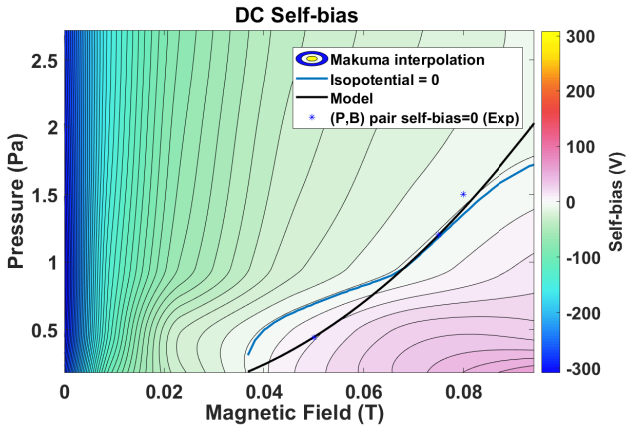

Figure 4.2: Interpolated plot of variation of DC self-bias voltage with gas pressure for different magnetic field (He gas, 25 MHz, 35 W coupled RF Power). The black curve depicts the predictions for null self-bias given by our model and blue stars are the experimentally verified (P,B) pairs for null self-bias.

except at the lowest pressure measurement, which is in accordance with the previously reported studies [107]. For 0.3 Pa measurements, the self-bias voltage increases first, reaching a maximum and then decreases linearly. As the coupled power increases, the electron flux (according to the presented model) increases due to its acceleration in the RF electric field inside the sheath, which explains the observed trends at higher pressures. At low pressures, the increase in the RF power enhances the plasma density, and at 0.1 T, the mobility of electrons across the magnetic field is lower compared to that of ions. This explains the maximum positive biasing (57 V) at 74 V RF voltage.

Effect of the tilt angle

In the next study, the angle between the electrode and the magnetic field has been varied from 0° to 90° for four different magnetic field values (0.024 to 0.096 T). Since the lateral and one of the circular sides of the electrode are covered with ceramic, at 0°, the total flux to the electrode is only due to the perpendicular mobility and the contribution due to the gyration of electrons (the electrode collects all the electrons in the layer of thickness of Larmor radius above it). At 0.1 T, the DC potential developed is still positive for grazing angles, but as the tilt angle increases from 0 to 5°, there is a significant fall in DC self-bias voltage (Figure 4.4). The minimum value of the self-bias is surprisingly at the tilt angle of 20°.
A possible explanation for this non-monotonic behaviour is the following : At grazing angles, the stochastic heating is proportional to the sheath velocity (see section 1.7.7) here along the magnetic field lines because electrons are well magnetized and can only go out of the electric field of the sheath by transiting axially, which means

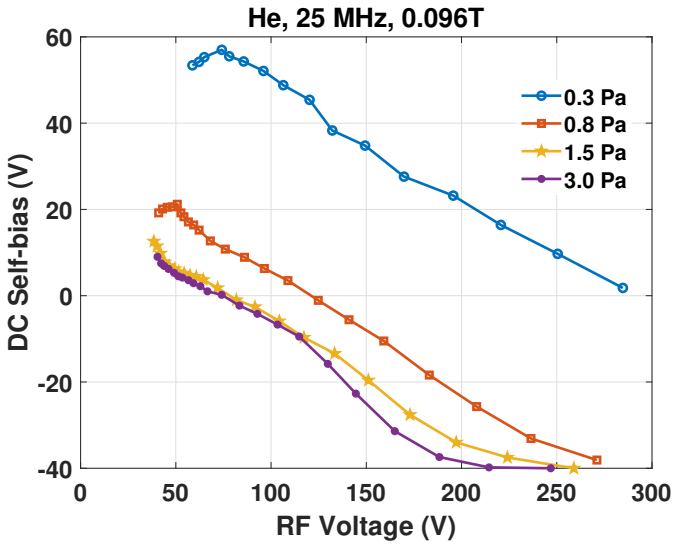

Figure 4.3: Variation of DC self-bias voltage with RF voltage on the electrode surface when the RF electrode is parallel to the magnetic field.

they are accelerated all along the diameter of the electrode . The energy gain of these hot electrons is then close to the maximum RF potential [62]. The self-bias of the electrode is proportional to the electron flux, which is proportional to electron temperature. As a result, the minimum self-bias appears at an angle which is low enough to create these hot electrons and high enough to increase the collecting surface of the electrode. There is an optimum angle at which the electron temperature and the collecting surface are high. While increasing the angle further up to 90°, hot electrons disappear because the electric field inside the sheath tends to be parallel to the magnetic field, so that the sheath velocity (as expressed in the stochastic power equation in section 1.7.7) decreases. Electrons are quickly ejected from the sheath, gaining less energy. This decreases the self-bias while the collecting surface does not vary so much between 45 and 90°. Similar observations have been reported already for a steady-state collisional plasma with an ambipolar model and PIC simulations in [27].

In the last study, the tilt angles at which self-bias is zero for different gas pressures and RF powers have been measured experimentally and compared with the theoretical predictions in figure 4.5. For three different gas pressures (0.3, 0.6 and 1 Pa) and a range of power from 10 to 120 W (corresponding to RF voltage between 50 and 300 V), the zero self-bias was observed at tilt angles lower than 4°, which is in agreement with predictions from the model based on equation 4.2. These angles shift to lower values with increasing power. At lower voltage values, the tilt angle deviates from the prediction. This seems to be due to the non-uniformity of the plasma density and the deviation of the electron distribution function from the Maxwellian at lower pressures.

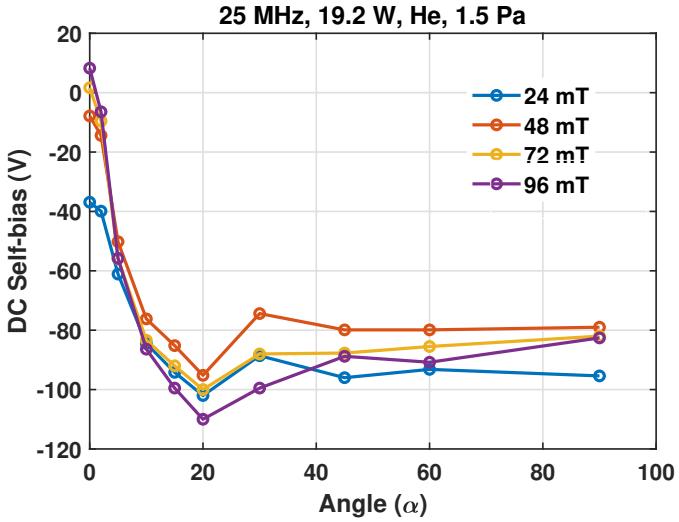

Figure 4.4: Variation of DC self-bias voltage with angle of electrode (He gas, 1.5 Pa, 25 MHz, 19.2 W coupled RF power) when the RF electrode is parallel to the magnetic field.

It has been observed in the density measurements for the tilted electrode configuration that the high-density region are magnetically connected to the top side of the RF electrode, as seen in figure 4.1. Unmagnetized ions diffusing from this high-density region to the electrode surface can be one of the reasons for positive self-bias of the electrode even at higher angles. Electron temperature measurements using the Langmuir probe above the surface of the RF electrode are not easy due to the stochastic heating and generation of hot electrons at grazing angles. A small population of hot electrons can shift the floating potential to large negative values and the estimation of high electron temperatures (as seen in the previous chapter). In a sake of simplicity, the average value of the electron temperature is still considered to be 3 eV for the whole modelling part. The inputs to fit the experimental curves using the analytical model have been taken from the Langmuir probe (Density) and RF power meter data to estimate the RF voltage and hence the electric field within the sheath in front of the RF electrode. It should be noted that the maximum error on the measured angle is 0.2°.

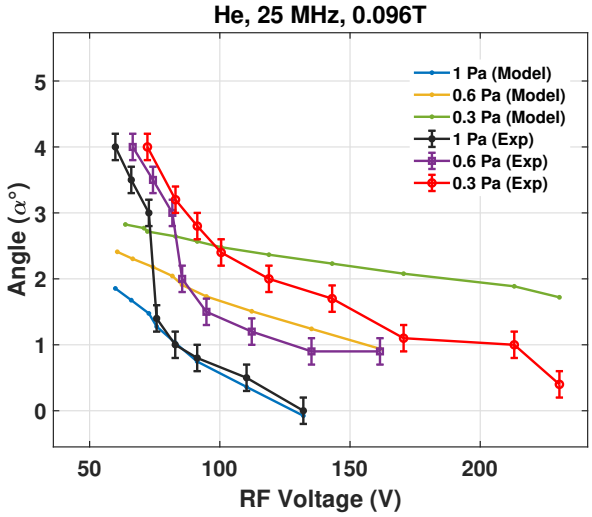

Figure 4.5: Angles at which the self-bias voltage developed is zero as function of coupled RF power for a fixed magnetic field and gas pressure.

4.2 Experimental observation of sheath reversal in magnetized asymmetric RF CCP Helium Discharge

4.2.1 Introduction

While experimenting with a tungsten electrode with a ceramic covering its lateral and bottom sides, eliminating the parallel flux of electrons to the surface of the electrode, we observed positive DC self-bias voltage on the surface of the RF electrode. But a positive self-bias does not necessarily mean reversed sheaths (or electronic sheaths by opposition to ionic sheaths).

The reversed sheath has been explored in the case of an electron-emitting surface through various simulation approaches by [108; 109; 110; 111]. Wang et al. observed the reversed sheath experimentally for the case when the surface is emitting a higher number of electrons compared to the plasma electron density for a surface in space [112]. This is not applicable in ALINE's case since the electrode is not an emitting surface. When the mobility of electrons is limited and ions are mobile, reversal of the potential drops inside the sheath has been explored using PIC and fluid simulation by Moritz et al. and Kushner [27; 29].

To diagnose such a sheath reversal, the plasma potential at the entrance of the sheath must be well known while the self-bias of the electrode is measured with a good accuracy. It is unfortunately not the case of the plasma potential measurement via the Langmuir probe. As it will be shown in the following sections, the IV charac-

teristics have to be carefully analysed using a double probe modelling to make appear 2 populations of electrons and find out the good plasma potential. Such analysis will be presented through 3 different cases at low pressure and low RF power, which are the most favourable condition to make appear the reversed sheaths.

4.2.2 Setup and Experimental Parameters

Experiments were carried out for two different gas pressures, 0.3 Pa and 0.6 Pa, at a 0.1 T magnetic field, when the electrode is parallel to the axial magnetic field ($\alpha = 0°$). Langmuir probe measurements were carried out near the surface of the RF electrode, to be able to measure the plasma potential close to the sheath entrance. 2D profiles were taken along the plane perpendicular to the direction of the magnetic field (X-Y) for the two gas pressures also along the X-Z plane thanks to the 3D manipulator. In the present study, the measurements were taken for each 3 millimeters above the RF electrode along the X axis from the X position -30 to +30, Y position ranging from +8 to 30 mm for Z=30 mm for every 2 mm, where the center of the RF electrode (0,0,0). Plasma parameters retrieved from the probe measurements for the present study are tabulated in the Table 4.1. The DC self-bias developed on the surface of the RF electrode is measured using the voltage probe connected to the output of the matching box.

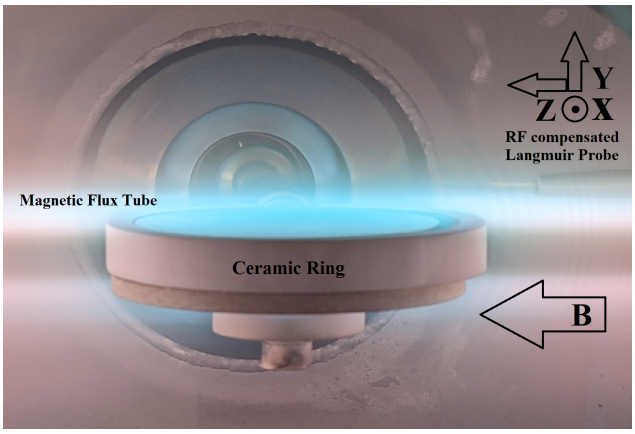

Figure 4.6: RF electrode with ceramic and the plasma around the electrode in ALINE device.

4.2.3 Model : IV analysis in case of hot and cold electron population

Langmuir probe measurements in a magnetized environment can be very challenging because of the reduction of the electron current due to the magnetic field, probe sheath

boundary effects and RF perturbations etc.[113; 53; 114; 115; 50]. When there is a deviation of the electron population from the Maxwellian distribution to bi-Maxwellian or shifted Maxwellian the analysis becomes more difficult [40; 116; 117].

But, in a magnetized plasma, Langmuir probe measurements can be fitted using an asymmetric double probe model [45], because of the saturation of both ion and electron currents at the left and right sides of the IV characteristics. For a symmetric double probe model, the current is of the form of a hyperbolic tangent, but in the case of an asymmetric characteristic, this modelling reads as follows

$$I = I_0 \frac{1 - exp(\frac{\phi - V_{f1}}{T_{e1}})}{1 + \frac{s1}{s2} exp(\frac{\phi - V_{f1}}{T_{e1}})} \tag{4.5}$$

S1/S2 is the ratio of the ion and electron saturation currents and the ratio decreases with increasing magnetic field. Such a theoretical model can nicely fit the IV characteristics we measure with the Langmuir probe in a magnetic field. From the first derivative of the characteristics, one can see there are two populations of electrons. It is then possible to fit double temperature characteristics based on the model above :

$$I = I_1 \frac{1 - exp(\frac{\phi - V_{f1}}{T_{e1}})}{1 + \frac{s1}{s2} exp(\frac{\phi - V_{f1}}{T_{e1}})} + I_2 \frac{1 - exp(\frac{\phi - V_{f2}}{T_{e2}})}{1 + \frac{s1}{s2} exp(\frac{\phi - V_{f2}}{T_{e2}})} \tag{4.6}$$

A sample characteristic based on the above equation corresponding to a plasma with two populations of electrons is shown in figure 4.7 where hot electron to cold electron mixture ratio equal to 3:1, with hot and cold electron temperatures of 25 eV and 8 eV respectively. Here I_h, I_t, I_{t+h} are sample IV curves corresponding to the hot and thermal electrons and their sum respectively. These plots are shown to illustrate how a double electron population can be identified in IV characteristics presented in the next sections. The following parameters have been chosen arbitrarily as an illustrative example. The ratio of ion saturation currents corresponding to the hot to cold electrons is 2.25, the peak electron current for hot electron population is 6.6 times than that of the cold electrons, and the floating potential for both hot and cold electrons curves are negative, -53 V and -45 V respectively.

The 5 parameters deduced by the non-linear fitting method (nlinfit - Matlab function) will be I_1 and I_2, the current of both electron populations, T_1 and T_2 their temperature, and V_{f2} the floating potential for the thermal population, V_{f1} being provided by the measured IV.

The first derivative of the obtained IV curve, the model curve (I_{t+h}) and the first derivative of both hot and thermal electron population are depicted in the figure 4.7*b*. The peak of the first derivative corresponding to hot electrons is at -31.15 V and the second peak (bump in the effective curve) for the cold electrons is at + 1.5 V. As mentioned before, the second derivative of the curve has no zero crossing corresponding

to the resultant IV curve, which makes determination of the plasma potential difficult. The results obtained from the fitting of the curves are discussed in subsection 4 with the Langmuir probe results.

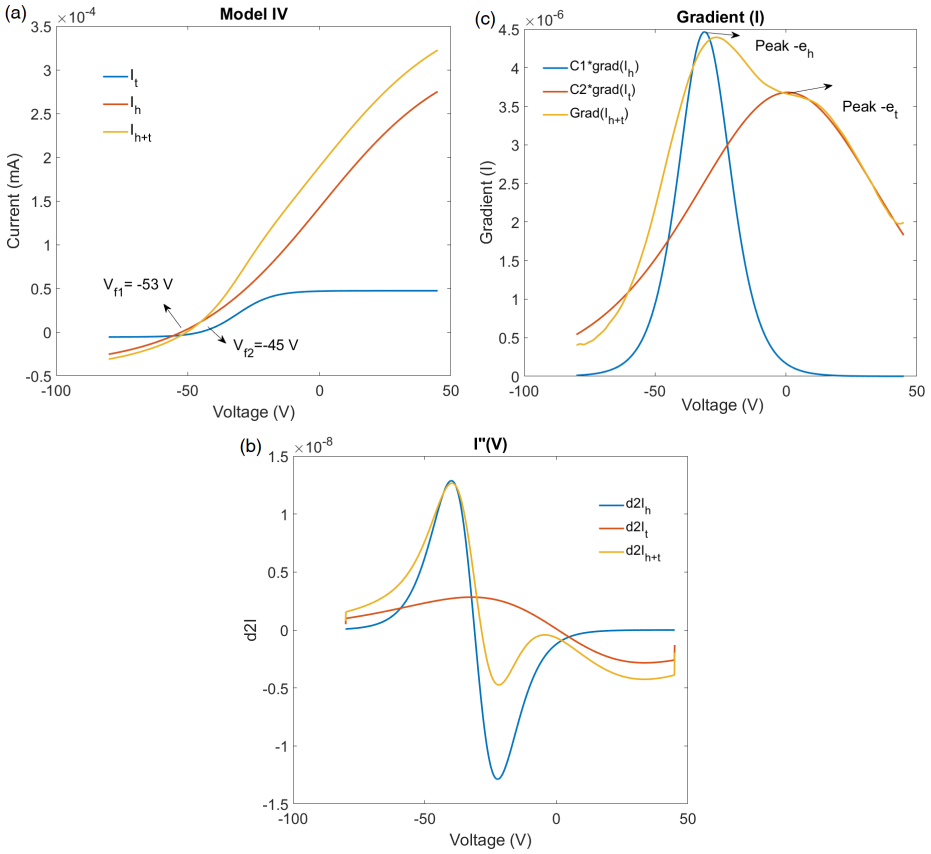

Figure 4.7: Model IV curve: (a) Curves corresponding to hot electrons, thermal electrons and sum fitted using equation (2) (b) First derivatives of the curves and (c) second derivative.

4.2.4 Results and Discussions

Langmuir probe analysis

In figure 4.8a, from the density profiles, it is evident that the thickness of the flux tube connected to the RF electrode narrows with improved confinement at higher magnetic fields. At the same time, the peak of the plasma density moves closer to the RF electrode as the bias on the surface of the RF electrode is more positive. As seen in figure 4.6, There is a bright region below the RF electrode because of the incomplete insulation

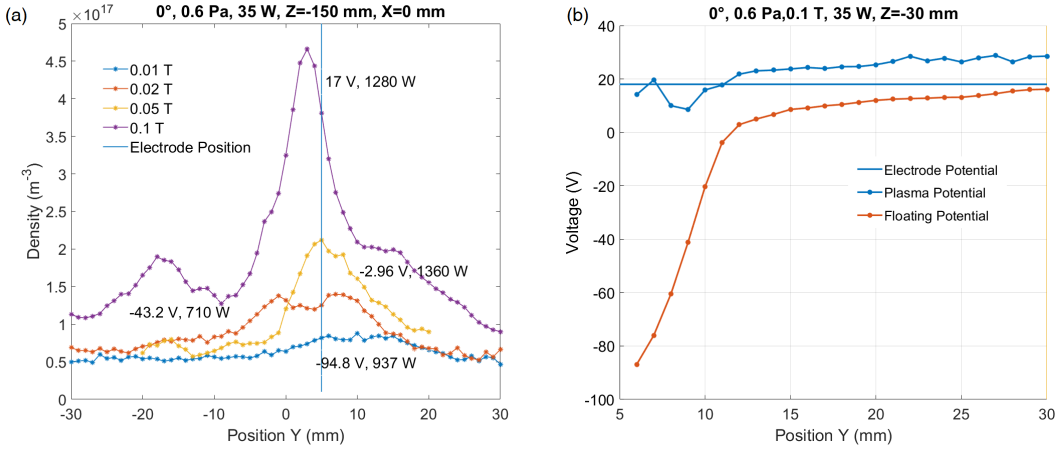

Figure 4.8: (a) Density profile corresponding to 0.6 Pa helium discharges at different magnetic fields measured at Z=-150 mm, (b) plasma and floating potential profiles close to the RF electrode (Z=-30mm) along Y direction corresponding to 0.1 T 0.6 Pa discharge.

of the RF electrode by the ceramic. This leads to a bump in the density profile below the electrode in figure 4.8a. A probe scan performed from Y=6 to 30 mm, for X=0 and Z= -30, yields potential profiles from the IVs is depicted in figure 4.8b. The plasma potential values in the figure are measured using the first derivative method (the peak of the first derivative). As one can see, the plasma and floating potential values are almost constant and positive a couple of centimetres away from the RF electrode. As moving close to the RF electrode inside the flux tube connected to the RF electrode, the floating potential drops substantially. The occurrence of highly negative floating potential values close to the RF antenna has been observed before in the ALINE device (Previous chapter). The 2D floating potential profiles near the RF electrode will be examined in the next subsection. The potential of the RF electrode is represented by the blue line (17 V). In this plot, it can be clearly seen that the plasma potential is lower than the electrode self-bias at a position close to the entrance of the sheath (few mm from the electrode surface), meaning this sheath potential drop is reversed. To be pretty sure of this observation, one needs to be sure of the plasma potential value, which can be quite inaccurate, several volts are common error bars.

Even though positive self-bias cases are reported in other systems [104], experimental evidence of reversed sheath has not been reported yet for capacitively coupled RF systems as predicted by [29; 27].

This is the reason why some IV characteristics corresponding to three experimental scenarios with large positive self-biasing will be analysed in details :

(1) 35 W, 0.6 Pa, 0.1 T where the self-bias is +17 V, (2) 23 W, 0.6 Pa, 0.1 T, where the

self-bias is +23 V since the power coupled to the plasma is lower, (3) 35 W, 0.3 Pa, 0.1 T, lower pressure discharge and the self-bias is +34 V. The results are discussed in the next subsection.

The big problem about case 1,2 and 3 is that they are all treated in a different way, only a profile for case 1, full 2 maps for case 2 and again IVs and derivatives, and potential (floating and plasma), and for case 3 IVs and derivative and floating potential profile (without plasma potential this time). It gives a taste of inconsistency. It's like there is no rigourous logic reasoning to bring consistent conclusions.

Case 1: 0.6 Pa, 35 W, He At 0.6 Pa pressure and 0.1 T magnetic field, The electrons are highly magnetized, ($\omega_{ce}/\nu_{eN} = 934$) but when the ions are assumed to be cold, they are nearly magnetized ($\omega_{ci}/\nu_{iN} = 34$). The IVs were measured using the probe, and are presented in figure (4.9) corresponding to different X positions. The ion saturation current, as well as the maximum of the electron current collected by the probes, are higher for the probe measurement at negative X values. The floating potential values of the curves for negative X values are significantly negative compared to the positive X side. The 21 IV curves obtained along X direction are averaged together, and next the first derivative is used to evaluate the plasma potential at the Y=10 mm position. There exists an elongated tail showing the presence of hot electrons in the double derivative curve. From the first derivative of the averaged IV curve, the average potential of the plasma above the RF electrode is obtained to be 14.9 V. The DC self-bias developed on the RF electrode is measured to be +17 V using the probe connected to the RF electrode. Here, the potential on the surface of the RF electrode is higher compared to the average potential above the RF electrode, implying the existence of an electric field directed from the electrode surface to the plasma, and thus a reversed averaged RF sheath.

The average values of plasma potential $\bar{V}_p < V_{DC}$, the DC self-bias on the surface of the RF electrode doesn't imply the reversed sheath at all the positions above the electrode. It means that, on average, the sheath is reversed and an electric field is pointing out of the electrode surface to the plasma. Since the developed self-bias on the surface of the RF electrode decreases with the input RF power/voltage, measurements were taken for a lower power. In the next case, the power coupled to the plasma was reduced to 23 W, keeping the pressure and the magnetic field constant and probe measurements were performed near the RF electrode.

Case 2: 0.6 Pa, 23 W, He Discharge Since the flux received by the RF electrode is only through the upper circular surface of the electrode, the probe scanned along the diameter X ranging from -30 mm to +30 mm with 3 mm step, and along Y from 8 mm to 30 mm every 2 mm. The IVs obtained were analysed, and the results are shown in figure 4.10. The probe connected to the RF electrode measured the DC self-bias

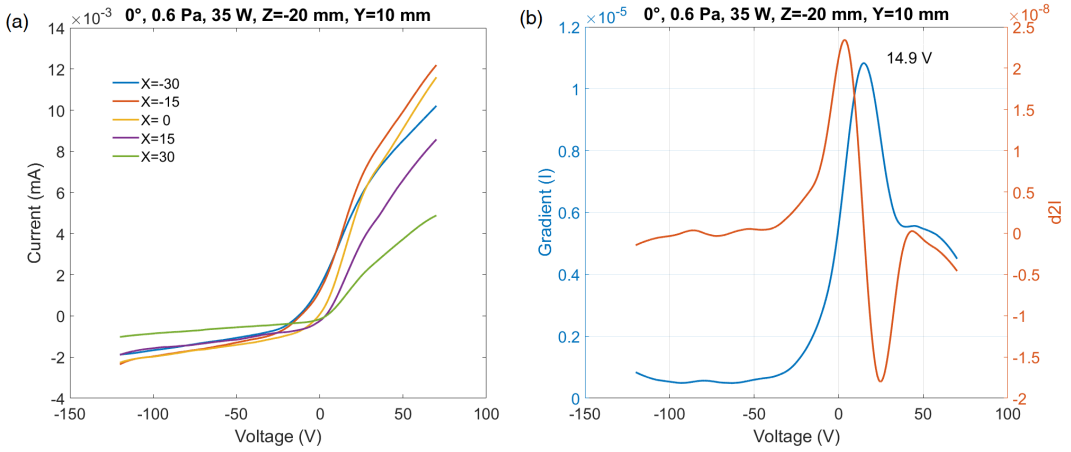

Figure 4.9: IVs, first and second derivative of the mean IV taken at Y=10 mm Z=-20 mm from X=-30 to +30 mm for 0.6 Pa, 35 W Helium discharge.

voltage on the surface of the RF electrode to be +23 V. The cross-field mobility of ions is higher than one of electrons (similar to the last case), and hence the higher flux of ions biases the electrode positively. Plasma density values were retrieved from the IV curves using the OML method. Analysis of the 2D density profile showed a strong in-homogeneity along the diameter of the RF electrode close to the RF electrode, see figure 4.10a. The peak of the density is near the surface of the RF electrode meaning that and the ionization center is shifted close to the RF electrode

At the same time, the peak density ($\approx 1 \times 10^{17}\ m^{-3}$) is shifted to the left of the RF electrode (to the negative X axis). It can only be explained by the potential and the drifts inside the plasma.

The floating potential values are nearly constant and positive a couple of centimetres from the RF electrode, figure 4.10(b). The floating potential values drop to highly negative (up to -65 V) close to the RF electrode, where the density values peak. The drop in the floating potential values close to the RF electrode and the magnetic flux tube connected to the RF electrode has been studied experimentally in ALINE earlier [62]. Faster electrons inside the flux tube reach the probe tip faster, shifting the floating potential values to negative values. The changes in the electron velocity distribution function inside the flux tube connected to the RF electrode have been studied by Faudot et al. using the PIC simulations, and the results are consistent with this observed behaviour and similar observation are already been reported in other magnetic plasma devices [118].

In figure 4.10 c, the plasma potential profiles follow the floating potential, which is positive a few centimetres away and close to zero near the RF electrode. The strong in-homogeneity along the X direction is also seen in the plasma potential profile. Several points near the RF electrode are at a lower potential than the RF electrode (23 V).

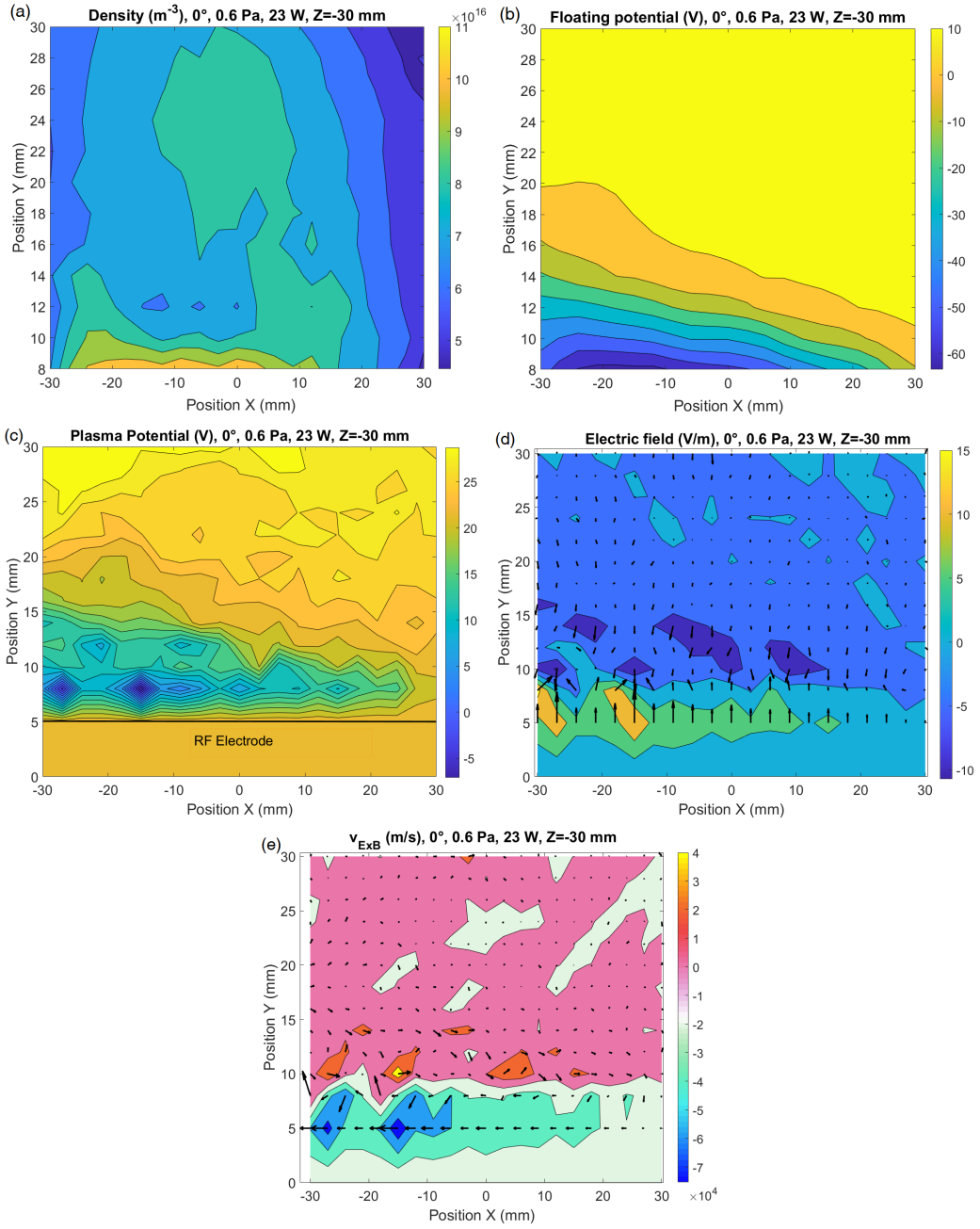

Figure 4.10: 2D profiles of density, Floating potential, Plasma potential including the potential of the electrode, the electric field and the E×B drifts above the RF electrode in ALINE.

These potential gradients create an electric fields with directions pointing opposite

to each other perpendicular to the magnetic field, along the Y direction. The negative gradient of the potential near the electrode yields the electric field map, as seen in the figure (4.10d). The magnitude of the electric field is higher near the RF electrode compared to the bulk plasma. These electric field components perpendicular to the magnetic fields create drift inside the plasma. The direction of the magnetic field is pointing away from the plane, making the particle drift to the -X axis right above the RF electrode and the to +X axis in the bulk plasma as indicated by the quiver in figure (4.10e). In ALINE device E×B drift is the dominant drift mechanism. Even though there is a significant density gradient along the Y direction, the magnitude of the diamagnetic drift velocities are 2-5 times less than the E×B drift velocities.

The mean drift velocity well above the RF electrode is nearly 5×10^3 m/s along the positive X direction. Whereas just above the RF electrode, due to the strong potential gradient and the reversed potential, there is a drift directed to the left, which is nearly 2.5×10^4 m/s, which is responsible for the observed density and the floating profiles. A detailed discussion of the drifts in ALINE for different electrode cases and input parameters are discussed in the next chapter.

To confirm what is happening near the RF electrode, the IVs corresponding to 21 points at Y= 8 mm and along the X axis between -30 mm to +30 mm have been analyzed in detail (6 samples are plotted in figure 4.11a). The 21 IV curves corresponding to Y=8 mm, Z=-30 position are averaged, and the first and second derivatives of the averaged curve are plotted in figure 4.11b. Both curves are distinctly different from one that has only Maxwellian electrons. Widened first derivative profile and multiple bumps in the second derivative indicates the presence of hot electron population near the surface of the RF electrode.

One can first notice that the floating potential is far from constant along the profile. This is clearly shown by the floating potential profile in Figure (4.11c). The most negative value appears in the left part of the profile due to combined E×B and diamagnetic drifts around the plasma column near the electrode. Similarly, the plasma potential also follows the floating potential. It seems this plasma potential values are lower than the electrode self-bias all along the profile except at the right edge.

The IV characteristics are quite different in the highly negative floating potential region and at the edge where it is close to 0. So, by comparing the first and second derivative of the IV characteristics corresponding to X=-18 mm and X=+30 mm, as shown in figure (4.12a and b), one can see the variations in the EEDF and in the plasma potential. The first derivative of the probe current corresponding to X=-18 mm and X=+30 mm in the figure (4.12a) are compared. There is one peak and a bump in the X=-18 mm plot, the peak is at a negative value (-40 V) for the potential and the bump close to 10 V. This double shape represents the distribution of electrons with two different temperatures as explained in the model section 4.2.3. That's why, in this particular case, the classical method of the maximum of the first derivative to find out the plasma potential can not

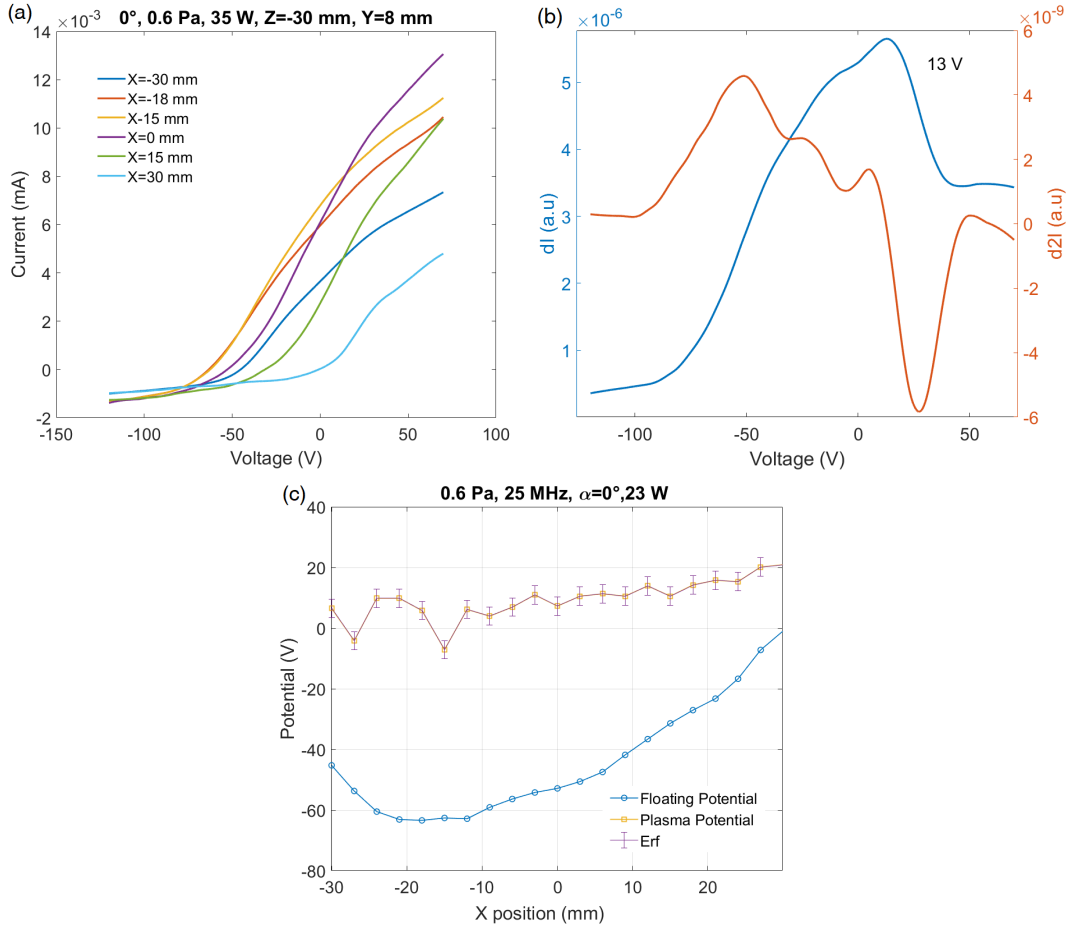

Figure 4.11: IVs, first and second derivative of the mean IV and floating and plasma potential profiles taken at Y=8 mm Z=-30 mm from X=-30 to +30 mm for 0.6 Pa, 23W Helium discharge.

work and the first derivative should be analysed in details. The good plasma potential value is then at the top of the second bump. For the X=+30 mm curve, the highest peak gives the plasma potential value close to 20 V. This means there are more fast electrons in the X=-18 mm curve than in the X= 30 mm curve. This is confirmed by the second derivative plot, in figure (4.12b), even if it is harder to analyse due to numerical noise. The X=-18 plot exhibits the main shifted distribution centred on -60 V, while in X=+30, the main distribution is centred close to the plasma potential corresponding to the thermal population. The conclusion is that the energy distribution is very different for different X positions, across the plasma column, depending on whether we are in the converging drift flux or not.

Considering an average of the whole first and second derivative of the IV charac-

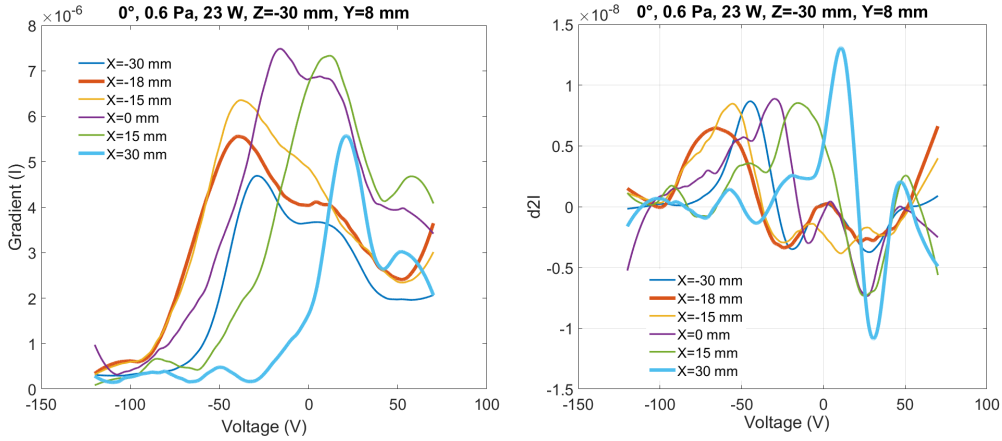

Figure 4.12: First and second derivatives of the IV curves (left) and (right) taken at Y=8 mm Z=-30 mm from X=-30 to +30 mm for 0.6 Pa, 23W Helium discharge.

teristics, the average plasma potential at z=-30 mm and y=8mm can be deduced with good precision, as it appears in Figures (4.11b). It comes out that the plasma potential is equal to 13 V while the self-bias of the electrode was measured to be 23 V. This is a confirmation of a reversed sheath potential drop. In that particular case, ions are repelled by the electrode surface while electrons are attracted. In this specific condition, the ion sputtering can be significantly reduced, avoiding the release of metal impurities in the core plasma and the coating of the windows.

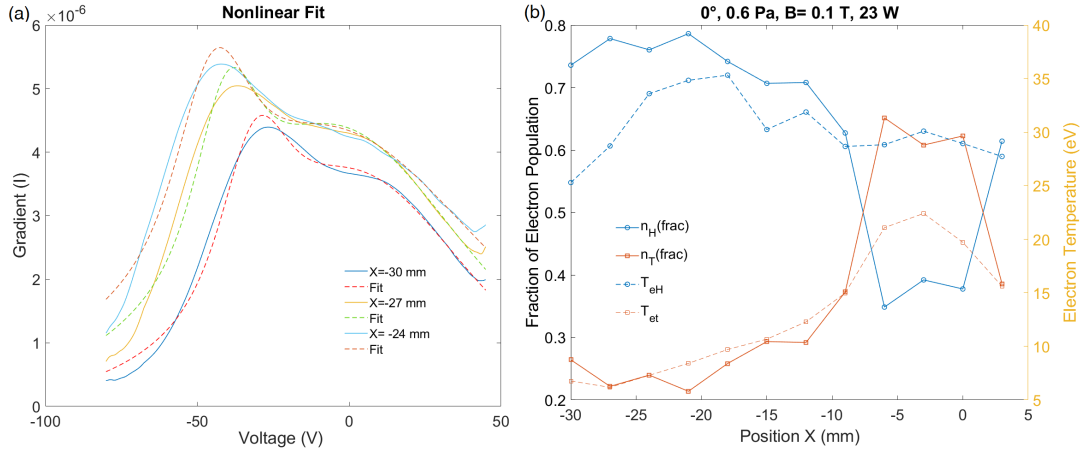

Figure 4.13: The fit of the first derivatives of IV curves and the temperature and fraction of population of hot and thermal electrons retrieved from the coefficient of the fit.

As explained in the model section, the first derivatives of the IV profiles taken at Y=8 mm are fitted as shown in figure (4.13*a*) and inputting the floating potential of

the Langmuir probe IV as input to the fit, the temperatures of the hot and thermal electron populations and respective fractions of density are evaluated from the fit parameters. The fraction of density for hot and thermal electrons is deduced from the fraction of their respective current and temperature from the fit. Three examples of the fits are shown in the figure (4.13*b*). On the left half of the RF electrode, the hot electron population is very high, which is consistent with the observed density and potential profiles. As it reaches the centre of the electrode, the fraction of the hot electron population drops near the centre. At the same time, the temperature of the hot electrons increases initially and reduces as it moves towards the centre of the RF electrode, while the temperature of the thermal electrons come close the hot electrons one, meaning there is only one warm electron population here. The fit could not provide consistent results from IVs from the right part of the electrode (for X>5 cm) because the double temperature model on which the fit is based is not valid anymore, meaning again that the electron population can be seen as a single temperature one. As a consequence, those results have not been included in the plots.

Case 3: 0.3 Pa, 35 W, He At lower pressure, the DC self-bias on the surface of the RF electrode becomes more positive. Keeping the coupled RF power to be 35W, IV curves close to the RF electrode correspond to 0.3 Pa, 0.1 T are analysed in detail. At these conditions (ω_{ce}/ν_{eN}) ratio for electrons and ions is 1870 and 47, respectively. The bias of the surface of the RF electrode to +34 V. Six samples of the 21 IVs measured using the RF-compensated Langmuir probe are plotted in the figure (4.15*a*). In the same way as for case 1 and 2, the averaged first and second derivatives are plotted in the figure 4.15b.

The floating potential profile along the X direction is shown in figure 4.14a. The minimum of the floating potential is shifted a bit to the centre compared to the 0.6 Pa, 23 W discharge. At 0.3 Pa, the collisions can be neglected. Closer to the RF electrode, electrons are not thermalised, and energy distribution is not Maxwellian. The fit of the first derivative is quite satisfactory (The Root-mean-square deviation - RMSE value of the fits are nearly in the range of 2×10^{-7}) corresponding to the ones on the left side above the RF electrode. In figure 4.14b, the fit corresponding to the first 3 IVs is shown. As said earlier, the assumption of the double distribution of the electron profile is not valid anymore in the right part of the profile, like in the 0.6 Pa, 23 W discharge. The temperature values and relative population of hot and thermal electrons retrieved from the IVs are plotted in figure 4.14c. Beyond X= 10 mm, both electron populations have almost the same temperature and are mixed. The algorithm can only provide the temperatures of two-electron populations and their respective currents. This explains the right side of figure 4.14c. But on the left part, there are two populations of electrons; the dominant one with an average energy of 40 eV (80%) and thermal electrons with average electron energy of 10 eV.

From the average curve, the average potential of the plasma (figure 4.15b) above the surface of the RF electrode is found to be 30.7 V, where the RF electrode is at 34 V. This confirms the sheath reversal in the third case. In all the cases mentioned in the present work, the hot electron population is more on the -X side of the RF electrode. This has been indicated by the improved density and lower floating potential values of the IV curves. This is consistent with the reversed sheath, direction of the electric field and the direction of the drift as explained in case 2. When the pressure is lower, the analysis of the IV curves are challenging, especially the evaluation of the plasma potential and hence the 2D maps are not presented for 0.3 Pa discharge case.

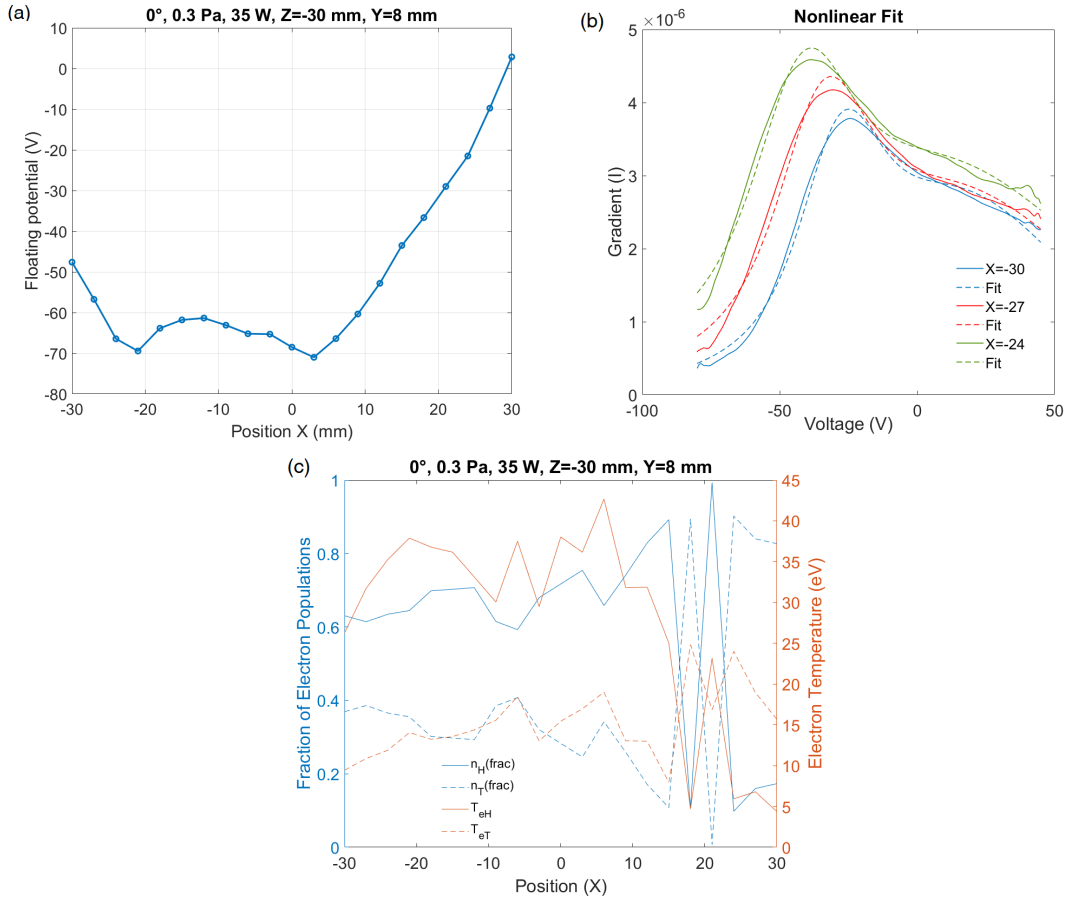

Figure 4.14: IVs, first and second derivative of the mean IV taken at Y=8 mm Z=-30 mm from X=-30 to +30 mm for 0.3 Pa, 35W Helium discharge.

To understand the potential drops inside a reversed sheath, extensive studies have to be performed at higher magnetic fields. All the cases when the positive self-bias is positive do not satisfy the conditions for the reversed sheath. At the same time, we have seen hot electrons in the vicinity of the RF electrode, meaning the interaction

of the oscillation electrons and the RF sheath is still efficient in the case of positive self-bias. For a reversed sheath scenario, the electrons can reach the RF electrode and heat the electrode at the same time, ionize the neutrals near the RF electrode. This has been evident from the density profiles along the Y direction. The positive self-bias on the surface of the RF electrode or the reversed sheath situation reduces the ion flux by repelling the ions back to the plasma but accelerates the electrons to the surface. Hence the result is the reduction in the sputtering of the RF electrode/wall in contact with the plasma, but not the heating in section 6.4.3.

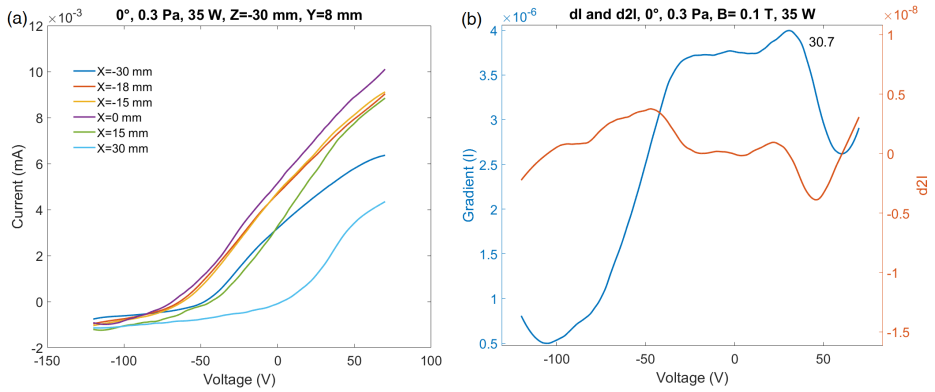

Figure 4.15: IVs, first and second derivative of the mean IV taken at Y=8 mm Z=-30 mm from X=-30 to +30 mm for 0.3 Pa, 35W Helium discharge.

4.3 Conclusion

The possibility of a positive self-bias in an asymmetric magnetized CCP discharge has been studied experimentally and analytically. Positive self-bias was achieved using a “one face" electrode surrounded with ceramic at the edge and bottom sides and by limiting the perpendicular electron flow to the electrode in the low collisionality regime and relatively high magnetic field ($\simeq 0.1$ T). Since ions are almost not magnetized, their motion is unaffected by the changes in the B values. Variations in the self-bias voltage with input parameters such as magnetic field, gas pressure, the tilt angle of the electrode and input RF power have been studied and compared with the results from the analytical model. The analytical model is developed on the basis of the flux balance condition since the electrode should not drive a net current from the surrounding plasma. The main results are in good accordance with the model, which shows that the transition angle from a negative to a positive self-bias is mainly lower than 3°, and that an increase of the RF power plays the same role as an increase of the pressure or a decrease of the magnetic field. This is due to the oscillating electric field in the sheath, which increases the perpendicular electron flux. The positive self bias developed practically repels the ions reaching the RF electrode and the sputtering of the RF electrode can be minimized.

In the second section, a detailed analysis of the plasma parameters around the RF electrode is done for low-pressure Helium discharge. Three case studies were performed to investigate the reversed sheath (1) 35 W, 0.6 Pa, (2) 23 W, 0.6 Pa and (3) 35 W, 0.3 Pa, all at 0.1 T magnetic field. From the potential profiles measured using the RF-compensated Langmuir probe, the plasma above the electrode is found to be at a lower potential with respect to the electrode. From the first and the second derivatives of the IV curves, the existence of the double Maxwellian is observed near the RF electrode indicating that stochastic heating is still efficient in heating the electrons near the RF electrode even when the self-bias is positive. Near the RF electrode, at lower pressure discharges the electrons are not thermalised and this is validated by the highly negative floating potential measured by the probe. The analysis of the IVs was performed by fitting the IVs using the double probe model, from which the population ratios of hot electrons, thermal electrons and their respective energies were obtained. Close to the RF electrode hot electrons are the dominant population of electrons especially in the region at which the floating potential is strongly negative. The reversal of the sheath was observed for the first time in the case of a non-emissive surface with a small electrode to wall area ratio. Further discussions about the effect of $E \times B$ drift and heating of the RF electrode and their parameter dependence are continued in next chapters.

Chapter 5

Experimental investigation on Effect of Drifts in ALINE Device

Contents

5.1 Introduction 100

5.2 Drift structures in the vicinity of an Electrode With Grounded Copper Shield 101

5.2.1 Setup and Experiment 101

5.2.2 Results and Discussions 102

5.3 Experiments with Tungsten Electrode with Ceramic Covering 114

5.3.1 Angle Dependence 114

5.3.2 Magnetic field dependence 119

5.3.3 Fast Camera results 123

5.4 Experiments with Tungsten Electrode 125

5.4.1 Capacitively Coupled Discharge Results 126

5.5 Conclusion 137

5.1 Introduction

In asymmetric capacitive RF discharge, the energy of ions reaching the surface of the electrode or material is determined by the bias on the RF electrode. This principle is utilized in material processing applications. In the fusion science perspective, due to continual deposition from the first wall materials of the fusion reactor vessel, the first mirrors, which are the front-end components in these diagnostic systems, significantly lose optical performance [119; 120]. In order to recover the efficiency cleaning of the first mirrors using CCP sputtering is currently under development [119; 121; 122]. Sputtering experiment without magnetic field showed uniform sputtering of substrate and cleaning observed to be improve significantly in magnetic environment [123]. But the magnetic field brings non uniformity in the plasma perpendicular to the magnetic field. In the presence of an axial magnetic field, a perpendicular component of electric field can create $E \times B$ drift [3]. Magnetic field creates asymmetry inside the plasma induce pressure gradient across the magnetic field which creates diamagnetic drift [124; 125]. Better understanding of magnetized discharges and drifts are necessary to achieve uniform sputtering in magnetic CCP environment. The effects of the magnetic field in low-pressure discharge have been studied vastly in the previous decades experimentally and theoretically [39; 9; 10; 126]. The effect of a transverse magnetic field in making the plasma more resistive and affecting the self-bias developed on the surface of the electrode has been studied theoretically in [29; 127; 128]. Multiple authors worked on the effect of magnetic field and associated complexities and non-uniformity in MERIE discharges [129; 130; 131; 132]. Barnet et al. observed the reduction in the RF voltage with increasing magnetic field strength for a fixed RF power input. In his work, he used Langmuir probes, optical emission, and laser-induced fluorescence to analyze how the magnetic field influences the plasma's distribution in planes that are parallel and perpendicular to the magnetic field. The magnetic field can also induce spatial electron temperature in-homogeneity in cylindrical plasma devices [133], as it has been seen in the previous chapter.

Experiments in ALINE device at 0.1 T magnetic field at 5° using electrode with grounded walls showed highly non uniform sputtering pattern [47], see figure 5.1. The non-homogeneity arose due the $E \times B$ and diamagnetic drifts inside the plasma. It has been reported that by applying optimal electric field value, both drifts can cancel each other [124; 134]. It has been seen that the potential and electric field profile varies significantly with tilt angle of the electrode with the axial magnetic field [59]. To explain the evolved sputtering pattern, 2D maps of density and potential are made using cylindrical Langmuir probe for 2 different tilt angles. Drift velocities were calculated from the maps and results were compared. These experiments have been extended to other types of electrodes and the results are discussed in this chapter. The chapter is structured as follows: Firstly, the discussion focuses on the copper electrode with grounded

walls. Then, a detailed study is conducted on the behaviour of the plasma formed with the electrode covered in ceramic. Finally, the discussion extended to the analysis of the plasma generated using the tungsten electrode without ceramic covering (Simple W electrode).

5.2 Drift structures in the vicinity of an Electrode With Grounded Copper Shield

Experiments were carried out in the ALINE reactor using an electrode with a grounded wall [47; 122] to study the sputtering pattern developed at grazing angles (see section 2.1.1).

5.2.1 Setup and Experiment

The self-bias on the surface is measured using the probe-connected electrode, and plasma parameters were measured using RF-compensated Langmuir probes with modified probe tip at Z position in range -100 to -150 mm so that the perturbations due to the RF electrode is lower during the measurement.

To study the effect of tilt angle and the direction of the magnetic field, the following scans have been performed:

- Langmuir probe measurements along the X-Y plane (-30≤X, Y≤+30) at Z=100 position were taken for 5° and 30° tilt angles for argon discharge at 1 Pa gas pressure for 35 W coupled RF power.
- Helium discharge at 1 Pa, 0.1 T magnetic field at 35 W coupled RF power for 5° and 45° tilt angles.
- X-Z scans above the RF electrode corresponding to Y=10 mm, for X position in the range -30 to +30 mm and Z ranging from -80 to +50 mm corresponding to helium and argon discharges at 2 different magnetic fields (0.05, 0.1 T) for 5 ° tilt angle, at 35 W coupled RF power and 1 Pa gas pressure.
- Scans along the X-Y planes corresponding to 0.05 and 0.1 T were taken at Z=-120 mm for both of the gases.
- Finally, the direction of the magnetic field is reversed, and scans along X-Y and X-Z planes were conducted at 0.05 and 0.1 T as before.

.

5.2.2 Results and Discussions

Sputtering Experiment with Argon

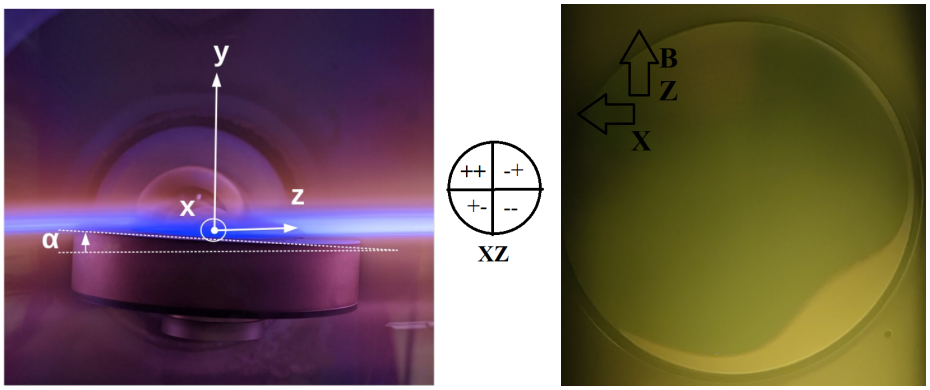

Figure 5.1: Discharge with (a) RF electrode with grounded walls at 5° tilt angle and the (b) sputtering pattern developed after 1.5 hours exposure. To explain the sputtering pattern the circular electrode is divided in to four different quadrants as depicted in the diagram in the middle.

5° Measurement results As previously stated, as part of the ITER's first mirror cleaning study by sputtering using CCP discharge, experiments were performed at a 5° tilt angle, 0.1 T magnetic field when the self-bias on the surface of the RF electrode is -100 V, 1 Pa argon gas pressure in the capacitive coupling. The image of the electrode after the exposure to the plasma is shown in figure 5.1. As one can see, the bottom right part of the RF electrode (– quadrant of the electrode surface (XZ plane)) is fully etched by the plasma, and it extends to the -+ XZ plane along the edges and bottom part of the +- quadrant. The details of the sputtering yield are not in the interest of our study, and the sputtering aspects of the study have been elaborated in [47].

To study the developed sputtering pattern, the results from the Langmuir probe scans along the XY plane taken at Z=-120 mm for the same experimental parameters are given in the figure 5.2. Since the bottom part of the RF electrode is covered with the grounded copper wall, the RF waves are shielded, and no significant stochastic heating process at the bottom part, leads to strong asymmetry in density along the Y direction 5.2(a). In 2D maps there are 2 ellipses drawn, the inside one representing the projections of active part of the RF electrode and the outer edge of the grounded copper wall along the B field. Around the RF electrode, the high-density regime is located in the upper half and primarily at the centre of the circular electrode. It is slightly shifted towards the negative X-axis on the left side, possibly due to E×B drift as we will discuss in later. The peak density structure is stretched to the right at the

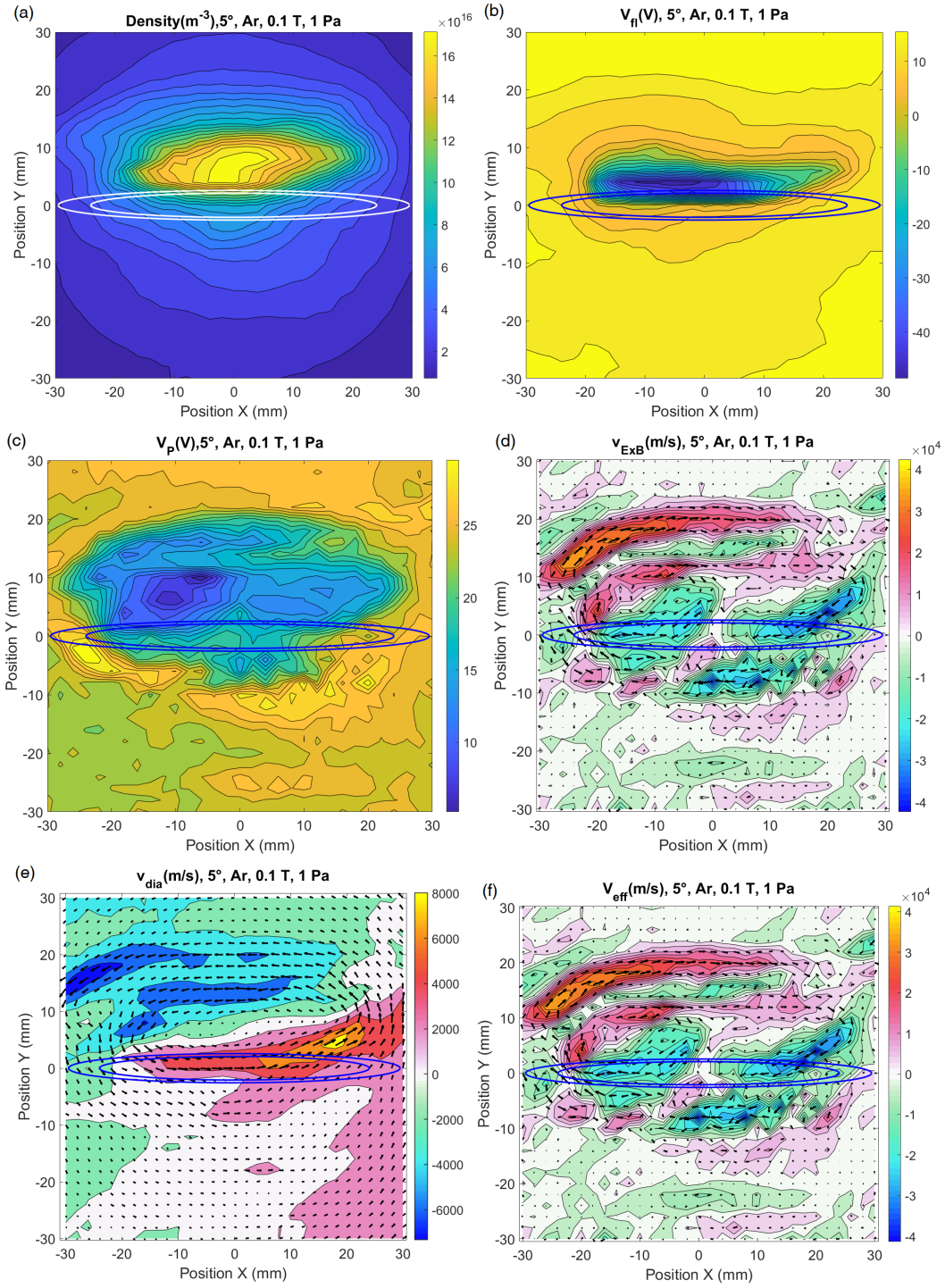

Figure 5.2: (a) Density, (b) floating potential, (c) plasma potential (d) electric field (e) E×B drift velocity (f) Diamagnetic drift velocity and (g) Effective drift velocities corresponding 1 Pa argon discharge at 5° tilt angle 35 W coupled RF power at 0.1 T magnetic field.

top and to the left at the bottom of the flux tube, which is connected to the parallel projection of the RF electrode along the direction of the axial magnetic field. This observation has been addressed in detail later in this subsection. As we have seen in the previous chapters, the density of the plasma drops drastically outside the flux tube connected to the active part of the RF electrode. Please note that in the electrode image in figure 5.1, the positive X axis is oriented towards the left to align with the direction of the manipulator.

The floating potential map is displayed in figure 5.2b. The floating potential values are positive and almost constant outside the flux tube connected to the RF electrode and drop significantly close to the RF electrode. Inside the flux tube connected to the edge of the RF electrode, the lowest value of the floating potential is nearly -50 V. Note that the measurements are taken 120 mm away from the RF electrode and as seen in Chapter II, as the probe moves closer to the RF electrode the value of the floating potential can be more negative. Similar to what we see in the density profile, the minimum of the floating potential value is shifted to a negative X direction, indicating the higher density of hot electrons in that regime. To analyze the localization of hot electrons, the potential maps on the X-Y plane are examined. The intersection method [135] is used to find out the plasma potential because the first derivative method was unable to find the peak due to the noise in the profile. As seen in the floating potential profile, plasma potential is positive outside the flux tube, and it is still positive inside the flux tube, but the magnitudes drop close to zero near the surface of the RF electrode, see figure 5.2c. The area of the projection of the RF electrode stays at a lower plasma potential compared to the surrounding plasma. The minimum of the plasma potential (8 V) is at the -X part of the RF electrode, where the sputtering is maximum.

The effect of this E×B drift and corresponding velocities in the X-Y plane perpendicular to the magnetic field is portrayed in figure 5.2d. The quiver and colour palette represent the direction and relative magnitude of the E×B drift velocities. As depicted in the figure, when electrons are produced at the lower Y positions of the sheath plasma interface, they drift and accumulate more towards the left side, resulting in a higher ionisation rate. Due to this lower potential region inside the plasma, there exists an area in which the particle drifts at a different speed with respect to the one generated due to the active electrode-grounded electrode interface. There exists a global rotation of particles at lower velocities outside the flux tube connected to the RF electrode ($10^3 - 2 \times 10^3$ m/s). One can see a counter E×B rotation of particles at the edge of the grounded electrode and the plasma outside the flux tube connected to the grounded part due to the sudden drastic potential change, as explained. Inside the flux tube connected to the active part of the RF electrode, the direction of the net electric field drifts the particles toward the left at the lower part (-Y values) and toward the right at the top part, which explains the in-homogeneous density map.

The in-homogeneity in the density distribution causes a pressure gradient in the

plasma (For constant T_e and T_i, $\nabla p = k_B T \nabla n$) [3], creating a diamagnetic drift inside the plasma, see figure 5.2e. The diamagnetic drifts corresponding in the X-Y plane are calculated from the density profile of the plasma. The average electron temperature of the plasma is taken as 3 eV for the calculations since our area of interest is to study the drifts inside the flux tubes connected to the RF electrode, and the average electron energy is significantly higher due to several factors explained in Chapter 3. From the diamagnetic drift velocities derived from the density profiles, it is seen that the diamagnetic drift drives the particles opposite to the direction of E×B drift. Diamagnetic drift is prominent inside the flux tube, and the velocities are lower outside the flux tube connected to the RF electrode, as seen in the case of E×B drift case. But the magnitude of the diamagnetic drift velocities (2000-6000 m/s), which are lower compared to the E×B (2-3 times higher) inside the flux tube. The effective drift, the sum of the $v_{E\times B}$ and v_{dia}, have been plotted in the figure, representing the relative magnitude using the colour palette and the directions by the quiver. The effective drift profile is almost similar to the E×B times showcasing the fact that it is the dominant drift mechanism inside ALINE.

Distribution of hot electrons around the RF electrode allows the diffusion of ions to that specific region, accelerating the ions to the surface of the RF electrode and sputtering the molybdenum layer on the surface of the RF electrode. Along with the observed drift, the shape of the sheath plays an important role in the observed sputtering pattern. When the RF electrode make a 5° angle with the magnetic field, due to the shape of the RF sheath, one can divide the space above the RF electrode based on the density of the plasma. As shown in figure 5.3, there are high density regions at the left and right hand side of the RF electrode at the intersection of the plasma column with the active part of the RF electrode due to the higher mobility of energetic electron generated due to stochastic heating along the field lines. Right above the RF electrode, due to the shape of the RF sheath and limited mobility of the electrons perpendicular to the magnetic field, the ionization is lower creating a low density region. Ions from the higher density regions are accelerated to the electrode surface as shown in figure. The cumulative effect of the The strong drift, as seen in the quiver plot, and the density distribution around the RF electrode, favours the observed edge-sputtering effect on the surface of the RF electrode.

30° Measurement results The 5° angle had been chosen because of the mirror configuration in ITER, but here we investigate what are the consequences at higher angles. It has been previously shown that increasing the angle, increase the self-bias of the RF electrode in capacitive coupling, and will reflect in the ExB drift. Then, a higher angle of 30° has been chosen to measure the same plasma parameters as at 5°. The results from the measurements are given in figure 5.4. The self-bias on the surface of the electrode is measured to be -140 V. At 30°, the projection area of the RF electrode along the

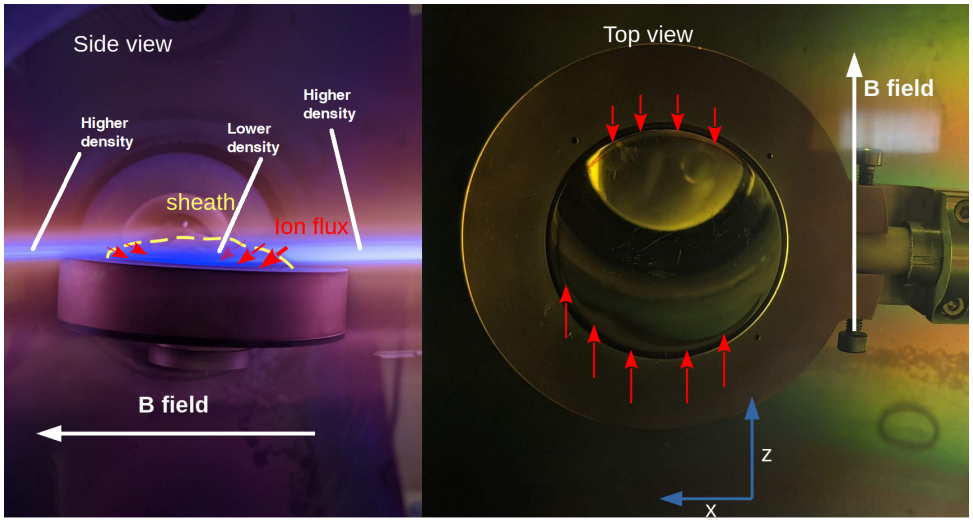

Figure 5.3: Argon discharge and plasma column in ALINE with first erosion pattern developed due to sputtering. The yellow dashed line represents the sheath above the RF electrode and the red arrows represents the motion of the ions from the plasma column to the RF electrode.

magnetic field lines is larger. Similar to what is observed for the 5° case, the density of the plasma is higher inside the flux tube connected to the edge of the electrode as seen in the figure 5.4a. The peak density is more shifted towards the right when compared with the 5° case. For the same coupled RF power, the peak density of the plasma is less for the 30° case and outside the flux tube, the density of the plasma is almost constant. The peak density value is dropped by half to 8×10^{16} m^{-3}, while comparing with 5° along the distribution of the density due to the projection of the active part of the RF electrode along the direction of the magnetic field.

The floating potential profile is depicted in 5.4(b). The floating potential inside the flux tube connected to the RF electrode is lower compared to the magnitude outside of the flux tube, but the values are always positive. The minimum value of the floating potential is found to be 10.1 V. Unlike the 5° cases, the position of the lowest value of the floating potential is more shifted to the positive X direction. The floating potential values are positive and higher compared to the 5° case, implying lower energy of electrons inside the flux tube. The average energy of electrons inside the plasma is measured to be 2 eV 5.5 .Hence, it can be seen that the floating potential shifts closer towards the plasma potential.

Similar to the floating potential, the plasma potential inside the flux tube connected to the active part of the RF electrode is lower compared to the surrounding plasma, see figure 5.4(c). Whereas the higher plasma potential regime around the active part due to the grounded electrode is only visible in ++ quadrant of the XY plane. Probe

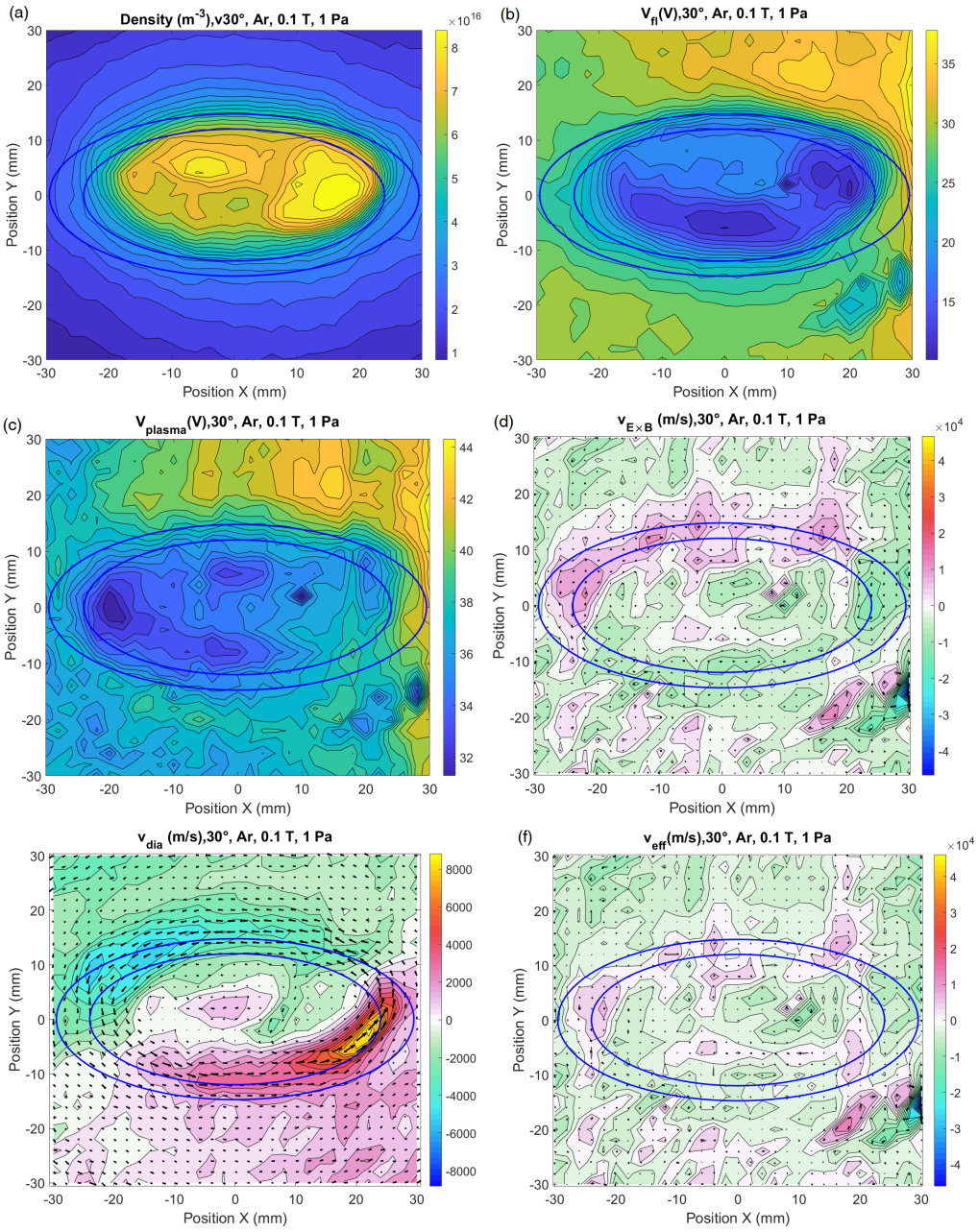

Figure 5.4: (a)Density, (b) Floating potential, (c) plasma potential (d) electric field (e) E×B drift velocity (f) Diamagnetic drift velocity and (g) Effective drift velocities corresponding 1 Pa argon discharge at 30° tilt angle 35 W coupled RF power at 0.1 T magnetic field.

measurement closer to the RF electrode can give an insight into the observed behavior.

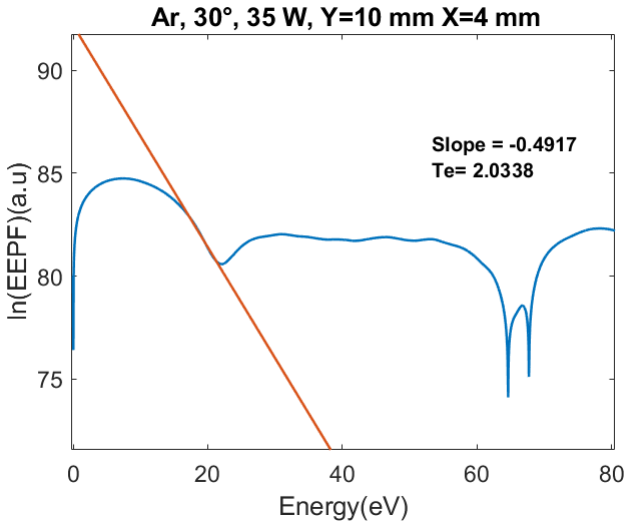

Figure 5.5: Temperature inside the plasma column connected to the RF electrode from natural logarithm of EEPF.

The electric field values were evaluated from the gradient of the potential profile, see figure 5.4(d). The electrons move from the negative X half to the positive X half by the electric field profile perpendicular to both electric field and magnetic field.

From the potential profile, the drift velocities due to the E×B have been evaluated and are given in figure 5.4d. From the density profiles, the diamagnetic drift velocities were evaluated see figure 5.4e. Unlike the 5° case, there are no significant gradient in potential around the active part of the RF electrode, leading to lower E×B drift velocities, nearly around 6-10× 10^3 m/s in the clockwise direction (CW). High density gradient around active part of the RF electrode creates strong diamagnetic drifts around in the counter clockwise direction (CCW) with average velocity 6-8 × 10^3 m/s. This lowers the effective drift velocity, giving a v_{eff}=1-1.5 × 10^3 m/s in the CW direction. In this particular case, ExB and diamagnetic drift almost cancel each other, which can lead to a more homogeneous sputtering pattern.

X-Y profiles-He Discharge

Experiments were also performed with helium gas to investigate the effect of the ion mass and to avoid sputtering and metallic coating on windows. X-Y profiles of density and plasma potential corresponding to each case have been measured using the Langmuir probe. From the potential profiles and density profiles, the drifts inside the plasma are calculated to attempt to explain the variation of the population distribution of particles around the RF electrode.

The density profile corresponding to 0.1 T, 35 W, 1 Pa helium discharge at a 5° tilt

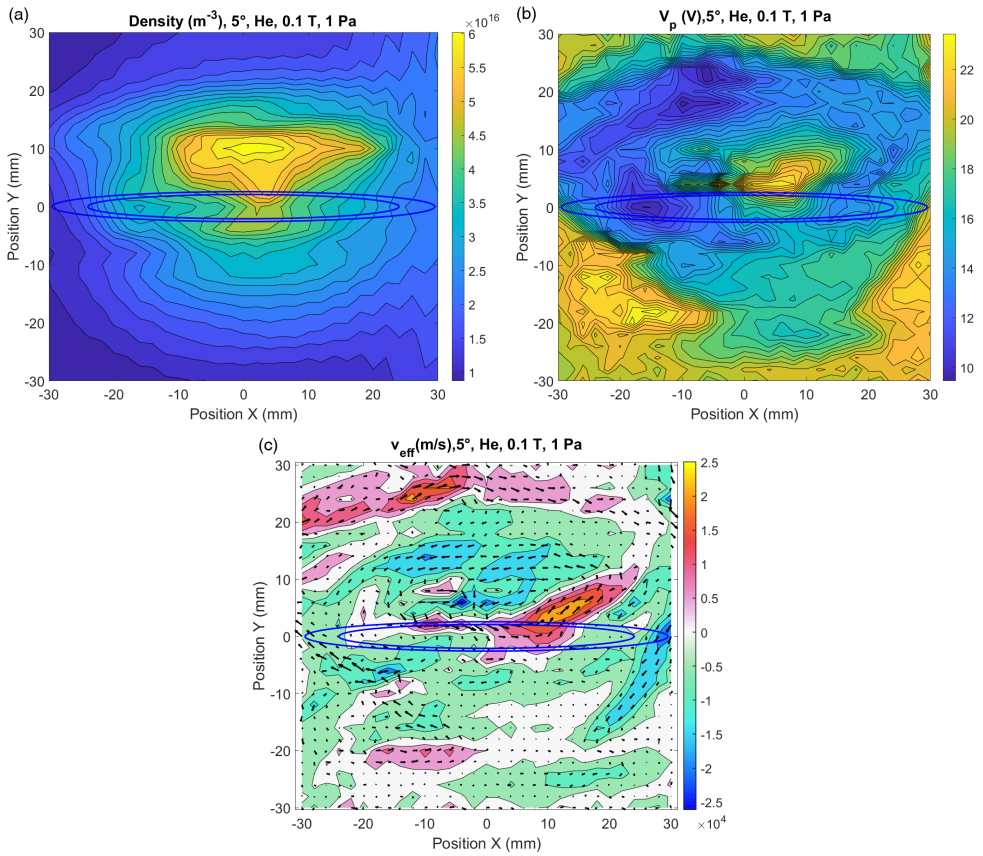

Figure 5.6: (a) Density (b) plasma potential (c) effective drift profiles corresponding to helium discharge at 1 Pa, 5° tilt angle and 35 W of coupled RF power.

angle is depicted in figure 5.6a. For this particular measurement, the floating potential near the surface of the RF electrode is measured to be highly negative. The probe was biased from -70 to +70 V, and when the floating potential was close to the minimum of the bias potential due to the effect of stochastic heating there was no ion saturation in the measured IVs and it was not possible to measure the density of the plasma using the OML method in a certain region where the floating potential was highly negative. The raw maps can be noisy and granulated, so the 'makima' 2D interpolation technique is used to display clearer plasma density inside the flux tube. The density profiles peak above the RF electrode, and the peak structure is almost at the centre. The peak value of the density is around $6\times10^{16}\ m^{-3}$ inside the flux tube connected to the active part of the RF electrode, and it drops to the minimum value of $1\times10^{16}\ m^{-3}$ outside. The profiles at 5° are distinct from the argon case, where the density values are significantly higher due to the lower ionization energy.

Plasma potential maps are depicted in figure 5.6b, the potential inside the flux tube

connected to the RF electrode is lower compared to the one from outside. Plasma potential is lower for the negative X values, compared to the positive X part. The plasma potential is positive in the flux tube, connected to the grounded electrode part. There is a higher potential region inside the flux tube connected to the active part of the RF electrode. From the density and plasma potential profiles, the diamagnetic and the E×B drifts are calculated and the effective drift velocities are calculated and displayed in figure 5.6. We observed in the inner loop, the diamagnetic drift is in same direction as the E×B drift but in the opposite direction outside the area of the RF electrode. As seen before, the E×B drift velocities (0.5-1.5 $\times$ 10^4) are higher compared to the diamagnetic drifts (3000-4000 m/s), and the effective drift almost follows the E×B drift. Due to the potential profile, there are two rotations of particles perpendicular to the magnetic field. Inside the flux tube, particles rotate in the CCW direction due to the radially inward pointing electric field. There is another structure rotating at a larger radius in the clockwise direction due to the potential on the active electrode. Velocities of the two loops have almost the same magnitude, and average drift velocity calculated from the probe is nearly in the range of 6-8 km/s inside the plasma.

Other measurements were taken at 45° for the same experimental parameters at Z position =-180 mm. When the probe was close to the RF electrode, it was seen that the probe was disturbing the plasma during the measurements. The density peaked at the edge of the active electrode part, where the interaction of the electrons with the sheath is more efficient, see figure 5.7a. At 45°, the peak density ($3.5\times10^{16}m^{-3}$) is dropped by half compared to the 5° ($6\times10^{16}m^{-3}$) case. The density is lower at the centre of the active electrode part. The peak density region forms a circular ring in the XY plane. The corresponding plasma potential profile is plotted in figure 5.7b. The potential distribution changes drastically at higher angles in the case of helium. The central flux tube connected to the active part of the RF electrode stays at a higher potential than the surrounding region. Plasma potential stays above 30 V for all the points in the XY plane and peaks around 40 V at the center. Similarly, the floating potential is high and positive, like in the argon 30° case, but stays at high values in the active part of the RF electrode. The floating potential has a minimum value at the centre of the high potential structure, indicating the presence of a fraction of hot electrons, see figure 5.7c. In contrast to the previous scenario, the floating potential values are positive in this case. This indicates that the average electron energies, even those of hot electrons, are relatively lower. This is due to the inefficiency of stochastic heating at higher angles, resulting in lower energy values.

From the plasma potential profiles, one can deduce the electric field profile. The electric field is directed from the central flux tube to radially outside all along the X-Y plane. The ions are repelled from the central region of the plasma, which creates a low ion region, meaning the sputtering due to the ions will be minimal in that region. One can assume that at the 45° case with helium, the central part of the RF electrode will

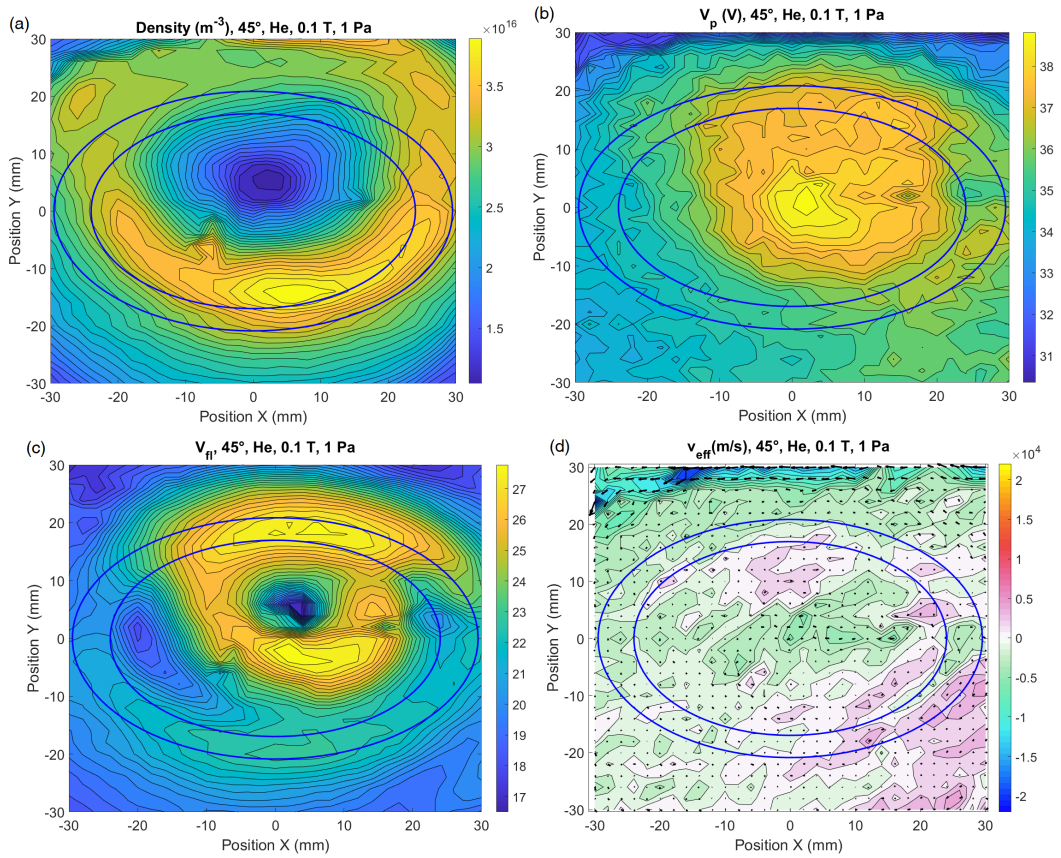

Figure 5.7: (a) Density (b) plasma potential (c) floating potential (d) effective drift profiles corresponding to helium discharge at 1 Pa, 45° tilt angle and 35 W of coupled RF power.

be the least sputtered part, and the edge of the electrode will be the most. From the potential profiles and density profiles, the total drifts inside the X-Y plane are evaluated see figure 5.7d. It is observed that the direction of the diamagnetic and E×B drifts are in the opposite directions (V_{dia} is nearly 4-6 $\times 10^3$ m/s), but the rotation inside the plasma is as whole in the counterclockwise direction due to slightly higher $V_{E\times B}$, which is quite different from the argon discharge at 30°. The effective drift velocities are lower compared to the grazing angle case. The average velocity of rotation is around 500-1000 m/s counterclockwise at the centre of the plasma column, and one can see from the size of the quiver that the velocity of rotation is increasing as the radius increases with respect to the origin in the X-Y plane. The observed density distribution can be explained by the rotation of the plasma with respect to the axial magnetic field. It has to be noted that the gradient of the potential in the X-Y plane is lower at higher angles compared to the grazing angles, which is seen in the case of both argon and helium

discharges, and the effective drift velocities are lower.

Effect of Magnetic field direction

To be sure that ExB drift is responsible for the density/erosion shift, the magnetic field has been tested at 0.05 and 0.1 T and also reversed at -0.05 T and -0.1 T. XY maps and XZ maps of density (n) corresponding to 2 different magnetic field values (0.05 T and 0.1 T) at 35 W coupled RF power and 1 Pa pressure for both argon and helium are compared. The density maps are sometimes noisy and difficult to process, so the difference between the maximum electron and ion currents measured by the probe is directly plotted. The purpose here is not to evaluate a precise density but to compare the relative shape changes in the plasma column with respect to the magnetic field. This current (I_{ei}) is proportional to the density, acoustic speed and sheath size (due to sheath expansion) of the probe tip, and it is also proportional to the flux received by the biased surface. In figure 5.8a and b, I_{ei} for 0.1 T and -0.1 T measured at XY plane for Z=-100 mm are given and the results compared. The position of the RF electrode has been represented by the square box in the XY maps and by the circle in the XZ maps.

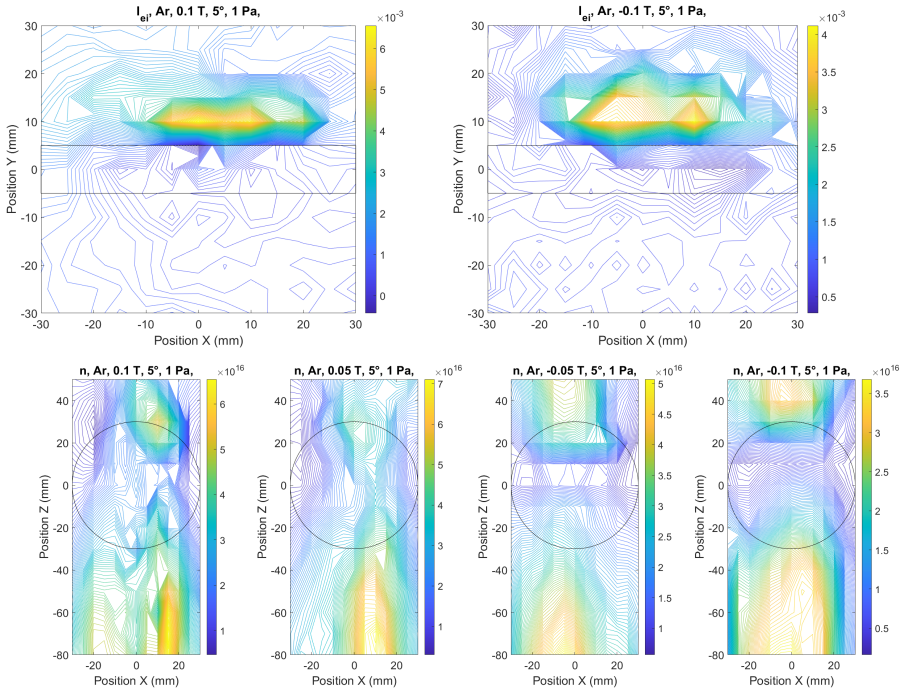

Figure 5.8: X-Y maps of I_{ei} for argon case when the magnetic field (a) 0.1 T (b) -0.1 T, for argon discharge at 1 Pa pressure, 35 W of coupled RF power for a tilt angle $\alpha = 0$ and X-Z maps of density n (m^{-3}) for (c) 0.1 T (d) 0.05 T (e) -0.05 T and (f) -0.1 T.

During the measurement process, the electrode is tilted by 5° with respect to the

+0.1 T axial magnetic field and by 175° when the magnetic field is reversed. When comparing the plots of I_{ei} in figures 5.8a and 5.8b, there is a noticeable shift in the current profile. When the magnetic field is 0.1 T, the peak of I_{ei} shifts slightly towards the positive X direction. Conversely, when the magnetic field is reversed, the peak shifts towards the negative X direction. This shift in the I_{ei} peak was expected due to the change in the direction of E×B drift resulting from the change in the magnetic field direction. This effect is also observed in the density profiles. Figure 5.8c to 5.8f shows the density distribution along the X-Z maps for the Z position ranging from -80 mm to +50 mm, corresponding to four different magnetic field values at the Y= 15 mm position. Similar to the I_{ei} maps, the peak density shifts more towards the right (positive X direction) of the RF electrode when the magnetic field is +0.1 T. Conversely when the magnetic field is reversed, the shift is observed to be towards the negative X direction. The shift of the density peak is more noticeable for the 0.05 T case in figures 5.8d and 5.8e, since the drift velocity is inversely proportional to the strength of the magnetic field ($v_{E\times B} = E \times B/B^2$). The density was measured to be lower right above the active part of the RF electrode compared to the bulk. The density maps along the X-Z plane of helium discharge at 0.1 T and 0.05 T are presented in the figure 5.9(a) & (b) respectively. Similar to the argon discharge case, the density is higher at the positive side of the RF electrode, and the shift is more observable at lower magnetic field values due to the higher drift velocities. The X-Z maps also show that the average density drops near (just above the active part) the RF electrode by 3-4 time compared to the bulk plasma because most of the ions are attracted at the sheath entrance directly to the front or back electrode edge. The other possible explanation is that most of ionization takes place outside the sheath along the plasma column, and the probe measurement are very close or may be a little bit inside the sheath where the plasma density in much lower.

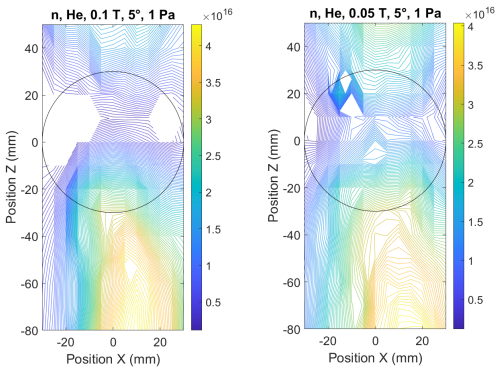

Figure 5.9: The density (m^{-3}) maps in X-Z plane (a) at 0.1 T and (b) at 0.05 T for 1 Pa helium discharge at 5° tilt angle.

5.3 Experiments with Tungsten Electrode with Ceramic Covering

In order to see the effect on E×B drift and the effective drift due to the change in electrode configuration, in this sections experiments were carried out with one-faced electrode. The dependence of the potential and density distribution around the RF electrode on the tilt angle and strength of the magnetic field is studied using the probe and compared with fast camera results.

X-Y maps were taken at Z=-150 mm at 0.6 Pa gas pressure and 0.1 T at 35 W coupled RF power. To study the dependence of the tilt angle on the distribution of plasma parameters around the electrode, measurements were taken at 0°, 5°, and 20° and the results were compared. The drifts inside the flux tube are calculated from the potential and density maps as performed before. To explore the relationship with magnetic field strength, Langmuir probe measurements were conducted at magnetic fields of 0.02, 0.05, and 0.1 T. The density values were measured using the OML method, and the plasma potential using the intersection method since the first derivative method giving noisy maps inside the plasma column connected to RF electrode especially at 5° and 20° angle measurements. In this section, the dependence of the plasma parameters along the X-Y plane on the tilt angles is discussed separately, followed by the dependence on the magnetic field.

5.3.1 Angle Dependence

Density Variation

The density maps corresponding to three different angles are plotted in figure 5.10. The self-bias developed on the RF electrode corresponding to 0°, 5°, and 20 ° are +17 V, -101 V and -143 V, respectively. In the sheath reversal section of Chapter 4.2 , it is already shown that at this magnetic field, the peak of the density inside the magnetic flux tube is shifted close to the RF electrode when the self-bias is positive. The peak of the density structure is observed to be squeezed along the diameter of the electrode. The ratio of cyclotron frequency to the collision frequency of electrons is 934, showing the high magnetization confines the electrons above the surface of the RF electrode, and explains the observed density profile. The magnitude of the peak density value is $4.5\times10^{17}\ m^{-3}$ for the case of 0° and reduces to lower values $1.8\times10^{17}\ m^{-3}$ and $1.3\times10^{17}\ m^{-3}$ for 5° and 20° respectively. In the case of the straight electrode case, the electrons gain energy from the oscillating sheath and are pushed back along the magnetic field lines creating a density area extending all along the Z axis. For 5° and 20°, one can see that the peak of the density structures are at the edges, both at the top and bottom of the RF electrode along the Y axis.

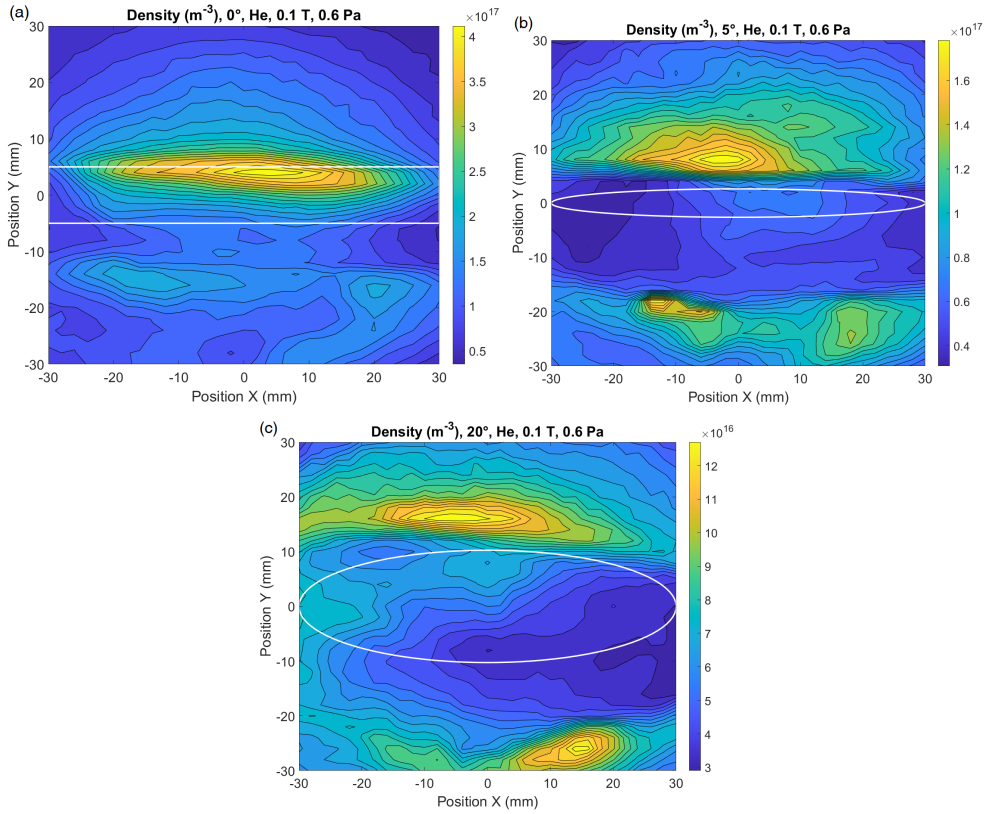

Figure 5.10: 2D density maps at (a) 0° (b) 5° (c) 20° tilt angles corresponding to 0.6 Pa helium discharge at 0.1 T magnetic field for 35 W coupled RF power.

When the electrode is parallel to the magnetic field $\alpha = 0$, the peak of the density structure is mostly centred but slightly shifted to the positive X side of the RF electrode. Below the RF electrode, due to the imperfection in the screening of the RF by the ceramic, high-density structures are formed. These structures have lower density and are separated by a low-density region due to magnetic flux connected to the ceramic ring. When the tilt angle is increased to 5°, the peak of the density structure is shifted slightly to the left of negative axis, the peak density is lower compared to the 0° case, and there are two density peaks present in the -Y part of the RF electrode. The density of the plasma is higher at the bottom part of the RF electrode, and the structures are closer compared to the 0° case. There exists a lower density region between the peaks where there is lower ionization due to the presence of the ceramic and less efficient stochastic heating at the centre of the active RF electrode. When the tilt angle is further increased the self-bias is more negative. The peak of the density structure at the top of the RF electrode is more shifted more to the negative X side of the RF electrode. At the same time, the peak at the bottom is more shifted to the right. The current

magnetic field corresponds to the -0.1 T of the last section 5.2.2, which explains why the structures are rotated in the counterclockwise direction (or to the left above the electrode) all along the X-Y plane, which will be revisited in detail at the effective drift part later in this section.

Floating Potential

Floating potential maps measured using the probe for three angles are plotted in figure 5.11. While comparing the values corresponding to three angles, the minimum of the floating potential value is found at 0° and becomes more positive for higher angles. The region of a minimum of the floating potential is at the edges of the RF electrode for all three cases. It is more evident in the case of the 20° case, where the region where the magnetic field is negative follows the edges of the disc, forming an oval structure around the projection of the RF electrode along the flux tube. It can be concluded that the lowering of the floating potential is closely linked to the presence of a hot electron population and the efficacy of stochastic heating. So these observation is also in agreement with the experiment results using the electrode with grounded walls and predictions from the PIC simulation results 3.2.

Looking closely at each figure, for the parallel case, the floating potential is positive and almost constant for Y values above 20 mm for all X values. For the measurements close to the RF electrode, the floating potential values are more and more negative and highly negative up to -30 V inside the flux tube corresponding to the peak density regime. The presence of the ceramic reduced the efficiency of the collision-less heating and the floating potential is more positive in the flux tube connected to the ceramic part of the RF electrode. Floating potential values get negative again in the region corresponding to the higher density region at the negative Y side of the RF electrode. For the 5° case, there is a projection of the electrode parallel to the magnetic field, and the region of a minimum of the floating potential stays at the edges of the RF electrode both above and below the RF electrode and inside the region in between the floating potential is positive. For the 20° case, the projection area of the electrode along B is higher. The floating potential is minimum at the edges (-10 V), and it is positive up to +30V at the right bottom of the area of the projection of the RF electrode.At the top left of the RF electrode, the floating potential has a positive value, but it is lower than the maximum possibly indicating the presence of hotter electrons in that region. The IVs corresponding to these regions are analysed separately show the difference in the EEDF and the presence of hot electrons have been confirmed in the blue region of the maps (position is indicated in the figure). The blue curve has higher width compared to the red one corresponding to the highest value of floating potential, showing the presence of hotter electrons.

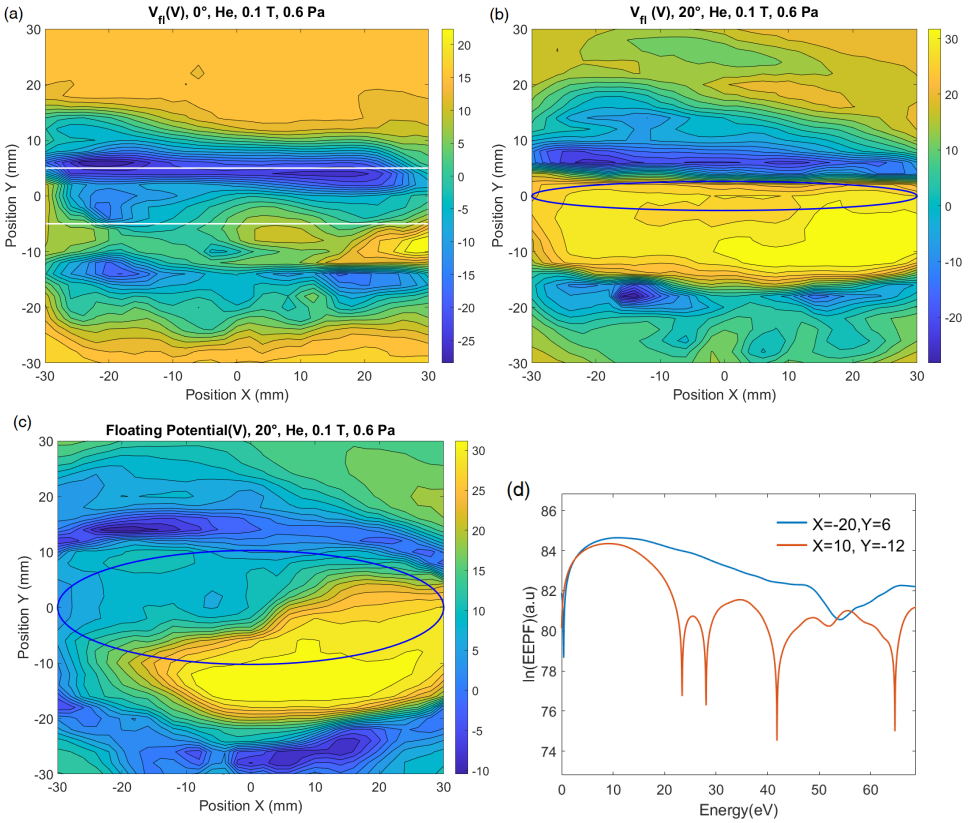

Figure 5.11: 2D floating potential at (a) 0° (b) 5° (c) 20° tilt angles corresponding to 0.6 Pa helium discharge at 0.1 T magnetic field for 35 W coupled RF power. In (d), natural logarithm of EEPF is plotted corresponding to 2 different points in the 20° maps, the blue curve corresponds to the lower floating potential region and red curve is from the high floating potential region.

Plasma Potential

The evolution of the plasma potential with the tilt of the RF electrode is plotted in figure 5.12. The potential of the plasma is always positive and above 25 V at all points in the XY plane.The plasma potential structures are very similar to the floating potential maps, except they are much more noisy, and all measured potentials are positive. As seen in the reversed sheath section, at 0° tilt angle, the sheath almost disappears because the self-bias (17 V) is close or even slightly higher than the local plasma potential just above the electrode. Here, the maps are taken 150 mm away from the electrode along the Z direction, which is beyond the mean free path (between 5 and 10 cm), explaining the higher plasma potential due to the thermalization of electrons. This can explain the slight shift of the density structure to the X positive (instead of X negative at 5 and 20°) in figure 5.10.

When the tilt angle is 5 degrees, the average plasma potential is slightly higher compared to the parallel case. The region corresponding to higher densities, the flux tube connected to the edge of the RF electrode, stays at lower potentials compared to other regions in space. At the same time, the flux tube connected to the RF electrode is at 8-10 V higher than the lower potential region. As seen from the density profiles, the density is lower inside the flux tube connected to the area of the projection of the active RF electrode, there are losses at the electrode and the grounded walls on the other end, which can explain this observed behaviour. Similarly, for the 20° case, the plasma potential in the X-Y plane varies from 28 to 41 V. The area of the projection of the active part of the RF electrode along the magnetic field is wider in this case with respect to the 5° case, and also the region of higher plasma potential. The region of plasma that is connected to the edge of the electrode stays at a lower potential, as seen in the 5° case. From the plasma potential profiles, the electric field on the X-Y plane is used further to determine the drift inside the X-Y plane.

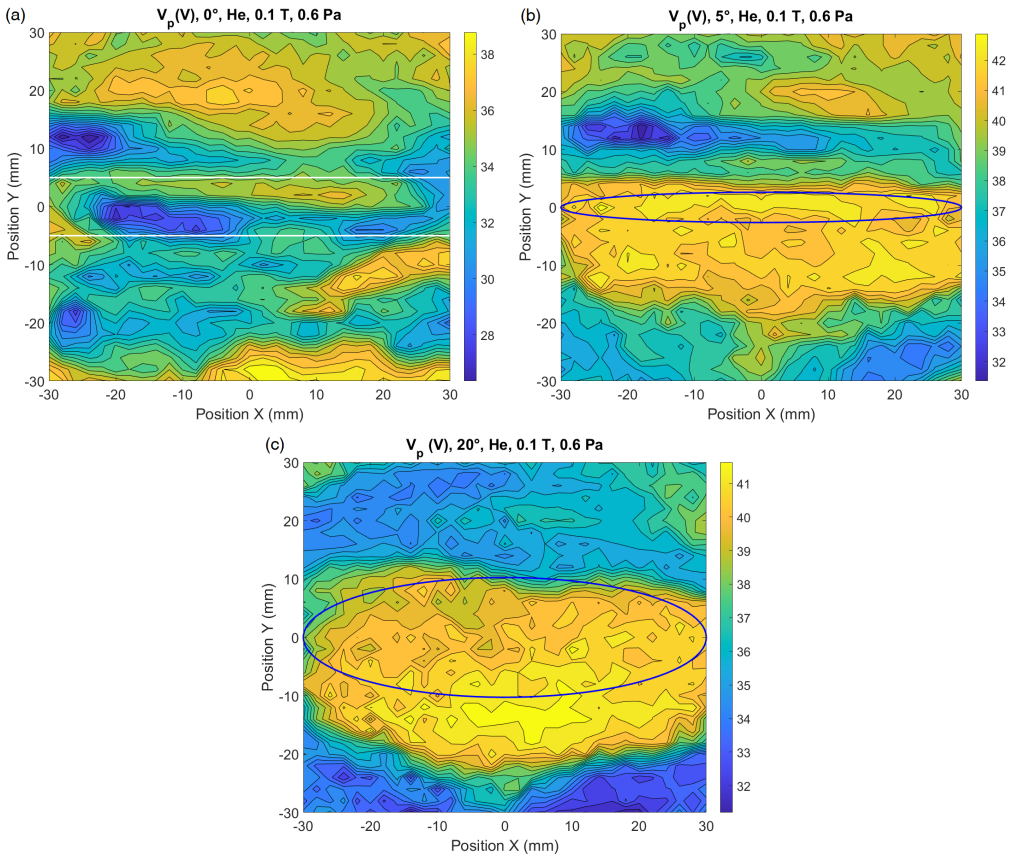

Figure 5.12: 2D plasma potential maps at (a) 0° (b) 5° (c) 20° tilt angles corresponding to 0.6 Pa helium discharge at 0.1 T magnetic field for 35 W coupled RF power.

Effective Drift

The effective drift velocities of three different tilt angles are plotted in the figure here. With increasing tilt angles we have seen that the average $v_{E\times B}$ is reduced in the area above the RF electrode. Whereas the diamagnetic drift velocity above the active electrode has almost the same magnitude ranging from 6-8$\times$ 10^3 m/s. Similar to the electrode with grounded walls case, the diamagnetic drift is in the opposite direction. Considering each scenario separately, the diamagnetic drift dominates (loop 1) the E$\times$B drift inside the plasma column connected to the floating part of the RF electrode at the 0° 5.13a. This explains the slight shift of the density peaks towards the positive X side of the RF electrode. Whereas a few mm above the RF electrode, E$\times$B drift dominates the diamagnetic drift forms loop 2 as in the figure with CCW rotation.

The projection of the RF electrode in 5° case is represented by the blue ellipse. Right above and below the RF electrode, a region of low effective drift is created (region 2) by the counteracting E$\times$B and diamagnetic drift. Strong E$\times$B forms the loops 1 and 3 as in figure 5.13(b). The magnitude of the diamagnetic drift is nearly the half of the average effective drift velocity, and v_{eff} is nearly 6-8 $\times$ 10^3 m/s with clockwise rotation. In discharge with 20° tilted electrode, inside plasma column connected to the RF electrode, the both drifts counteracts creating a low effective drift 5.13(c). There is a E$\times$B dominated CCW rotation which is responsible for the high density structure around the RF electrode.

In all three angle cases, the drift structures derived from the probe data could explain the density profiles. There is a significant change in the self-bias values with the changing tilt of the RF electrode. Reduction in the magnetic field values can also change the bias of the RF electrode since more electrons are reaching the electrode surface due to the lower magnetization. The effect of the magnetic field has been discussed in the next subsection for the parallel electrode situation.

5.3.2 Magnetic field dependence

Density and potential maps corresponding to lower magnetic fields (0.05 and 0.02 T) are taken at Z=-150 mm, are compared with the 0.1 T maps. 2D maps corresponding to 0.1 T magnetic field are already presented in the previous subsection. The decrease in the magnetic field reduces the confinement of electrons, and the corresponding ratio of cyclotron frequency to the collision frequency of electrons is 476 and 187 at 0.05 and 0.02 T magnetic field respectively. More electrons can reach the electrode surface which leads to the biasing of the electrode negatively. At 0.05 T, the self-bias recorded was -3 V and at 0.02 T, -43 V.

The density plot corresponding to the two magnetic fields is presented in figure 5.14. When the magnetic field is reduced to 0.05 T, the nature of the peak density structure evolved to thicker shape, and it is shifted to the positive X side of the RF

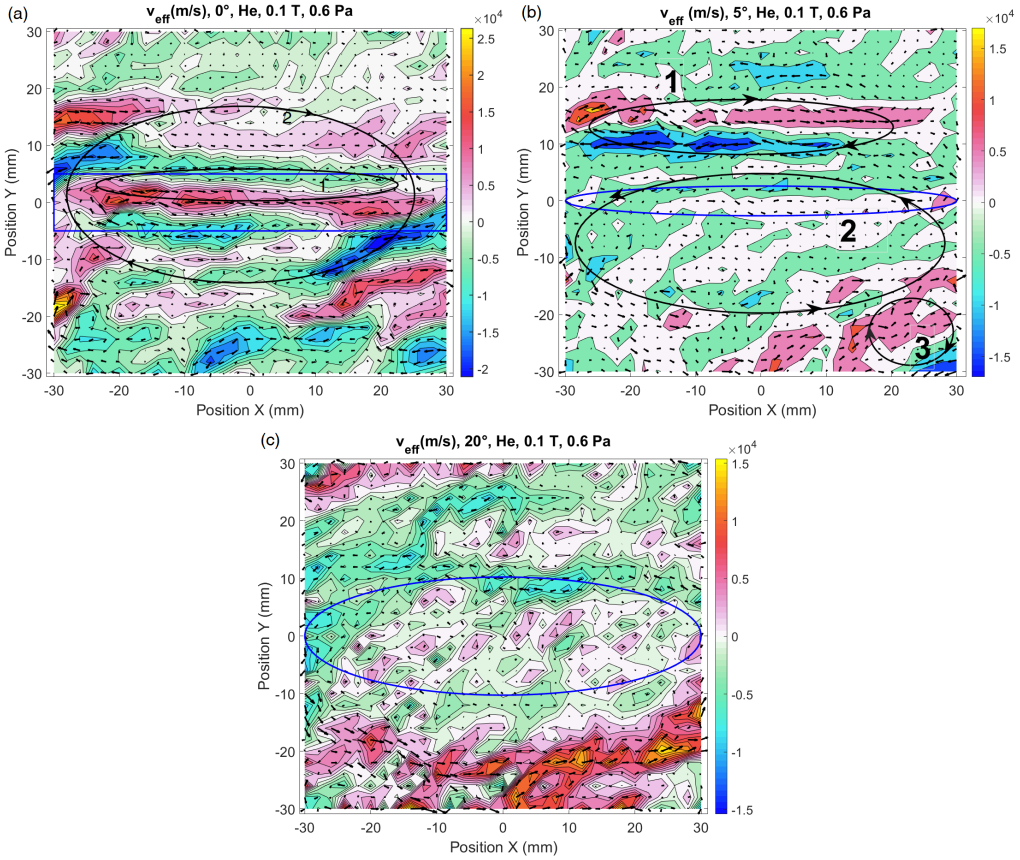

Figure 5.13: Effective maps at (a) 0° (b) 5° (c) 20° tilt angles corresponding to 0.6 Pa helium discharge at 0.1 T magnetic field for 35 W coupled RF power. The direction of the quiver represents the direction of the drift.

electrode. For the 0.02 T, the peak density structure is at the negative X side of the RF electrode. The peak density value has been reduced by 2-2.5 to 3 times respectively, for the 0.05 and 0.02 T cases while comparing with the 0.1 T case. One can notice the shift of the peak density structure to the positive Y directions when the magnetic field is lower due to negative bias on the electrode. This shift of the peak density structure from the negative to the positive X side with the increase in the magnetic field is visually observable and has been recorded using a camera. Outside of the flux tube, the density drops significantly, and there are low-density regions connected to the RF electrode in the case of 0.05 T, which can be explained by analysing the potential profiles. The density maps corresponding to 0.01, 0.02, 0.05, and 0.1 T in the X-Z planes are presented in figure 5.15. X-Z profiles were taken for the Z in the range -20mm to -80 mm for every 5 mm and -30 to +30 along the X axis for every 3 mm for Y =10 mm. The density values are dropping close to the RF electrode since the distance of

measurements is less or in the same order of magnitude of the electron mean free path. It has to be noted that the peak of the density structure shifts close to the RF electrode at higher magnetic fields due to the more positive self-bias compared to lower magnetic field measurements. Hence the profiles can give an insight in the radial electric field above the electrode. The relative Y positions of the density peaks are in both X-Y and X-Z maps in agreement with each other. For all the cases except 0.05 T in figure 5.15, The peak of the density structure is shifted to the negative X side of the RF electrode. A localized higher density flat structure is observed for the case of 0.05 T between Y position in range -70 to -60 mm. An attempt to explain the density distribution around the RF electrode by analysing the potential profile is made as following.

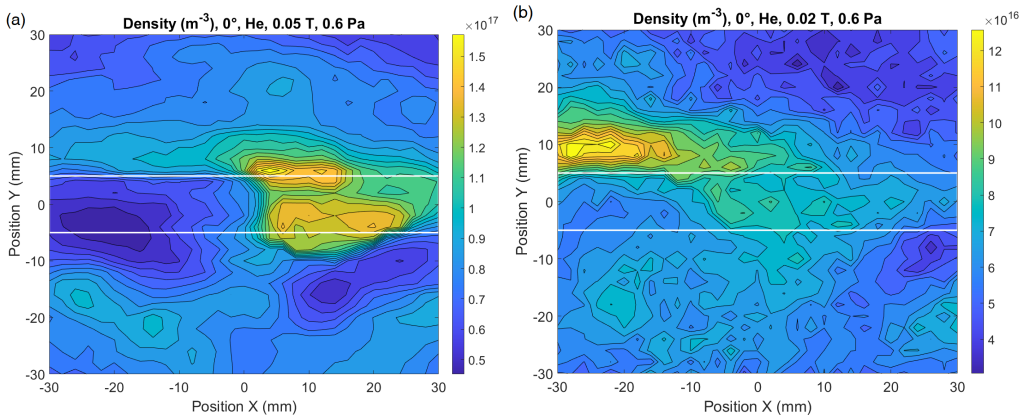

Figure 5.14: 2D density maps at 0° tilt angle corresponding to 0.6 Pa helium discharge at (a) 0.05 T (b) 0.02 T magnetic field for 35 W coupled RF power.

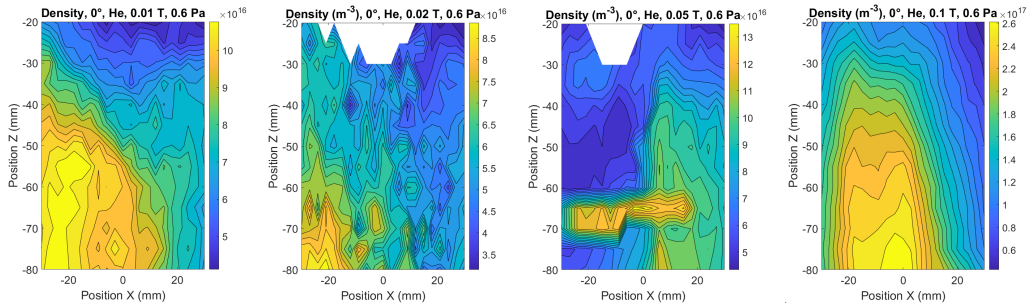

Figure 5.15: 2D X-Z density maps at 0° tilt angle corresponding to 0.6 Pa helium discharge at (a) 0.01 T (b) 0.02 T (c) 0.05 T and (d) 0.1 T magnetic field for 35 W coupled RF power.

Corresponding floating potential and plasma potential profile are presented in the figure 5.16. The plasma potential presented here is noisy, hence the discussions are

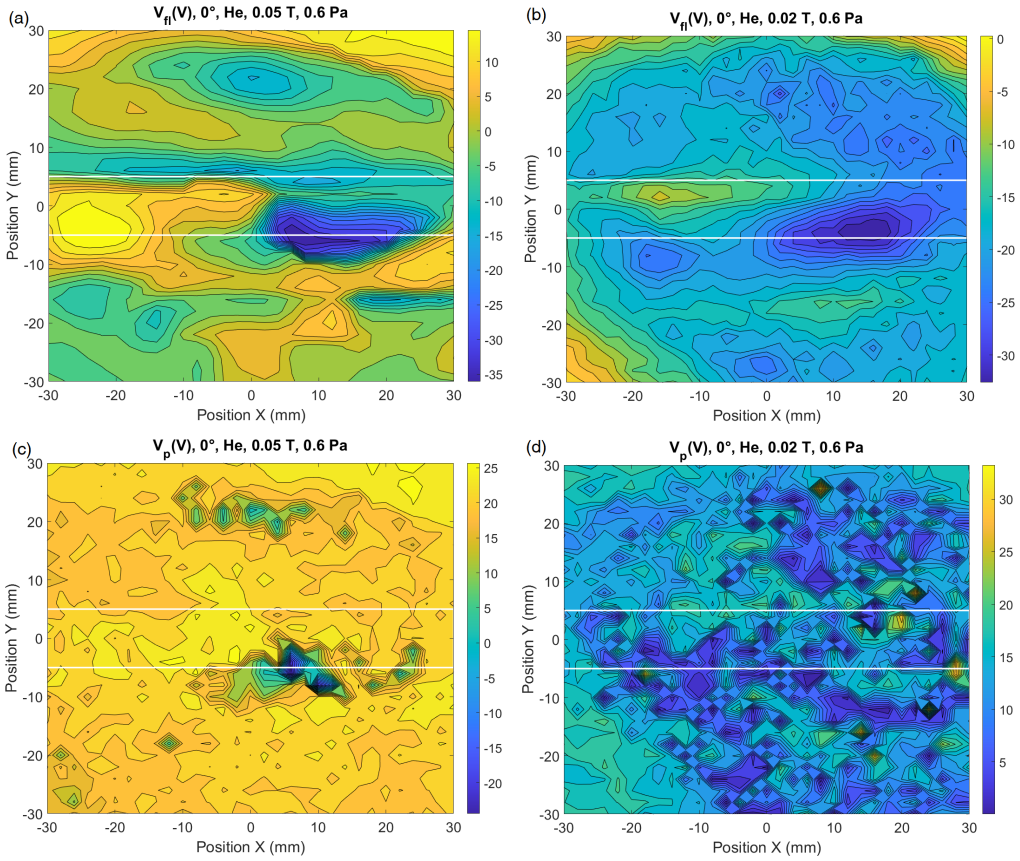

Figure 5.16: 2D floating potential (a) and (b) at 0.05 T and 0.02 T, and plasma potential (c) and (d) at 0.05 T and 0.02 T maps at 0° tilt angle corresponding to 0.6 Pa helium discharge for 35 W coupled RF power.

continued on the basis of the floating potential profile. X-Z maps of the floating potential corresponding to 4 magnetic field values are presented in figure 5.17. If we interpret the decrease in the floating potential as indicative of the presence of energetic electrons within the plasma, we can attribute the shift in the minimum of the floating potential to the migration of these energetic electrons from the positive X side to the negative X side as the magnetic field strength changes from 0.01 to 0.1 T 5.17. At higher magnetic field values, the energetic electrons become confined to a narrow region along the X-axis but exhibit an elongated distribution in the Z-direction 5.17(d).

Due to the noisy potential profile the drift maps are not clear and are not presented here. For the 0.05 T case, the peak density structure is observed at the position where the floating potential is minimum. Similar to what we have seen for 0.1 T maps, the diamagnetic drift 7-12 $\times$ 10^3 m/s inside the plasma column connected to the floating part of RF electrode which pushes the plasma to the right. The resulting density struc-

ture can be explained by the combined effect of strong E×B and diamagnetic drift. Whereas at 0.02 T case, where the density peak is higher, the average $\Delta n/n$ is nearly 0.1 considering the average electron temperature to be 3 eV (Locally it is even higher) the average diamagnetic drift is in the range 1.5-2.5× 10^4. In this region, diamagnetic drift is the dominant drift mechanism responsible for the density peak at the negative X side of the RF electrode.

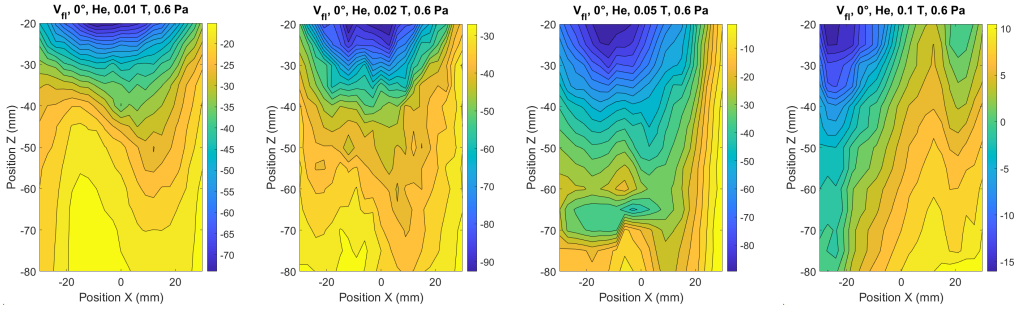

Figure 5.17: 2D X-Z floating potential maps at 0° tilt angle corresponding to 0.6 Pa helium discharge at (a) 0.01 T (b) 0.02 T (c) 0.05 T and (d) 0.1 T magnetic field for 35 W coupled RF power.

5.3.3 Fast Camera results

Fast camera measurements were taken corresponding to 2 different magnetic fields (0.05 T and 0.1 T) at 10^5 frames per second for one-faced electrode case. The background subtracted image after normalising the light intensity field is presented in figure 5.18. The plasma emitted light integrated over the whole visible range is a function of the average density and energy of electrons in that specific region [136; 137]. In ALINE plasma discharge, even though there is a fraction of hot electrons present near the RF electrode, the temperature of the thermal electrons are nearly the same inside the plasma column connected to the RF electrode. Here the intensity of the plasma light is represented in arbitrary units shows the relative population density in the plane of analysis. The images presented here are corresponding to the discharges at 0.6 Pa for a coupled RF power 35 W, which is corresponding to the density profiles that are discussed in section 5.3.2 and 5.3.1.

From the images it is clear that for 0.02 T case, the higher intensity structure is located at the -X side of the RF electrode similar to what observed using the probe. The bright structure above the RF electrode is broadened along the Y axis. Where as for the 0.1 T case, the peak intensity structure is observed to be right above the RF electrode surface and it squeezed along the Y axis and shifted slightly to the positive X axis. The relative intensity is significantly higher above the RF electrode while comparing with

the 0.02 T case, and the density distribution above the RF electrode is matching with the probe measurement.

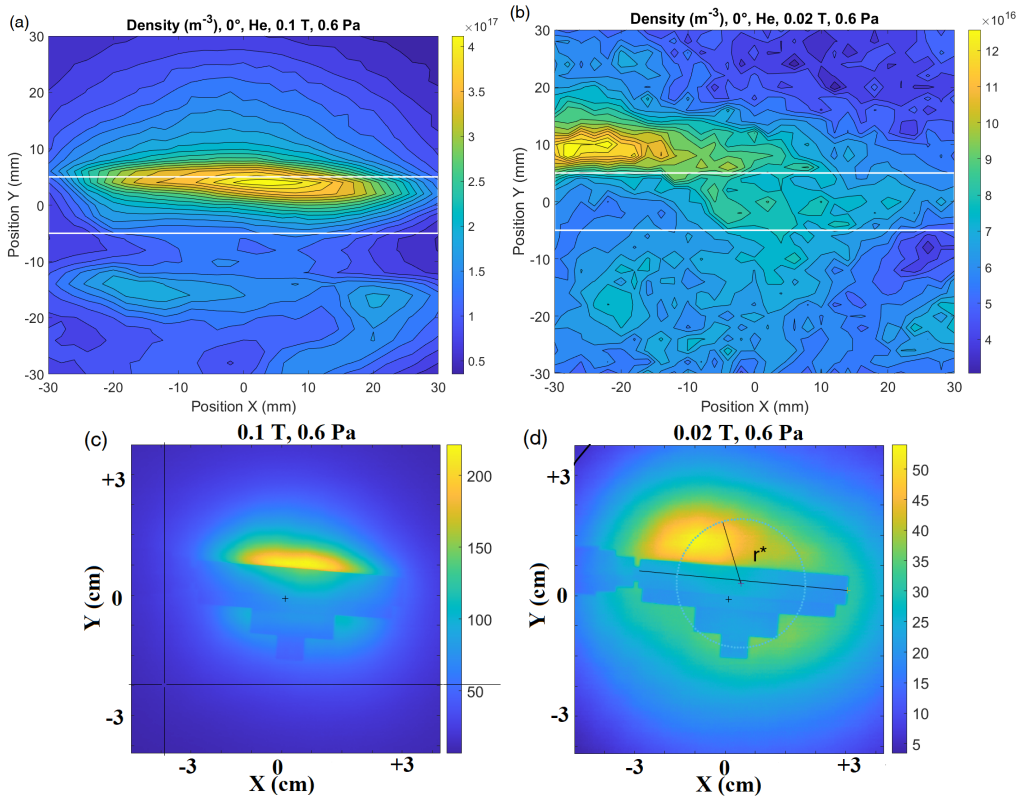

Figure 5.18: Density measurements from the probe (a), (b),and background subtracted Image from fast camera measurements (c),(d) corresponding to 0.1 T and 0.02 T, 0.6 Pa He discharge.

The analysis of the spatio-temporal dynamics of light fluctuations recorded at a frame rate of 67500 fps is presented in 5.18 and 5.20. The light profile is very much similar to the density maps measured using the Langmuir probe while comparing the figure 5.18 and 5.14(b) and 5.10(a) corresponding to 0.02 and 0.1 T measurements. As seen in the density profiles, the peak density structure is at the left side above the RF electrode and wide along the X axis. At 0.1 T the peak density structure is more centered about the RF electrode and squeezed along the Y direction. For a fixed radius about the center point of the RF electrode, 2D-FT inversion is performed to obtain the spatial temporal modes in the poloidal direction, which is shown in figure 5.19. These results reveal the existence of a dominant azimuthal mode m = 1 rotating as a rigid body at the frequency 4 kHz, and a much weaker m=2 mode at 8 kHz, corresponding to weak velocities of the order of 1 km/s.

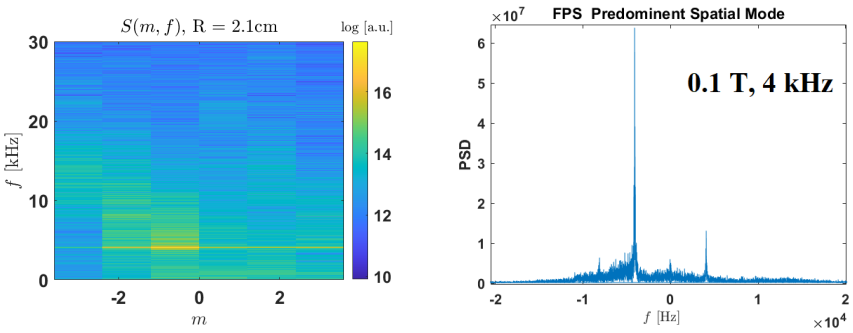

Figure 5.19: Frequency power spectrum corresponding to 0.1 T, 0.6 Pa discharge

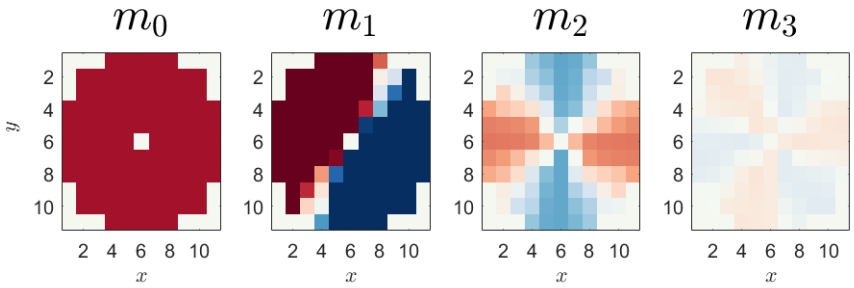

Figure 5.20: Background subtracted Image from fast camera measurements.

One of the possible explanations for the observed discrepancy between the velocity measured using the fast camera and calculated from the probe data could be the Simon-hoh instability [138; 139; 140]. In a weakly ionized plasma with axial magnetic field and radial electric field, the electrons and ions are rotated at different $E \times B$ drift velocities. This difference in the mobility creates a charge separation and electric field in the θ direction. This, along with the density gradient in the direction of the radial electric field, can trigger Simon-hoh instability and can cause a difference of 10 between the electron $E \times B$ velocities and ion azimuthal velocities[141; 142; 143]. Dedicated measurement should be performed to conclude this beyond any reasonable doubt.

5.4 Experiments with Tungsten Electrode

When there is no shielding on the bottom part of the RF electrode, the plasma is generated symmetrically above and below the RF electrode. The bias on the surface is more negative due to the larger collecting area for electrons 5.21 and the shift of the density structures are clearer. To study this, experiments were performed with tungsten RF electrode (the same as before but without the ceramic shield). 2D density profiles

and potential profiles distant from the RF electrode, at Z=-150 mm, are taken using the Langmuir probe, which is discussed in the current section of this chapter. At the same time, in the case of direct coupling, the time average potential (DC component) of the active electrode is zero. Hence, the potential structure around the RF electrode and the density profiles inside the plasma column connected to the RF electrode are strongly modified. 2D scans for different tilt angles of the RF electrode for the direct coupling case are also discussed later in this section.

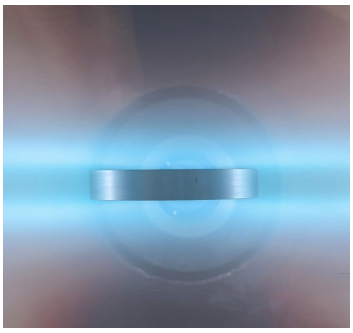

Figure 5.21: Discharge in ALINE device using tungsten electrode

5.4.1 Capacitively Coupled Discharge Results

Effect of Magnetic field

Unlike the ceramic case, the variation of the self-bias with change in magnetic field is less significant, and the self-bias developed on the surface of the RF electrode corresponding to 0.1 T, 0.05 T and 0.02 T magnetic fields when $\alpha = 0$ are -103 V, -129 V and -137 V, respectively for a coupled RF power 35 W at 1 Pa helium gas pressure. All the measurements here are performed at 1 Pa, The gas pressure and electrons are highly magnetized for all the values of magnetized, and the ions are nearly magnetized. The ratio of the cyclotron to collision frequency at 0.1, 0.05 and 0.02 T are 560, 280 and 112, respectively, for electrons and 27.3, 13.6 and 5.45, respectively, for helium ions.

The density maps corresponding to the three magnetic field values are depicted in the figure 5.22. One can see the density peaks at both the top and bottom sides of the RF electrode. The area inside connected to the RF electrode edge, has lower density compared to the surrounding plasma. This is the case for all three magnetic field measurements, but the gradient of the density inside the flux tube is lower for the case of lower magnetic field cases. 128.6, 138.8 and 140 V are the RMS RF voltage of the RF electrode [144] corresponding to 0.1, 0.05 and 0.02 T magnetic fields. The difference in the magnitude between the bias and the peak RF voltage decreases as the magnetic field is reduced. The peak density values have almost the same magnitude

for all three magnetic fields (2-3$\times 10^{17} m^{-3}$). It has to be seen that the peak density structure is shifting to the left as the magnetic field is lowered. This will be addressed in the analysis of the potential and the drift part. As seen before, outside the flux tube connected to the top of the circular sides, the density is dropping on either side. Unlike the one-faced RF electrode, the plasma structure is almost symmetric with respect to the electrode centre.

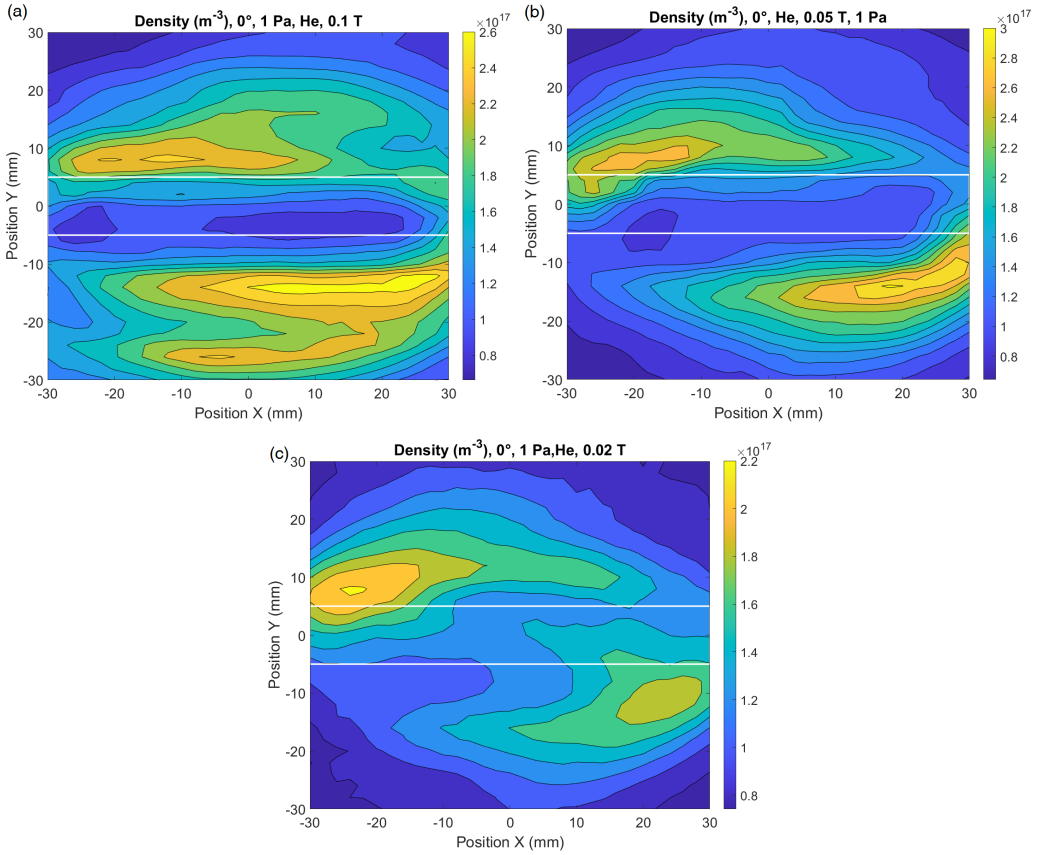

Figure 5.22: 2D density maps of 1 Pa helium discharge with simple W RF electrode for different magnetic field (a) 0.1 T (b) 0.05 T and (c) 0.02 T at $\alpha = 0°$.

The floating potential profile for the three cases are plotted in the figure 5.23. In the region directly connected to the RF electrode edge, where the density is lower, the floating potential values are higher and positive corresponding to the surrounding in yellow. This observation is more evident in the higher magnetic field measurement. The highest value of the floating potential at this region being +15 V, 5 V and -14 V respectively for 0.1, 0.05 and 0.02 T magnetic field respectively.

At higher magnetic field, 0.1 T, the Larmor radius of He ion is 0.1 mm for $T_i = 0.026eV$, the confinement is high and the hot electrons also are confined inside the flux

tube connected to the edge of the RF electrode. The floating potential is negative up to -26 V and at the flux tube connected to the edge of the RF electrode where the density is higher. As the magnetic field is lower, lesser the confinement and hot electrons can diffuse inside the flux tube and hence lower the floating potential even in the flux tube connected to the lateral side of the RF electrode. This also mean the electrons are less energetic inside that region of the flux tube compared to the edge. There is some interesting pattern about the distribution of the hot electrons with changing magnetic field. One can see that the peak corresponding to the minimum of the floating potential value is shifting to the left at the top of the RF electrode and towards the right at bottom side of the RF electrode with decreasing magnetic field. We have seen a similar shift in distribution of the density and floating potential for the case of one faced electrode both from the fast camera and probe measurement results at lower B values.

The plasma potential measured from the IVs using the intersection method is plotted in the figure 5.24 (The profiles using the first derivative method was giving noisy profiles inside the plasma column connected to the RF electrode). The plasma potential values are positive in all the three cases. For the previous cases we have seen that the profile of the plasma is following the floating potential profile. One can see the similar trend in this case especially for the case of 0.1 T measurement. The plasma column connected to the top and bottom circular sides of the active electrode stays at lower potentials and the part which is connected to the RF electrode it self is at higher plasma potential.

Taking input from the 2D potential and the density profiles in the plasma the $E \times B$ and the diamagnetic drift velocities are calculated, the effective drift velocity maps are depicted in figure 5.25.For the 0.1 T case there are two distinct loops around the RF electrode. One is just along the edges of the RF electrode and the direction of rotation is counter clockwise 5.25 (a). The second one is global rotation around a few centimeters away from the RF electrode where the direction of rotation is clockwise. At 0° the diamagnetic drift velocities are in the range of 2-6$\times$ 10^3 m/s. Inside the plasma column connected to the RF electrode, the CW rotation is dominated by the $E \times B$ with drift velocities in range 1-2 10^4 m/s. In the outer loop where the rotation is in CCW direction, is driven by the diamagnetic drift with effective drift speed of 2-3$\times 10^3$ m/s, can explain the shift of the density peak about the RF electrode.

When the magnetic field is reduced to 0.05 T, the drift velocities are higher and effective drift in XY plane can be split in to 3 loops, figure 5.25(b). The first loop is represented by the ellipse in the centre in the CW direction. Along the region around the loop, diamagnetic drift dominates the $E \times B$ with V_{Eff} around 5000 m/s. But inside the loop there is motion of particles to the negative X axis which is driven by the $E \times B$ drift. Outside the loop there are rotation in CCW direction with velocities 2-3 $\times 10^4$ due to a strong $E \times B$ drift. When the magnetic field is 0.02, $E \times B$ drifts are much more stronger and dominates the diamagnetic drifts (4-6 times higher), figure 5.25(c).

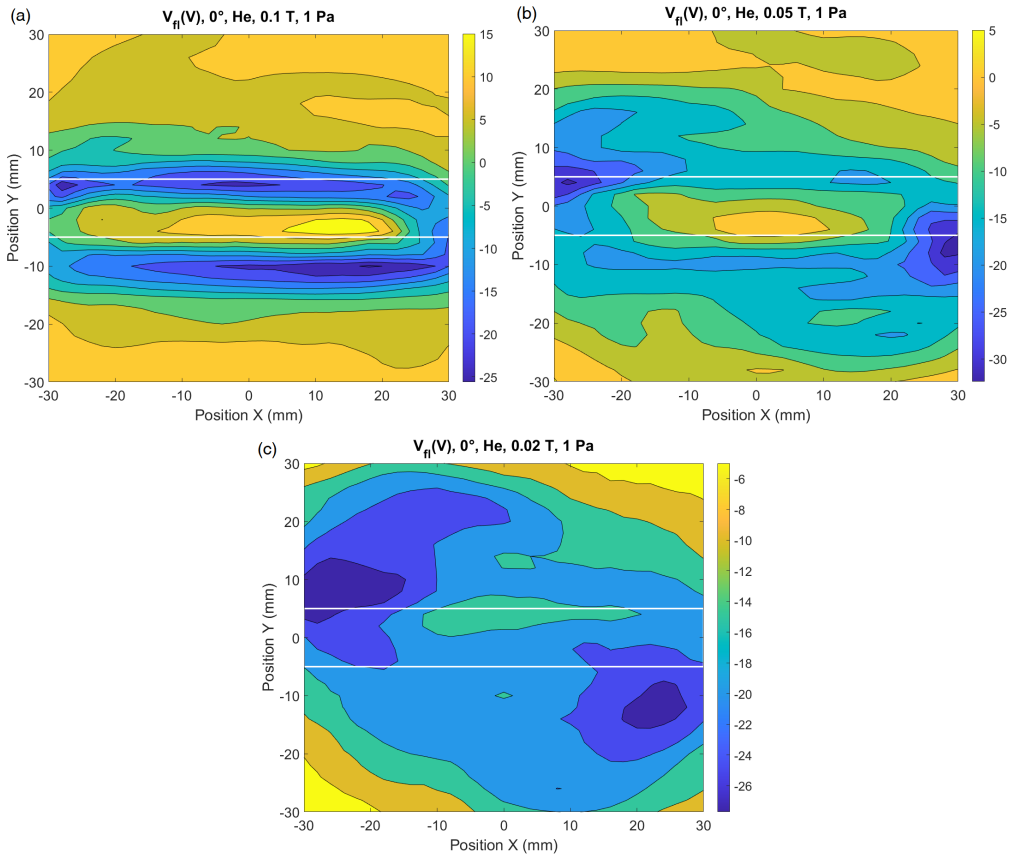

Figure 5.23: 2D floating potential maps of 1 Pa helium discharge with simple W RF electrode for different magnetic field (a) 0.1 T (b) 0.05 T and (c) 0.02 T at $\alpha = 0°$.

Effective drift velocities are nearly in the range of 5 $\times 10^4$ range, in CCW direction inside the plasma column connected to the RF electrode and CW direction outside.

Effect of the tilt angle

The dependence of the tilt angle on the plasma parameters and the distribution of the density and potential has been looked in detail in this section. Plasma parameters around the RF electrode at grazing angles 5° and higher angle 20° are mapped in X-Y plane at Z=-150 mm. When the tilt angle α =5° and 20°, the self bias on the RF electrode is -120 V and -170 V respectively. All the measurements were taken at 0.1 T magnetic field and 1 Pa gas pressure for a coupled RF power of 32-35 W. The RF voltage on the surface of the RF electrode for 5° and 20° are +136 and 163.4 V respectively.

The density maps corresponding to the two tilt angles are presented in the figure 5.26. At the plasma column connected to the RF electrode the density of the plasma

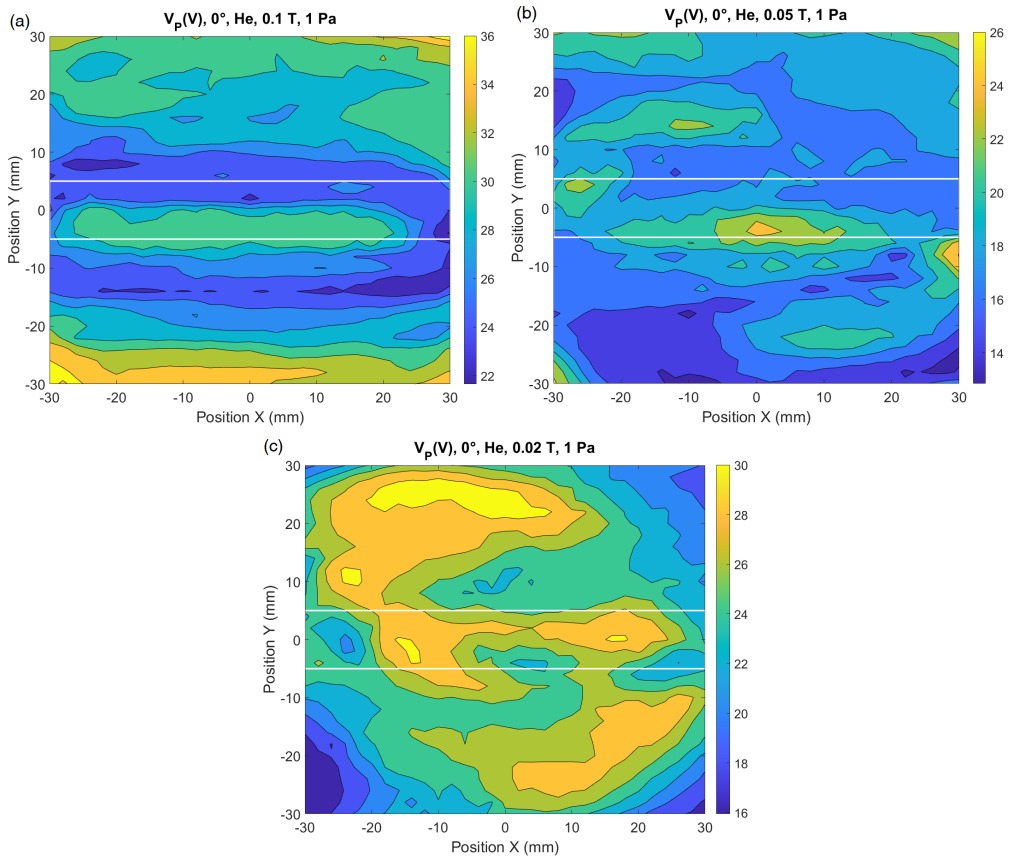

Figure 5.24: 2D plasma potential maps corresponding to 1 Pa helium discharge with simple W RF electrode for different magnetic field (a) 0.1 T (b) 0.05 T and (c) 0.02 T at $\alpha = 0°$.

is lower. As seen before, the peak densities are inside the flux tube connected to the edge of the RF electrode. The magnitude of the peak density values are reduced for the case of 20° case $1.9 \times 10^{17}\ m^{-3}$ compared to the 5° tilt angle case $2.6 \times 10^{17}\ m^{-3}$, which is in turn almost equivalent to the 0° case discussed before. The relative position of the peak density is slightly shifted to the left for the case of 5° with respect to the 20° discharge.

2D Floating potential and plasma potential maps corresponding to the 5° and 20° are displayed in the figure 5.27 (a) & (b). The area of the 2D profile where there is a depletion in the density stays at higher floating potential values as seen in the previous case. At the regions which is connected to the edge of the RF electrode, lowest values of floating potentials are measured, which is -25 V for the case of 5° and close to -5 V for the 20° case.

Plasma potential follows the floating potential profiles in all the presented cases

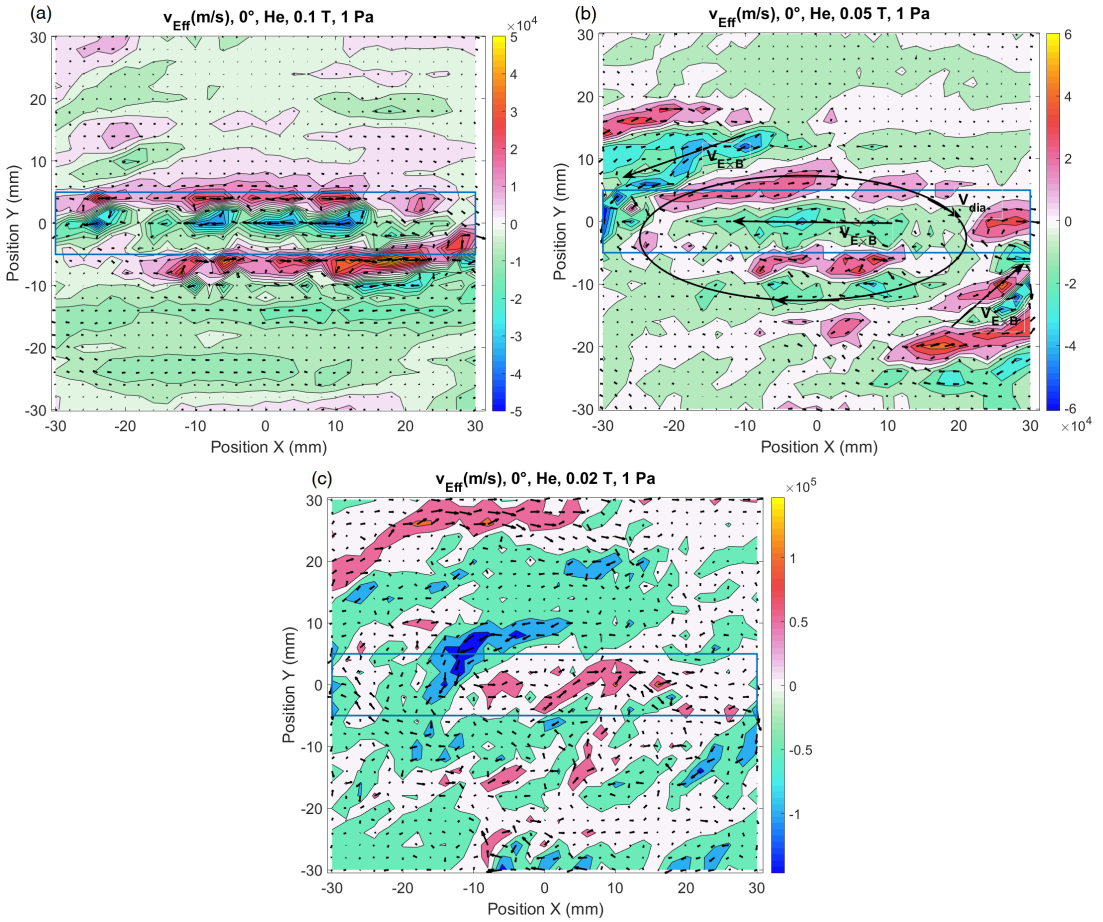

Figure 5.25: 2D effective potential maps corresponding to 1 Pa helium discharge with simple W RF electrode for different magnetic field (a) 0.1 T (b) 0.05 T and (c) 0.02 T at $\alpha = 0°$. In figure (b) the arrow and the loop represents the dominant drift mechanism and its direction locally inside the plasma.

here 5.27c & d. The values are ranging from 17-28 V in the case of 5° and for 20° case the values vary from 29-39 V. The area inside the plasma column which is connected to the RF electrode stays at higher potential. From the 2D potential and the density profiles the effective drift velocities are calculated, see figure 5.27e & f

While comparing the maps between 0°, 5°, 20°; effective drift velocities are reduced with increasing tilt angle. For 5° case, above the RF electrode, there is combined effect of E×B and diamagnetic drift, which are represented by arrows. The effective drift push the plasma to the negative X side of the RF electrode above the RF electrode and in the opposite direction below the RF electrode with average drift velocities 6-8 $\times 10^3$ m/s. At 20°, outside the projection of the RF electrode, the E×B drift dominates

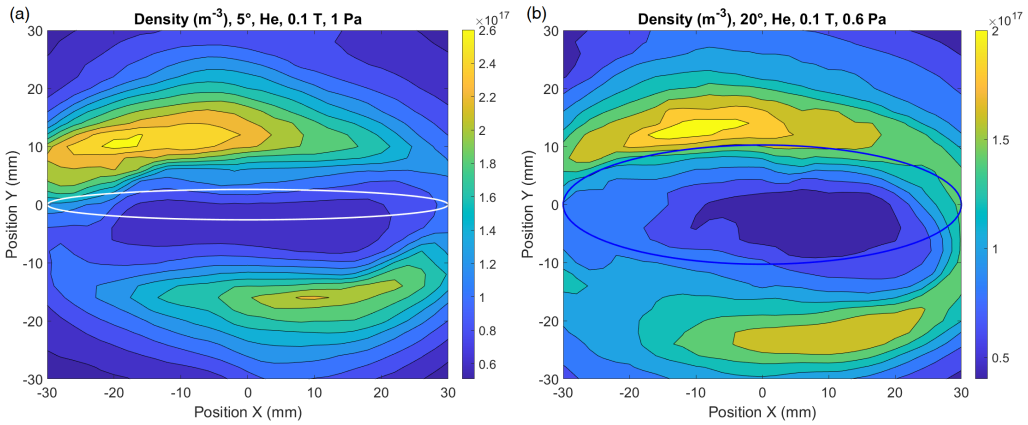

Figure 5.26: 2D density profiles corresponding to 0.1 T, 1 Pa helium discharge at (a) 5° and (b) 20°.

the diamagnetic drift (v_{eff}= 6 $\times 10^3$ m/s). However, the diamagnetic drift is stronger inside the projection of the electrode counteracts the E×B drift resulting a lower drift inside the plasma column (1-2 $\times 10^3$ m/s).

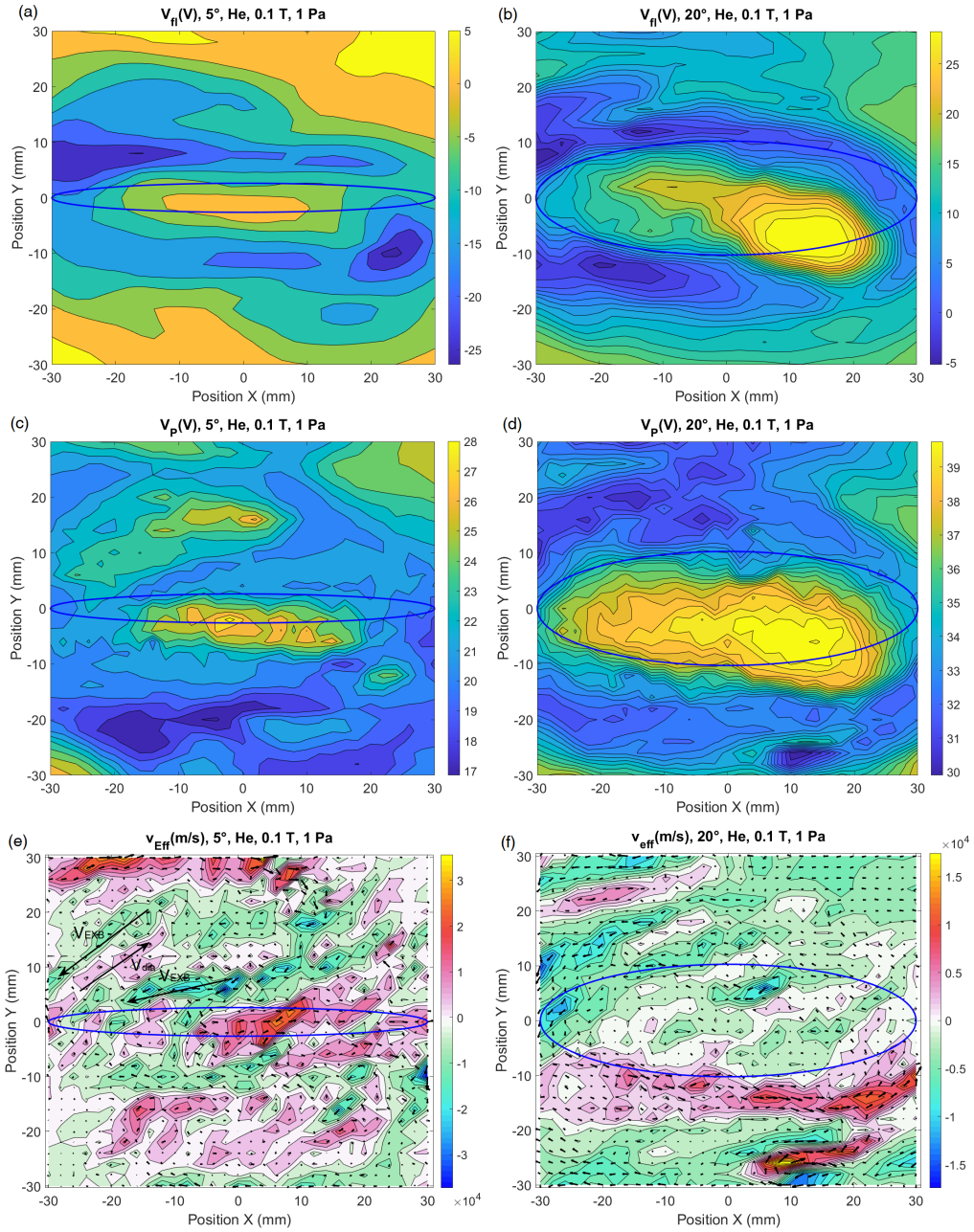

Figure 5.27: 2D density maps of floating potential (a) and (b), plasma potential (c) and (d) and effective drift (e) and (f), corresponding to 0.1 T, 1 Pa helium discharge at 5° and 20° respectively. The arrow in figure (e) represents the dominant drift mechanism and its direction locally inside the plasma.

Effect of tilt Angle- Direct Coupling

In direct coupling, the antenna allows a net DC current through the electrode and hence net DC voltage on the surface of the RF electrode. 2D density and potential profiles were taken in the X-Y plane at Z=-150 mm position for the helium discharge at 1 Pa, coupled power of 32-35 W. Keeping the strength of the magnetic field is 0.1 T, the tilt angle α varied from 0° to 5° and further to 20°. There are no changes in the operating pressure and strength of the magnetic field, which keeps the $\omega_c/\nu_{e/iN}$ values same as in the case of CCP discharge. Since the DC bias on the surface of the electrode is zero, the average energy of ions reaching the RF electrode is proportional to the DC potential of the plasma with respect to the average potential on the surface of the RF electrode (0 V). Whereas the electrons follow the instantaneous RF potential variations and collected by the RF electrode during one of the half cycle of the RF electrode.

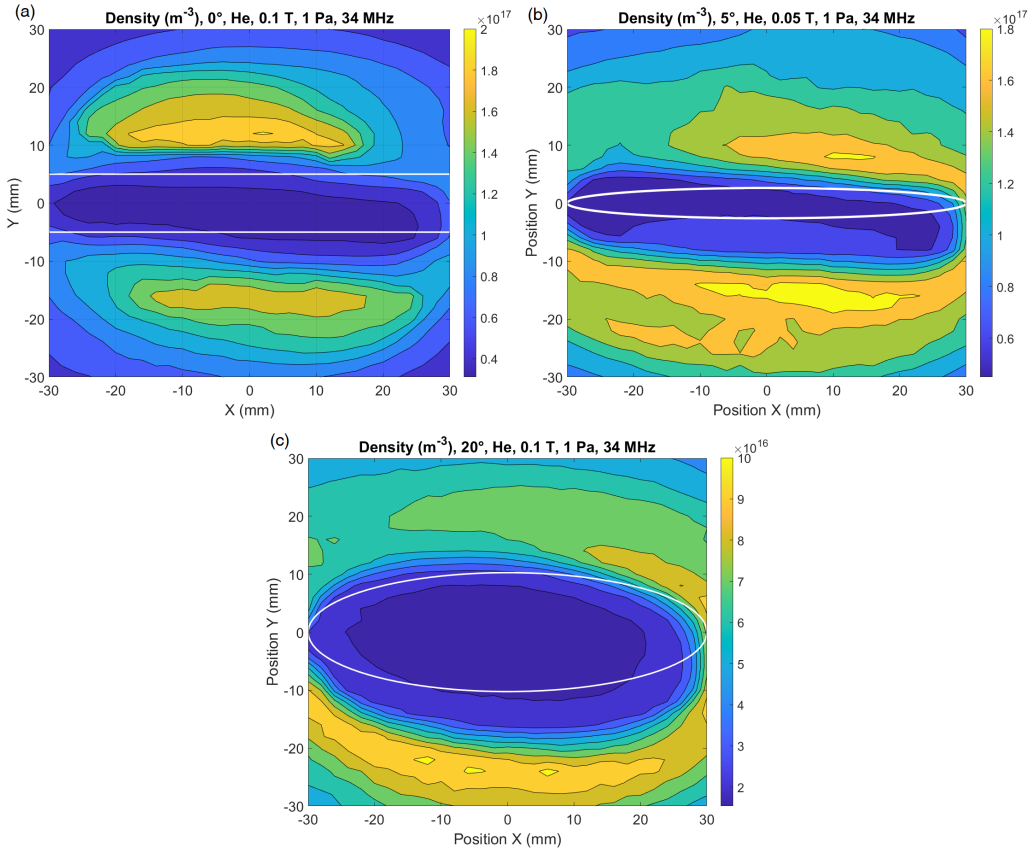

Figure 5.28: 2D density maps of density at (a) 0° (b) 5° and (c) 20° corresponding to 1 Pa helium discharge at 0.1 T magnetic field in direct coupling.

The density profiles in the XY plane for three different tilt angles are plotted in the figure 5.28. At 0°, there are two peak density structures above and below the RF

electrode. The peak density structures are centered with respect to the X position= 0 mm. Whereas there was a shift of the peak density structure to the negative X direction in the case of CCP discharge. There is a strong reduction in the density in the area of in the X-Y plane which is connected to the lateral side of the RF electrode. The peak density values are dropping slightly with increasing tilt angle (2×10^{17} ,1.8×10^{17}, 1×10^{17} m^{-3} for 0°, 5° and 20° respectively). The density distribution around the RF electrode forms continuous structure around the RF electrode in the 5° case unlike the CCP discharge at 5°. In direct coupling in the flux tube connected to the RF electrode, the RF electrode drains the electrons during the positive half cycle and lost on the other side of the chamber during the negative half cycle and to maintain the quasi neutrality the ions are repelled perpendicular to the magnetic field [60].

The floating potential profiles are depicted in the figure 5.29a, b and c. The floating potential measured to be higher at the region connected to the RF electrode for all the three cases. The highest floating potential for all three cases are around 15-25 V. The value of the floating potential out side the area connected to the RF electrode is lower and negative in the surrounding plasma. The minimum of the floating potential values are more positive for higher tilt angles. Similar observations have been seen in the case of CCP discharge in the previous subsections. The lower floating potential regions can be attributed to the presence of hot electrons in the flux tube.

Plasma potential values are evaluated using intersection method due to noisy 2D plasma potential maps using first derivative method. Plasma potential follows the floating potential profiles for all three angles in figure 5.29d, e and f. The values are positive when the flux tube connected to the electrode and at the area lower outside. In all the cases the ions are repelled away from the central flux tube to the edges. Plasma potential values close to zero near the RF electrode which is due to the hot electron generation near the RF electrode and it is extended along the magnetic field lines. It is crucial to acknowledge the direct correlation between these positions and the minimum floating potential values.

Effective drift velocities are calculated using the density and potential profiles as the sum of diamagnetic and E×B drift velocities. At 0°, on the top-left of the RF electrode, there are some high velocity structures. This comes from the noisy potential maps due to the noisy IVs. Disregarding this part, E×B and diamagnetic drifts are in the opposite direction (CW and CCW respectively). The average value of diamagnetic drifts are almost equal or slightly lower than E×B drift velocities, resulting effective drift velocity of electrons ranging from a few 100s to 1500 m/s. For 5° case the direction of the drifts follows the same trend but, $v_{E\times B}$ are 2-3 times higher than v_{dia}. For 20°, there is motion of electrons in the clockwise direction due to the E×B drift with average speed of 1-2$\times 10^4$ m/s around the RF electrode. Average velocity due to diamagnetic drift is around 0.6-1$\times 10^4$ m/s around the RF electrode but in the counter clockwise direction. This gives a effective drift velocity around 0.5-1 10^4 m/s in the

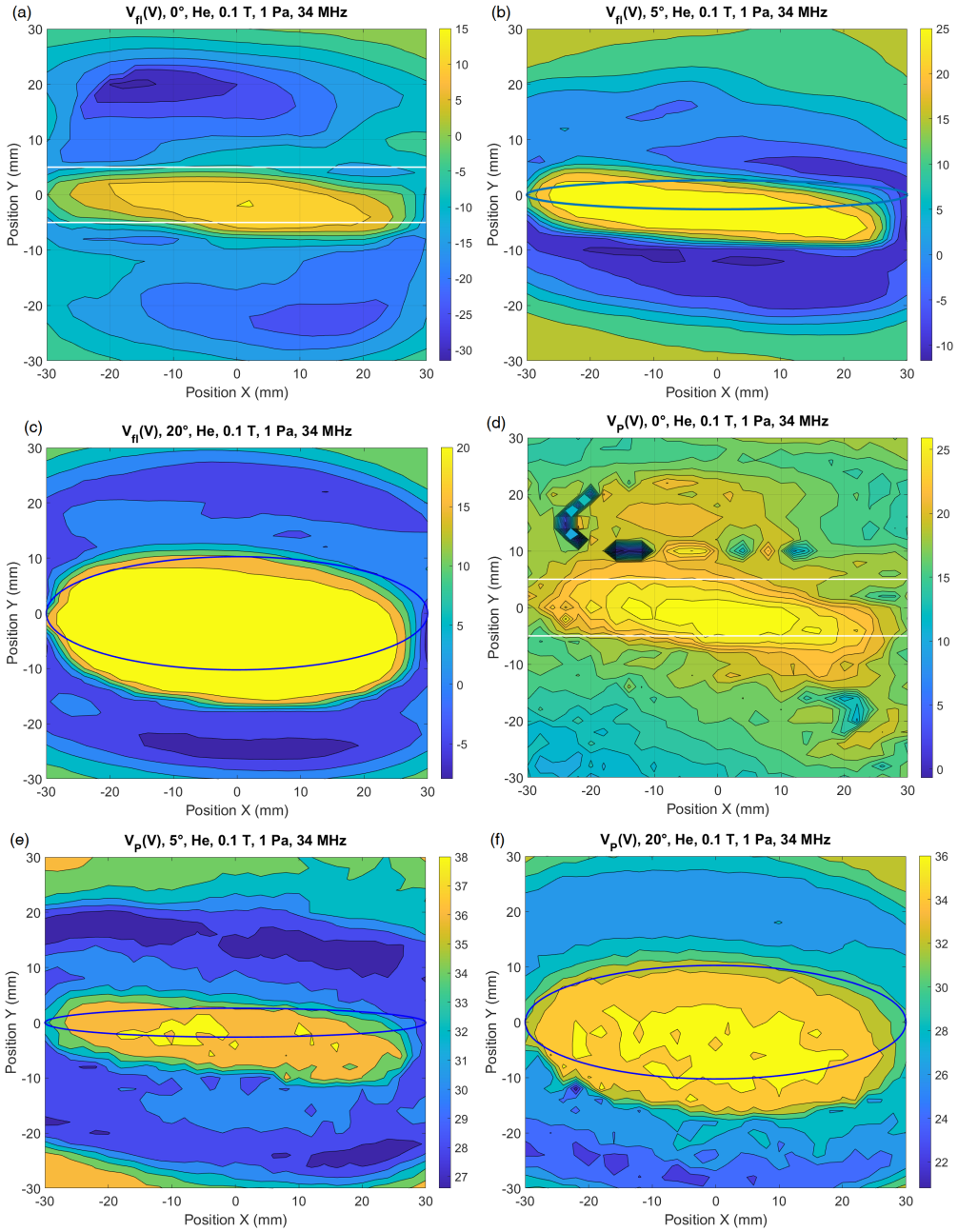

Figure 5.29: 2D floating potential maps for (a) 0, (b) 5°, (c) 20° tilt angles and plasma potential maps (d) 0, (e) 5°,(f) 20° corresponds to helium discharge in direct coupling at 1 Pa pressure and 35 W coupled RF power.

clock-wise direction due to the dominant E×B drift. While comparing the effective drift velocities of three angles, the lowest of all is found for the straight electrode

where the diamagnetic and E×B drifts have almost the same magnitude. There are two rotation of electrons at higher angles counter clockwise around the projection of RF electrode and clockwise a few centimeter above it. Drift velocities are higher at 5° and 20° compared to parallel electrode.

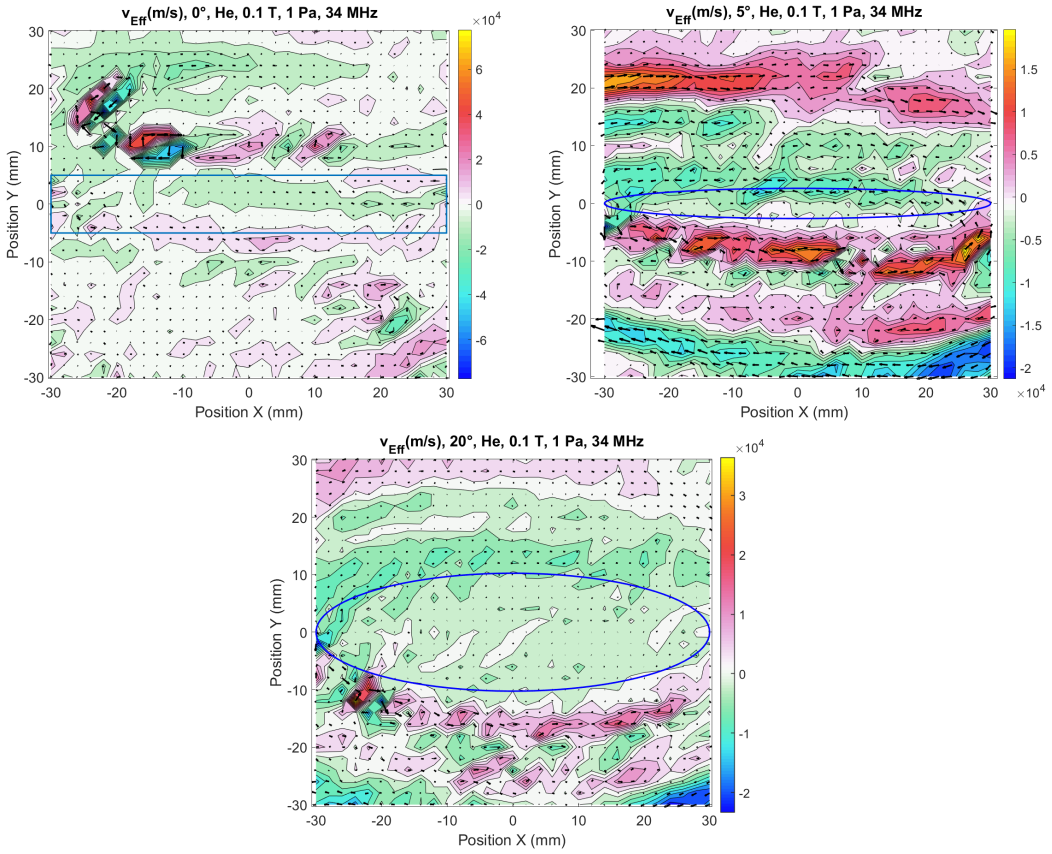

Figure 5.30: 2D effective drift maps of density at (a) 0° (b) 5° and (c) 20° corresponding to 1 Pa helium discharge at 0.1 T magnetic field in direct coupling.

5.5 Conclusion

2D density potential maps were studied for 3 different electrodes, by varying the tilt angle and the strength of the magnetic field in ALINE device. Diamagnetic and E×B velocities are evaluated from the probe data, which shed light on the distribution of the density of plasma around the RF electrode. The plasma around the RF electrode is highly in-homogeneous especially at 0° or 5° tilt angles due to the drifts in ALINE, the peak E×B drift velocities are 2-5 times higher than v_{dia} in all the cases but locally, however the diamagnetic drifts can dominate.

Experiments were performed to investigate the evolved sputtering pattern at 5° grazing angles at -100 V self-bias using RF electrode with grounded copper walls. From the obtained 2D density and potential maps, it is found that the direction of the magnetic field and the tilt of the RF electrode modify the localisation of the hot electron populations and the distribution of the density around the RF electrode due to the effective drift. At lower angles, the $E \times B$ drifts dominate the diamagnetic drifts. However, at higher angles, the diamagnetic drift counteracts $E \times B$ drift and the effect drift velocity is lowered. This is observed for both argon at 30° and helium at 45°. Similar observation is found in experiments with other 2 electrodes irrespective of the coupling mechanism. The shift of density peaks in the opposite direction observed in the X-Y and X-Z maps due to the reversal of the magnetic field direction confirmed the influence of drifts in the density distribution around the RF electrode. The evolved asymmetric sputtering pattern is a cumulative effect of the drifts and the sheath structures which explains the strong sputtering at the edges. Sputtering experiments at higher angles should give more uniform patterns at the cost of lower sputtering yield due to the reduction in the average density.

For the one-faced tungsten electrode with floating ceramic wall, from the analysis of the probe data it is seen that in most of the case the E×B drift and diamagnetic drifts are in opposite direction. Higher magnetic field creates higher asymmetry of potential, density and pressure (the electron temperature variation has not been considered in our analysis) around the RF electrode. For parallel electrode discharge, V_{dia} is higher above the electrode surface than $V_{E\times B}$, so that the shift in the peak density is in the direction of the diamagnetic drift. Although both drift velocities increase with decreasing magnetic field, the average increase in effective drift velocity is not large because they oppose each other. In chapter 3, it has been seen that the average electron temperature is higher inside the plasma column right above the RF electrode with the presence of a fraction of hot electron population. Taking electron temperature as 3 eV, might lead to underestimation of the diamagnetic drift. Background subtracted image showed the similar shift in the peak density structure as measured by the RF compensated Langmuir probe. But the velocities of the structure measured using the fast camera, which is the global rotation is measured to be around 0.6-1.5 km/s which is far from the probe measurements results. The probe measures the local drift velocities, where as averaging over the whole 2D plane can give close to fast camera values. But, fast rotations with nearly the magnitude of 15-30 kHz are observed in hall thrusters locally with average velocities of structures nearly 2-3 km/s in [145; 146]. Probe measurements presented here are far away from the RF electrode, where the camera look in to a plane right above the RF electrode which can also be responsible for the observed discrepancies (2D scans has been performed close to the RF electrode, not presented here due to noisy potential profiles).

Experiments with tungsten electrode showed similar variations in the drift veloc-

ities with magnetic field and the tilt angles. Drift velocities were smaller inside the plasma column connected to the RF electrode in direct coupling compared to the capacitive coupling discharges. The effective drift velocities were higher at grazing angles in direct coupling in comparison with 0° and 20° discharges due to the strong E×B drift, explains the shift of the density peak above the RF electrode at 5° tilt angle discharge. This also explains the smaller shift in the density peak in the case of direct coupling compared to the capacitive coupling for parallel electrode case. By varying the tilt angle, one can find an optimum point (Which has to be investigated detail by taking more 2D profiles) at which the diamagnetic drift counteracts the E×B resulting in a more homogeneous distribution, which can give a more homogeneous sputtering pattern. This can only be confirmed by sputtering experiments. This also gives an insight to the heat flux which won't be uniform to the RF electrode. The heat fluxes will be discussed in the next chapter.

Chapter 6

Experimental Investigation of Heat Flux to the RF antenna at grazing angles in Magnetized RF Discharge

Contents

6.1 Introduction . . . 142
6.2 Experiment and Analysis . . . 143
6.3 Script of the Heat flux Analytical Model . . . 143
6.4 Results : One faced Electrode . . . 147
6.4.1 Langmuir probe results . . . 147
6.4.2 IR Camera Measurements . . . 149
6.4.3 IR Camera Results using TEDDY . . . 151
6.4.4 Results : $\alpha = 0^{\circ}$ . . . 152
6.4.5 α=5° Measurements . . . 157
6.4.6 $\alpha = 20^{\circ}$ Results . . . 160
6.5 Experiments with Tungsten Electrode . . . 161
6.5.1 DC self-bias . . . 161
6.5.2 Heat flux Measurement results . . . 162
6.5.3 Comparison to the Analytical Model . . . 164
6.6 COMSOL Results . . . 165
6.7 Conclusions . . . 169

6.1 Introduction

In modern fusion reactors, even though all the plasma-facing components (PFC) are made of high-refractory metals such as tungsten, the threat of high heat flux and the erosion of the tungsten creating impurities in the plasma persist as a challenge [7]. Plasma surface interactions and surface erosion experiments are being carried in differents tokamaks such as ASDEX-Upgrade (AUG with tungsten) or Alcator C-mod (Molybdenum) as a major step towards fusion reactors [147; 7; 148]. Ion cyclotron resonance heating is one of the main auxiliary heating mechanisms used in fusion devices; the electric fields parallel to the magnetic field generated by RF sheath rectification accelerate ions to the surface [6; 149]. This effect can be further intensified by self-sputtering of impurities [6]. The distribution of ion energies near the Faraday shield of an RF antenna has been studied in experiments, and in a computational model by Caughman in [150]. Hot spot formation in the main limiter of Alcator C-Mod during the ICRH operation is understood to be due to the fast ion impact [151; 147]. In Tore Supra, hot spot formation on the IRCH antenna has been observed during the high power operations using IR camera imaging [152]. Garrett et al. have shown the reduction in RF potential by studying the alignment of the RF antenna with the magnetic field by finite element method [153]. It is also possible to work on the antenna's design to significantly reduce the impurity production, for instance by using multistrap antennas to cancel the RF image current at the antenna's PFCs [154]. In light of this background information, to understand the fundamentals of the heating of the RF antenna/electrode in a magnetic environment, a parametric investigation was carried out in ALINE by varying the RF power, magnetic field, gas pressure, and the angle between the RF electrode and the magnetic field.

The plasma environment in the ALINE device is far from the edge plasma in a tokamak, but these experiments can give insight into the physics of energy influx to the RF electrode. Linear cylindrical geometry offers versatility in the operation, and the results can also be useful for plasma-based material processing applications. From a material treatment perspective, the heating of the substrate surface can affect the quality and the efficiency of etching, deposition or surface modification of thin films in low-temperature, low-pressure plasmas [155]. In low-temperature plasma, the heating of the electrode can be due to ions, electrons and their recombinations. Biasing the substrate and measuring the heating of the RF electrode using the thermal probe has shown that the heating is predominantly due to ions when the bias is negative and that electrons are responsible for the heating when the bias is positive [155]. Frequency dependence on the ion bombardment on a grounded surface in both direct and capacitive coupling has been explored experimentally by Kohler et al. in [13]. Ohter experiments have been performed to study energy influx measurements using thermal probes and calorimetric probes [156; 157; 158; 159]. An overview of this topic is presented in [160].

In this chapter, the heating of the RF electrode is measured using the IR camera. The thermography inversion algorithm (TEDDY) developed by Fedorczak et al [70] is used to estimate the heat flux. The results from the IR camera are then compared with a simple analytical model, taking input from the Langmuir probe measurements.

6.2 Experiment and Analysis

The heat flux experiments were carried out for two different electrode configurations (a) Tungsten electrode with ceramic covering (one-faced electrode) and (b) simple tungsten electrode (without ceramic). In the first part, heating of the RF electrode has been measured corresponding to 0°, 5°, 20° at 0.6 and 1 Pa He gas pressures for 0.01, 0.02, 0.05 and 0.1 T at -4,-7 and -10 dB RF power (35, 70 and 135 W respectively). Corresponding plasma parameters were measured using an RF-compensated Langmuir probe with a cylindrical probe tip. In the second part, the experiments were performed with the simple tungsten electrode. There is a parallel flux to the RF electrode at 0° tilt angle when there is no ceramic cover, which biases the electrode negatively, which is discussed in detail in the results section 6.5. The heat flux to the RF electrode is studied for two different power inputs (35 W and 130 W) at 1 Pa helium gas pressure for two different magnetic fields (0.05 T and 0.1 T). In capacitive coupling, when the bias on the surface of the RF electrode is negative, the heat flux predominantly depends on the ion heat flux, electrons being mainly repelled except for the hottest ones according to their energy distribution inside the flux tube connected to the RF electrode. The heat flux measurement to the simple electrode is performed at 0° and 5° for both direct and capacitive coupling.

Scans along the Y axis and in the X-Y planes have been performed to study the evolution of the plasma parameters and have been used as inputs in the analytical modelling. The scan along the Y axis is performed for Z=-150 mm, which does not reflect the density values near the RF electrode. Hence, a correction factor is introduced based on the measurements close to the RF electrode in the analytical model, which is explained in the model section. The density is evaluated using the OML method and plasma potential using the first derivative method in all the cases. The heating of the RF electrode has been modelled using the COMSOL-heat flux module, and results from all these models are compared with the IR camera results obtained using TEDDY [70]. The details of the analytical model are presented in the next section.

6.3 Script of the Heat flux Analytical Model

Experiments were performed with a tungsten electrode covered with ceramic shielding, which allows the heat flux collection only through one of the circular faces of the

electrode (see figure 6.3). In ALINE plasma, the electrons are magnetized even at the low magnetic field value of the presented work, whereas the ions are weakly magnetized at the operational pressure of the presented work. However, the ion flux can be evaluated using the simple Bohm approximation. The electrons are considered to follow the Maxwellian distribution of the RF electrode.

The velocity distribution of Maxwellian electrons can be represented by the expression:

$$f(v_x, v_y, v_z) = n_0 \left(\frac{m}{2\pi k T_e}\right)^{3/2} \exp\left(-\frac{m({v_x}^2 + {v_y}^2 + {v_z}^2)}{2kT_e}\right) \tag{6.1}$$

Heat flux of species x (electrons or ions) following a distribution function *f(v)* and having velocities v_x, v_y, v_z along x , y and z directions to an attracting (equation 6.2a) or repelling wall biased at potential ϕ (equation 6.2b) can be represented by:

$$H_x = \int_0^\infty \int_{-\infty}^\infty \int_{-\infty}^\infty \left(\frac{1}{2}mv_x^2 + \frac{1}{2}mv_y^2 + \frac{1}{2}mv_z^2 - q\phi\right) v_x f(v) dv_x dv_y dv_z \tag{6.2a}$$

$$H_x = \int_{v_{xlim}}^\infty \int_{-\infty}^\infty \int_{-\infty}^\infty \left(\frac{1}{2}mv_x^2 + \frac{1}{2}mv_y^2 + \frac{1}{2}mv_z^2 - q\phi\right) v_x f(v) dv_x dv_y dv_z \tag{6.2b}$$

As of now, the ion and the electron flux are obtained for capacitive coupling using the equations given as follows [21]. If the potential difference between the plasma and the biased wall is$(V_P - \phi_{DC})$ the heat flux due to ions (considered to be cold, $T_i = 0.026$ eV) to the surface is evaluated as given below.

$$H_i = n_0 C_s (\gamma_i k T_i + \frac{1}{2} k T_e + e(V_P - \phi_{DC})) \tag{6.3a}$$

Here, γ_i represents the ion sheath transmission coefficient [21]. The heat flux due to electrons to the RF electrode can be formulated under the potential difference $V_P - \phi_{DC}$ as:

$$H_e = n_0 \sqrt{\frac{kT_e}{2\pi m_e}} 2kT_e \exp\left(-\frac{e(V_P - \phi_{DC})}{kT_e}\right) \tag{6.3b}$$

The total heat flux to the surface of the electrode can be written as:

$$H = C_1 H_i + C_2 H_e \tag{6.3c}$$

Here n_0, C_s, T_i, Φ_{DC}, T_e, m_e, V_P are the density, ion-acoustic speed, ion temperature, DC self-bias on the surface of the RF electrode, electron temperature, mass of the electron and the plasma potential respectively. The source areas for the flux of particles to the surface of the RF electrode for the ions electrons are different. An effective area

factor is introduced to include these changes in the source areas. The energy reflection coefficient for tungsten material is reported to be in between 0.6-0.7 in literature [161]. The constant C_1 and C_2 are introduced in these equations to incorporate the reduction in the density factor (in the range 0.33-0.5) near the RF electrode along with the energy reflection coefficient and the effective flux collection area (effective area factor) of the RF electrode. Values of C_1 and C_2 are different for the electrode with ceramic and without ceramic which has been calculated separately in each case during calculations.

For direct coupling at low-pressure discharges, the constant plasma potential can be approximated as follows [12]:

$$\overline{V_P} \approx \frac{1}{\pi}\int_0^{\pi} \phi_{RF} sin(\omega t) d(\omega t) \approx \frac{\phi_{RF}}{\pi} \tag{6.4}$$

Knowing the plasma potential or the RF voltage, the ion flux to the RF electrode can be estimated as:

$$H_i = n_0 C_s(\gamma_i k T_i + \frac{1}{2} k T_e + e\phi_{RF}/\pi) \tag{6.5a}$$

For Maxwellian electrons, the flux of electrons to the electrode surface can be expressed by:

$$H_e = n_0 \sqrt{\frac{kT_e}{2\pi m_e}} 2kT_e exp\left(-\frac{e\phi_{RF}}{\pi k T_e}\right) \tag{6.5b}$$

ϕ_{RF} RF voltage on the surface of the RF electrode. Total heat flux to the surface of the RF electrode is calculated using 6.3c.

Determination of the Effective area factor for electron and ions

One of the biggest problems in the analytical model is optimising the size of the source column from which the ions and electrons are reaching the electrode surface. Since there is relatively low ionization in the sheath above the RF electrode, the source of electron and ion flux is predominantly the plasma column connected to the sheath surface, see figure 6.1. The size of the source changes with the electrode configuration, magnetic field and the choice of electrode. So, an effective area factor (ratio of source area to the total collection area of the electrode) is introduced to include this variation in this model.

For electrons, the effective collection area by the RF electrode for different electrode configurations and tilt angles are found as follows.

Case 1 : For the 0° case, it is assumed that all the electrons above the RF electrode in the range of $2r_{Le}$ are collected by the RF electrode. To take this into account, an ellipse of major radius R and minor radius r_{Le} is considered as the area of the source of

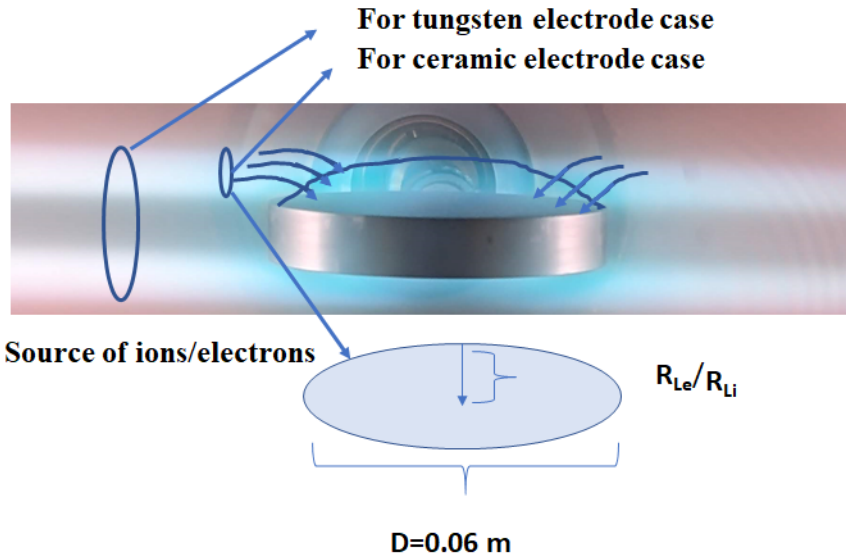

Figure 6.1: Drawing to illustrate the source of electrons and ions from the plasma to the RF electrode.

electrons from both sides to the RF electrode. The effective area factor A_{eff} is calculated as

$$A_{eff} = \frac{2A_{ellipse}}{A_{electrode}} = \frac{2\pi R r_{Le}}{R^2\pi} = \frac{2r_{Le}}{R} \tag{6.6}$$

Factor 2 is to include the contribution from both the sides.

case 2 : For α° case, it is assumed that the electrons are collected from an ellipse of major radius R and minor radius $r_{Le} + Rsin(\alpha^\circ)$. Hence to introduce this factor, the source area is normalised to the total collection area of the RF electrode which is evaluated as:

$$A_{eff} = \frac{2A_{ellipse}}{A_{electrode}} = \frac{2\pi R(r_{Le} + Rsin(\alpha^\circ))}{R^2\pi} = \frac{2(r_{Le} + Rsin(\alpha^\circ))}{R} \tag{6.7}$$

case 3 : For α° simple tungsten electrode case, there is an area of projection for the RF electrode parallel to the magnetic field lines. Unlike the last case there is an additional factor of projection length of the RF electrode along the Z direction is added to the minor radius, which will be (t/2+$r_{Le} + Rsin(\alpha^\circ)$).

For weakly magnetized ions, defining the source area based on the ion Larmor radius will underestimate the flux to the RF electrode. So, for the one-faced electrode

case, the size of the bright column, which is nearly 2 cm above the RF electrode is considered to be the size of the source at 0° and 5°. So, the effective area factor is evaluated considering an ellipse of major radius R and minor radius 1 cm and dividing with the total collection area of the electrode. At 20°, half of the projection length of the RF electrode along the perpendicular to the B is taken as the minor radius of the RF electrode.

An ellipse of minor radius $t/2 + R * sin(\alpha)$ and major radius R is considered as the ion source area for the simple tungsten electrode case.

6.4 Results : One faced Electrode

The measurements of the heating of the one faced RF electrode from IR camera are presented in this section for different tilt angles. IR measured heat fluxes are then compared to the analytical model presented in the previous section.

6.4.1 Langmuir probe results

Table 6.1: ALINE plasma parameter.

Quantity	Electrons
Pressure(Pa)	0.6 - 1
Magnetic field B (T)	0.01- 0.1
Density(n)(m^{-3})	$5 - 70 \times 10^{16}$
Power (W)	35, 70, 130
T (eV)	5 (T_e)
$\omega_c/\nu_{(e/i)N}$	17-1870 (e), 2.7-33.7 (He^+)

In an asymmetric RF discharge, operations with a one-faced RF electrode allow variation in the self-bias on the RF electrode in the range of 20 to -250V depending on the working gas pressure, power and magnetic field. Depending on the relative potential between the plasma and the electrode, the ions are either repelled (Only when the sheath is reversed) or accelerated and collected by the RF electrode. The operational and plasma parameters corresponding to the discharges are summarised in Table 6.1

At low pressures, the plasma generation is dominated by stochastic heating due to the electron-sheath interaction. With increasing magnetic field, the bias on the RF electrode becomes positive, and one can observe the narrowing of the plasma column in the discharge, especially along the Y direction, see figure 6.2. This brings the peak of the density closer to the electrode since the sheath size is reduced due to two reasons:

for the same amount of RF power, (a) the RF voltage is smaller at a higher magnetic field, electron collection of the RF electrode is less lowering the magnitude of the self-bias and (b) improved density of the plasma, maybe due to the ionization of the helium meta-stable states, the Debye length decreases and hence the sheath size [162]. It is observable in the 2D maps and the density profiles as a function of the magnetic field, which has been already discussed in the previous chapter.

The total electron flux to the electrode has three components, (a) all the electron gyrating above the RF electrode in the distance range $2r_L$ are collected by the RF electrode, (b) the factor arising due to the perpendicular mobility and (c) the polarization current due to the RF sheath oscillation. The model has not incorporated the latter two factors, considering it is negligible compared to the direct fluxes arriving parallel to the magnetic field.

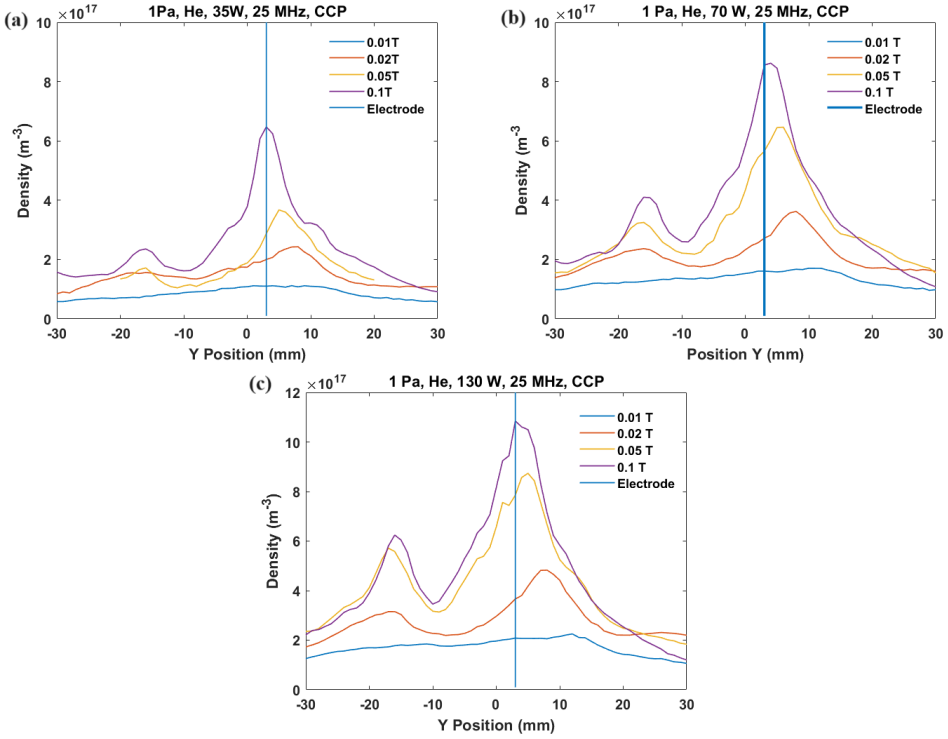

Figure 6.2: Density profile along Y direction in ALINE reactor for different power and magnetic field values (a) 35 W (b) 70 W (c) 130 W. The blue line represents the position of the RF electrode edge.

The image of the plasma discharges corresponding to 0.02 and 0.1 T at 35 W RF coupled RF power and 0.6 Pa discharge are given in figure 6.3. The bright column above the RF electrode is narrower at higher magnetic field discharge. To give input to the analytical model, the density values are averaged over the minor radius of the

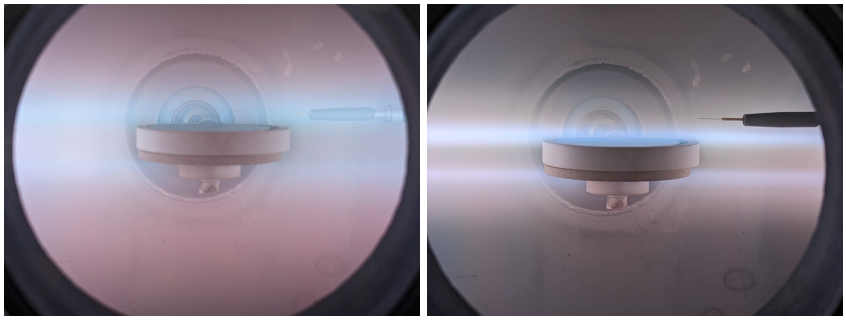

Figure 6.3: Plasma discharge corresponding to 0.02 T and 0.1 T magnetic field, when the self bias on the RF electrode is -43 V and +17 V respectively.

ellipse which is considered as the source for electrons and ions to the electrode. For the one faced electrode case, the density variation along the y direction for different coupled RF power and the strength of the magnetic field is depicted in figure 6.2.

6.4.2 IR Camera Measurements

Measurement of emissivity using two temperature method

Correct estimation of the emissivity of the electrode surface is necessary to measure the heating of the electrode. The method employed here is the two-temperature method. The electrode is heated to 80°C from room temperature by exposing it to the plasma [70; 163]. The chamber was opened to use the thermocouple to measure the actual temperature of the electrode surface. The IR camera was switched on one hour before so that the components inside the camera were in thermal equilibrium and there was no change in temperature during the measurement time. During the cooling down period of the electrode, several temperatures have been measured using the IR camera with an emissivity value of 0.08, along with corresponding true temperature values using the thermocouple. The ambient temperature and the temperature of the grounded wall remained the almost same during the time of operation (nearly 23.2°C). Relation between the temperature measured using the IR camera T_{IR} and the surface temperature T_{surf} can be written using the Planck luminance function $L_p(T)$. The first temperature is given by:

$$L_p(T_{IR1}) = \varepsilon L_p(T_{surf1}) + (1-\varepsilon)\varepsilon_{amb} L_p(T_{amb}) \tag{6.8}$$

and for the second temperature:

$$L_p(T_{IR2}) = \varepsilon L_p(T_{surf2}) + (1-\varepsilon)\varepsilon_{amb} L_p(T_{amb}) \tag{6.9}$$

Subtracting 6.9 from 6.8 eliminates the contribution from the ambiance and yields

$$\varepsilon = \frac{L_p(T_{IR2}) - L_p(T_{IR1})}{L_p(T_{surf2}) - L_p(T_{surf1})} \tag{6.10}$$

Here, L represents the radiance, which is the measure of radiant flux emitted by a surface. The $T_{IR1}, T_{IR2}, T_{surf1}$ and T_{surf2} are measured to be 56.1, 34.9, 47.8, and 32.7° C, respectively. Corresponding luminance values were calculated by integrating Planck's law at the temperature T over the wavelength range of the IR camera. Using equation (4), the emissivity value is measured to be 0.1256. This initial experimental measurement of the emissivity value is close to the reported emissivity value of tungsten [163]. The emissivity of a surface depends on the temperature of observation, the roughness, the angle of the measurement, ambient conditions etc. [164]. The transmission coefficient of the IR window is not considered here since the calibration is performed through the IR window.

The emissivity measurements using the two-temperature method are validated using a thermocouple. The RF electrode is heated up to 120° C. During the cooling down process, the temperature of the electrode is measured using a thermocouple (K-type-wired) [165], and the emissivity of the IR camera is adjusted to match with the temperature values obtained using the thermocouple. Note that the error range during the measurement is +/- 2°C. This exercise has been performed several times to reduce the error bar in the emissivity value measurement. After several measurements, the value of the emissivity measured converged to 0.127 in the case of the tungsten electrode. For the 5° tilt angle, the same emissivity value gave precise temperature values. For 20° tilt angle measurements, the emissivity values for the accurate temperature measurement are obtained using the calibration techniques mentioned above and the emissivity value is found to be 0.070.

Image Subtraction Method

IR camera measurements are highly challenging in a highly reflective environment. In ALINE, the Optris IR camera is placed right above the electrode, and the measurements are taken through an IR window. There is always an effect of the reflection of the IR camera on the electrode surface. Taking measurements at an angle can reduce these reflection effects, but this is practically impossible in the ALINE setup. With the IR camera placed outside the chamber, and assuming the temperature change of the camera is minimal during the time interval of the operation, the effect of these reflections from inside the vacuum chamber can be minimized using the image subtraction technique. Image subtraction is an image processing technique used to eliminate or reduce the effect of ambient reflections in the system. Neglecting the atmospheric influences, this can be formulated as [166]:

$$L_{det}(x,y) = \varepsilon(x,y) L^{BB}_{object}(T_{object}) + [1 - \varepsilon(x,y)] L_{amb}(T_{amb}) \tag{6.11}$$

L_{det} is the detected radiance, which is the sum of the radiation from the object (L^{BB}_{object}) and the contribution from the reflected radiation of the background. $\varepsilon(x,y)$ is the object emissivity at the position (x, y). If we calculate the difference in signals detected for two different object temperatures but the same ambient temperatures, the signal is no longer affected by the reflections from the surrounding:

$$\Delta L_{det}(x,y) = \varepsilon(x,y)\{[L^{BB}_{object}(T_{2,object}) - L^{BB}_{object}(T_{1,object})]\} \tag{6.12}$$

The subtracted image will depend only on the temperature difference. To achieve accurate measurements, there are two methods for subtracting reference images. The first involves subtracting one reference image from all other frames at the beginning or end of the measurement process (The method used in the thesis). The second method involves actively subtracting each frame from the next frame.

The Optris software allows the first method and helps in reducing the effect reflections during the IR measurements. This gives a new sequence of temperature values with little effect on reflection in the system. An example of the image subtraction applied for the RF electrode is depicted in figure 6.4. The image on the left is the raw before subtraction is applied. One can see the effect of the reflection of the camera lens on the surface of the RF electrode. There are secondary reflections due to the optical window surrounding the primary reflection. The image subtraction (right) leaves a low-temperature region (the dark region) on the surface of the RF electrode. However, the effect of the higher-order reflection has been removed effectively due to the image subtraction. In the raw image, the temperature difference between the hot and the cold region on the surface was around 15-20° C. After the subtraction, the temperature difference between the hot and cold region is less than 5° C, and the slope of the time-temperature diagram stays the same for different positions on the surface of the RF electrode. The prevailing problem can be minimized by removing the final frame of the recording and averaging it.

6.4.3 IR Camera Results using TEDDY

The time-temperature measurements obtained using the IR camera serve input to the TEDDY code [70] along with the dimension of the tungsten electrode. Initially, the temperature of the electrode increases with time and saturates after several minutes due to the radiation losses from the RF electrode. During the 15-minute-long measurement, the electrode temperature was observed to be saturated after the first half. Assuming the plasma density and potential are constant as a function of time, we can expect a constant flux during the whole 15 min. So, the linear part of the time-temperature curve is used to evaluate the heat flux. The first 6 minutes of the heating profile is linearly fitted corresponding to different measurement points (11 points) on the RF electrode and given as input to the TEDDY. The results corresponding to the straight

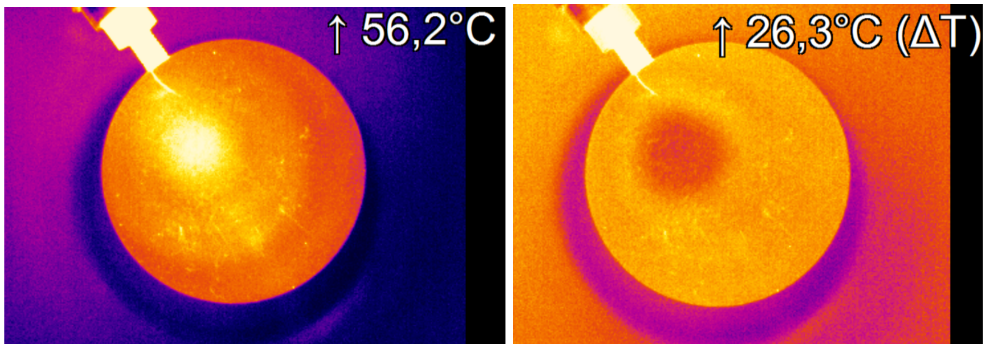

Figure 6.4: The image of the RF electrode through IR camera after 15 minutes (a) before image subtraction (b) after subtracting the first frame of the recorded video. The temperature value on the image on the left is the final temperature of the RF electrode before subtraction and the value on the left is the difference between the present frame and first frame.

and tilted electrodes are presented in the following section. Time-temperature plots corresponding to 3 cases are presented in the figure 6.5. The plots are corresponding to 0.6 Pa Helium discharge at 35, 70 W, and 130 W coupled RF power with the one-faced RF electrode at 0° tilt angle. The linear part of the plot is fit linearly and corresponding heat flux (H) values are measured using the specific heat equation, given by:

$$H = Mc_p \left(\frac{T_2 - T_1}{t_2 - t_1} \right) = Mc_p * slope \tag{6.13}$$

M is the mass of the RF electrode, which is 0.54 kg, c_p is the specific heat capacity of tungsten material (134 J/Kg.K), and the unit temperature rise of the RF electrode ($dT_{electrode}$/dt) values are the slope of the time-temperature fit. The slopes corresponding to 35 W, 70 W, and 130 W discharge are 0.0483, 0.1108, and 0.195 K/s respectively. The heat flux values for the 3 cases are measured using equation 6.13 and are 1234, 2847, 4998.7 W/m^2, which is close to the values using TEDDY, are 1357, 3111, 5350 W/m^2.

6.4.4 Results : $\alpha = 0°$

For α= 0°, the heating of the RF electrode is due to the accelerated particles from the plasma column connected to the circular face of the RF electrode. The ceramic receives the parallel flux and is also heated with time, but the material has high specific heat compared to the tungsten (950 J/kg-K) and remains at lower temperatures. The heat flux measurement results using the IR camera corresponding to three RF powers, two gas pressures and their dependence on the B field are shown in figure 6.6.

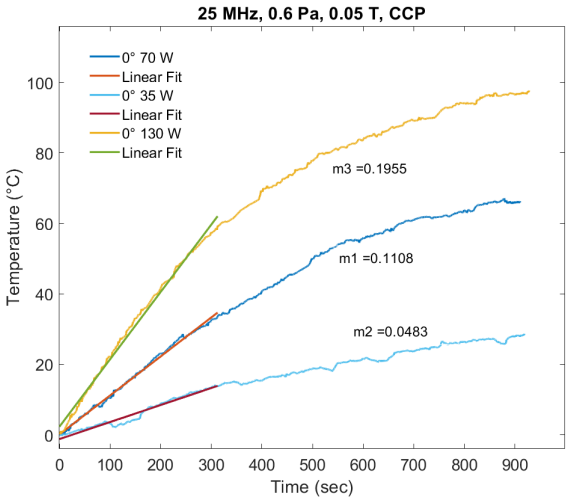

Figure 6.5: Time temperature diagram and fit of time temperature diagram corresponding to 1 Pa helium discharges at 35, 70 and 130 W coupled power and 0.05 T magnetic field with one-faced RF electrode

In Figure 6.6a, the heat flux obtained using the IR camera-TEDDY is plotted as a function of magnetic field strength for different power and pressure cases. The heat flux variation with B follows a similar trend in almost all cases: the minimum value of heat flux is around 0.02 T and gets higher as B increases. While comparing the heating at the 0.6 Pa and 1 Pa discharges, the heating is observed to be higher at higher pressures in all the cases. Since the self-bias and the density are considered to be the major factors contributing to the heating process, both density and self-bias are plotted as a function of B in figure 6.6b and c. Density is increasing significantly as a function of the magnetic field and saturates at higher B values for all the power and pressure cases. The density is higher at higher gas pressure, especially at lower magnetic field values. The absolute magnitude of the DC self-bias drops exponentially as a function of B. The self-bias values are more negative at higher gas pressures and lower magnetic field values, as explained in Chapter 4.

The heat flux measured using TEDDY was normalised with the density in figure 6.6d, these values drop initially with an increasing magnetic field and are found to be saturated since there are no significant variations between 0.05 and 0.1 T values. At lower magnetic fields, the density is lower, and the self-bias is highly negative, especially at 0.01 T, which accelerates ions from the plasma above the RF electrode and heats the electrode surface. Heat flux values normalised with the coupled RF power are plotted in figure 6.6e. Except for 0.6 Pa -7dB (75 W) discharge, all other cases show a dip in the normalised heat flux values. The power coupled to the plasma improved slightly with the magnetic field. There is no significant difference change in the normalised

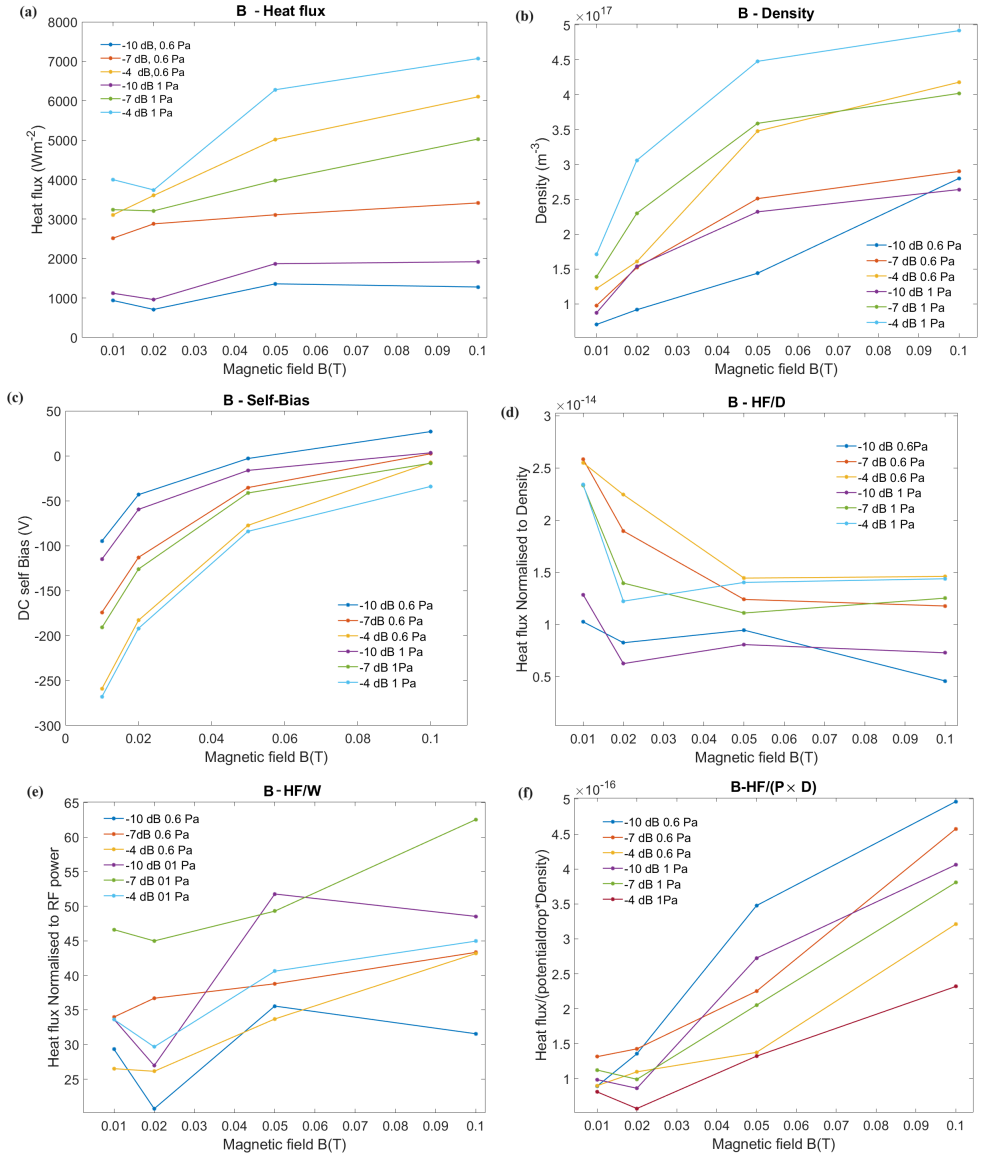

Figure 6.6: TEDDY Results, (a) heat flux (b) density (c) DC self-bias (d) heat flux normalised to the density and (e) heat flux normalised to power (f) Heat flux normalised to potential drop and density variation with magnetic field (B) corresponding to $\alpha = 0°$ discharge .

value when the magnetic field is changed from 0.05 T to 0.1 T. In figure 6.6f, heat flux normalised with the product of the potential drop and the average density value (proportional to ion flux) was found to be increasing for higher magnetic field values 6.3. At 0.01 and 0.02 T, the normalised heat flux values are almost constant, meaning

the ion flux is responsible for the heating process.

The heat flux received by the antenna is higher at a higher magnetic field. At the same time, the heating due to ion flux is significantly reduced due to close to zero or positive values of self-bias on the electrode. At a higher magnetic field, the density has improved significantly, the bias on the RF electrode is more positive, and the electrons are less repelled by the RF electrode shifting the plasma column closer to the RF electrode. In the case of 0.6 Pa and 0.1 T discharge, we have seen that the direction of the RF electrode is reversed. The value of the RF voltage on the surface of the RF electrode is significantly higher than the absolute value of the self-bias on the RF electrode. Hence, the combined effect of higher density of the electrons, the acceleration electrons and presence of higher hot electron population can explain the higher heating of the electrode at 0.05 and 0.1 T discharges.

Analytical model results

Heat flux is evaluated using the analytical model inputting the Langmuir probe data for the straight electrode case. The electron temperature in the model is considered uniform in all the cases and is taken to be 5 eV. The analytical results were compared with the teddy one for 0.6 and 1 Pa in figure 6.7(a). The magnetic field and the pressure values are shown corresponding to each point representing different discharge parameters. The heat flux values calculated using the analytical model are closer to the experimental values at lower power measurements, especially at the lower magnetic field values. However, the model deviates from the experimentally observed values at high powers. In figure 6.7(b), the RF potential and the absolute value of the DC self-bias on the RF electrode are plotted for all the 0° discharges. In lower magnetic field cases, the self-bias is negative, and the magnitude of the self-bias is closer to the RF potential. As explained before, electrons are collected by the RF electrode during a small fraction of the RF cycle. Whereas at higher magnetic fields, even though the RF voltage decreases slightly, the self-bias is closer to zero or positive. Hence, one could expect the RF electrode to collect electrons during almost half of the RF cycle.

The quantitative deviation of the model results from the experimental values can be due to multiple reasons. All the probe scans are taken at Z=-150 mm, X=0 mm, along the Y axis. The plasma above the RF electrode is highly non-uniform due to the drift, and the peak position changes significantly with the self-bias values. The density variation along the Z direction is incorporated in the input to the model based on 35 W power measurements, which may not be the same at higher powers. This has not been verified because of the challenges in the probe measurements near the RF electrode at higher powers.

The Equation 6.3b gives the average value of electron flux and underestimates the electron flux at higher magnetic fields. For example, the difference between the plasma potential and self-bias is nearly 26 V for 70 W, 0.1 T, 0.6 Pa case. The peak RF Volt-

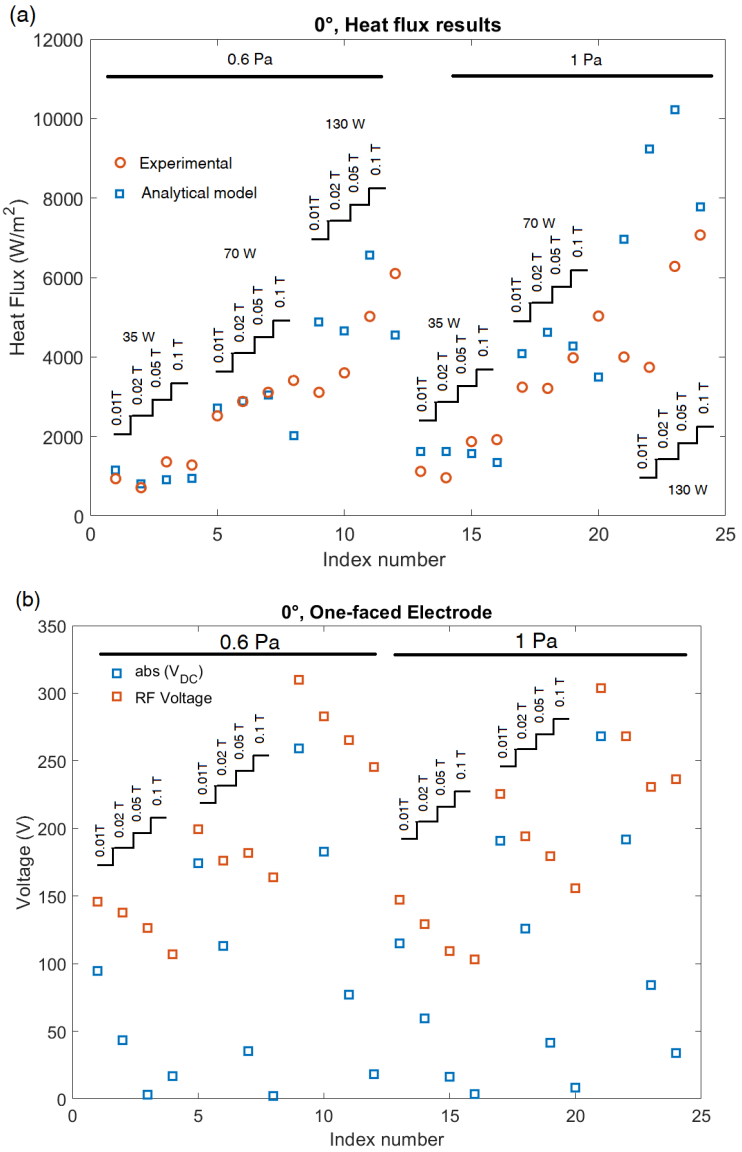

Figure 6.7: (a) Heat flux results comparison between TEDDY and analytical model, (b) The plot showing the RF potential and the absolute value of the self bias on the RF electrode corresponding to $\alpha = 0°$ experiment with one-faced RF electrode. The pressure and the magnetic field values for each discharge is indicated near each point and it is similar for both plots.

age is 163 V, meaning the electrode collects electrons during most of the positive RF cycle. What one gets using equation 6.3b is far from the actual heat flux value. Experiments have shown that there is a fraction of the hot electron population close to

the RF electrode. The distribution and the fraction of hot electrons in the plasma vary significantly along the diameter of the RF electrode, which is not considered in the presented model. The ions are nearly magnetized at a higher magnetic field, and keeping the size of the source the same for all the magnetic field values overestimates the heat flux to the RF electrode. If the source area of the ions is based on the ion Larmor radius, similar to the electrons, the model underestimates flux values in all the cases.

6.4.5 α=5° Measurements

When the electrode tilts by 5°, the self-bias developed on the surface of the RF electrode is always negative, and ions are the dominant factor of heating. There is a short interval during the RF cycle, when the electrons are collected by the electrode surface. Considering a parallel component of the electronic current to the electrode surface creates a thick visible ionic sheath on the active electrode for all magnetic field values. The heating of the electrode is studied using the IR camera and TEDDY setup and compared with the analytical model. The result from TEDDY is presented in Figure 6.8.

While looking at the heat flux vs magnetic field (B) plot for different RF powers and pressures, the heat flux variations are found to be similar to the straight electrode case in figure 6.8 (a). There is a dip in the heat flux values at 0.02 T and then increase with increasing B due to reduction in the absolute value of self bias and density. The effect of increased pressure in the heating of the RF electrode is visible for high power (-4 dB, equivalent to 130 W) measurements, but at a higher magnetic field, the difference in heat flux values is lower compared to the lower B values. Unlike $\alpha = 0°$, there is a projection of the RF electrode along the magnetic field lines. From the 2D potential profiles in the previous chapters, it is seen that the electrode bias the plasma column connected to it to higher potential values. While comparing plasma potential values along the Y direction, the average plasma potential values are observed to be higher at lower pressure discharges.

The density and the self-bias values corresponding to these heat flux measurements are presented in Figures 6 (b) and 6(c). Density improves with the magnetic field values. This can be due to improved collisionless heating at higher magnetic fields, better confinement and ionization of meta-stable states. Whereas with increasing the magnetic field value from 0.01 to 0.02 T, there is a drop in the absolute magnitude of the self-bias and the later does not evolve at higher magnetic fields. The saturation of the self-bias voltage can be explained by the density improvement locally balancing the reduced source area for electrons.

In Figure 6(d), the heat flux is normalised with the density and what is observed is similar to the straight electrode case; an initial drop in the normalised value and the saturation part is similar for the 5° case.But here the normalised values do not vary significantly from B=0.02 values. While normalising the heat flux with the product of

the total potential drop and the density (proportional to the ion flux) and plotting the values as a function B, the normalised values were found to be constant irrespective of the B value. When there is a parallel component of electron flux to the RF electrode, which biases the electrode negatively, ions are the dominant heating factor, and the contribution from the electron side is negligible.

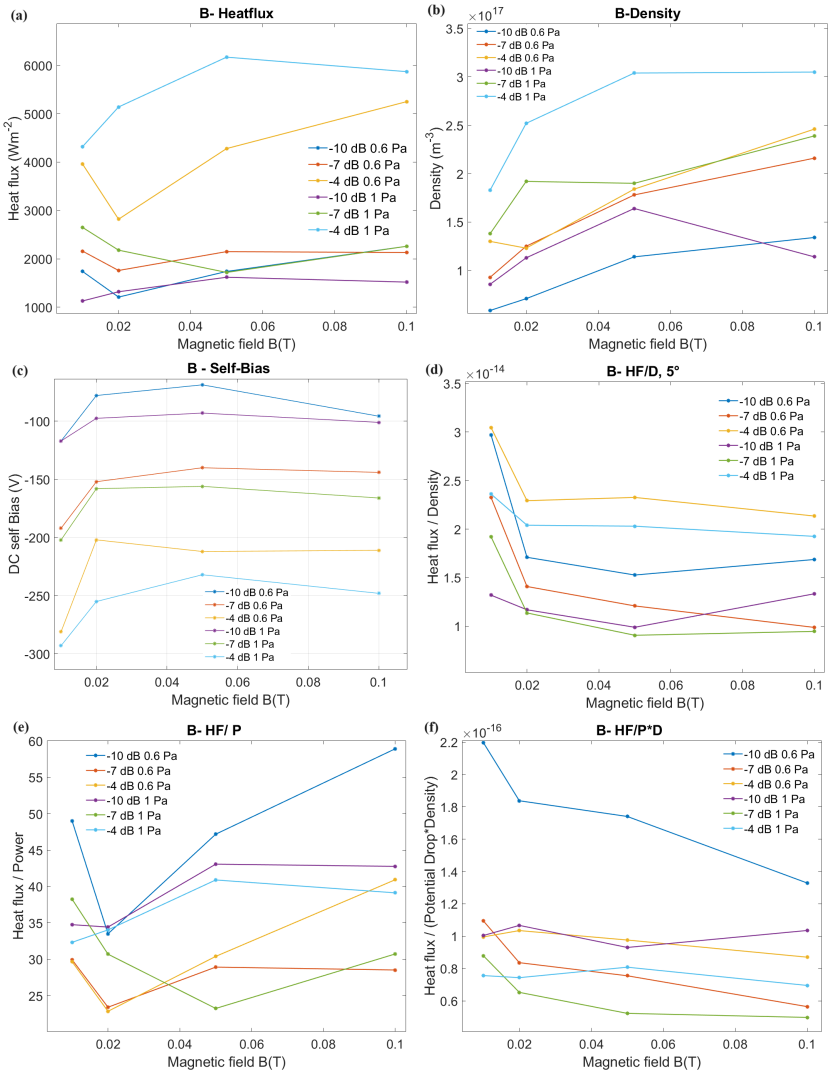

Figure 6.8: TEDDY Results, (a) heat flux (b) density (c) self bias (d) heat flux normalised to the density and (e) power, and (f) heat flux is normalised to the product of potential drop and the density variation with magnetic field (B) corresponding to 5° tilt angle.

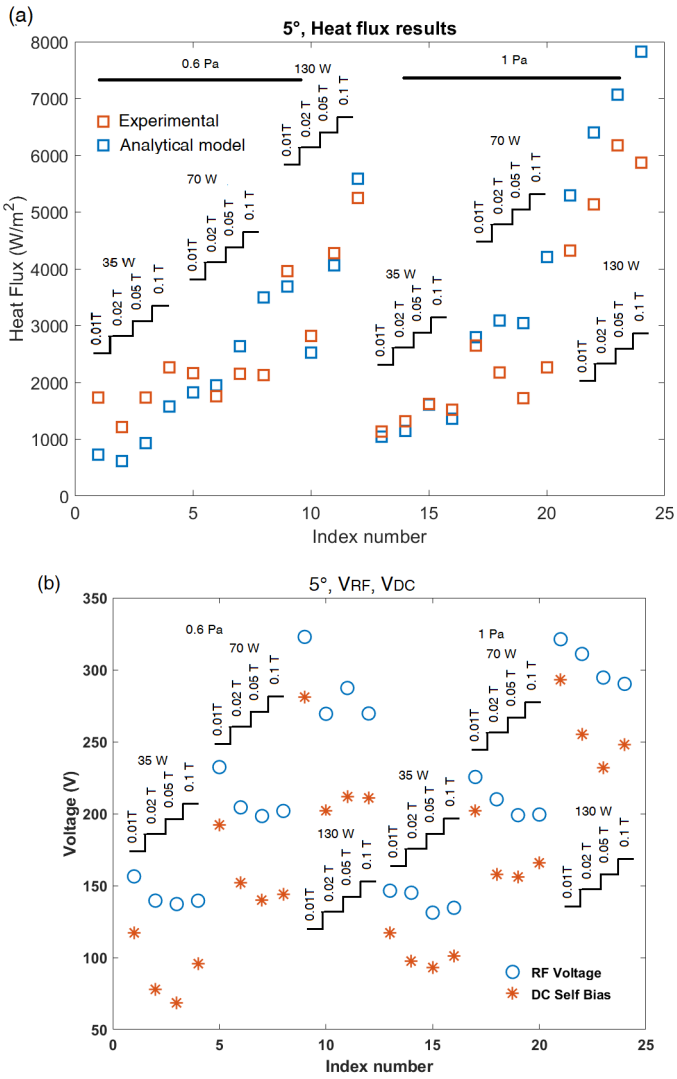

Figure 6.9: (a) Comparison between heat flux values obtained experimentally and from the analytical model (b) RF voltage and absolute value self-bias values for different experimental parameters.

Analytical model results

The heat flux to the RF electrode is calculated using the analytical model presented in section 6.3 and based on equations 6.3a, 6.3b and 6.3c and the model values are plotted along with the experimental values in figure 6.9(a). The RF voltage on the electrode and the absolute value of the DC self-bias on the RF electrode is plotted in figure 6.9(b).

Similar to the 0° tilt angle, the first 12 measurements correspond to 0.6 Pa measurements, and the latter corresponds to the 1 Pa case. In the 5° case, the self-bias is

always negative, and the magnitude is closer to the RF potential values compared to the 0° case. Ion flux is the major contributor to the heating of the RF electrode, even though the electron flux heats the RF electrode when the difference magnitude of the self-bias and the RF voltage is higher, and this contribution cannot be neglected. The model is not consistent in predicting the heat flux values to the RF electrode despite the experimental and analytical values being closer at some discharges. The deviation of analytical values from the experimentally observed values is lower at 5° compared to the 0° cases. However, the contribution of electrons heating during the positive half cycle of the RF period is underestimated by the model. The source area for ions cannot be taken as the same for all magnetic fields and the coupled RF power. But at 5°, the model can predict the variation of the heat flux values with changing experimental parameters from the average density and plasma potential values.

6.4.6 $\alpha = 20°$ Results

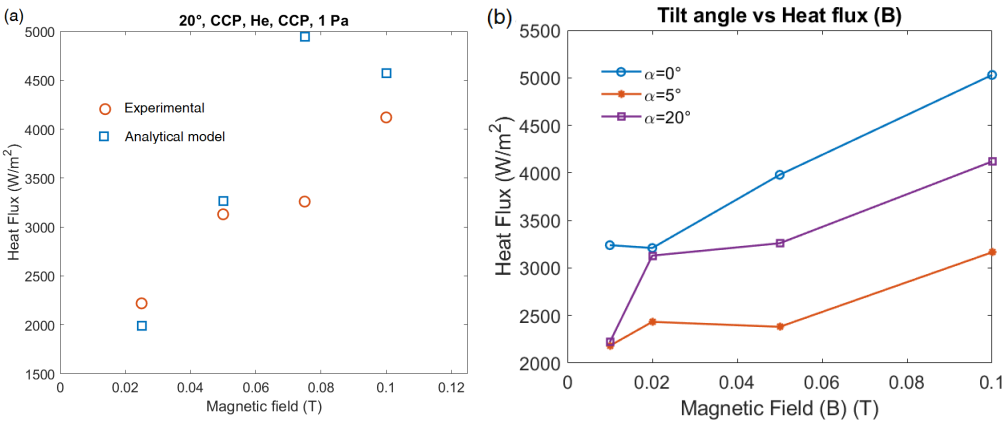

Figure 6.10: Comparison between experimental and analytical value of heat flux for (a) 20°. (b) Heat flux as a function of magnetic field for 3 tilt angles (75 W coupled RF power and 1 Pa Helium gas pressure).

Finally, the experimental and analytical heat fluxes corresponding to the 20° tilt angle are presented in figure 6.10c. Experiments were performed at intermediate input RF power (70 W) for four different magnetic field values at 1 Pa helium gas pressure. While looking at the experimental values, the heat flux is lower for 0.01 T measurements and higher at 0.1 T magnetic field. The analytically obtained heat flux values for analytical heat flux values were calculated from the probe inputs and found that the heat flux values match with the experimental values for 0.01, 0.02 and 0.1 T. The analytical model overestimates the heat flux value at 0.05 T. This can come from the averaging of the density. Due to the drift, the peak of the density structure could be aligned with the Y=0 mm position for 0.05 T measurement.

Heat flux received by the RF electrode (experimental), at 75 W coupled RF power at 1 Pa pressure for three different tilt angles is compared as a function of magnetic field and the results are plotted in figure 6.10 (b). 5° measurements showed the lowest heating of the RF electrode and heating and heat flux to the electrode was higher in all the magnetic field values at 0°.

6.5 Experiments with Tungsten Electrode

6.5.1 DC self-bias

When there is no ceramic covering the RF electrode, there is always a direct parallel flux from plasma to the electrode edge. As discussed in Chapter 4, the self-bias on the surface of the RF electrode strongly depends on the coupled RF power, gas pressure, strength of the magnetic field and the tilt of the RF electrode. In figure 6.11 (a), the variation of the self-bias with tilt angle is presented for four magnetic field values at 1 Pa helium discharge at 34 W of coupled RF power.

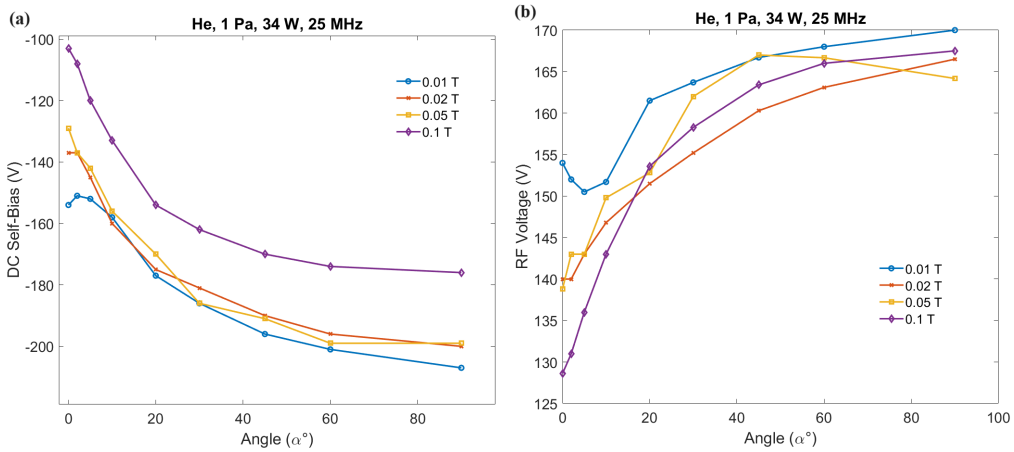

Figure 6.11: Variation of the (a) self-bias and (b) RF voltage with magnetic field at 1 Pa helium discharge for approximately 34 W coupled RF power.

The power coupled varies slightly around 34 W for different tilt angles and magnetic field values. From the figure, it is clear that the self-bias decreases (magnitude increases) with the increasing tilt angle, and it saturates at higher tilt angles. The change in the projected area with an increase in tilt angle has been shown in 2D maps in the last chapter. Increase in the collection is responsible for the drop in the self bias value. At higher tilt angles, increase in the collection area is balanced by a decrease in the density inside the plasma column connected to the RF electrode explains the saturation of the self-bias.

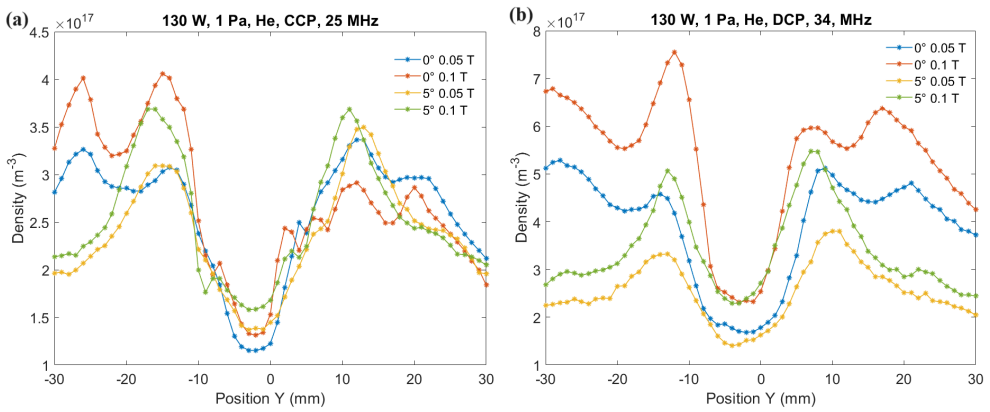

Figure 6.12: Density profile along Y direction at X=0, Z=-150 mm for 1 Pa helium discharge for 130 W coupled RF power (a) for capacitive coupling and (b) direct coupling.

Figure 6.11b shows the variation of the rms RF voltage on the active electrode's surface with the angle and magnetic field strength. Increase in the magnetic field helps in confining the energetic electrons without escaping the plasma, which improves the ionization and excitation in the plasma and the voltage required to drive the RF current decreases [167]. The rms RF voltage increases with the tilt angle, and saturates at higher tilt angles for a fixed magnetic field. The increase in the RF voltage with tilt angle can be due to the increased effective area ratio (A_{RF}/A_{Ground}). The value of the RF voltage is almost the same magnitude as the self-bias on the RF electrode.

6.5.2 Heat flux Measurement results

Experiments were performed at 35 W for 1 Pa helium gas pressure for both capacitive coupling and direct coupling. At lower power operations (35 W), the heating of the electrode is lower and the analysis does not helped in understanding the trend. So experiments were performed at higher power (130 W) at 1 Pa for 0° and 5° tilt angle for both direct and capacitive coupling at 0.05 T and 0.1 T magnetic fields.

The heat flux measurement from the IR camera+ TEDDY corresponding to 8 different experimental conditions are depicted in the figure 6.13, where the red colored squares represent the direct coupling measurements and the green color squares represent the capacitive coupling measurements. The heat flux values and the tilt angle are shown next to each square. From the figures, it is clear that for a fixed RF power the heating of the RF electrode is higher for the direct coupling case. While comparing the 0° and 5° case, the heating is higher for the 0° discharge, the trend is same for both direct coupling and capacitive coupling. The highest heat flux measured is 2890 W/m^2 for 0°, 0.05 T measurement direct coupling discharge. In capacitive coupling the heating of the electrode is observed to be higher at high magnetic field unlike the 0° direct

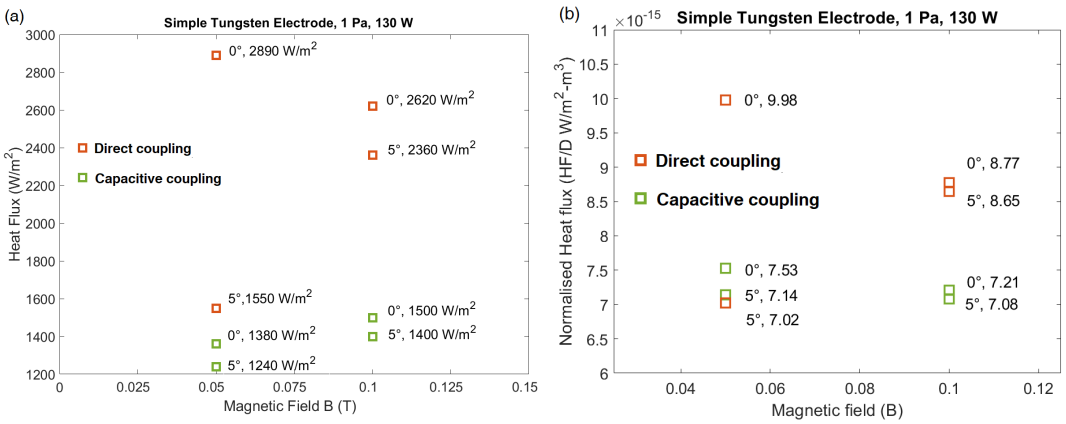

Figure 6.13: (a) Heat flux measurement results and (b) heat flux normalised to the density values corresponding to tungsten electrode for both direct coupling and capacitive coupling obtained using IR camera.

coupling case.

The heat flux to the RF antenna is normalised with the average density inside the plasma column, and the results are depicted in the figure 6.13b. Similar to the last plot the normalised values are given along with the angle of measurements for each case in the figure. While analysing the capacitive coupling results, the normalised heat flux values are close to each other. The self-bias voltage and RF voltage on the the RF electrode at different discharge conditions are given in the table below.

Parameters CCP discharge			
Experiment	DC self-bias (V)	RF voltage (V)	Average density (m^{-3})
0°, 0.05 T	-297	303	1.81×10^{17}
0, °0.1 T	-261	281.4	2.08×10^{17}
5°, 0.05 T	-322	315.28	1.74×10^{17}
5°, 0.1 T	-286	297.22	1.98×10^{17}

The observed high heating of the RF electrode is due to the higher density at higher magnetic field. Higher normalised heat flux at 0°,0.05 T can be explained by higher negative bias on the RF electrode. However, lower heating of the RF electrode at 5°,0.05 T, even though the self-bias is higher has to be investigated more.

The exact power value and the potential on the RF electrode is not available for the direct coupling case since the RF power meter is suitable for measuring the power at 25 and 40 MHz and these measurements are performed at 34 MHz. The choice of the operational frequency is only to ensure the maximum power coupling to the plasma and the power power coupled is assumed to be similar as CCP case. The normalised values are higher for the direct coupling measurements. The density of the plasma is higher inside the plasma column in the case of 0° see figure 6.12.

while the magnitude of the self-bias is much smaller compared to the peak RF voltage (-34 V , 245 V respectively for 1 Pa +130 W helium discharge) in one faced electrode case. Hence the observed high heat flux for the one faced electrode case can be explained as follows, the electrode collects electrons during most of the RF cycle leading to high electron heating of the RF electrode. Reversal of the electric field and acceleration of electrons locally to a conducting surface in a magnetron discharge has been reported in [168; 169] . Whereas for the pure tungsten electrode case, in CCP, the heating is due to highly negative DC self-bias the electron flux to the RF electrode is negligible and heating is predominantly due to ions.

6.5.3 Comparison to the Analytical Model

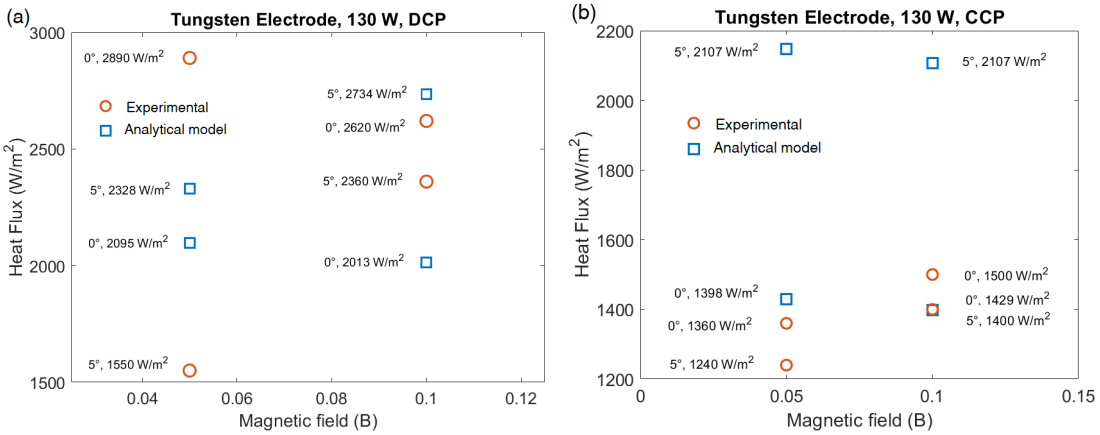

Figure 6.14: Analytical heat flux values in comparison with the experimental values corresponding to simple tungsten electrode measurements for (a) direct coupling and (b) capacitive coupling.

The analytically evaluated values of heat flux in the case of direct coupling and capacitive coupling based on section 6.3, are compared with the experimental values and presented in figure 6.14. In direct coupling (figure 6.14a), since the voltage values are unknown, the plasma potential values are given as the input to the analytical model, and the model underestimates the heat flux values. In order to get heat flux values close to the experimental values, the source area has to be modified to an ellipse of minor radius 1.5 cm. Even though the source area is modified, the model gives higher flux values at 5° tilt angles since the projection area of the RF electrode along the magnetic field is higher at 5°. Hence, the model fails to explain the heating in the direct coupling.

In capacitive coupling considering the collection area as explained in section 6.3, the model gives close to experimental values at 0°. However, the model overestimates the heat flux at a 5° tilt angle due to the higher source area for ions. So, at grazing

angles, the effective collection area is not exactly the effective projected area of the RF electrode along the magnetic field lines. One can stretch the analytical model to get close to experimental values by changing the parameters in each case, but it won't work in all cases.

6.6 COMSOL Results

A simple 3D heat flux model is developed based on COMSOL's "Heat transfer in Solids Module". The tungsten electrode is held by the stainless steel rod. When the electrode is heated due to the plasma exposure, the heat from the electrode is transferred to the electrode holder. A model of RF electrode is developed with tungsten as the electrode material and stainless steel as the electrode holder material. For the single-faced RF electrode case, the heat load is exclusively applied to one of the circular surfaces of the RF electrode, and for the without ceramic configuration, heat flux is given along all the surfaces of the simple tungsten RF electrode. The experimentally measured heat flux values are given as input for the COMSOL model and compared with the experimental temperature evolution with time. The model is based on the following equations:

$$\rho C_p \frac{\partial T}{\partial t} + \rho C_p u.\nabla T + \nabla.q = Q + Q_{ted} \tag{6.14}$$

$$q = -k\nabla T \tag{6.15}$$

Where C_p is the specific heat capacity of the material, Q_{ted} is the thermo-elastic damping ρ the density of the material, Q represents the heat source, u is velocity field defined by the "Translational Motion subnode", and k represents the thermal conductivity. The length of the stainless steel rod holding the RF electrode is 15 cm long. The whole stainless steel rod is covered with a ceramic hollow rod. Hence there is no direct heating of the rod by the plasma.

The density value of the stainless steel is given as input to the model. In the experiments with the one-faced RF electrode, the electrode is covered with mullite C-610 (C_p=950 J/Kg.K), which has a higher specific heat capacity than tungsten(C_p=134 J/Kg.K). Since ceramic is floating in the plasma and the plasma is highly non-uniform, the estimation of the heating of the ceramic is challenging. To match the model curve with the experimental curve, the thermal conductivity (80 W/m.K is the real value) and the length of the stainless steel rod is modified. So, for the presented model, the thermal conductivity is considered to be 100 W/m.K for the one-faced electrode and the length of the RF electrode is taken as 2.5 cm. In the simple tungsten electrode case, the thermal conductivity of the stainless steel is kept as the real value and the length is taken as 5 cm. The results from the COMSOL model are compared for different

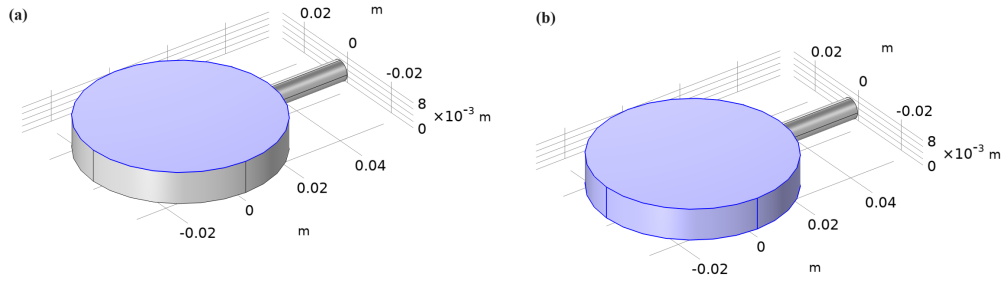

Figure 6.15: RF electrode model (a) one faced and (b) tungsten electrode case using COMSOL. The blue region represents the area over which the heat flux is received by the RF electrode.

heat flux inputs and compared with the experimental results for the one-faced RF electrode in figure 6.16. There is an oscillation in the temperature measurements in these curves, which can be explained by the flag feature associated with the Oprtis IR camera: when the sensor gets saturated by the radiation, it will lead to an underestimation of the temperature. So, in every 12-second interval (interval can be varied), the flag feature blocks the sensor from radiation exposure, leads to a drop in the temperature measurement and provides the average temperature of the RF electrode over the flag period.

The model results corresponding to high heat flux and low heat flux are plotted and compared separately. For the case of the electrode with ceramic ring, the high heat flux results are plotted in figure 6.16a. At high and intermediate heat flux inputs, both experiment and model curves are in agreement with each other, even though there is a slight deviation in the slope of the curves. The COMSOL model could predict the temperature of the RF electrode within the error range of the IR camera (+/- 3°). With time, the tungsten will get heated fast, and after several minutes, there will be heat flow from the electrode to the ceramic. The experimental curves that are presented here are the mean temperature of 11 positions on the electrode surface and not the fitted curve. Lower heat flux measurements are depicted in figure 6.16b. The model and measurement curves agree in the initial minutes, but with time, the experiment results get noisy and deviate from the model. At lower heat flux inputs, the heating of the RF electrode is lower, and the higher rate of sample collection of the IR camera leads to noisy temperature measurements, which partially explains this deviation. In figure 6.16(c), a time-temperature diagram of the RF electrode comparing the COMSOL and the IR camera is given for (960 sec). In this image, one can see that the curve starts to saturate after 400 seconds. In this plot, even though the slope of the linear part of the curve is higher for the experimental curve, it reaches the saturated temperature faster than the model curve.

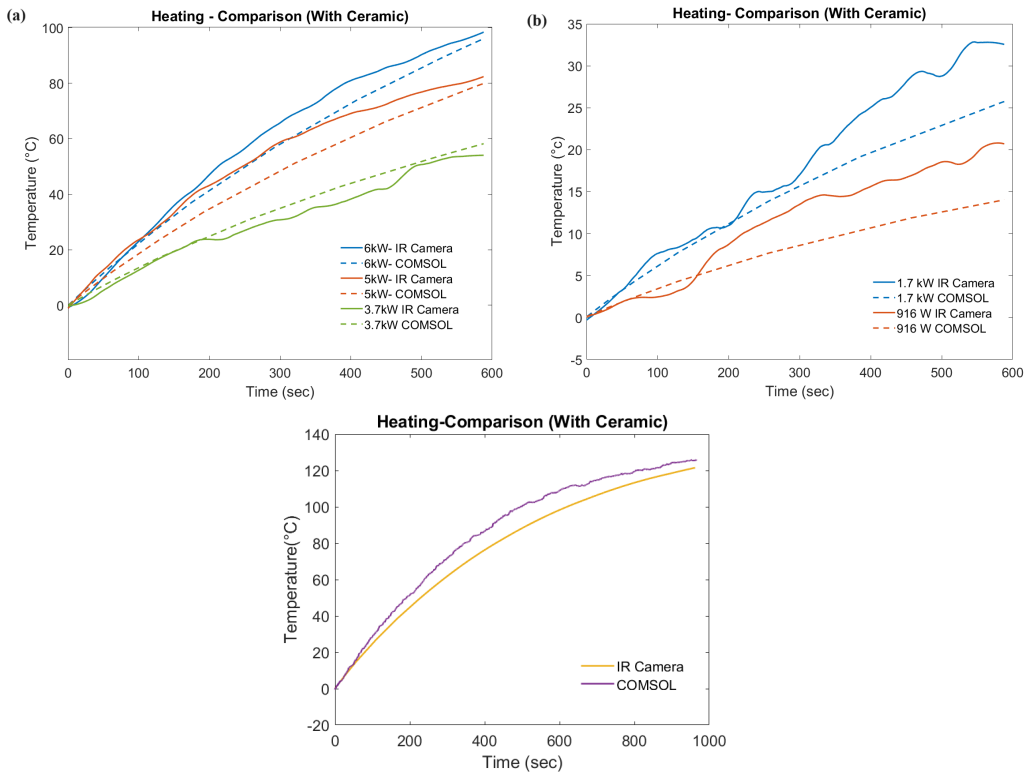

Figure 6.16: Time-temperature plot comparison, IR camera vs COMSOL for one faced electrode case (a) high heat flux (b) low heat flux and (c) 5000 W/m^2 for 15 minutes.

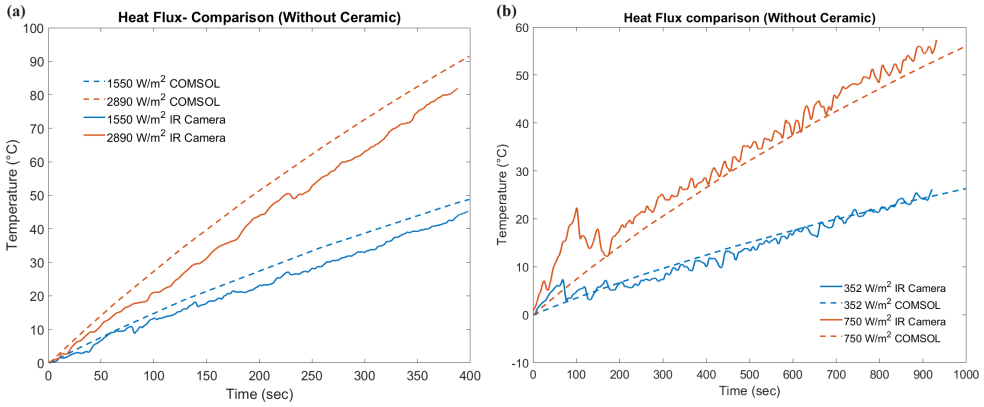

Figure 6.17: Time-temperature plot comparison, TEDDY vs COMSOL for simple tungsten electrode case.

The results from the model for electrode without ceramic covering is depicted in figure 6.17. There was no saturation for the time-temperature curve for 15 minutes

for the simple tungsten electrode case. However, the curves presented in these figures correspond to the first seven minutes of the time-temperature diagram. In 6.17a, the temperatures increase during the first minutes, and the model and experimental curves have the same slope, validating the experimental results. The lower heat flux measurements are compared with the model in figure 6.17b. As seen in the high heat flux case, after the first minutes, the experimental and the model curves are in good agreement with each other. The red curve line representing the experimental curve corresponding to 740 W/m^2 was found noisy and is different from the model even though the slope of the curves becomes parallel to each other after the first 3 minutes of the time-temperature profile.

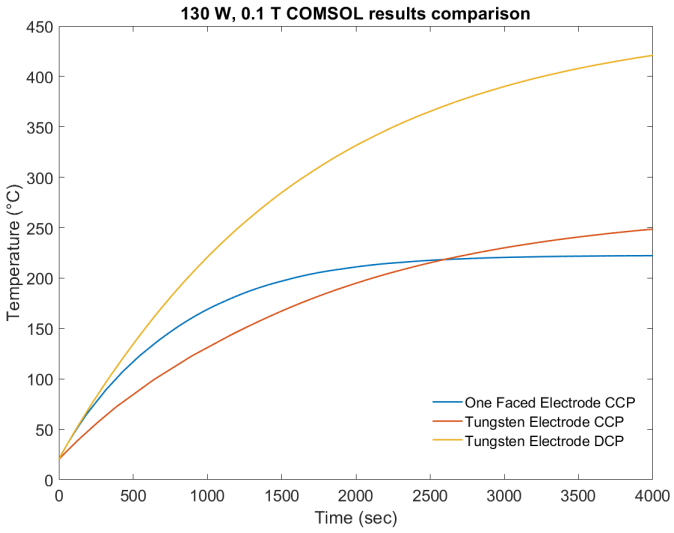

Figure 6.18: Time-temperature plot comparison between one faced electrode and tungsten electrode at capacitive and direct coupling at 0° tilt angle, 130 W coupled RF power and 0.1 T magnetic field.

While comparing the heating of the RF electrode for the one-faced case and tungsten electrode case, the total energy received by the RF electrode in one-faced RF electrode CCP, simple tungsten electrode DCP and CCP are 19.98 W (7070 W/m^2), 20.24 W(2620 W/m^2) and 11.31 W (1500 W/m^2) respectively. But there is heat flow to the ceramic in the one-faced electrode case. To compare, the time-temperature diagram corresponding to 130 W, 1 Pa Helium discharge for both capacitive and direct coupling for one-faced RF electrode (CCP only) and tungsten electrode are compared in figure 6.18 based on the COMSOL result. During a long operation, since the one-faced electrode reaches saturation faster, the temperature of the electrode is maintained at a lower temperature compared to simple tungsten electrode discharges. The temperature of the RF electrode is observed to be highest for the direct coupling DCP discharge

for the same coupled RF power.

6.7 Conclusions

Heat flux measurement experiments were performed in ALINE using a one-faced RF electrode and simple tungsten electrode varying gas pressure, RF power, tilt angle, strength of the magnetic field and the coupling mechanisms. Heat flux was measured using the IR camera, which was calibrated using a thermocouple during each phase of the experiment. From the time-temperature profile of the RF electrode measured using the IR camera the heat flux received by the electrode is estimated using the TEDDY code.

Experiments with the one-faced electrode in CCP showed that the heating of the RF electrode is higher at a 0° tilt angle compared to 20° and 5°. For a fixed RF power, heating of the RF electrode is observed to be higher at higher magnetic field and gas pressure. The improved density of the plasma near the RF electrode and higher electron flux to the electrode due to lower self-bias can be the reason for this observed behaviour. At 0.6 Pa, 0.1 T, the average potential of the plasma is observed to be at a lower potential than the electrode. Even though it reduces the ion flux to the RF electrode and reduces the sputtering, the heating of the RF electrode is observed to be higher due to the acceleration of electrons to the electrode surface. Experiments showed that the heating of the RF electrode is minimal at 5° tilt angles compared to 0° and 20° in one-faced RF electrode experiments.

Experiments with simple tungsten electrode at 0° and 5° tilt angles showed minimum heating of the RF electrode at 5°, 0.05 T discharge in both direct and capacitive coupling. Significantly higher heating of the electrode is observed at a higher magnetic field and 0° tilt angles in direct coupling. More experimental investigations are required to explain this observation. However, the simple tungsten electrode measurements revealed that the heating of the RF electrode is higher in direct coupling at 0° for both 0.05 and 0.1 T discharges. While comparing with the faced electrode case, the temperature of the RF electrode is observed to be highest in simple tungsten electrode DCP discharge.

Even though the heat flux to the one-faced electrode is higher due to the electron flux, it reaches saturation faster due to heat diffusion to the ceramic, which maintains the electrode at lower temperature for long-term operations compared to all other cases. This has been verified using a simple COMSOL model. The heating and the heat diffusion to the ceramic need to be investigated further.

An analytical model has been used to validate the experimental results. Even though the model gives an approximate flux value close to the experimentally observed value in some cases, the model was inconsistent due to several reasons. Plasma inside ALINE is highly non-uniform, and probe measurement along Y=0 mm, Z=-150 mm and

averaging over the source area lead to deviation from the experimental values even if a density factor is introduced. Optimisation of the source area is another challenge since the heat flux to the electrode surface depends on the magnetic field, pressure and the power coupled, and it changes the source area for electrons and ions each time. The model does not account for the hot electron contribution since the ratio of hot to cold electron populations is unknown close to the RF electrode. The electron temperature is not a constant inside the plasma column connected to the RF electrode. It varies along the X and Y directions. A PIC model or a COMSOL model could provide a better insight into the heat flux values and also for understanding the particle/heat flux to a surface at grazing angles in a magnetic environment.

Chapter 7

Conclusions, limitations and future perspectives

The main focus of this thesis was to measure and model the heat flux on the RF antenna in a magnetic environment. There are several factors that affect the heat flux, which includes the average energies of the species responsible for heating the RF electrode, the average potential drop inside the sheath where ions/electrons are accelerated, and potential and density distribution around the RF electrode. The work presented in this thesis is an exploration of these factors by varying the discharge conditions, in order to identify the experimental parameters where the heating of the RF electrode is either minimum or maximum. Additionally, the thesis aimed to explore the possibility of controlling the heat flux.

In this work, it has been verified experimentally and theoretically that the floating potential shift to extremely negative values observed in ALINE is due to stochastic heating. The presence of a hot electron population is confirmed by the Druyvesteyn method near the RF electrode inside the plasma column connected to the RF electrode. The efficiency of the stochastic heating as a function of the tilt angle has been studied using the PIC code for both direct and capacitive coupling discharges. The theoretical model could produce floating potential profiles similar to those observed experimentally.

While experimenting with a one-faced electrode with floating walls at low pressures and a high magnetic field in CCP discharge at grazing angles, the probe connected to the RF electrode measured positive bias on the surface of the RF electrode. At 0.1 T, the electrons are highly magnetized, and their cross-field motion is limited. Weakly magnetized ions are more likely to reach the electrode surface than electrons, biasing the electrode positively. At low pressures, the bias on the electrode was positive even at 6° angle. Measurements were taken using a probe at two different RF power levels of 23 and 35 watts, with pressures of 0.3 and 0.6 Pa and a magnetic field strength of

0.1 T near the RF electrode. This was done in three case studies, and the results confirmed that the electrode maintained a higher potential than the surrounding plasma potential. All these measurements were at a 0° tilt angle, showing that the sheath in front of the RF electrode is reversed. 2D maps of density and floating potential distribution (which represents the hot electron population) around the RF electrode were in the direction of the effective drift calculated using the potential profile near the RF electrode. One of the main challenges during the experiment was to find the plasma potential from the IVs close to the RF electrode. There was a high non-uniformity of IV curves in the X direction (along the diameter) due to hot electron localization caused by E×B drift. A bump appeared after the peak of the first derivative, and two peaks in the second derivative represented hot and thermal electron populations. By fitting the IV curves using a double saturated probe model, the relative population of the thermal and hot electrons were evaluated along the diameter of the RF electrode and found to be highly non-uniform.

Experiments were also performed with a copper electrode with grounded walls as part of a collaboration with L. Marot's group from the Basel University, in the frame of the ITER mirror cleaning project. Sputtering experiments were performed using a one-faced RF electrode with grounded walls in capacitive coupling in order to investigate the reasons behind the formation of highly non-uniform sputtering patterns. Diamagnetic drifts and the E×B drifts were calculated from the 2D potential and density profiles far from the RF electrode. Drift maps revealed that the distribution of plasma density around the RF electrode is decided by the effective drift. At grazing angles, one or the other kind of drift dominates locally, which leads to the non-uniform distribution of the plasma around the RF electrode at grazing angles. This, along with the shape of the sheath, explains the non-uniformity and strong sputtering at the edges. The shift of the population distribution is observed to be in the opposite direction when the magnetic field is reversed, doubling down our interpretation. At higher angles, the drifts counteract each other, forming a low drift region inside the plasma column connected to the RF electrode, which can generate a uniform sputtering pattern. Measurements of 2D density and potential maps were taken for other electrodes, revealing a strong dependence on effective drift velocities. An attempt has been made to benchmark the probe measurements with the fast camera. The camera measures the global rotation speed far from the local drift velocities calculated from the RF-compensated probe data. The dependence on the strength of the magnetic field is studied, and drift velocities are increasing with the decreasing magnetic field due to $V_{dia}, V_{E\times B} \propto 1/\mathrm{B}$. Drifts inside the plasma, especially at grazing angles, create highly asymmetric plasma, leading to the highly non-uniform particle flux and heating of the RF electrode.

In the final chapter, heat flux to the RF electrode was measured using an Optris PI 400i IR camera and TEDDY code for a one-faced RF electrode with a floating ceramic cover as well as for the tungsten RF electrode. In CCP discharge, the heating of the

RF electrode strongly depends on the bias. When the DC self-bias on the electrode is close to zero, both ions and electrons can heat the electrode, though the energy of ions reaching the electrode surface is lower. It can effectively reduce the sputtering of the RF electrode caused by ions, but the heating of the electrode is higher due to electron heating. This can explain the observed high heating of the RF electrode at a higher magnetic field at grazing angles while experimenting with the one-faced RF electrode. Magnetic field improves the confinement and density inside the plasma column right above the RF electrode and is also responsible for higher heating. At low magnetic fields and higher tilt angles, the bias on the RF electrode is negative, repelling the electrons, and ions are responsible for heating the RF electrode, which can be analytically approximated as the Bohm flux. Experiments with tungsten electrodes revealed that heating of the RF electrode is higher in direct coupling compared to the direct coupling. In direct coupling, electrons collected by the RF electrode during the positive half cycle are responsible for the heating of the RF electrode. A simple COMSOL model has been developed to benchmark the experimentally observed time-temperature profile of the RF electrode, giving results close to experimental plots. Even though the heat flux to the RF electrode is higher for the ceramic electrode for the same discharge condition, the final temperature of the electrode is found to be lower than with the pure tungsten electrode in the direct coupling case due to the lower collection area of the heat flux and heat flow to the ceramic covering. For that reason, the "ceramic" electrode is an interesting alternative for long discharge operations.

Several improvements of the presented study could enhance its quality. Although several kinetic or fluid models predict the reversal of the sheath, a simple analytical model to benchmark experimental observation could strengthen the results. 2D maps of density and potential would have enabled the direct comparison with the fast camera results. However, the determination of plasma potential above the RF electrode is a cumbersome task.

The modelling part of the heat flux is incomplete due to several factors. All the modelling is performed under the assumption that the ions are cold and assign uniform temperatures for electrons. Even though a density correction factor is introduced to incorporate the density variations in the Z direction, the non-uniformity of the plasma around the RF electrode is not incorporated. The probe measurements close to the RF electrode are highly challenging, especially at low-pressure discharges, since there is a deviation of the EEDF from the Maxwellian distribution. The current model underestimates the electron flux since it is only capable of evaluating the time-averaged flux.

There are several perspectives this thesis puts forward. Investigation of the efficiency of stochastic heating when the DC self-bias on the surface of the electrode is positive, and with the reversed sheath is worth investigating. Similarly, a PIC model to investigate the drifts in plasma to understand and benchmark the experimental ob-

servation would be really interesting. Even though the reversal of the electric field in front of a conducting surface and acceleration electron to the surface has been investigated using PROES (Phase-resolved optical emission spectroscopy) and PIC modelling in a non-uniform magnetic field, a COMSOL model or a PIC model to investigate non-uniform flux and the hot spot formation locally on the surface of the RF electrode would be fruitful for the fusion physics point of view.

Bibliography

[1] EURO FUSION. https://euro-fusion.org/.

[2] Qingxi Yang, Wei Song, and Qunshan Du. Thermal analysis and optimization of the east icrh antenna. Plasma Science & Technology, 20:25603–025603, 2018.

[3] Francis Chen. Introduction to Plasma Physics and Controlled Fusion. 01 2016.

[4] G Bonizzoni and E Vassallo. Plasma physics and technology; industrial applications. Vacuum, 64(3-4):327–336, 2002.

[5] Francis F Chen. Industrial applications of low-temperature plasma physics. Physics of Plasmas, 2(6):2164–2175, 1995.

[6] J-M Noterdaeme. Interaction between icrh and the plasma edge: an overview. In AIP Conference Proceedings, volume 244, pages 71–87. American Institute of Physics, 1992.

[7] Rudolf Ludwig Neu. Experience with high-z plasma-facing materials and extrapolation to future devices. IEEE transactions on plasma science, 38(3):453–460, 2010.

[8] Mariia Usoltceva. Advancements in Langmuir probe diagnostic for measurements in RF sheath and in modelling of the ICRF slow wave. PhD thesis, 04 2019.

[9] Pascal Chabert. Physcs of Radio-Frequency Plasmas, volume 64. Cambridge University Press, 2011.

[10] Michael Lieberman and Alan Lichtenberg. Principles of plasma discharges and materials processing: Second edition. Principles of Plasma Discharges and Materials Processing, 2nd Edition, by Michael A. Lieberman, Alan J. Lichtenberg, pp. 800. ISBN 0-471-72001-1. Wiley-VCH , September 2003., 30, 09 2003.

[11] J. Ledig. Étude des structures de courant et de potentiel autour d'une antenne radio-fréquence dans un plasma magnétisé. PhD thesis, 09 2020.

[12] Yu.P. Raizer, M.N. Shneider, and Nikolai Yatsenko. Radio-Frequency Capacitive Discharges. 04 1995.

[13] K. Köhler, Donald E. Horne, and J. W. Coburn. Frequency dependence of ion bombardment of grounded surfaces in rf argon glow discharges in a planar system. Journal of Applied Physics, 58:3350–3355, 1985.

[14] K. Köhler, J. W. Coburn, Donald E. Horne, Eric Kay, and John H. Keller. Plasma potentials of 13.56-mhz rf argon glow discharges in a planar system. Journal of Applied Physics, 57:59–66, 1985.

[15] Mark J. Kushner. Distribution of ion energies incident on electrodes in capacitively coupled rf discharges. Journal of Applied Physics, 58:4024–4031, 1985.

[16] A. D. Kuypers and H. J. Hopman. Measurement of ion energy distributions at the powered rf electrode in a variable magnetic field. Journal of Applied Physics, 67:1229–1240, 1990.

[17] Emi Kawamura, Vahid Vahedi, Michael A. Lieberman, and Charles K. Birdsall. Ion energy distributions in rf sheaths; review, analysis and simulation. Plasma Sources Science and Technology, 8, 1999.

[18] E. Faudot. Capacitive and resistive double sheath model in an asymmetric radio frequency plasma discharge. Physics of Plasmas, 22:083506, 2015.

[19] E. Faudot, A. Cherukulappurath Mana, F. Brochard, and S. Heuraux. Effect of the electrode/wall area ratio on the plasma potential in discharge and tokamak plasmas. IEEE Transactions on Plasma Science, 50(4):799–809, 2022.

[20] A. Aanesland, C. Charles, R. W. Boswell, and M. A. Lieberman. Grounded radio-frequency electrodes in contact with high density plasmas. Phys. Plasmas, 12(10):1–7, 2005.

[21] P.C. Stangeby. The Plasma Boundary of Magnetic Fusion Devices. Series in Plasma Physics and Fluid Dynamics. Taylor & Francis, 2000.

[22] P. C. Stangeby. The bohm–chodura plasma sheath criterion. Physics of Plasmas, 2:702–706, 1995.

[23] R. Chodura. Plasma–wall transition in an oblique magnetic field. Physics of Fluids, 25:1628–1633, 1982.

[24] K. U. Riemann. The bohm criterion and sheath formation. Journal of Physics D, 24:493–518, 1991.

[25] K.-U Riemann. Theory of the plasma–sheath transition in an oblique magnetic field. Contributions to Plasma Physics, 34:127 – 132, 01 1994.

[26] Natalia S. Krasheninnikova, Xianzhu Tang, and Vadim S. Roytershteyn. Scaling of the plasma sheath in a magnetic field parallel to the wall. Physics of Plasmas, 17(5):057103, 2010.

[27] J. Moritz, M. Lesur, E. Faudot, S. Devaux, S. Heuraux, and J. Ledig. The plasma-wall transition with collisions and an oblique magnetic field: Reversal of potential drops at grazing incidences. Phys. Plasmas, 26(1):013507, 2019.

[28] J. Moritz, E. Faudot, S. Devaux, and S. Heuraux. The plasma-wall transition layers in the presence of collisions with a magnetic field parallel to the wall. Phys. Plasmas, 25(1):013534, 2018.

[29] Mark Kushner. Modeling of magnetically enhanced capacitively coupled plasma sources: Ar discharges. Journal of Applied Physics, 94:1436–1447, 08 2003.

[30] Oleg A Popov and Valery A Godyak. Power dissipated in low-pressure radio-frequency discharge plasmas. Journal of Applied Physics, 57:53–58, 1985.

[31] V. A. Godyak and R. B. Piejak. Abnormally low electron energy and heating-mode transition in a low-pressure argon rf discharge at 13.56 MHz. Phys. Rev. Lett., 65(8):996–999, 1990.

[32] Michael A. Lieberman. Analytical solution for capacitive rf sheath. IEEE Transactions on Plasma Science, 16:638–644, 1988.

[33] Turner. Pressure heating of electrons in capacitively coupled rf discharges. Physical review letters, 75 7:1312–1315, 1995.

[34] Michael Lieberman and V. Godyak. From fermi acceleration to collisionless discharge heating. Plasma Science, IEEE Transactions on, 26:955 – 986, 07 1998.

[35] Blake P. Wood, Michael A. Lieberman, and Allan J. Lichtenberg. Stochastic electron heating in a capacitive rf discharge with non-maxwellian and time-varying distributions. IEEE Transactions on Plasma Science, 23:89–96, 1995.

[36] Maheswaran Surendra and David Vender. Collisionless electron heating by radio-frequency plasma sheaths. Applied Physics Letters, 65:153–155, 1994.

[37] V Vahedi, C K Birdsall, M. A. Lieberman, G DiPeso, and T D Ronhlien. Capacitive rf discharges modelled by particle-in-cell monte carlo simulation. ii. comparisons with laboratory measurements of electron energy distribution functions. Plasma Sources Science and Technology, 2:273 – 278, 1993.

[38] B.P. Wood. Sheath heating in low-pressure capacitive radio frequency discharges. 01 1991.

[39] M.A. Lieberman, A.J. Lichtenberg, and S.E. Savas. Model of magnetically enhanced, capacitive rf discharges. IEEE Transactions on Plasma Science, 19(2):189–196, 1991.

[40] V. Godyak, R. Piejak, and Benjamin Alexandrovich. Probe diagnostics of non-maxwellian plasmas. Journal of Applied Physics, 73:3657 – 3663, 05 1993.

[41] C.E. Thomas, Jeffrey Harris, G. HASTE, Christopher Klepper, J. HOGAN, S. TOBIN, F. BAITY, Ralph Isler, T. UCKAN, D. BATCHELOR, Mark Carter, P. RYAN, D. HOFFMAN, TEAM, , B. SAOUTIC, B. BEAUMONT, A. BECOULET, H. KUUS, and and SUPRA. Icrf/edge interaction guidelines for icrf antenna design, and initial icrf/edge interaction experiments on the tore supra tokamak. Fusion Science and Technology, 30:1, 09 1996.

[42] J. Sorensen, D.A. Diebold, R. Majeski, and N. Hershkowitz. Comparison of the effects of an icrf antenna with insulating side limiters with and without a faraday screen on the edge parameters of a tokamak plasma. Nuclear Fusion, 33:915, 11 2002.

[43] E. Faudot, Stephane Heuraux, and L. Colas. Parametric study of 2d potential structures induced by rf sheaths coupled with transverse currents in front of icrh antenna. Czechoslovak Journal of Physics, 55:243–254, 03 2005.

[44] Christopher Klepper, D. Borodin, Mathias Groth, Ane Lasa, Markus Airila, V Bobkov, L Colas, Philippe Jacquet, A Kirschner, Alexis Terra, Theodore Biewer, Ephrem Delabie, and C Giroud. Estimates of rf-induced erosion at antenna-connected beryllium plasma-facing components in jet. Physica Scripta, 2016:014035, 02 2016.

[45] E. Faudot, S. Devaux, J. Moritz, S. Heuraux, P. Molina Cabrera, and F. Brochard. A linear radio frequency plasma reactor for potential and current mapping in a magnetized plasma. Rev. Sci. Instrum., 86(6):063502, 2015.

[46] Stephane Devaux, E. Faudot, J. Moritz, and Stephane Heuraux. Aline: A device dedicated to understanding radio-frequency sheaths. Nuclear Materials and Energy, 12, 07 2017.

[47] Paul Hiret, Kunal Soni, Anil Cherukulappurath Mana, Eric Faudot, Lucas Moser, Roland Steiner, Alessandro Geraldini, Stefano Alberti, Ivo Furno, Jérôme Moritz, Frédéric Brochard, Stéphane Heuraux, Laurent Marot, and Ernst Meyer. Plasma

sputtering of biased electrodes in an oblique magnetic field. Plasma Sources Science and Technology, 2023.

[48] Milan Tichy, P Kudrna, J Behnke, C. Csambal, and S. Klagge. Langmuir probe diagnostics for medium pressure and magnetised low-temperature plasma. http://dx.doi.org/10.1051/jp4:1997432, 7, 10 1997.

[49] Elke Passoth, P Kudrna, C Csambal, J Behnke, Milan Tichy, and V Helbig. An experimental study of plasma density determination by a cylindrical langmuir probe at different pressures and magnetic fields in a cylindrical magnetron discharge in heavy rare gases. Journal of Physics D: Applied Physics, 30:1763, 01 1999.

[50] Tsv Popov, Miglena Dimitrova, Pavlina Ivanova, Jernej Kovačič, Tomaz Gyergyek, R. Dejarnac, J. Stockel, M Pedrosa, Daniel López-Bruna, and Carlos Hidalgo. Advances in langmuir probe diagnostics of the plasma potential and electron-energy distribution function in magnetized plasma. Plasma Sources Science and Technology, 25:033001, 03 2016.

[51] Francis Chen. Langmuir probes in rf plasma: Surprising validity of oml theory. Plasma Sources Science and Technology, 18:035012, 05 2009.

[52] V. Godyak, Vladimir Meytlis, and Henry Strauss. Tonks–langmuir problem for a bi-maxwellian plasma. Plasma Science, IEEE Transactions on, 23:728 – 734, 09 1995.

[53] Mariia Usoltceva, Eric Faudot, Stephane Devaux, Stephane Heuraux, Jordan Ledig, Georgiy Zadvitskiy, Roman Ochoukov, Kristel Crombe, and Jean-Marie Noterdaeme. Effective collecting area of a cylindrical langmuir probe in magnetized plasma. Physics of Plasmas, 25:063518, 06 2018.

[54] Hiden ESPion. Advanced langmuir probe for plasma diagnostics characterisation. https://www.hidenanalytical.com/wp-content/uploads/2020/06/ESPion.pdf, verified on September 2023 2023.

[55] P.A Chatterton, John Rees, W.L Wu, and K ALASSADI. A self-compensating langmuir probe for use in rf (13.56 mhz) plasma systems. Vacuum, 42:489–493, 12 1991.

[56] H. Mott-Smith and Irving Langmuir. The theory of collectors in gaseous discharges. Physical Review - PHYS REV X, 28:727–763, 01 1926.

[57] L Pilling and Dale Carnegie. Validating experimental and theoretical langmuir probe analyses. Plasma Sources Science and Technology, 16:570, 06 2007.

[58] Ian H Hutchinson. Principles of plasma diagnostics. Plasma Physics and Controlled Fusion, 44(12):2603–2603, 2002.

[59] Jordan Ledig, Eric Faudot, J. Moritz, Stephane Heuraux, Nicolas Lemoine, and Stephane Devaux. Experimental and theoretical study of density, potential and current structures of a helium plasma in front of a rf antenna tilted with respect to the magnetic field lines. Contributions to Plasma Physics, 07 2020.

[60] J Ledig, E Faudot, J Moritz, S Heuraux, N Lemoine, and M Usoltceva. Experimental and theoretical study of bumped characteristics obtained with cylindrical langmuir probe in magnetized helium plasma. Plasma Sources Science and Technology, 29(3):035007, 2020.

[61] A. Cherukulappurath, E. Faudot, Frédéric Brochard, Stephane Heuraux, Paul Hiret, L. Marot, Kunal Soni, and Lucas Moser. Langmuir probe measurements in a magnetized capacitive discharge around a tilted rf electrode. page 040008, 01 2023.

[62] E. Faudot, A. Cherukulappurath, Frédéric Brochard, and Stephane Heuraux. Pic simulation of the electron energy distribution function in a rf magnetized plasma column connected to a tilted electrode. page 060001, 01 2023.

[63] Petr Vondráček. Plasma heat flux to solid structures in tokamaks. 2019.

[64] DJ Nille. Bayesian Inference of Heat Load Patterns in ASDEX Upgrade. PhD thesis, Technische Universität Graz Graz, 2020.

[65] I Balboa, G Arnoux, T Eich, B Sieglin, S Devaux, W Zeidner, C Morlock, U Kruezi, G Sergienko, D Kinna, et al. Upgrade of the infrared camera diagnostics for the jet iter-like wall divertor. Review of Scientific Instruments, 83(10), 2012.

[66] B Sieglin, M Faitsch, A Herrmann, B Brucker, T Eich, L Kammerloher, and S Martinov. Real time capable infrared thermography for asdex upgrade. Review of Scientific Instruments, 86(11), 2015.

[67] E Gauthier, H Roche, E Thomas, S Droineau, B Bertrand, JB Migozzi, W Vliegenthart, L Dague, P Andrew, T Tiscornia, et al. Iter-like wide-angle infrared thermography and visible observation diagnostic using reflective optics. Fusion Engineering and Design, 82(5-14):1335–1340, 2007.

[68] Masaki Takeuchi, Tatsuo Sugie, Hiroaki Ogawa, Masao Ishikawa, Takahiko Shimada, and Yoshinori Kusama. Development of divertor ir thermography for iter. Plasma and Fusion Research, 8:2402147–2402147, 2013.

[69] Adrien Autricque. Dust transport in tokamaks. PhD thesis, Aix-Marseille, 2018.

[70] Nicolas Fedorczak, Jonathan Gaspar, Mehdi Firdaouss, V. Moncada, Alex Grosjean, R. Dejarnac, Sebastijan Brezinsek, E Tsitrone, J. Bucalossi, and Th Loarer. Infra-red thermography estimate of deposited heat load dynamics on the lower tungsten divertor of west. Physica Scripta, T171:014046, 03 2020.

[71] Nobuhiro Nishino, Yousuke Nakashima, Yuta Higashizono, Shinji Kobayashi, Yuusuke Kubota, Masayuki Yoshikawa, Yoshiyuki Mishima, and ting ting Cho. First observation of plasma motion in gamma 10 using a fast camera. Plasma and Fusion Research, 1:35–035, 09 2006.

[72] Davoud Iraji, Ahmed Diallo, A Fasoli, I. Furno, and S Shibaev. Fast visible imaging of turbulent plasma in torpex. The Review of scientific instruments, 79:10F508, 11 2008.

[73] Ghassan Antar, Jonathan Yu, and George Tynan. The origin of convective structures in the scrape-off layer of linear magnetic fusion devices investigated by fast imaging. Physics of Plasmas, 14, 02 2007.

[74] L. Cui, George Tynan, Patrick Diamond, Saikat Thakur, and C. Brandt. Upgradient particle flux in a drift wave-zonal flow system. Physics of Plasmas, 22:050704, 05 2015.

[75] Adam Light, Saikat Thakur, C. Brandt, Yancey Sechrest, George Tynan, and Tobin Munsat. Direct extraction of coherent mode properties from imaging measurements in a linear plasma column. Physics of Plasmas, 20, 08 2013.

[76] Simon Vincent. Azimuthal waves modification by current injection in a magnetized plasma column. PhD thesis, 12 2021.

[77] https://photron.com/fastcam-sa-z-2/?gclid=cj0kcqjwpc-obhcgarisah6ote9c6gagtqageb0irqqkxehcxamkaavxzpwfvo$_u$*de*6*ebicysebneusaat*5*aealw*$_w$*cb*.

[78] V A Godyak, R B Piejak, and B M Alexandrovich. Plasma Sources Science and Technology Measurement of electron energy distribution in low-pressure RF discharges Measurements of electron energy distribution in low-pressure R F discharges. Plasma Sources Sci. Technol, 18:36–58, 1992.

[79] D. Vender and Rod Boswell. Electron–sheath interaction in capacitive radio-frequency plasmas. Journal of Vacuum Science Technology A: Vacuum, Surfaces, and Films, 10:1331 – 1338, 08 1992.

[80] Harold M Mott-Smith and Irving Langmuir. The theory of collectors in gaseous discharges. Physical review, 28(4):727, 1926.

[81] JE Allen. Probe theory-the orbital motion approach. Physica Scripta, 45(5):497, 1992.

[82] MA Lieberman, GS Selwyn, and M Tuszewski. Plasma generation for materials processing. Mrs Bulletin, 21(8):32–37, 1996.

[83] K. Bartschat S.F. Biagi M.C. Bordage I. Bray C.E. Brion; M.J. Brunger L. Campbell A. Chachereau B. Chaudhury L. G. Christophorou E. Carbone N. A. Dyatko C. M. Franck D. V. Fursa R. K. Gangwar V. Guerra P. Haefliger G. J. M. Hagelaar A. Hoesl Y. Itikawa I. V. Kochetov R. P. McEachran W. L. Morgan A. P. Napartovich V. Puech M. Rabie L. Sharma R. Srivastava A. D. Stauffer J. Tennyson J. de Urquijo J. van Dijk L. A. Viehland M. C. Zammit O. Zatsarinny S. Pancheshnyi L.C. Pitchford, L.L. Alves.

[84] A.I. Akhiezer and A.S. Bakai. Stochastic plasma heating by rf fields. Sov. J. Plasma Phys. (Engl. Transl.); (United States), 2:4, 07 1976.

[85] Thomas Mussenbrock, R Brinkmann, M Lieberman, A Lichtenberg, and E Kawamura. Enhancement of ohmic and stochastic heating by resonance effects in capacitive radio frequency discharges: A theoretical approach. Physical review letters, 101:085004, 09 2008.

[86] Capacitive Discharges, chapter 11, pages 387–460. John Wiley Sons, Ltd, 2005.

[87] Tsv Popov, Miglena Dimitrova, M Pedrosa, Daniel López-Bruna, J. Horacek, Jernej Kovačič, R. Dejarnac, J. Stockel, Milan Aftanas, P Böhm, Petra Bilkova, Carlos Hidalgo, and Radomir Panek. Bi-maxwellian electron energy distribution function in the vicinity of the last closed flux surface in fusion plasma. Plasma Physics and Controlled Fusion, 57:115011, 10 2015.

[88] M. A.Mansour Elsabbagh, M. D. Bowden, K. Uchino, and K. Muraoka. Observations of bi-Maxwellian and single Maxwellian electron energy distribution functions in a capacitively coupled radio-frequency plasmas by laser Thomson scattering. Appl. Phys. Lett., 78(21):3187–3189, 2001.

[89] M. M. Turner, D. A.W. Hutchinson, R. A. Doyle, and M. B. Hopkins. Heating mode transition induced by a magnetic field in a capacitive rf discharge. Phys. Rev. Lett., 76(12):2069–2072, 1996.

[90] T. Lafleur, P. Chabert, and J. P. Booth. Electron heating in capacitively coupled plasmas revisited. Plasma Sources Sci. Technol., 23(3), 2014.

[91] V Vahedi, C K Birdsall, M A Lieberman, G DiPeso, and T D Ronhlien. Capacitive RF discharges modelled by particle-in-cell monte carlo simulation. II. comparisons with laboratory measurements of electron energy distribution functions. Plasma Sources Science and Technology, 2(4):273–278, nov 1993.

[92] D. Ruscanu, V. Anita, and G. Popa. Plasma parameters in a multidipole plasma system. The European Physical Journal D, 10:449–456, 01 2000.

[93] J.P. Verboncoeur, A.B. Langdon, and Tom Gladd. An object-oriented electromagnetic pic code. Computer Physics Communications, 87:199–211, 05 1995.

[94] H. Mott-Smith and Irving Langmuir. The theory of collectors in gaseous discharges. Physical Review - PHYS REV X, 28:727–763, 01 1926.

[95] K. Günther and Andrew Carlson. Fluid theory of langmuir probes in a magnetized plasma with open flux tubes. Contributions to Plasma Physics, 34:484 – 489, 01 1994.

[96] L. Colas, S. Heuraux, S. Brémond, and G. Bosia. RF current distribution and topology of RF sheath potentials in front of ICRF antennae. Nucl. Fusion, 45(8):767–782, 2005.

[97] Spilios Riyopoulos. Effects of static magnetic fields on rf-driven plasma sheaths. Phys. Plasmas, 3(7):2511–2522, 1996.

[98] Spilios Riyopoulos. Theory of magnetized, coupled, rf-driven plasma sheaths in one dimension. Phys. Rev. E - Stat. Physics, Plasmas, Fluids, Relat. Interdiscip. Top., 59(1):1111–1121, 1999.

[99] R. Chodura. Plasma-wall transition in an oblique magnetic field. Phys. Fluids, 25(9):1628–1633, 1982.

[100] P.C. Stangeby. The Plasma Boundary of Magnetic Fusion Devices. Series in Plasma Physics and Fluid Dynamics. Taylor & Francis, 2000.

[101] D. L. Holland, B. D. Fried, and G. J. Morales. Sheath structure in a magnetized plasma. Phys. Fluids B, 5(6):1723–1737, 1993.

[102] K. Theilhaber and C. K. Birdsall. Kelvin-Helmholtz vortex formation and particle transport in a cross-field plasma sheath. Phys. Rev. Lett., 62(7):772–775, 1989.

[103] Th Daube, K. U. Riemann, and H. Schmitz. Particle simulation of a magnetized plasma contacting the wall. Phys. Plasmas, 5(1):117–126, 1998.

[104] M Oberberg, J Kallähn, P Awakowicz, and J Schulze. Experimental investigations of the magnetic asymmetry effect in capacitively coupled radio frequency plasmas. Plasma Sources Science and Technology, 27(10):105018, oct 2018.

[105] J. Rubinstein and J. G. Laframboise. Upper-bound current to a cylindrical probe in a collisionless magnetoplasma. The Physics of Fluids, 21(9):1655, 1978.

[106] A. H. Sato and M. A. Lieberman. Electron-beam probe measurements of electric fields in rf discharges. J. Appl. Phys., 68(12):6117–6124, 1990.

[107] Soon-Youl So. Simulations of Capacitively Coupled Plasmas Between Unequal-sized Powered and Grounded Electrodes Using One- and Two-dimensional Fluid Models. KIEE Int. Trans. EA, , No. 5, pp. 220-229,, Vol. 4-C, 2004.

[108] M. Campanell. Entire plasmas can be restructured when electrons are emitted from the boundaries. Physics of Plasmas, 22:040702, 04 2015.

[109] Francesco Taccogna. Non-classical plasma sheaths: Space-charge-limited and inverse regimes under strong emission from surfaces. The European Physical Journal D, 68, 07 2014.

[110] Rebecca Masline, Roman Smirnov, and Sergei Krasheninnikov. Influence of the inverse sheath on divertor plasma performance in tokamak edge plasma simulations. Contributions to Plasma Physics, 60, 12 2019.

[111] M. Campanell. Possible mitigation of tokamak plasma–surface interactions using thermionic divertor plates with inverse sheaths. Physics of Plasmas, 27:042511, 04 2020.

[112] Xu Wang, Juliet Pilewskie, H.-W Hsu, and Mihaly Horanyi. Plasma potential in the sheaths of electron-emitting surfaces in space. Geophysical Research Letters, 43:n/a–n/a, 01 2016.

[113] V. Godyak and V. Demidov. Probe measurements of electron-energy distributions in plasmas: What can we measure and how can we achieve reliable results? Journal of Physics D: Applied Physics, 44:233001, 05 2011.

[114] Ilarion Mihaila, Stefan Costea, C. Costin, and G. Popa. On negative slope of probe characteristics in magnetized plasmas. Contributions to Plasma Physics, 54, 04 2014.

[115] Francis Chen. Langmuir probe measurements in the intense rf field of a helicon discharge. Plasma Sources Science Technology - PLASMA SOURCES SCI TECHNOL, 21, 10 2012.

[116] ChinWook Chung. Experimental investigation on the floating potential of cylindrical langmuir probes in non-maxwellian electron distributions. Physics of Plasmas, 12:123505–123505, 12 2005.

[117] D Darian, Sigvald Marholm, Mikael Mortensen, and W Miloch. Theory and simulations of spherical and cylindrical langmuir probes in non-maxwellian plasmas. Plasma Physics and Controlled Fusion, 61:085025, 08 2019.

[118] P Stangeby. A problem in the interpretation of tokamak langmuir probes when a fast electron component is present. Plasma Physics and Controlled Fusion, 37:1031, 01 1999.

[119] Laurent Marot, E Meyer, Marek Rubel, D Ivanova, A Widdowson, JP Coad, Jari Likonen, Antti Hakola, Seppo Koivuranta, G De Temmerman, et al. Performances of rh and mo mirrors under jet exposure. Journal of Nuclear Materials, 438:S1187–S1191, 2013.

[120] Marek Rubel, Sunwoo Moon, Per Petersson, A Widdowson, RA Pitts, S Aleiferis, E Fortuna-Zaleśna, G De Temmerman, and R Reichle. First mirror erosion–deposition studies in jet using an iter-like mirror test assembly. Nuclear Fusion, 61(4):046022, 2021.

[121] A Litnovsky, Vladimir S Voitsenya, Roger Reichle, M Walsh, Alexey Razdobarin, Artem Dmitriev, N Babinov, Laurent Marot, Lucas Moser, Rong Yan, et al. Diagnostic mirrors for iter: research in the frame of international tokamak physics activity. Nuclear Fusion, 59(6):066029, 2019.

[122] Kunal Soni, Santhosh Iyyakkunnel, Roland Steiner, Rodrigo Antunes, Lucas Moser, Oliver Bieri, Laurent Marot, and Ernst Meyer. Effect of 3T magnetic field on RF plasma sputtering in a ITER-relevant first mirror unit. Nucl. Fusion, 2022.

[123] Rong Yan, Lucas Moser, Baoguo Wang, Jiao Peng, Christian Vorpahl, Frank Leipold, Roger Reichle, Rui Ding, Junling Chen, Lei Mu, et al. Plasma cleaning of iter edge thomson scattering mock-up mirror in the east tokamak. Nuclear Fusion, 58(2):026008, 2017.

[124] Jun Takeda, Atsushi Nezu, and Hiroshi Akatsuka. Drift of electrons in a radial electric field and longitudinal magnetic field. IEEE Transactions on Plasma Science, 47(9):4250–4259, 2019.

[125] GJM Hagelaar and Noureddine Oudini. Plasma transport across magnetic field lines in low-temperature plasma sources. Plasma Physics and Controlled Fusion, 53(12):124032, 2011.

[126] Miles Turner. Collisionless heating in radio-frequency discharges: A review. Journal of Physics D: Applied Physics, 42:194008, 09 2009.

[127] Mark Carter, P. Ryan, D. Hoffman, W. Lee, D Buchberger, and V. Godyak. Combined rf and transport effects in magnetized capacitive discharges. Journal of Applied Physics - J APPL PHYS, 100, 10 2006.

[128] Geun Yeom and Mark Kushner. Magnetic field effects on cylindrical magnetron reactive ion etching of si/sio2 in cf4 and cf4/h2 plasmas. Journal of Vacuum Science Technology A: Vacuum, Surfaces, and Films, 7:987 – 992, 06 1989.

[129] Yashashri Patil, Shikha Binwal, and S. Karkari. Fluid modeling of exb drift occurs in magnetized ccp discharge using comsol multiphysics. 11 2019.

[130] Dennis Gerst, Stéphane Cuynet, Mihaela Cirisan, and S. Mazouffre. Plasma drift in a low-pressure magnetized radio frequency discharge. Plasma Sources Sci. Technol., 22:015024, 02 2013.

[131] Melisa Buie, J. Pender, and M. Dahimene. Characterization of the etch rate non-uniformity in a magnetically enhanced reactive ion etcher. Journal of Vacuum Science Technology A: Vacuum, Surfaces, and Films, 16:1464 – 1468, 06 1998.

[132] R.A. Lindley, C.H. Bjorkman, H. Shan, K.-H Ke, K. Doan, Richard Mett, and M. Welch. Magnetic field optimization in a dielectric magnetically enhanced reactive ion etch reactor to produce an instantaneously uniform plasma. Journal of Vacuum Science Technology A: Vacuum, Surfaces, and Films, 16:1600–1603, 05 1998.

[133] Swati Dahiya, Pawandeep Singh, Satadal Das, Nishant Sirse, and Shantanu Karkari. Magnetic field induced electron temperature inhomogeneity effects on discharge properties in cylindrical capacitively coupled plasmas. Physics Letters A, 468:128745, 03 2023.

[134] Etienne Gravier, Emmanuel Plaut, Xavier Caron, and Mathieu Jenny. Transitions between drift waves in a magnetized cylindrical plasma: experiments and fluid model, solved with a spectral method. The European Physical Journal D, 67:1–8, 2013.

[135] Francis Chen and Jane Chang. Langmuir Probes, pages 79–93. 01 2003.

[136] Stewart J. Zweben, J. L. Terry, D. P. Stotler, and Ricardo Jose Maqueda. Invited review article: Gas puff imaging diagnostics of edge plasma turbulence in magnetic fusion devices. The Review of scientific instruments, 88 4:041101, 2017.

[137] S. Oldenbürger, Christian Brandt, F. Brochard, N. Lemoine, and Gérard Bonhomme. Spectroscopic interpretation and velocimetry analysis of fluctuations in a cylindrical plasma recorded by a fast camera. The Review of scientific instruments, 81 6:063505, 2010.

[138] Albert Simon. Instability of a partially ionized plasma in crossed electric and magnetic fields. The physics of fluids, 6(3):382–388, 1963.

[139] FC Hoh. Instability of penning-type discharges. The physics of fluids, 6(8):1184–1191, 1963.

[140] Y-Q Tao, RW Conn, L Schmitz, and G Tynan. Ion flow in a strongly sheared electric field. Physics of Fluids B: Plasma Physics, 5(2):344–349, 1993.

[141] Y-Q Tao, RW Conn, L Schmitz, and G Tynan. Collisionless simon–hoh instability in a strongly double-sheared electric field. Physics of plasmas, 1(10):3193–3198, 1994.

[142] Kentaro Hara, Adnan R Mansour, and Sedina Tsikata. Theory of gradient drift instabilities in low-temperature, partially magnetised plasmas. Journal of Plasma Physics, 88(4):905880408, 2022.

[143] Y Sakawa, C Joshi, PK Kaw, FF Chen, and VK Jain. Excitation of the modified simon–hoh instability in an electron beam produced plasma. Physics of Fluids B: Plasma Physics, 5(6):1681–1694, 1993.

[144] https://www.impedans.com/octiv-mono-rf wattmeter/. Impedance plasma measurements, Verified: September 2023.

[145] CL Ellison, Y Raitses, and Nathaniel J Fisch. Cross-field electron transport induced by a rotating spoke in a cylindrical hall thruster. Physics of Plasmas, 19(1), 2012.

[146] JB Parker, Y Raitses, and NJ Fisch. Transition in electron transport in a cylindrical hall thruster. Applied Physics Letters, 97(9), 2010.

[147] AN James, D Brunner, B Labombard, C Lau, B Lipschultz, D Miller, ML Reinke, JL Terry, C Theiler, GM Wallace, et al. Imaging of molybdenum erosion and thermography at visible wavelengths in alcator c-mod icrh and lhcd discharges. Plasma Physics and Controlled Fusion, 55(12):125010, 2013.

[148] R Dux, V Bobkov, N Fedorczak, K Iraschko, A Kallenbach, R Neu, T Pütterich, V Rohde, ASDEX Upgrade Team, et al. Tungsten erosion at the icrh limiters in asdex upgrade. Journal of nuclear materials, 363:112–116, 2007.

[149] SJ Wukitch, B Lipschultz, E Marmar, Y Lin, A Parisot, M Reinke, J Rice, J Terry, and C-Mod Team. Rf plasma edge interactions and their impact on icrf antenna performance in alcator c-mod. Journal of nuclear materials, 363:491–497, 2007.

[150] John Belton O'Neall Caughman II. The distribution of ion energies incident on an ICRH antenna Faraday shield. University of Illinois at Urbana-Champaign, 1989.

[151] DC Pace, RS Granetz, R Vieira, A Bader, J Bosco, DS Darrow, C Fiore, J Irby, RR Parker, W Parkin, et al. Energetic ion loss detector on the alcator c-mod tokamak. Review of Scientific Instruments, 83(7), 2012.

[152] Ph Moreau, O Barana, S Brémond, L Colas, A Ekedahl, F Saint-Laurent, C Balorin, G Caulier, C Desgranges, D Guilhem, et al. Rf heating optimization on tore supra using feedback control of infrared measurements. Fusion Engineering and Design, 82(5-14):1030–1035, 2007.

[153] ML Garrett and SJ Wukitch. Mitigation of radio frequency sheaths through magnetic field-aligned icrf antenna design. Fusion Engineering and Design, 87(9):1570–1575, 2012.

[154] V. Bobkov, Diogo Aguiam, Roberto Bilato, Sebastijan Brezinsek, L. Colas, Agata Chomiczewska, P. Dumortier, R. Dux, H. Faugel, H. Fünfgelder, Ph Jacquet, A. Kallenbach, Alena Krivska, Christopher Klepper, E. Lerche, Y. Lin, Daniele Milanesio, Riccardo Maggiora, I. Monakhov, and Wei Zhang. Impact of icrf on the scrape-off layer and on plasma wall interactions: From present experiments to fusion reactor. Nuclear Materials and Energy, 18:131–140, 01 2019.

[155] H Kersten, Eva Stoffels, Winfred Willem Stoffels, M Otte, C Csambal, H Deutsch, and R Hippler. Energy influx from an rf plasma to a substrate during plasma processing. Journal of Applied Physics, 87(8):3637–3645, 2000.

[156] Matthias Wolter, Marc Stahl, and Holger Kersten. Spatially resolved thermal probe measurement for the investigation of the energy influx in an rf-plasma. Vacuum, 83(4):768–772, 2008.

[157] BB Sahu and Jeon G Han. Comparison of plasma excitation, ionization, and energy influx in single and dual frequency capacitive discharges. Physics of Plasmas, 23(12), 2016.

[158] Pierre-Antoine Cormier, Marc Stahl, Anne-Lise Thomann, Rémi Dussart, Matthias Wolter, Nadjib Semmar, Jacky Mathias, and Holger Kersten. On the measurement of energy fluxes in plasmas using a calorimetric probe and a thermopile sensor. Journal of Physics D: Applied Physics, 43(46):465201, 2010.

[159] Ruben Wiese, Holger Kersten, Georg Wiese, and René Bartsch. Energy influx measurements with an active thermal probe in plasma-technological processes. EPJ Techniques and Instrumentation, 2:1–10, 2015.

[160] Jan Benedikt, Holger Kersten, and Alexander Piel. Foundations of measurement of electrons, ions and species fluxes toward surfaces in low-temperature plasmas. Plasma Sources Science and Technology, 30(3):033001, 2021.

[161] W. Eckstein and J. Biersack. Reflection of heavy ions. Zeitschrift für Physik B Condensed Matter, 63:471–478, 12 1986.

[162] M. Goto and K. Sawada. Determination of electron temperature and density at plasma edge in the large helical device with opacity-incorporated helium collisional-radiative model. Journal of Quantitative Spectroscopy and Radiative Transfer, 137:23–28, 04 2014.

[163] Jonathan Gaspar, M.-H Aumeunier, Mickaël Le Bohec, Fabrice Rigollet, Sebastijan Brezinsek, Y. Corre, Xavier Courtois, R. Dejarnac, Mathilde Diez, L. Dubus, Nicolas Fedorczak, M. Houry, V. Moncada, P. Moreau, Christine Pocheau, Charly Talatizi, and

E. Tsitrone. In-situ assessment of the emissivity of tungsten plasma facing components of the west tokamak. Nuclear Materials and Energy, 25:100851, 12 2020.

[164] Etienne Brodu, M. Balat-Pichelin, Jean-Louis Sans, and J. Kasper. Influence of roughness and composition on the total emissivity of tungsten, rhenium and tungsten–25 Journal of Alloys and Compounds, 585:510–517, 02 2014.

[165] RSgroup. https://docs.rs-online.com/31af/a700000007660830.pdf.

[166] Michael Vollmer and Klaus-Peter Möllmann. Infrared Thermal Imaging: Fundamentals, Research and Applications. 10 2013.

[167] E. Barnat, P Miller, and Alex Paterson. Rf discharge under the influence of a transverse magnetic field. Plasma Sources Science and Technology, 17:045005, 08 2008.

[168] Birk Berger, Denis Eremin, Moritz Oberberg, Dennis Engel, Christian Wölfel, Quan-Zhi Zhang, Peter Awakowicz, Jan Lunze, Ralf Peter Brinkmann, and Julian Schulze. Electron dynamics in planar radio frequency magnetron plasmas: Iii. comparison of experimental investigations of power absorption dynamics to simulation results. Plasma Sources Science and Technology, 32(4):045009, 2023.

[169] D Eremin, B Berger, D Engel, J Kallähn, K Köhn, D Krüger, L Xu, M Oberberg, C Wölfel, J Lunze, et al. Electron dynamics in planar radio frequency magnetron plasmas: Ii. heating and energization mechanisms studied via a 2d3v particle-in-cell/monte carlo code. Plasma Sources Science and Technology, 32(4):045008, 2023.

Résumé

Le chauffage excessif d'une électrode ou d'une antenne RF en raison d'un flux de chaleur élevé est un problème majeur dans la réalisation d'un futur réacteur à fusion thermonucléaire ou dans les application de plasma de décharge. L'accélération des ions dans le potentiel redressé des gaines RF devant l'antenne peut éroder le matériau et créer des impuretés à l'intérieur du plasma. Le chauffage dû aux électrons rapides peut également augmenter la température de surface et faire fondre le matériau, limitant l'efficacité du couplage de puissance de l'antenne.

Dans le but de diminuer le flux de chaleur reçue par les dispositifs de chauffage RF (ICRF, électrode RF) ou de l'augmenter dans des dispositifs de nettoyage des miroirs utilisés dans les systèmes de chauffage électronique, des études paramétriques ont été menées pour mesurer les paramètes plasma autour d'une électrode RF de référence. Cette thèse tente donc de comprendre et de mesurer expérimentalement ces flux de chaleur reçus grâce à une électrode dont on peut modifier l'angle d'inclinaison avec le champ magnétique, tout en les comparant à un modèle théorique.

Les expériences ont été réalisées dans le dispositif expérimental ALINE (A LINEaire) avec trois électrodes différentes utilisant deux mécanismes de couplage RF (couplage direct et capacitif). Des expériences d'érosion sont réalisées en utilisant une électrode cuivre entouré d'un bouclier thermique mise à la terre. Les mesures par sonde de Langmuir ont révélé que le motif d'érosion inhomogène à la surface d'une électrode est dû à la distribution non uniforme de la densité du plasma causée par les dérives ExB et diamagnétique ainsi que par des flux d'électrons rapides générés par la gaine RF.

L'échauffement de l'électrode RF est mesuré à l'aide d'une caméra infrarouge, et le flux de chaleur est calculé à l'aide du code TEDDY pour différentes électrodes en tungstène. Dans les décharges capacitives, les mesures de sonde près de l'électrode RF montrent une auto-polarisation positive et une inversion de la gaine à champs magnétiques élevés et basses pressions (0,6 Pa, 0,1 T). Un échauffement plus élevé de l'électrode RF est observé lorsque l'auto-polarisation est positive. Des expériences supplémentaires avec l'électrode en tungstène ont montré un échauffement plus élevé en couplage direct qu'en couplage capacitif. Enfin les flux de chaleur mesurés sont plus importants en incidence rasante et à plus fort champ magnétique.

Mots-clés: Flux thermique,mesures de sonde de Langmuir, caméra IR, gaine RF.

Abstract

Excessive heating of the RF electrode/antenna due to high heat flux has detrimental impacts on fusion or plasma material processing perspectives. Acceleration of ions in the rectified potential in front of the RF antenna can sputter the material and create impurities inside the plasma. Heating due to electrons can raise the surface temperature and melt the material, eventually reducing the power coupling efficacy of the antenna. Since ion cyclotron resonance heating (ICRH) is one of the auxiliary heating mechanisms in modern fusion reactors and a new system is being developed based on capacitive coupling discharge for first mirror cleaning in tokamaks, investigations of particle flux/heat flux to the antenna/electrode surface in a magnetized RF environment has supreme importance. The presented thesis attempts to understand factors affecting heat flux by performing an experimental exercise and benchmarking the same with simple analytical/theoretical models. Experiments are performed in the ALINE (A LINEar) Experimental device with three electrodes using two RF power coupling mechanisms (Direct and capacitive coupling). Sputtering experiments are performed using RF electrodes with a grounded copper wall. RF compensated Langmuir probe measurements revealed that the in-homogeneous sputtering pattern is due to the non-uniform distribution of the plasma density around the RF electrode caused by the drift and hot electron beams due to stochastic heating at the surface of the RF sheaths. This can also lead to non-uniform heating of the RF electrode. The heating of the RF electrode is measured using an IR camera, and heat flux is calculated using the code TEDDY for the one-faced tungsten and pure tungsten electrodes. In CCP mode, probe measurements near the one-faced RF electrode show positive bias and reversal of the electric field in front of the RF electrode at high magnetic fields and low pressures (0.6 Pa, 0.1 T). Higher heating of the RF electrode is observed when the bias is positive, meaning the positive bias can reduce the sputtering of the RF electrode by pushing the positive ions back into the plasma, but not the heating. Experiments with the tungsten electrode showed higher heating of the RF electrode in direct coupling than in capacitive coupling. Higher heat flux and normalized heat flux (normalization with density) are measured for direct coupling at 0° tilt angle than the grazing angle (5°).

Keywords: Heat flux, RF-compensated Langmuir probe, IR camera, RF sheath.